

https://dspace.org/

Sedimentology and structural geology of the Gariep belt in Southern Namibia.

Jasper, Marold Jens Uwe

1994
https://hdl.handle.net/10539/25466

Downloaded from a DSpace repository. https://dspace.org/

SEDIMENTOLOGY AND STRUCTURAL GEOLOGY OF THE GARIEP BELT IN SOUTHERN NAMIBIA

Marold Jens Uwe Jasper

A Dissertation Submitted to the Faculty of Science, University of the Witwatersrand, Johannesburg, in Fulfilment of the Requirements of the Degree of Doctor of Philosophy.

Johannesburg, July 1994.



The objects stayed firm but the opinions moved manyfold.

Goethe (1817): About the knowledge of the Bohemian Orogen.

In the mountains and nowhere else is the place where one has to study the natural history of the earth.

J.A. de Luc (1778): Phys. and moral letters about the mountains.

ABSTRACT

The Gariep Belt is an arcuate north-south trending tectonic unit extending along the western coast of southern Namibia and northwestern South Africa. It forms part of the Pan-African Damara Orogen, which consists of a north-south trending coastal branch (Kaoko and Gariep Belts) and an east-west trending inland branch. The Gariep Belt is subdivided into an eastern parautochthonous passive continental margin on the western edge of the Kalahari Craton, the Port Nolloth Zone, and a western allochthonous ophiolitic terrane, the Marmora Superterrane, thrusted on the Port Nolloth Zone.

The sedimentary evolution of the Gariep Belt was initiated with the deposition of sediments of the Rosh Pinah Formation into fluvial, alluvial and lacustrine depositional systems, which are associated with bimodal volcanic activity and related Zn-Pb-Cu-Ag-(+Ba) sulphide mineralization. The overlying mixed continental/shallow marine deposits of the Gumchavib Formation are overlain by the carbonate dominated Pickelhaube Formation, which was deposited in shallow marine to pelagic depositional settings. The Rosh Pinah, Gumchavib and lower Pickelhaube Formations are intruded by basic volcanic sills of the "Gannakouriep dyke swarm". The conformably overlying Obib Peak Formation was deposited into a fluvial/alluvial palaeoenvironment. The Numees Formation unconformably overlies the underlying stratigraphic units and consists predominantly of glaciomarine massive diamictites and occasionally interbedded iron formations, which are occasionally interbedded with interglacial sediments and volcanics.

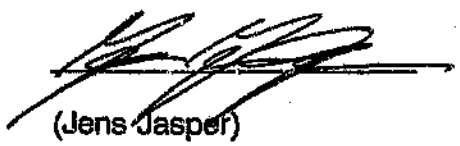
The regional structural pattern is characterized by three phases of deformation. The earliest deformational event, D1, comprises intrafolial small scale recumbent and isoclinal F1 folds, a penetrative bedding-subparallel S1 cleavage and a preferred elongation of boulders, pebbles, grains and minerals (l1). Associated with D1 are bedding-subparallel thrust faults. The D2 deformational phase is characterized by small to large scale, north to northwest trending F2 folds with a generally easterly vergence, which can change into a westerly direction due to backfolding. The F2 folds are associated with a penetrative axial planar S2 cleavage. Thrusting continued during the D2 deformational phase. The latest deformational event, D3, is characterized by small

to large scale open F3 folds with southerly to southwesterly trending fold axes. The metamorphic evolution of the Gariep Belt during the Damara Orogeny was associated with barrovian-type metamorphism with a geothermal gradient of about 20°C/km, reaching greenschist to lower amphibolite facies metamorphism.

The sedimentological and structural features are explained in a tectono-sedimentary model, which started with rift initiation during the deposition of Rosh Pinah Formation lithologies along old tectonic weakness zones of Middle Proterozoic age at about 780Ma. Supercontinental breakup is documented by the initial transgression of Gumchavib Formation sediments and the continuous transgression of the Pickelhaube Formation, which is related to thermal subsidence after the initiation of oceanic spreading of the Adamastor Ocean. Renewed rifting and/or glacial outwash heralding the advance of the Numees glaciation and associated sealevel changes may be responsible for the sudden break in marine sedimentation during the deposition of the Obib Peak Formation. The Numees glaciation is probably contemporaneous with the 670Ma old Varangian glacial and the Rapitan glacial episodes and provides a minimum age for the deposition of Gariep Group lithologies. Rifting and spreading was followed by the closure of the Adamastor Ocean, associated with a southeastward directed subduction of oceanic crust under the Kalahari Craton and was accompanied by intense southeastward and subsequently eastward directed tectonic transport during D1 and D2. During D3, a late sinistral movement developed along the defined fault zones in the late stages of the Adamastor Orogeny. Metamorphic ages from the Nama and Vanrhynsdorp Groups indicate that the tectonic evolution of the Gariep Belt only ceased at about 500Ma.

DECLARATION

I declare that this dissertation is my own, unaided work. It is being submitted for degree of Doctor of Philosophy in the University of the Witwatersrand, Johannesburg. It has not been submitted before for any degree or examination in any other University.



(Jens Jasper)

29th day of July, 1994

ACKNOWLEDGEMENTS

I would sincerely like to thank the Geological Survey of Namibia for providing financial and logistical support of this project.

I am most grateful to my supervisor, Prof. Ian G. Stanistreet, for the initiation of this project, for his incouragement, the invaluable guidance during all phases of the study, for his neverending willingness for discussions and his constructive critisism, which gave me many new insights about how the geological world works. Thanks a lot, Ian.

Very special thanks are extended to Dr. E. Guy Charlesworth of the Geology Department, University of the Witwatersrand, for his enthusiastic and invaluable supervision throughout this project not only of the structural part of the study. Thanks also for the constructive critisism and discussions, which trashed many of my misconceptions on how tectonics work. Dear Guy, thanks for all your help and support.

Further thanks are extended to Prof. Martin Okrusch and Dr. Leander Franz of the Mineralogy Institute of the University of Würzburg/Germany for their great support during my research leave at Würzburg in October 1992.

I would like to thank Dr. Roy Miller for the introduction to the study area and his support of this research project during his time as Director of the Geological Survey of Namibia.

Thanks also to Dr. Brian Hoal, the present Director of the Geological Survey of Namibia and all the staff for all the invaluable support.

C.D.M. Ltd. is thanked for granting me access to Diamond Area No.1, whithout which this research project would not have been possible. Thanks also to the Geology Department of C.D.M. Ltd. for giving me some valuable geological hints.

Sincere thanks are extended to Mr. Dennis Alchin, Mr. Louie Jacobs and Mr. Dick Randall of the Geology Department of the Rosh Pinah Mine (IMCOR Zinc Ltd.) for their willingness to explain and discuss the complex geology of the Rosh Pinah area.

Special thanks are also extended to Mr. John Dean and Mr. Clint Williams of Goldfields Namibia for their willingness to grant access to the Trekpoort Farm area, which helped me substantially in the understanding of the geology of the Gariep Belt. Thanks also for the hospitality and the many potjies I enjoyed at the Goldfields camp.

The work has furtner benefited from discussions with Dr. George Henry (now Rand Gold) and Dr. Thomas Wallmach (now Geology Department, University of Pretoria) of the Geology Department, University of the Witwatersrand. This department is also thanked for logistical and financial support and for the use

of in-house facilities.

The project has further benefited from discussions with Mr. David Pieter Dingeldey of the Mineralogy Institute, University of Würzburg/Germany, as well as from discussions with Mr. Boris F.F. Reczko of the Geology Department, University of Pretoria.

Mr. Peter Siegfried, Managing Director of Geoafrica Prospecting, Windhoek, is thanked for his geological advice in the field, his friendship and hospitality in Windhoek. Thanks a million, Ziggi.

I would also like to thank the Rosh Pinah Mine for their fabulous support, in particular the workshop for their invaluable help after several breakdowns of my vehicle.

Very special thanks are adressed to the people of Rosh Pinah whose hospitality and support were fabulous. I want to particularly thank my friend Frits Schreijnders, with whom I spent many days and nights at the Orange River trying to catch "Bruno the killer carp", hiked through some magnificent parts of the Namib desert and who dedicated the adventure tales "Rivierpraat", developed at the fire over long thoughts about the surounding environments. Thanks a lot for all the friendship and support, Fidel.

Thanks also to Ms. Judy Wilmot and Mrs. Elizabeth Sole for their administrative help, Mrs. Lyn Witfield and Mrs. Diane Du Toit for the many drawings and hot coffee in the early mornings, and to Mr. Mark Hudson for the photographic work. Messrs. Mitch Miles, Mathew Kitching and Alex Mathebula are thanked for their technical support and the preparation of thin and polished sections.

All the post-graduates of the Geology Department of the University are thanked for the many hours of discussion on geology, life, the universe and everything. Thanks a lot for the great time I had.

Very special thanks are due to Ansie Chorn for all her love and her relentless support and understanding which accompanied me during some very significant phases of this work.

Last, but not least, I want to thank my late father and my mother, to whom this thesis is dedicated. Their support throughout my education did eventually enable me to begin this project, which taught me so much not only about geology, but also about life in general. Thank you for all your confidence and support.

TABLE OF CONTENTS

Abstract		
Declaration		I
Acknowledgements		II
Table of contents		IV
List of tables		IX
List of figures		X
CHAPTER 1		
INTRODUCTION		1
1.1	Geographical setting of study area	2
1.2	Previous work	4
1.3	Objectives of study	6
1.4	Methods of investigation	6
CHAPTER 2		
GEOLOGICAL SETTING		
2.1	Introduction	8
2.2	Pre-Gariep basement	12
	2.2.1 De Hoop Subgroup	13
	2.2.2 Vioolsdrif Igneous Suite	15
2.3	Gariep Group	17
	2.3.1 Marmora Superterrane	17
	2.3.2 Stratigraphy of the Port Nolloth Zone	23
2.4	Intrusive rocks	27
2.5	Radiometric ages of the Gariep Group stratigraphy	29
CHAPTER 3		
SEDIMENTOLOGY		

3.1 Introduction 33

3.2 The Rosh Pinah Formation: rift sedimentation within a fluvially/lacustrine/fan delta-dominated depositional system with volcanism 34

3.2.1 Massive conglomerate/sandstone/mudstone facies association: fan deltas prograding into a lacustrine palaeoenvironment 35

3.2.2 Coarse to fine clastics/carbonate facies association: proximal to distal braid plain, alluvial fan and lacustrine depositional system 43

3.2.3 Clastics/carbonate/bimodal volcanic facies association: fluvially, alluvial fan and lacustrine dominated depositional system with volcanism 5

3.2.4 Conglomerate facies association: a transgressive basal conglomerate depositional system 56

3.2.5 The geology of the Rosh Pinah and Spitzkop area (Imcor Zinc Ltd. Mine Grant Area) 57

3.2.6 Regional distribution of the facies associations 62

3.2.7 Vertical sedimentary facies association variations 64

3.2.8 Lateral sedimentary facies association variations 65

3.2.9 Palaeogeographic reconstruction 67

3.3 The Gumchavib Formation: opening of the Adamastor Ocean 70

3.3.1 Sandstone/mudstone/carbonate facies association: mixed continental and marine carbonate depositional system 70

3.3.2 Quartz arenite/mudstone facies association: foreshore and shoreface depositional system 74

3.3.3 Interleaving of previously defined facies associations 78

3.3.4 Regional distribution 79

3.3.5 Vertical sedimentary facies association variations 79

3.3.6 Lateral sedimentary facies association and stratigraphic variations 81

3.3.7 Palaeogeographic reconstruction 81

3.4 The Pickelhaube Formation: carbonate platform and carbonate shelf depositional system 83

3.4.1 Carbonate/carbonaceous carbonate facies association:carbonate shelf depositional system 83

3.4.2 Carbonate/calcareous clastics facies association:

shallow marine sea and prograding distal fan deltas 87

3.4.3 Carbonate/coarse to fine clastics facies association: mixed carbonate platform, slope apron and deep basin depositional system 91

3.4.4 Regional distribution 102

3.4.5 Vertical sedimentary facies association variations 104

3.4.6 Lateral sedimentary facies association variations 104

3.4.7 Palaeoenvironmental reconstruction: synthesis and summary 105

3.5 The Obib Peak Formation: regression of the Adamastor sea and advance of fluvial sedimentation 108

3.5.1 Sandstone/carbonate facies association: mixed continental and marine depositional system 108

3.5.2 Mixed coarse to fine clastics facies association: fluvial braided plain depositional system 108

3.5.3 Regional distribution 110

3.5.4 Vertical and lateral facies association variations 112

3.5.5 Palaeoenvironmental and palaeogeographic interpretation 112

3.6 The Numees Formation: glaciomarine and interglacial sedimentation 114

3.6.1 Diamictite facies: glaciomarine sedimentation 114

3.6.2 Iron formation/pebbly sandstone facies association: dropstones in a glaciomarine setting 118

3.6.3 Conglomerate/sandstone/mudstone facies association: gravity mass flow within a marine se g 122

3.6.4 Carbonate facies association 125

3.6.5 Coarse to fine clastics/carbonate/bimodal volcanics facies association: interglacial mixed continental /marine depositional system 127

3.6.6 Regional distribution 131

3.6.7 Vertical and lateral sedimentary facies association variations 133

3.6.8 Palaeoenvironmental reconstruction 134

3.6.9 Discussion 136

CHAPTER 4

STRUCTURAL GEOLOGY

4.1 Introduction 140

4.1.1 Deformational events 142

4.2 Tectonostratigraphy 144

4.2.1 The autochthonous unit 145

4.2.2 Parautochthonous units 145

4.3 Time sequence of deformational events 165

4.3.1 D1 phase of deformation 165

4.3.2 D2 phase of deformation 168

4.3.3 D3 phase of deformation 174

4.3.4 Recognition of thrust faults and time sequence of thrusting 177

4.4 Kinematic interpretation 179

4.4.1 Transpressive phase 180

4.4.2 Strike-slip phase 183

4.4.3 Interpretation 184

CHAPTER 5

METAMORPHISM

5.1 Introduction 186

5.2 Methods of study 187

5.2.1 Selection of samples 188

5.2.2 Mineral chemistry analyses methods 188

5.3 Petrography and phase relations of the selected samples 190

5.4 Mineral chemistry 192

5.5 Metamorphic evolution 196

5.6 Conclusions 200

CHAPTER 6

TECTONICS AND SEDIMENTATION OF THE SOUTHERN COASTAL BRANCH OF THE DAMARA OROGEN (GARIEP BELT)

6.1 Introduction 202

6.2 Previous geodynamic models for the evolution of the

southern coastal branch of the Damara Orogen (Gariep Belt) 203
6.3 Tectonic inversion within the Gariep Belt in southern Namibia 211
6.3.1 Location of inverted faults 211
6.3.2 Stratigraphic thickness variations along inverted faults 211
6.3.3 Tectono-sedimentary history of the study area 212
6.3.4 Inversion tectonics within other fold and thrust belts 214
6.4 Tectonics and sedimentation 216
6.4.1 Tectonic framework and evidence of rifting 218
6.4.2 Sedimentary response to intracontinental rifting 218
6.4.3 Dating of rifting and oceanic opening 221
6.4.4 Oceanic opening and thermal subsidence 222
6.4.5 Renewed rifting and/or glacial outwash? - the Obib Peak Formation 222
6.4.6 Glaciation 223
6.5 Mineralization and volcanism in the western vicinity of the inverted Rosh Pinah fault 224
6.6 Effects of oceanic closure and continental collision 225
6.7 Correlation of the Gariep Belt with other parts of the Damara Orogen 227
6.7.1 Stratigraphic correlation of the Gariep Belt with other parts of the Damara Orogen 228
6.6.2 Correlation of tectonic events of the Gariep Belt and other parts of the Damara Orogen 234

REFERENCES 240

APPENDIX

LIST OF TABLES

Table 2.1: *Stratigraphic subdivision of the Orange River Group.*

Table 2.2a: *Past and present stratigraphic classification schemes for the Gariep Belt.*

Table 2.2b: *Past and present stratigraphic classification schemes for the Gariep Belt.*

Table 4.1: *Structural elements associated with the deformational events within the Gariep Belt, southern Namibia.*

Table 5.1: *Mineral assemblages of investigated samples.*

Table 6.1: *Stratigraphic correlation of Gariep Group lithologies of southern Namibia.*

Table 6.2: *Lithostratigraphic correlation of the northern and southern coastal branches of the Damara Orogen.*

Table 6.3: *Correlation of deformational events of the Gariep Belt (southern coastal branch) and the Kaoko Belt (northern coastal branch) of the Damara Orogen.*

LIST OF FIGURES

Fig. 1.1: *Position of the coastal branch and inland branch of the Damara Orogen* 1

Fig. 1.2: *Geographical setting of the study area.* 3

Fig. 2.1: *Simplified geological map of the Garlep Belt (modified after Hartnady et al., 1990)* 9

Fig. 2.2: *Pan African framework of Southern Africa and South America (modified after Porada, 1989)* 10

Fig. 2.3: *Position of the various thrust slices and the parautochthonous unit within the study area.* 11

Fig. 2.4: *Geological map of the Rosh Pinah - Sendelingsdrif area, Southern Namibia.* 16

Fig. 2.5: *Oolitic dolomite of the Gais Formation east of Rooilepel, about 20 km north-east of Oranjemund, Southern Namibia.* 18

Fig. 2.6: *Schematic NW-SE profile across the Marmora Terrane showing fabric relationships between Schakalsberge (Sb), Oranjemund (Or), and Chamais (Ch) thrust-sheets, overlying Bogenfels and Hilda/Holgat (Hi-Ho) foot-wall formations (see Fig. 2.1; after Hartnady et al., 1990)* 20

Fig. 2.7: *Stereonets showing D1 and D2 structural elements in the area approximately 7 km south of Bogenfels.* 22

Fig. 2.8: *Simplified geological map of parts of the Richtersveld and southern Namibia (modified after Allsopp et al., 1979).* 28

Fig. 3.1: *Measured section through the Rosh Pinah Formation at locality 7, south-east of Pickelhaube (Fig. 2.4).* 35

Fig. 3.2: *Massive dolomite boulder within the conglomerates of the Rosh Pinah Formation at locality 7, south-east of Pickelhaube (Fig. 2.4).* 36

Fig. 3.3: *Massive conglomerate (Cms) displaying normal and inverse grading in beds with gradational contacts at locality 7, south-east of Pickelhaube (Fig. 2.4).* 37

Fig. 3.4: *Sharp scour contact within massive conglomerate (Cms) at locality 7, south-east of Pickelhaube (Fig. 2.4).* 37

Fig. 3.5: *Thickly laminated and very thinly bedded wave-ripple cross-laminated sand-/siltstone (Swr), interlaminated with mudstone (Mfl) at locality 7, southeast of Pickelhaube (Fig. 2.4); note penetrative S2 cleavage from bottom left to top right.* 38

Fig. 3.6: *Thinly laminated mudstone (Mfl) at the transition from sandstone to mudstone lithologies at locality 7, south-east of Pickelhaube (Fig. 2.4); note the penetrative bedding-subparallel s1 cleavage.* 40

Fig. 3.7: *Wave-ripple marks within the mudstones (Mfl) and sand-/siltstones (Swr) of the Rosh Pinah Formation at locality 9 (Fig. 2.4).* 40

Fig. 3.8: *Black, graphite-rich mudstone (Mm) of the Rosh Pinah Formation displaying sulphur efflorescence (locality 22; Fig. 2.4).* 44

Fig. 3.9: *Graded beds within arkosic sandstones of the Rosh Pinah Formation in the core of the Annisfontein Anticlinorium near locality 1, immediately north of the Orange River (Fig. 2.4).* 45

Fig 3.10: *Measured section through a portion of the Rosh Pinah Formation in the core of the Annisfontein Anticlinorium at locality 1 immediately north of the Orange River (Fig. 2.4).* 46

Fig. 3.11: *Linguoid out-of-phase ripple marks within sandstones of the Rosh Pinah Formation, about 2 km south of Gumchavib trigonometrical beacon (Fig. 2.4).* 46

Fig. 3.12: *Sinuous out-of-phase ripple marks within sandstones of the Rosh Pinah Formation, about 2 km south of Gumchavib trigonometrical beacon (Fig. 2.4).* 47

Fig. 3.13: *Tabular planar cross-bedded quartzitic sandstone (Spc) of the Rosh Pinah Formation at locality 22, about 4 km south of Gumchavib (Fig. 2.4)* 47

Fig. 3.14: *Measured section through the Rosh Pinah Formation at locality 22, about 4 km south of Gumchavib trigonometrical beacon (Fig. 2.4).* 48

Fig. 3.15: *Measured section through parts of the Rosh Pinah Formation at locality 30, west of Gumchavib Mountain.* 48

Fig. 3.16: *Trough cross-bedded quartzitic sandstone (Stc) of the Rosh Pinah Formation at locality 22, about 4 km south of Gumchavib trigonometrical beacon (Fig. 2.4).* 49

Fig. 3.17: *Measured section through a portion of the Rosh Pinah Formation in the central part of the Rooikat thrust slice (Fig. 2.2).* 52

Fig. 3.18: *Measured section through a portion of the Rosh Pinah Formation in the northern part of the Rooikat thrust slice (Fig. 2.2).* 54

Fig. 3.19: *Regional distribution of the several facies associations developed within the Rosh Pinah Formation; for position of thrust slices and localities see Figs. 2.3 & 2.4.* 63

Fig. 3.20: *Schematic reconstruction of the palaegeographic setting present during the deposition of Rosh Pinah Formation rocks within the study area.* 68

Fig. 3.21: *Measured section through parts of the Gumchavib Formation overlying granitic basement at locality 29, approximately 5 km northwest of Gumchavib Mountain (Fig. 2.4).* 71

Fig. 3.22: *Measured section through parts of Gumchavib Formation at locality 17, approximately 5 km WNW of Gumchavib Mountain (Fig. 2.4).* 72

Fig. 3.23: *Measured section through parts of the Gumchavib Formation at Obib waterhole (Fig. 2.4).* 75

Fig. 3.24: *Wave-ripple cross laminated and low angle plane laminated quartz arenitic sandstones at Obib waterhole (Fig. 2.4).* 76

Fig. 3.25: *Measured section through parts of the Gumchavib Formation at locality 28, approximately 1 km northeast of Obib Peak (Fig. 2.4).* 78

Fig. 3.26: *Regional distribution of the several facies associations developed within the Gumchavib Formation; for position of thrust slices and localities see Figs. 2.3 & 2.4.* 80

Fig. 3.27: *Laminated carbonate of the Pickelhaube Formation about 5 km southwest of Pickelhaube Peak; note the slump structure in the upper left part of the photograph (Fig. 2.4); photo is rotated 90 degrees in an anticlockwise direction.* 84

Fig. 3.28: *Measured section through part of the Pickelhaube Formation, showing graded beds of carbonate (Lg) at a locality about 7 km northwest of Pickelhaube Peak (Fig. 2.4).* 85

Fig. 3.29: *Measured section through parts of the Pickelhaube Formation at locality 3, about 2,5 km NNW of Obib waterhole (Fig. 2.4).* 86

Fig. 3.30: *Measured section through parts of the lower Pickelhaube Formation at locality 4, about 5 km southwest of Rosh Pinah (Fig. 2.4).* 88

Fig. 3.31: *Measured section through parts of the Pickelhaube Formation at locality 17, about 5 km northwest of Gumchavib Mountain; sections*

are taken along strike approximately 100 m apart (Fig. 2.4). 89

Fig. 3.32: *Measured section through parts of the Pickelhaube Formation at Dreigratberg (Fig. 2.4).* 92

Fig. 3.33: *Measured section through parts of the Pickelhaube Formation at a locality about 5 km north of Dreigratberg (Fig. 2.4).* 94

Fig. 3.34: *Thickly to thinly laminated sandstone and mudstone (Sng/Mm) of the Pickelhaube Formation at Dreigratberg (Fig. 2.4); every single lamination consists of a normal graded bed.* 94

Fig. 3.35: *Tabular carbonate clasts within a calcareous matrix within the mixed carbonate conglomerate/carbonate breccia (Cms/Lbr) of the Pickelhaube Formation at Dreigratberg.* 95

Fig. 3.36: *Massive carbonate conglomerate with carbonate clasts in a carbonate matrix of the Pickelhaube Formation at locality 13 A, about 5 km south-east of Namuskluft Farmhouse (Fig. 2.4).* 96

Fig. 3.37: *Stromatolitic carbonate of the Pickelhaube Formation at a locality about 1km west of Obib Peak (Fig. 2.4).* 97

Fig. 3.38: *Pisoliths and carbonate rock fragments within a carbonate matrix at locality 13A, about 3 km north of Dreigratberg (Fig. 2.4).* 97

Fig. 3.39: *Regional distribution of the several facies associations recognized within the Pickelhaube Formation in the study area; for position of thrust slices and locations see Figs. 2.3 & 2.4.* 103

Fig. 3.40: *Measured section through parts of the Obib Peak Formation at locality 3, about 3 km NNW of Obib waterhole (Fig. 2.4); note the sharp contact to the underlying Pickelhaube Formation.* 109

Fig. 3.41: *Measured section through parts of the Obib Peak Formation at Obib Peak (Fig. 2.4); note the gradational contact to the underlying Pickelhaube Formation.* 109

Fig. 3.42: *Erosional channel of conglomerates within arkosic sandstone of the Obib Peak Formation at locality 15, approximately 3,5 km northwest of Obib waterhole (Fig. 2.4).* 110

Fig. 3.43: *Regional distributon of the Obib Peak Formation within the study area; for position of thrust slices and localities see Figs. 2.3 & 2.4.* 111

Fig. 3.44: *Measured sections through parts of the Numees Formation at Trekpoort Farm, approximately 25 km northwest of Rosh Pinah.* 115

Fig. 3.45: *Massive diamictite of the Numees Formation showing poor sorting and a variety of clasts at Dreigratberg (Fig. 2.4).* 116

Fig. 3.46: *Brown weathering and light grey to blue-grey diamictite of the Numees Formation 8 km north of Dreigratberg (Fig. 2.4).* 116

Fig. 3.47: *Carbonate clast within massive diamictite of Numees Formation immediately north of Dreigratberg (fig. 2.4); note alligrnment of clasts along penetrative s1 foliation from bottom left to top right and s2 cleavage perpendicular to S1.* 117

Fig. 3.48: *Granitic dropstone erratic disrupting laminations of the banded iron formation within the Numees Formation at the western flank of Dreigratberg (Fig. 2.4).* 119

Fig. 3.49: *Magnetite-rich graded pebbly sandstone with granitic dropstone erratics at Trekpoort Farm, approximately 25 km northwest of Rosh Pinah (Fig. 2.4).* 119

Fig. 3.50: *Measured section through the graded beds of the conglomerate/sandstone/mudstone facies association within the Numees Formation, about 2 km south-east of Namuskluft Farmhouse (Fig. 2.4).* 123

Fig. 3.51: *Graded beds of the conglomerate/sandstone/mudstone facies association within the Numees Formation, about 2 km south-east of Namuskluft Farmhouse (Fig. 2.4).* 124

Fig. 3.52: *Measured section through parts of the Numees Formation about 3 km north of Dreigratberg (Fig. 2.4), displaying interbedded carbonate and diamictite.* 126

Fig. 3.53: *Regional distribution of the several facies associations of the Numees Formation within the study area; for position of thrust slices and localities see Figs. 2.3 & 2.4.* 132

Fig. 3.54: *Model proposed for the origin of the glaciomarine Numees Formation sediments (modified after Henry et al., 1986).* 134

Fig. 4.1: *A) Structural SW to NE cross-section D1-D2 cutting through parts of the Obib thrust slice south of Obib Peak in the SW, and parts of the Ostrich, Roolkat, Pickelhaube, Gemsbok, and Dreigratberg thrust slices, as well as the parautochthonous zone in the NE.*
B) Structural SW to NE cross-section E1-E2, cutting through the Ostrich thrust slice approximately 8 km S of Gumchavib in the SW, and parts of the Gumchavib, Gemsbok, and Dreigratberg thrust slices, as well as the parautochtonous zone in the NE. Position

of cross-sections are shown in Fig. 2.4. 147

Fig. 4.2: *Structural SW to NE cross-sections F1-F2, F3-F4, F5-F6, F7-F8, situated within the imbricate zone in the east of the Dreigratberg thrust slice. Positions of cross-sections are shown in Fig. 2.4.* 148

Fig. 4.3: *Structural SW to NE cross-section H1-H2 situated within the imbricate zone in the east of the Dreigratberg thrust slice about 4 km north of Dreigratberg. Positions of cross-section is shown in Fig. 2.4.* 149

Fig. 4.4: *Stereonet projections of structural data for the Dreigratberg thrust slice.* 149

Fig. 4.5: *Structural profile G1-G2 through parts of the Rosh Pinah thrust slice (modified after Van Vuuren, 1986). Position of cross-section is shown in Fig. 2.4.* 151

Fig. 4.6: *Stereonet projections of structural data for the Rosh Pinah thrust slice.* 151

Fig. 4.7: *Stereonet projections of structural data for the Pickelhaube thrust slice.* 153

Fig. 4.8: *F2 backfolds within the imbricate thrust zone immediately south of Pickelhaube at locality 7 (Fig. 2.4), showing the change from an easterly to a westerly vergence caused by backfolding.* 155

Fig. 4.9: *Large scale isoclinal overturned to recumbent F2 fold within the imbricate thrust zone west of Pickelhaube, at locality 7, south of Pickelhaube (Fig. 2.4).* 156

Fig. 4.10: *Stereonet projections of structrural data for the Gemsbok thrust slice.* 156

Fig. 4.11: *Stereonet projections of structural data for the Gumchavib thrust slice.* 158

Fig. 4.12: *A) Structural SW to NE cross-sections A1-A2 through parts of the Oblb and Pickelhaube thrust slices.*
B) Structural SW to NE cross-section B1-B2 through parts of the Oblb, Ostrich, Rooikat, and Pickelhaube thrust slices.
C) Structural SW to NE cross-section C1-C2 through parts of the Oblb, Ostrich, Rooikat, Pickelhaube, and Gemsbok thrust slices. Position of cross-sections are shown in Fig. 4.1. 160

Fig. 4.13: *Stereonet projections of structural data for the Ostrich thrust slice.* 161

Fig. 4.14: *Stereonet projections of structural data for the Rooikat thrust slice.* 162

Fig. 4.15: *Stereonet projections of structural data for the Obib thrust slice.* 164

Fig. 4.16: *Intrafolial, southerly verging F1 folds within dolomitic carbonate at locality 13A, approximately 5 km southeast of Namuskluft Farmhouse (Fig. 2.4).* 166

Fig. 4.17: *Stereonet projections of data associated with D1 throughout the study area; A) poles to S0/S1; B) F1 fold axes; C) poles to F1 axial planes.* 166

Fig. 4.18: *Bedding subparallel penetrative S1 cleavage developed within mudstones of the Rosh Pinah Formation south of Pickelhaube (Fig. 2.4).* 167

Fig. 4.19: *Rose diagram showing the main trend elongation of clasts of the Rosh Pinah Formation and pisolites of the Pickelhaube Formation from throughout the study area.* 167

Fig. 4.20: *Elongation of clasts of a Rosh Pinah Formation conglomerate associated with D1 at locality 13B, approximately 3 km north of Dreigratberg (Fig. 2.4). Flattening of clasts parallel to subparallel to bedding and S1 cleavage. Note the cigar-like shape of clasts.* 168

Fig. 4.21: *Stereonet projections of data associated with D2 throughout the area; A) poles to S0/S1; B) F2 fold axes; C) poles to F2 axial planes.* 169

Fig. 4.22: *Disharmonic F2 fold within arkosic sandstones of the Rosh Pinah Formation at Trekpoort Farm (Fig. 1.2).* 170

Fig. 4.23: *Penetrative S2 axial planar cleavage within a northwest-trending, overturned tight F2 fold near Daberas, NW of the Oranjemund road (Fig. 1.2).* 170

Fig. 4.24: *Refraction of S2 cleavage around folded layers of of different competencies within folded mudstone and sandstone of the Rosh Pinah Formation at locality 7, south of Pickelhaube (Fig. 2.4); note the characteristic flattening of the cleavage in the pelitic layers and the higher angle between cleavage and bedding in the psammitic layers.* 171

Fig. 4.25: *S2 crenulation lineation l2 within phyllite of the Gumchavib Formation, about 3 km northwest of Obib waterhole; crenulation lineation l2 is parallel to pencil and developed on the bedding plane.* 172

Fig. 4.26: *Axial planar S2 cleavage deforming So-subparallel S1 cleavage within mudstones of the Rosh Pinah Formation at locality 7, east of Pickelhaube (Fig. 2.4).* 172

Fig. 4.27: *D2 thrust fault at locality 1 (Fig. 2.4); note the fold limb of the F2 fold is cut-off by thrust fault.* 173

Fig. 4.28: *D2 thrust fault immediately south of Pickelhaube Peak (Fig. 2.4), carbonates of the Pickelhaube Formation are thrust over sandstones and conglomertaes of the Rosh Pinah Formation. Note the relatively undeformed carbonate in the upper thrust slice overlying folded sandstones and conglomerates with a clearly developed S2 axial planar foliation beneath the thrust fault.* 173

Fig. 4.29: *Stereonet projections of data associated with D3 throughout the area; A) F3 fold axes (n=68); B) poles to F3 axial planes (n=46).* 175

Fig. 4.30: *F3 open fold developed within carbonates of the Pickelhaube Formation at locality 17 (Fig. 2.4).* 175

Fig. 4.31: *F3 open chevron fold developed within carbonates of the Pickelhaube Formation at locality 17 (Fig. 2.4) in the Ostrich thrust slice.* 176

Fig. 4.32: *Fold interference structure caused by a F3 fold deforming the fold hinge of a F2 fold at Dreigratberg (Fig. 2.4).* 176

Fig. 4.33: *D2 thrust fault cutting through the stratigraphy at a locality south of Gumchavib trigonometrical beacon, probably caused by the failure of the footwall ramp.* 178

Fig. 4.34: *Flinn plots of strain data from (A) locality 13B; (B) locality 7; and (C) locality 8 (localities are shown in Fig. 2.4).* 182

Fig. 4.35: *Schematic diagram summarizing the structural variations and change of strain ellipsoids during the earliest kinematic phase (D1) in the central and southern parts of the Port Nolloth Zone (modified after Von Veh, 1988).* 185

Fig. 5.1: *ACF diagram showing mineral compositions within the amphibolites.* 190

Fig. 5.2: *A'KF digram showing mineral compositions within the paragneisses.* 191

Fig. 5.3: *Nomenclature of clinopyroxenes in the system $CaMgSi_2O_6$ -$CaFeSi_2O_6$-$Mg_2Si_2O_6$-$Fe_2Si_2O_6$ (after Poldervart & Hess, 1951).* 192

Fig. 5.4: *Leake (1978) amphibole nomenclature of calcic amphiboles: $(Na + K)_A \geq 0.50$p; $Ti < 0.50$; $Fe^3 \leq Al^{VI}$.* 193

Fig. 5.5: *Leake (1978) amphibole nomenclature of calcic amphiboles: $(Na + K)_A < 0.50$; $Ti < 0.50$.* 193

Fig. 5.6: Diagram showing the Fe-Si composition of samples P1, 235,

35, RP 185. 195

Fig. 5.7: *Plagioclase-hornblende thermobarometry after Plyusnina (1982) showing plot of coexisting amphiboles and plagioclases from amphibolite samples; note the great variability of pressures and temperatures.* 197

Fig. 5.8: *P-T diagram with "isopiethes" for Si-contents of phengites after Massone (1991); note great variability of pressures and temperatures of the investigated samples.* 198

Fig. 5.9: *Facies fields of metabasites and coexisting pelites after Laird & Albee (1981).* 199

Fig. 6.1: *Oroclinal bending model as suggested by Kasch (1983).* 204

Fig. 6.2: *Cross-sections showing the gravitational collapse model of Davies & Coward (1982).* 205

Fig. 6.3: *Schematic diagram showing the proposed southward migrating subduction zone, responsible for the development of the arcuate shape of the Gariep Belt (Von Veh, 1988).* 207

Fig. 6.4: *Schematic diagram showing the cratonic motions during the closure and collisional phases of the Khomas Sea and Adamastor Ocean (modified after Stanistreet et al., 1991). KC= Kalahari Craton; CC= Congo Craton; SAC= South American Continent.* 209

Fig. 6.5: *A) - (modified from Hoffman, 1991; and Hartnady, 1991): Rodinia in its pre-750 Ma old configuration with Laurentia.*
B) - (modified after Hartnady, 1991): the 650-600 Ma old configuration of Rodinia after it has been turned inside out. EPG= East proto-Gondwanaland; WPG= West proto-Gondwanaland; L= Laurentia; B=Baltica; SA= southern African block; G= Grenville belt; N= Namaqua belt; Lu= Lurio belt; S= Sverdrupfjella belt; V= Vijayan belt, E= Eastern Ghats belt; R= Rayner belt; AO= Adamastor Ocean; MO= Mozambique Ocean; PPO=protp-Pacific Ocean; IO= Iapetus Ocean; M= Mozambique metamorphic belt; ANS= Arabian-Nubian Shield. 210

Fig. 6.6: *Schematic diagram showing stratigraphic thickness variations within the study area (for locations see Figs. 1.2 and 2.4).* 213

Fig. 6.7: *Interpretation of Fig. 6.6, showing the proposed position of syn-sedimentary faults, which controlled the deposition of the Gariep Group sediments within the study area.* 213

Fig. 6.8: *Schematic model for the inversion of the Rosh Pinah half graben;*

(a) Pre-inversion geometry of the half graben with deposition of syn-rift sediments and volcanics; (b) Initial inversion showing reactivation of the listric normal fault which bounds the half graben; (c) Continued deformation with ramping and bedding sub-parallel thrusting along the extensional listric fault plane (D1); (d) Subsequent folding and associated thrusting (D2) along the reactivated extensional fault plane. 215

Fig. 6.9: *(Fig. 6.9a, b and c on opposite page) Summary diagrams showing stages during the deposition of the sedimentary and volcanic rocks of the Gariep Group. (a) Deposition of Rosh Pinah fluvial, lacustrine, and alluvial fan sediments associated with volcanism during the rift stage. (b) First marine transgressions characterized by interbedded distal fluvial and shallow marine carbonates and beach deposits, indicating continued rifting. (c) Marine transgression accompanied by influx of siliciclastic sediments and the formation of a carbonate platform, a carbonte shelf, and deep sea deposition of the Holgat beds during Pickelhaube times, indicating that the Kalahari Craton and South America separated, and sea floor spreading began in the Adamastor Ocean. (d) Regression of marine sediments and deposition of continental sediments. (e) Deposition of mainly glaciomarine sediments during Numees glaciation, associated with the development of a major unconformity prior to Numees sedimentation.* 219

Fig. 6.10: *Tectonostratigraphic zones of the Damara Orogen (from Miller, 1983).* 235

Fig. 6.11: *Structural E-W cross-section across the Kaoko Belt, Sesfontein area (from Miller, 1983).* 236

CHAPTER 1

INTRODUCTION

The Damara Orogen in Namibia and the north-western Richtersveld is one of the best preserved Late Proterozoic/Early Palaeozoic orogenic belts in the world. It comprises an "inland branch" and a "coastal branch" (Fig. 1.1). The coastal branch is subdivided into the northern Kaoko Belt and the southern Gariep Belt, which has been linked with the Saldanha Belt of the south-western Cape Province (Clifford, 1967; Stowe et al., 1984). Because of the remoteness and harshness of the area north and south of the Orange River, few detailed studies have been undertaken in the southern coastal branch of the Damara Orogen.

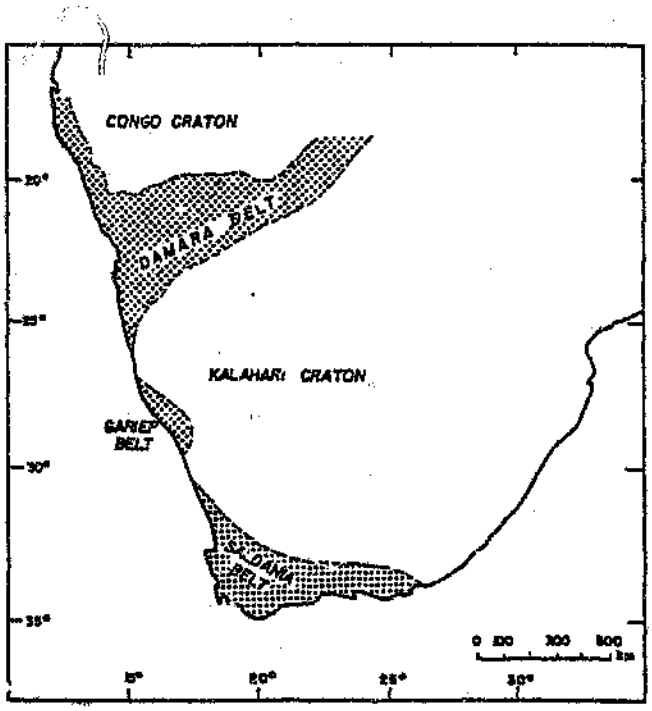


Fig. 1.1 *Position of the coastal branch and inland branch of the Damara Orogen.*

The major aim of this study is to gain understanding of the depositional history of the Gariep Group and the tectonics which controlled it, as well as to understand the collisional history of the Gariep Belt. It forms a contribution to our present understanding of Late Precambrian/Early Palaeozoic tectonics and sedimentation.

1.1 GEOGRAPHICAL SETTING OF THE STUDY AREA

The study area is located immediately north of the Orange River near Octa, extending northwards to north of Rosh Pinah mining village and including the Obib Mountains and the Jackalsberge to the west of the Obib Mountains within the eastern part of Diamond Area No.1 (Fig. 1.2). To the south the study area is bounded by the Orange River and to the north by latitude 27-45 S (Fig. 1.2).

The climate is arid, with average annual rainfall varying from 42 mm at Oranjemund, to 75 mm at Rosh Pinah. The study area falls into the winter rainfall belt that extends northwards from the Western Cape. The prevailing wind is a cool south wind blowing obliquely off the sea. Temperatures during the winter season vary between below 0°C at night and 30°C during the day. Conditions during the summer months become unbearable for field work, with temperatures rising to a maximum of about 50°C in the shade.

The morphology of the region comprises the mountainous country along the escarpment in the east of the study area, with a maximum elevation of 1647 m a.m.s.l. at Namuskluft trigonometrical beacon, the Obib Mountains and the Jackalsberge in the west of the study area (Fig. 1.2). Another type of morphology is the peneplain consisting of fine alluvium and the pedeplain comprising coarse debris and

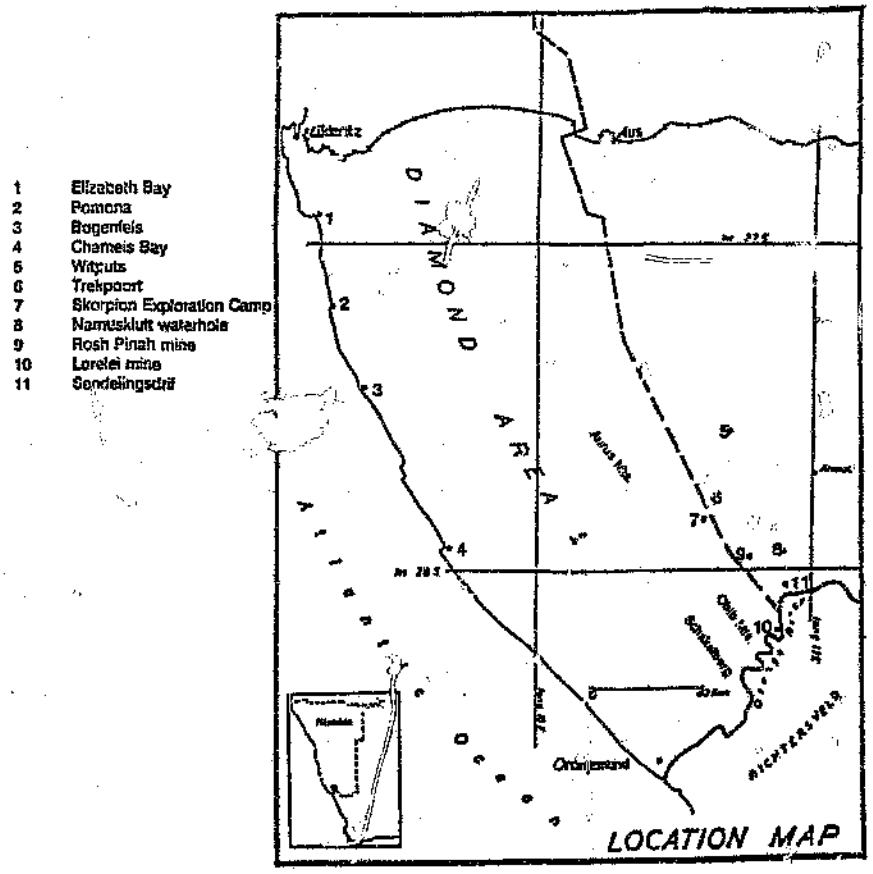


Fig. 1.2: *Geographical setting of the study area.*

conglomerate. The area between the Obib Mountains and the Jackalsberge is covered by extensive sand dunes. The topographic relief shows up to 1600 m of variation from the bed of the Orange River (~40 m amsl) to the top of Namuskluft trigonometrical beacon (1647 m amsl).

The vegetation varies with elevation and distribution of precipitation along the escarpment. The most common plants are melkbos (Euphorbia gummifera), geelpen, driedoring (Rhigozum trichotonum), brakbos (Acacia giraffae), bushman's candle (Sarcocaulum burmanni), and halfmens (Brachypodum), the latter being most conspicuous in the mountains and always directing its head towards the north. Common trees are the witgatboom (Boscia albitrunca), the kokerboom (Aloe

dichotoma), and the bastard ebony.

Wildlife, especially within the Diamond Area No.1, is most abundant, consisting of gemsbok, springbok, klipspringer, duiker, wild donkey, mountain zebra, ostrich, brown hyena, jackal, rooikat, baboon and blue vervet, the two latter being the main prey of leopards, which can be found near the Orange River.

1.2 PREVIOUS WORK

Little geological research has been undertaken so far in the Gariep Belt north of the Orange River. The earliest survey of the Gariep Belt north of the Orange River was carried out by German workers as part of a regional survey of the eastern Sperrgebiet (Diamond Area No.1) south of Lüderitz from 1912 to 1913, as summarized by McMillan (1968). The first detailed geological account of the study area was made by Beetz (1926), who concentrated on the Witputs area approx. 40 km north of Rosh Pinah. Further geological work within the Sperrgebiet was undertaken by Kaiser (1926) and Knetsch (1937). Söhnge & De Villiers (1946) published a brief report on the geology of the eastern Sperrgebiet, immediately north of the Orange River. Martin (1965) undertook some reconnaissance work in the Obib Mountains within the Sperrgebiet. The first comprehensive geological mapping at a 1:100 000 scale was undertaken by McMillan (1968) in the Witputs-Sendelingsdrif area during the course of doctoral thesis research. Geological studies of the Rosh Pinah Zn-Pb-Cu-Ag-deposit and its immediate surroundings have been undertaken by Page & Watson (1976), Watson (1980), Van Vuuren (1986), de Kock (1987), Siegfried (1990), and Lickfold (1990). Davies & Coward (1982) undertook structural studies within Diamond Area No.1. The

geochemistry of the Grootderm volcanics was analysed by Smith & Hartnady (1984). Hartnady et al. (1985) subdivided the Gariep Belt into the parauthochtonous Port Nolloth Assemblage in the east and the allochthonous Marmora Terrane in the west of the Gariep Belt. Joubert et al. (1986) compiled a 1:250000 scale geological map and report of the Alexander Bay Sheet (Sheet 2816).

The first geological account of the Gariep Belt in the Richtersveld dates back to the last century (Alexander, 1838; Wyley, 1857; Dunn, 1872). Rogers (1916) first established a stratigraphic succession for the Gariep Belt south of the Orange River. Geological mapping of the western Richterveld was undertaken by Söhnge & De Villiers (1946) and De Villiers & Söhnge (1959). Further geological studies in the northern and western Richtersveld were undertaken by Range (1912), Van Biljon (1939), Haughton (1961, 1963), Martin (1965), Kröner & Germs (1971), Joubert & Kröner (1972), Kröner (1972, 1974, 1974a, 1975, 1977), Kröner & Rankama (1972), Kröner & Welin (1973), Kröner & Jackson (1974), Kröner & Blignault (1976), Kröner & Hawkesworth (1977), and Kröner et al. (1980). Ritter (1978, 1980) and Theart (1980) examined the Gariep-basement contact relationships and metamorphic overprinting in the eastern and southern Richterveld. Allsopp et al. (1979) undertook geochronological work on Gariep rocks and rocks of the Kuboos-Bremen line of intrusives and the Richtersveld and Bremen Igneous Complexes of southwestern Namibia and the Richtersveld. The latest geological work on the structural evolution and the stratigraphic succession of the Gariep Belt south of the Orange River was undertaken by Von Veh (1988) in the course of doctoral thesis research.

1.3 OBJECTIVES OF STUDY

Previous studies of the Gariep Belt have concentrated mainly on regional mapping, the structural development and stratigraphic relationships (Söhnge & de Villiers, 1946; De Villiers and Söhnge, 1959; McMillan, 1968; Hoffmann, 1972; Kröner, 1974; Von Veh, 1988). Little attention has been given to the pre-orogenic depositional and tectonic history and metamorphic development of the Gariep Belt and related rocks. The major aims of this study are:

(i) to determine the pre-orogenic sedimentological evolution of the Gariep basin in the study area and the effects of syn-sedimentary tectonism on deposition,

(ii) to resolve the structural and metamorphic development of the Gariep Belt,

(iii) to determine stratigraphic relationships from the sedimentolgical and structural analysis,

(iv) to construct a geodynamic model for the tectono-sedimentary evolution of the Gariep Belt,

(v) to compare the geodynamic evolution of the Gariep Belt with events in the northern coastal branch and the inland branch of the Damara Sequence.

1.5 METHODS OF INVESTIGATION

Exceptionally good outcrop conditions occur in most parts of the Jackalsberge, Obib Mountains and the Dreigratberg area and its northerly and easterly extents (Fig. 1.2). Outside these areas exposure is obscured by alluvium and sand cover.

Detailed geological mapping was undertaken along selected traverses. The geological

map of the Witputs/Sendelingsdrif area compiled by McMillan (1968) constituted a helpful aid for this purpose. Important information of large scale structures and stratigraphic boundaries has additionally been obtained from aerial photographs and SPOT 2 imagery.

A large number of detailed profiles and sequences on a variety of scales was measured along strike within the several thrust slices.

Since no detailed work on the sedimentology and the depositional palaeoenvironment has been undertaken so far, lithotypes and sedimentary structures were documented and a detailed facies analysis was carried out.

A large number of structural data was collected in the field in order to understand the structural evolution and associated compressional directions.

Approximately 150 thin sections were studied in order to identify the mineralogical composition of the metasediments and metavolcanics.

Selected samples from different stratigraphic horizons from throughout the study area were studied by microprobe analysis at the Mineralogy Institute of the University of Würzburg, Germany, during a research leave as a help for the understanding of the metamorphic evolution.

CHAPTER 2

GEOLOGICAL SETTING

2.1 INTRODUCTION

The Gariep Belt is an arcuate north-south trending tectonic unit extending along the coast of Namibia and South Africa from immediately south-east of Lüderitz in Namibia to Kleinzee in South Africa, situated about 80 km south-east of Oranjemund, over a distance of nearly 400 km with a maximum exposed width of about 80 km (Fig. 2.1). The Gariep Belt is part of the southern coastal branch of the extensive Damara Orogen, which links with the Saldanha Belt of the south-western Cape Province and northwards with the coastal branch comprising the Kaokoveld of northern Namibia. It forms part of the Late Proterozoic/Early Palaeozoic Pan African system of orogenic belts (Fig. 2.3; Clifford, 1967; Stowe et al., 1984). Porada (1979) has suggested that the western extension of the Damara Orogen is represented by the Ribeira Orogen of Brazil (Fig. 2.3), which is also supported by geochronological data of Cordani et al. (1990).

The Gariep Belt consists of an eastern, parautochthonous terrane, named the Port Nolloth Zone, developed as a passive continental margin on the western edge of the Kalahari Craton and a western allochthonous ophiolitic terrane, the Marmora Terrane (Von Veh, 1988; Hartnady et al., 1990), thrusted onto the Port Nolloth Zone along the Schakalsberge thrust (Fig. 2.1). Rocks within the Port Nolloth Zone are intensely folded and thrusted throughout the Gariep Belt and rest with a marked unconformity on lithologies of the Namaqua and Richtersveld Provinces (Kröner, 1975). Within the study

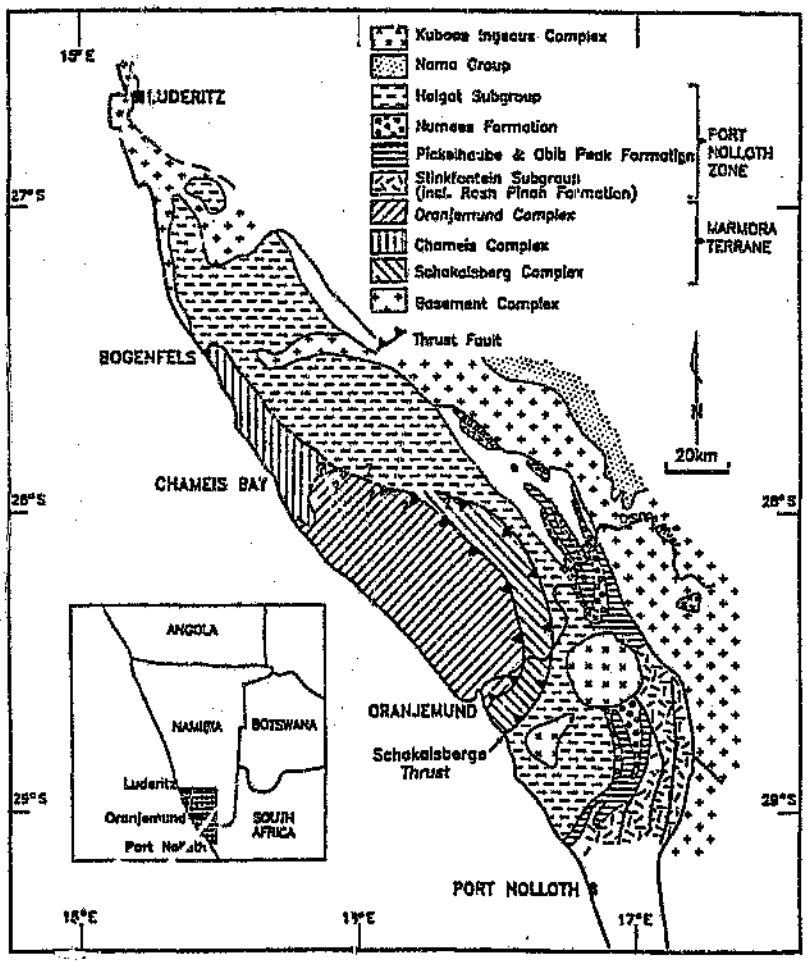


Fig. 2.1: *Simplified geological map of the Gariep Belt (modified after Hartnady et al., 1990)*

area, fieldwork has established the presence of various thrust slices, bounded by northerly to northwesterly trending thrust faults in the western parts of the study area, and an autochthonous unit in the eastern parts of the study area are present (Fig. 2.3; see chapter 4). Lithologies of the Gariep Group are unconformably overlain by clastic and carbonate sediments of the Late Proterozoic and Early Palaeozoic Nama Group in the east, which were deposited into active foreland basins associated with the Adamastor and Khomas Orogens, which were formed as a result of the closure of the Adamastor Ocean and the Khomas Sea respectively (Germs & Gresse, 1991;

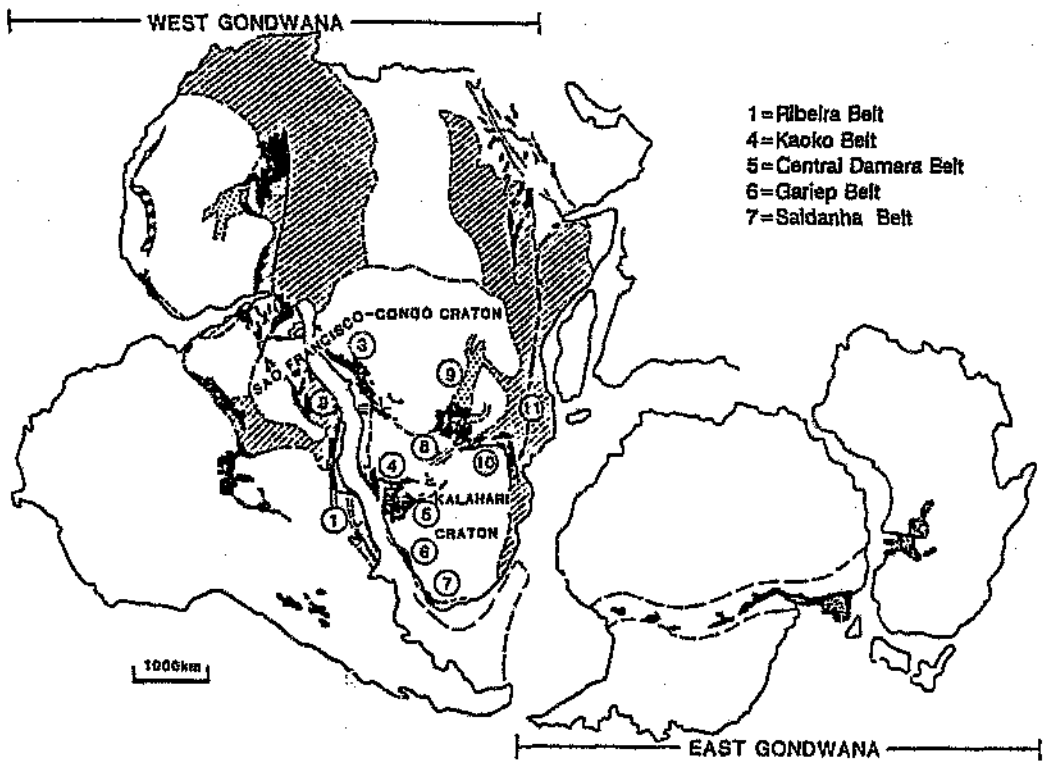


Fig. 2.2: *Pan African framework of Southern Africa and South America (modified after Porada, 1989)*

Stanistreet et al., 1991).

Within the Gariep Belt a number of pre-, syn- and post-tectonic intrusions are present. South of the study area, across the Orange River, a large batholith and two smaller plutons of granite and leucogranite form part of the Richtersveld Igneous Suite. Both south and north of the Orange River, the Gannakouriep dyke and sill swarm, with an Rb-Sr mineral-isochron age of 717 +/- 11 Ma (Ransome & Reid *in*: Hartnady & Von Veh, 1990) and up to 100 km wide, consisting of north- to northeast-trending mafic and ultramafic sills and dykes (De Villiers & Söhnge, 1959; Middlemost, 1964; McMillan, 1968; Kröner & Blignault, 1976; Reid, 1979) is intrusive into the basement rocks and basal Gariep Group cover rocks south of the Orange River and into the

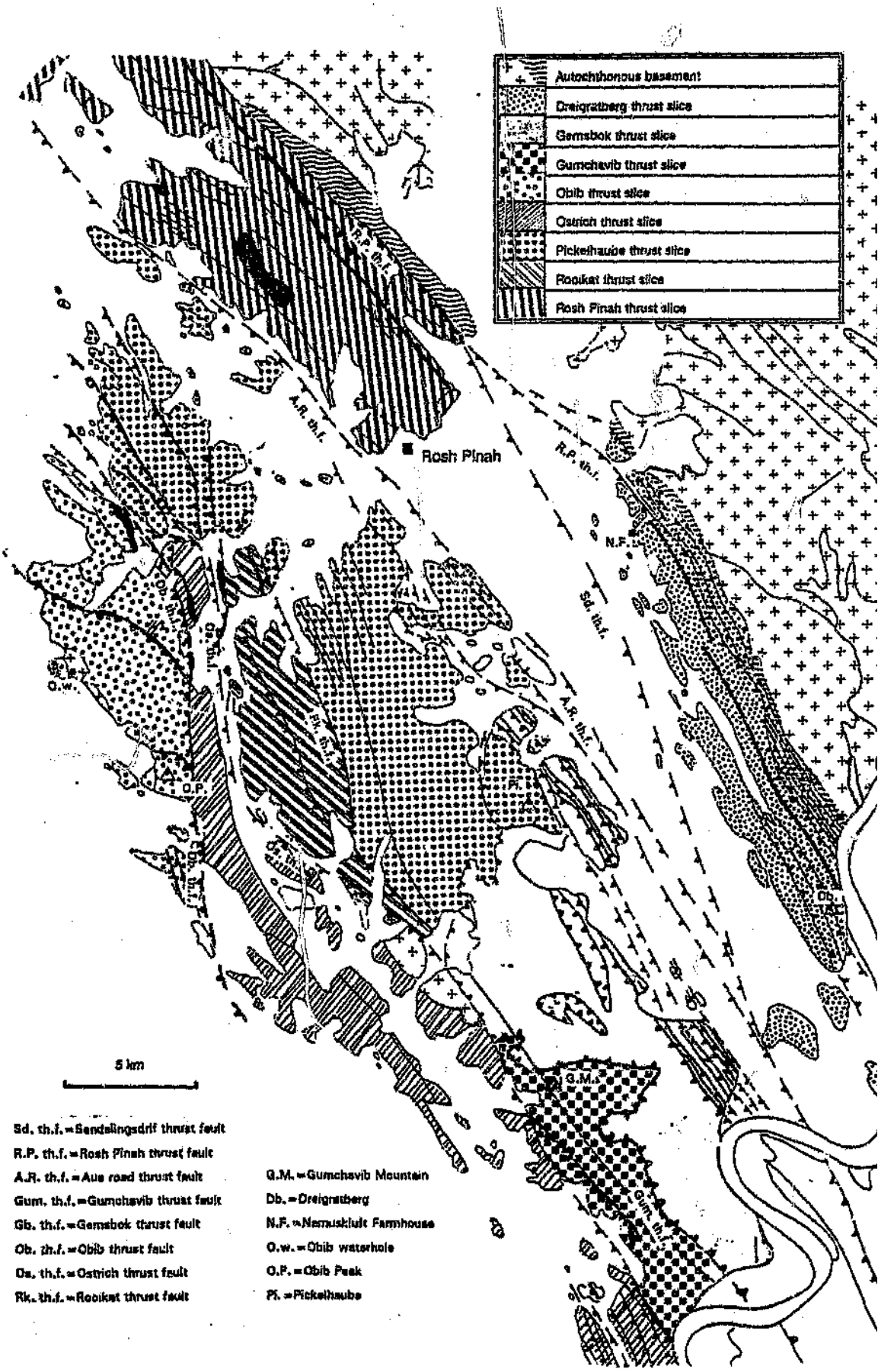


Fig. 2.3: *Position of the various thrust slices and the parautochthonous unit within the study area.*

rocks of the Stinkfontein and lower Hilda Subgroups in southern Namibia. Syntectonic stocks, dykes, and sills have been decribed from the central and internal parts of the Gariep Belt north and south of the Orange River by Kaiser (1926) and De Villiers & Söhnge (1959). In the Richtersveld, two plutons, namely the Swartbank and Kuboos Plutons, which form part of the NE-trending Kuboos-Bremen line of intrusives, intrude rocks of the Gariep Group (Van Biljon, 1939; Söhnge & De Villiers, 1946). These plutons are cut by an Early Phanerozoic set of aplite, porphyry granite and basic and bostonite dykes (Kröner & Hawkesworth, 1977).

The metamorphism within the Port Nolloth Zone ranges from greenschist to lower amphibolite facies, thus not affecting the sedimentary and volcanic structures dramatically.

2.2 PRE-GARIEP BASEMENT

The pre-Gariep basement consists of rocks of the Orange River Group and forms the oldest lithostratigraphic unit in south-western Namibia and the Richtersveld Province of South Africa (Fig. 2.4 and Table 2.1). It was formerly called the "Kheis System", but was later renamed in order to avoid an association with the Kheis Sequence in the eastern parts of the Namaqua Province (Blignault, 1974). The Orange River Group comprises the lower volcanic De Hoop Subgroup, the middle sedimentary Rosyntjieberg Formation, and the upper volcanic Haib Subgroup (Table 2.1; De Villiers & Söhnge, 1959; Kröner & Blignault, 1976; SACS, 1980). The entire Orange River Group is intruded by rocks of the granitoid Vioolsdrif Igneous Suite. The rocks of both the Orange River Group and the Vioolsdrif Suite show the effects of low to medium

grade metamorphism (Kröner & Blignault, 1976), and, according to Bertrand (1976) and Ritter (1978), locally led to migmatization and

Table 2.1: *Stratigraphic subdivision of the Orange River Group.*

GROUP	SUBGROUP
Orange River Group (Kheis System)	Haib Subgroup
	Rosyntjieberg Subgroup
	De Hoop Subgroup

anatexis of the Vioolsdrif granitoids.

Towards the margins of the Namaqua Province, a gradual increase in the grade of metamorphism and deformation is encountered, together with penetratively foliated Vioolsdrif Igneous Suite granitoids and Orange River Group metalavas. Rocks of the Vioolsdrif Igneous Suite, which are found both in the Namaqua and Gariep Belts, bear a strong structural imprint of both the Namaqua and Pan-African episodes. Within the study area and its immediate easterly vicinity, only rocks of the De Hoop Subgroup and the intrusive Vioolsdrif Igneous Suite are exposed.

2.2.1 De Hoop Subgroup

The rocks of the De Hoop Subgroup, immediately north of the Orange River, were first described in detail by McMillan (1968). From the Orange River to about 3 km

southeast of Namuskluft Farmhouse (Fig. 2.4), the rocks of the De Hoop Subgroup form the basement to the Gariep Group lithologies.

Basic Lavas

The westernmost portion of the De Hoop Subgroup consists of metamorphosed lavas and intercalated agglomerates. Otherwise, no primary volcanic textures are present within these green, strongly sheared, lineated, fine-grained chlorite epidote schists. Intermediate to felsic agglomerate units are abundant throughout the sequence and contain light-coloured, medium to large, subangular to subrounded clasts. Occasionally, granodiorite apophyses intrude the basic volcanic sequence sub-parallel to the dominant foliation.

Phyllitic Schists

The basic lavas are overlain by an assemblage of silver-grey phyllitic schists. Textural evidence suggests that these schists represent metamorphosed shales, greywackes and grits with intercalated thin, persistent conglomerate bands (Viljoen et al., 1986). A younging direction to the east is indicated by normally graded beds. Quartz veins are abundant and commonly occur as short, massive bodies, lying parallel to the dominant foliation.

Intermediate volcanics

The uppermost stratigraphic unit of the De Hoop Subgroup comprises chlorite-rich felsic schists. Intermediate volcanics are most abundant to the north of Lorelei copper-mine (Fig. 2.4), but also occur in thin slivers (Viljoen et al., 1986). These rocks are

nterpreted as metamorphosed intermediate pyroclasts and agglomerates (Viljoen et al., 1986). Occasionally, schist with an intermediate volcanic composition grades into sericite schists, which represent either altered intermediate volcanic schists or a more felsic stratigraphic facies of the volcanic sequence (Viljoen et al., 1986).

2.2.2 Vioolsdrif Igneous Suite

The Vioolsdrif Igneous Suite north of the Orange River is exposed east of Lorelei copper-mine, at Namuskluft Farmhouse and at Namuskluft, where it is intrusive into the De Hoop Subgroup, and at Trekpoort Farm approximately 25 km northwest of Rosh Pinah. Within the Sperrgebiet it is exposed at the Obib waterhole and northwest of Gumchavib Mountain (Fig. 2.4). It comprises partly gneissic granite, grey to red, containing dark greenish-black, irregularly shaped clusters of mica and chlorite, light yellow-green specks of epidote, sericitic felspar and grey-white unaltered feldspar. North of Gumchavib Mountain (Fig. 2.4), the granite has been strongly sheared and is usually gneissic displaying porphyroblasts of pink feldspar with up to 1 cm in length, as well as elongate lenticles of mica, chlorite, and occasional hornblende and epidote. As in the Richtersveld (De Villiers & Söhnge, 1959), the granites in the study area always contain two feldspars (plagioclase and K-feldspar), biotite and sericitized plagioclase. In addition, north of the Orange River, epidote represents a common constituent of the Vioolsdrif granites.

Leucogranite and aplite dykes extensively intrude the granodiorites north of the Orange River. A number of lit-par-lit granite veins also intrude the volcanic rocks of the De Hoop Subgroup.

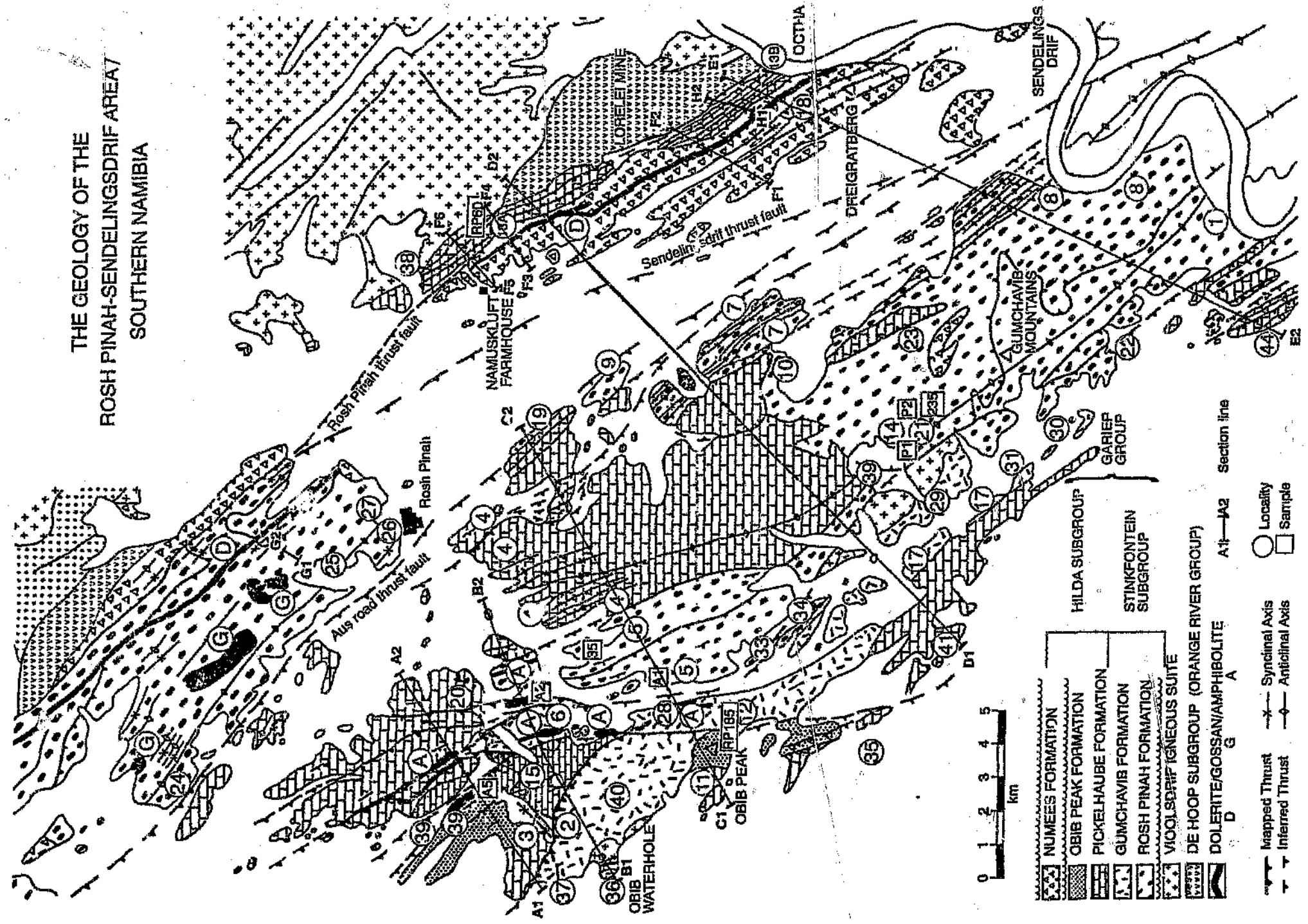


Fig. 2.4: *Geological map of the Rosh Pinah - Sendelingsdrif area, Southern Namibia.*

2.3 GARIEP GROUP

2.3.1 Marmora Terrane

The Marmora Terrane is subdivided into three tectonostratigraphic units, namely: the Schakalsberge Complex in the southeast and the Oranjemund and Chamais Complexes in the northwest (Fig. 2.1; Hartnady et al., 1990). These fault-bounded tectonostratigraphic units are significantly different in character, to the extent that they may be regarded as subterranes or even separate accreted terranes within a composite Marmora Superterrane.

The *Schakalsberge Complex* has been subdivided into metabasic lavas of the Grootderm Formation, which are capped by and interfinger with dolomites of the Gais Formation (Hartnady et al., 1990).

The Grootderm Formation comprises an up to 6 km thick pile of metabasic lavas, including pillow lavas, pillow breccia, tuffs and lava-flows. The volcanics consist of tholeiitic basalts, but in the upper sequences alkali basalts may occur (Smith & Hartnady, 1984), which may be related to a series of vesicular alkali-gabbroic dykes, acting as high level volcanic feeders during a post-shield stage of volcanic activity (Hartnady et al., 1990). Geochemical analysis of the Grootderm metabasalts (Smith & Hartnady, 1984) indicate that the lavas were erupted in an ocean floor environment. The absence of siliciclastic terrigeneous material within the Gais Formation suggests an origin in an intraplate environment away from a continental margin, possibly similar to a Hawaiian-type sea channel-mount chain, a Walvis-type aseismic ridge, or an Ontong Java-type oceanic plateau. Kröner (1974, 1975, 1979) also interpreted the metabasalts as having originated as oceanic seapeaks or guyots, subsequently

incorporated in a subduction complex. The Gais Formation comprises a pinkish dolomite, including abundant cherty intercalations, fine laminations, stromatolite bioherms which locally contain intertidal channels and oolitic dolomite (Fig. 2.5), thus indicating reef-growth and deposition possibly capping the guyot or seapeak during dwindling phases of Grootderm volcanism.

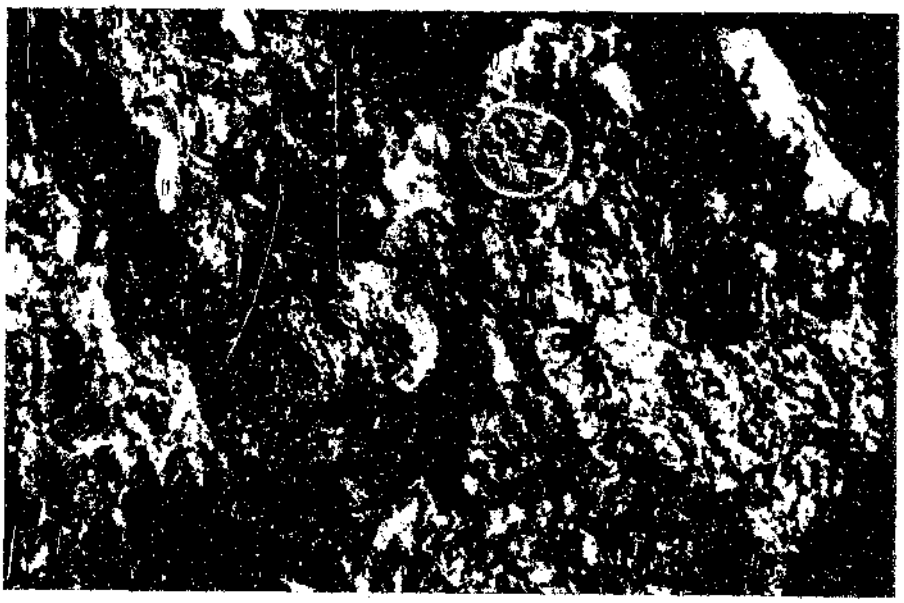


Fig. 2.5: *Oolitic dolomite of the Gais Formation east of Roollepel, about 20 km north-east of Oranjemund, Southern Namibia.*

The Grootderm Formation was intruded as dykes and sills by the Roollepel bostonite suite. Hartnady et al. (1990) maintain that the bostonites were emplaced late in the history of the Grootderm volcanic pile, prior to the deposition of the overlying Gais Formation. Detailed metamorphic studies in the Marmora Superterrane, undertaken by Frimmel and Hartnady (1992), indicate a multiphase metamorphic history for this superterrane. The first metamorphic event, M1, has been interpreted as a very low-

pressure hydrothermal oceanic metamorphism that affected the igneous protoliths at up to amphibolite facies temperatures. The following M2 metamorphic event was syn-tectonic and characterized by temperatures similar to those reached during M1 but with higher pressures, indicating burial to 10 to 15 km. This event has been interpreted as being related to a subduction process. A third metamorphic event, M3, was low grade and of regional nature. These results indicate that subduction and subsequent obduction have occured in the Gariep Belt, although blueschist facies metamorphism has not been reached (Frimmel and Hartnady, 1992).

The *Oranjemund Complex* comprises metagreywacke rock-types varying from little deformed cyclothemic turbiditic varieties to intensely transposed, poly-deformed mica-schists, and locally minor intercalations of metavolcanic chlorite schists (Hartnady et al., 1990), as well as phyllites, schists and minor quartzite, resembling the Holgat Sequence of the Port Nolloth Zone (Von Veh, 1988).

The *Chamais Complex* was interpreted by Hartnady et al. (1990) as a heterogeneous mélange, consisting of various exotic blocks, 0.1-100 m in size, from different oceanic environments in close proximity to each other. These blocks occur within a highly tectonized metasedimentary sequence, incorporating interbedded chloritic, talcose, quartzitic, quartzo-feldspathic, dolomitic, graphitic and ferruginous schists, and showing evidence of a distinct metamorphic history prior to that recorded by the metasedimentary country rocks, which experienced a regional metamorphic event under lower greenschist facies conditions. This latter metamorphic event is concordant with metamorphism experienced by the Schakalsberge nappe and has, therefore, been interpreted as a syntectonic metamorphism which occurred during Marmora Terrane emplacement (Hartnady et al., 1990). Geochemical data from serpentenized

metapyroxenites, metaperidotites, massive and layered metagabbros, metadolerites and metabasalts, which in places are amygdaloidal, delineate a tholeiitic trend consistent with an oceanic origin (Frimmel & Hartnady, 1992).

The structural relationships within the Marmora Terrane were first described by Davies & Coward (1982) and later by Hartnady et al. (1990). The most prominent structural elements characterizing the Marmora Terrane are major arcuate thrust faults, juxtaposing the Oranjemund, Chameis, and Schakalsberg Complexes. The most prominent thrust fault is the Schakalsberge thrust fault, which juxtaposes the Marmora

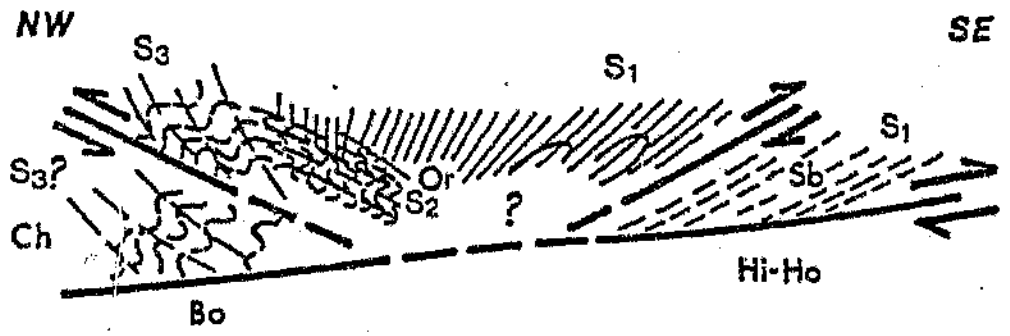


Fig. 2.6: *Schematic NW-SE profile across the Marmora Terrane showing fabric relationships between Schakalsberge (Sb), Oranjemund (Or), and Chameis (Ch) thrust-sheets, overlying Bogenfels (Bo) and Hilda/Holgat (Hi-Ho) foot-wall formations (see Fig. 2.1; after Hartnady et al., 1990)*

Terrane and the Port Nolloth Zone (Figs. 2.1 & 2.6). The thrust fault at the contact between the Chameis and Oranjemund Complexes dips in a south-easterly direction, whereas the thrust faults at the contact between the Oranjemund and Schakalsberge Complexes dips in a westerly to north-westerly direction (Hartnady et al, 1990), possibly representing a "pop up" structure of major dimensions (Fig. 2.6).

Three deformational phases were described by Hartnady et al. (1990) within the

Marmora Terrane. Near the contact between the Oranjemund and Chameis Complexes and at the Schakalsberge sole thrust, the D1 deformation is characterized by an early NW-dipping S1 cleavage, which is co-planar to the axial planes of minor D1 folds (F1; Fig. 2.6). The S1 schistosities in both the Oranjemund and Schakalsberge Complexes are approximately co-planar to the F1 axial planes within Bogenfels footwall lithologies and are nearly coplanar with the Chameis thrust fault.

Near the contact between the Oranjemund and Chameis Complex, the D2 deformational phase is characterized by a pentrative S2 schistosity, which trends in a northerly direction with a south-easterly dip, transposing the S1 cleavage and minor F1 folds. At the Schakalsberge sole thrust near Bogenfels, D2 folds (F2) are truncated by the thrust fault in the hanging-wall of the Bogenfels lithologies. In both the Oranjemund and Schakalsberge Complexes, minor F2 kink-bands locally affected the co-planar S1 schistosities.

Hartnady et al. (1990) described late-stage D3 backfolding with folds verging in a north-westerly direction (F3; Fig. 2.6) for both the Chameis and Oranjemund Complexes. Near the contact of the Chameis and Oranjemund Complexes, the S2 schistosity was deformed by F3 folds. At the Schakalsberge sole thrust near Bogenfels (Fig. 2.6), F2 and possibly F3 folds were truncated by the thrust fault in the hanging-wall of the Bogenfels lithologies. According to Hartnady et al. (1990) structural evidence shows that the Schakalsberge sole thrust in the north post-dates the late juxtaposition of the Oranjemund over the Chameis Complex by D3 back-thrusting. These thrust nappes or subterranes may have been originally juxtaposed in reverse order during D1. In the south, the juxtaposition of the Oranjemund over the Schakalsberge Complex could have taken place either before or after the D3

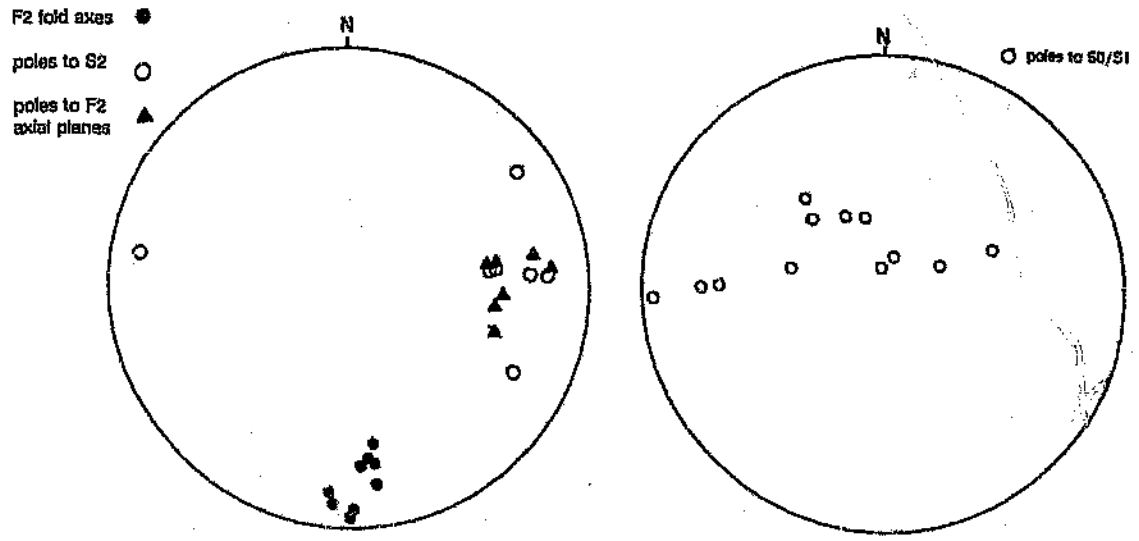


Fig. 2.7: *Stereonets showing D1 and D2 structural elements in the area approximately 7 km south of Bogenfels.*

backthrusting event (Hartnady et al., 1990).

Reconnaissance mapping in the area immediately south of Bogenfels has shown, that the earliest deformation phase (D1-Bo) is characterized by an intense bedding-subparallel foliation, indicated by mineral and grain elongation, as well as growth of mica. This foliation is associated with bedding-subparallel quartz-veinlets, which in places display fish structures indicating shearing in a southerly to south-easterly direction (Fig. 2.7). This foliation is sub-parallel to thrust faults (D1-Bo), which are indicated by quartz veins up to several metres thick, containing quartz-feldspar pegmatoids, mylonites, intense shearing and a strong D1-Bo cleavage.

Small to large scale, open to isoclinal, and in places overturned folds (<5 cm to 100 m wavelength) have deformed this earliest bedding-subparallel foliation (D1; Fig. 2.7) and are thus ascribed to a later D2 deformational event. The D2 folds plunge moderately in a southerly direction (Fig. 2.7). A weak axial planar cleavage, dipping in a westerly direction and indicated by the elongation of minerals and grains, is associated with the D2 deformational event. Stereonet data of structural elements from

the Bogenfels area are shown in Figure 2.7.

2.3.2 Stratigraphy of the Port Nolloth Zone

Previous stratigraphic subdivisions

Several efforts have been made to classify the stratigraphy of the Gariep Belt. Attempts were undertaken by Rogers (1915, 1929), De Villiers & Söhnge (1959), Haughton (1961, 1963), Martin (1965), McMillan, 1968; Kröner (1972; 1974); and Von Veh (1988; Table 2.2). SACS (1980) subdivided the Gariep Belt into a "miogeosynclinal" facies (central Richtersveld), and a "eugeosynclinal" facies (western Richtersveld and coast). The miogeosynclinal facies was subdivided into the Stinkfontein Formation, constituting the Lekkersink, Vredefontein and Kaigas Members, which are overlain by the Hilda Suite and the Numees Suite. The eugeosynclinal facies consists of the Grootderm Suite, which is overlain by the Oranjemund and Holgat Suites (Table 2.2b). The Rosh Pinah-Witputs area north of the Orange River was subdivided by McMillan (1968) into the basal Kapok Formation, which is equivalent to the Rosh Pinah Formation, the Hilda Series (Gariep System), and the overlying Numees Formation. SACS (1980) renamed these stratigraphic units Rosh Pinah Formation, Hilda Suite and Numees Formation, being confined to the "miogeosynclinal" facies (Table 2.2b). Diamond Area No.1 of the Sperrgebiet, which lies to the east of the Rosh Pinah-Witputs area, was also subdivided into a "eugeosynclinal facies" (coastal region) and a "miogeosynclinal facies" (northeastern belt). The "eugeosynclinal facies" comprises the Grootderm and the overlying Oranjemund Suites, whereas the "miogeosynclinal facies" is made up by

the Hilda Suite and the overlying Bogenfels Formation (SACS, 1980; Table 2.2).

Port Nolloth Zone-stratigraphy of the north-western Richtersveld

The latest stratigraphic studies in the north-western Richterveld were undertaken by Von Veh (1988), who subdivided the Garlep Group into the Stinkfontein, Hilda, Numees, and Holgat Sequences (Table 2.2b) . The Stinkfontein Sequence comprises the Lekkersink, Vredefontein, and Gumchavib Formations, consisting of quartz arenites, conglomerates, feldspathic grit and arenite, as well as the diamictitic Kaigas Formation. The Hilda Sequence incorporates the Pickelhaube Formation, consisting of dolomitic limestone, the Wallekraal Formation, comprising conglomerate of well rounded boulders with dolomite boulders with sizes up to 10 m, and the Dabie River Formation, including dolomite with rare stromatolitic mats. The Numees Sequence was subdivided by Von Veh (1988) into the basal Jakkalsberg Formation, incorporating an interbedded sequence of magnetite-quartzite, iron-rich and iron-poor schist, arkose and diamictite, as well as iron formation with polymict dropstones. The Jakkalsberg Formation is overlain by the Sendelingsdrif Formation, consisting predominantly of a massive or very poorly bedded diamictite. The Holgat Sequence was described by Von Veh (1988) as a sequence of interbedded arkoses, greywackes, schists, and dolomitic limestone.

Port Nolloth Zone-stratigraphy of southern Namibia

Results of the present work suggest, that the Port Nolloth Zone-stratigraphy north of the Orange River consists of the Stinkfontein Subgroup, comprising the Rosh Pinah Formation, a mixed clastic/volcanic rift phase, and the Gumchavib Formation, a mixed

Table 2.2a: *Past and present stratigraphic classification schemes for the Gariep Belt.*

Rogers (1916; 1929)	De Villiers & Söhnge (1959)	Haughton (1961; 1963)	Martin (1965)
	NAMA SYSTEM	NAMA SYSTEM	Kuboos Granite
Kuboos granite	Numees Formation		Numees Formation with Kaigas Substage (part of NAMA SYSTEM)
	xxxxxxxxxxxxxxxxxxxxxxxxxxx	Numees Formation	xxxxxxxxxxxxxxxxxxxxxxxxxxx
Grootderm Series	Kaigas Formation	xxxxxxxxxxxxxxxxxxxxxxxxxxx	Stinkfontein Formation
			xxxxxxxxxxxxxxxxxxxxxxxxxxx
Numees Series	Stinkfontein Formation	Holgat Series	Grey gneiss, etc.
Western folded Nama System xxxx?xxxx?xxxx	xxxxxxxxxxxxxxxxxxxxxxxxxxx	Hilda-Kaigas Series GARIEP Black Hill Series SYSTEM	Holgat Series
	Grey gneisses, etc.	Stinkfontein Series	Hilda Series GARIEP
Kaigas Series		xxxxxxxxxxxxxxxxxxxxxxxxxxx	Black Hills Series SYSTEM
	Grootderm Series		Grootderm Series
Stinkfontein Series	Holgat Series		xxxxxxxxxxxxxxxxxxxxxxxxxxx
xxxxxxxxxxxxxxxxxxxxxxxxxxx	Hilda Series		
	Black Hill Series		
Ancient gneisses	xxxxxxxxxxxxxxxxxxxxxxxxxxx		
	KHEIS SYSTEM	KHEIS SYSTEM (Grootderm Series?)	

Table 2.2b: *Past and present stratigraphic classification schemes for the Gariep Belt.*

Kröner (1974)	SACS (1980)		Von Veh (1988)			Jasper (this work)	
	Miogeosynclinal facies	Eugeosynclinal facies	Port Nolloth Zone		Namaqua Terrane	Port Nolloth Zone	
Kubas Igneous Complex NAMA GROUP xxxxxxxxxxxxxxxxxxxxxxxxxxxx	NAMA GROUP xxxxxxxxxxxxxxxx		Holgat Sequence			NAMA GROUP xxxxxxxxxxxxxxxxxxxxxxxxxxxx	
Numees Formation Helskloof Formation Oranjemund Formation	Numees Formation xxxxxxxxxxxxxx		Numees Sequence	Sendelingsdrif Formation Jakkalsberg Formation		Hilda Subgroup	Numees Formation xxxxxxxxxxxxxx Obib Peak Form. Pickelhaube Form. (= "Holgat Form.")
Hilda Formation GARIEP Holgat Formation GROUP Grootderm Formation	Hilda Suite Stinkfontein Formation	Holgat Suite Oranjemund Suite Grootderm Suite	Hilda Sequence	Doble River Formation Wallekraal Formation Pickelhaube Formation	Oranjemund Suite Grootderm Suite		
Stinkfontein Formation xxxxxxxxxxxxxxxxxxxxxxxxxxxx	xxxxxxxxxxxxxxxx		Stink-fontein Sequence	Keiges Formation Cumchaib Formation Vredefontein Formation Lekkersing Formation		Stinkfontein Subgroup	Gum[illegible] Form. Ros[illegible]n Form.
Basement Complex			xxxxxxxxxxxxxxxxxxxxxxxxxxxx Basement Complex			xxxxxxxxxxxxxxxxxxxxxxxxxxxx Basement Complex	

terrigenious/marine clastic phase, and the Hilda Subgroup, comprising the Pickelhaube Formation, a platform carbonate and continental shelf clastic phase, the Obib Peak Formation, a fluvial p[illegible] and the Numees Formation, a mixed glaciomarine/interglacial phase (Table 2.2b). The "Holgat Subgroup" (Von Veh, 1988) within the study area was assigned to the Pickelhaube Formation, representing a deepwater equivalent to the latter (see chapter 3).

2.4 INTRUSIVE ROCKS

In the north-western Richtersveld, the Stinkfontein Subgroup is intruded by mafic dykes of the Gannakouriep Suite. In southern Namibia however, the Gannakouriep Suite occurs exclusively as sills interlayered with the Rosh Pinah Formation, Gumchavib Formation and the lower Pickelhaube Formation (Fig. 2.4). The sills all contain the paragenesis green amphibole-plagioclase-epidote-chlorite-quartz-+/- biotite, +/- calcite and in some cases, relics of pale brown magmatic pyroxene, rimmed by hornblende and epidote, indicating the sub-volcanic origin of these sills. Accessory minerals include tabular ilmenite, hematite and sphene.

In the Richtersveld Gariep Group lithologies are intruded by the Kuboos-Bremen and Garub Intrusives.

The Bremen Plutonic Complex (Fig. 2.8) forms a sheeted arcuate complex, as if part of a multiphase ring structure (Allsopp,et al., 1979). The rocks comprise mostly alkali-feldspar (+/- quartz) syenite (< 7% hornblende, riebeckite and iron oxide) and minor alkali-feldspar granite. The granite has a markedly variable quartz content and, in places, is of quartz-syenite composition (Allsopp et al., 1979).

The Kuboos Pluton (Fig. 2.8) consists of a medium-grained granite phase, comprising a nearly equigranular reddish rock consisting of quartz, K-feldspar, plagioclase and scattered flakes of biotite in an allotriomorphic matrix and small phenocrysts of K-feldspar (Allsopp et al., 1979). This granite phase is intruded by a coarse porphyritic granite phase comprising euhedral pinkish phenocrysts of zoned perthite up to 4 cm long, set in a medium- to coarse-grained matrix of andesine and quartz with minor K-feldspar, accessory minerals and rare relics of green hornblende, largely altered to chlorite (Allsopp et al., 1979).

A zone of carbonate-bearing intrusives trending northeast from the Bremen Complex links up with the area of the Garub carbonate-bearing sills (Fig. 2.8), which have a carbonatitic affinity (Schreuder, 1975).

The Gariep Group north of the Orange River is intruded by Karoo dolerite dykes (Fig.

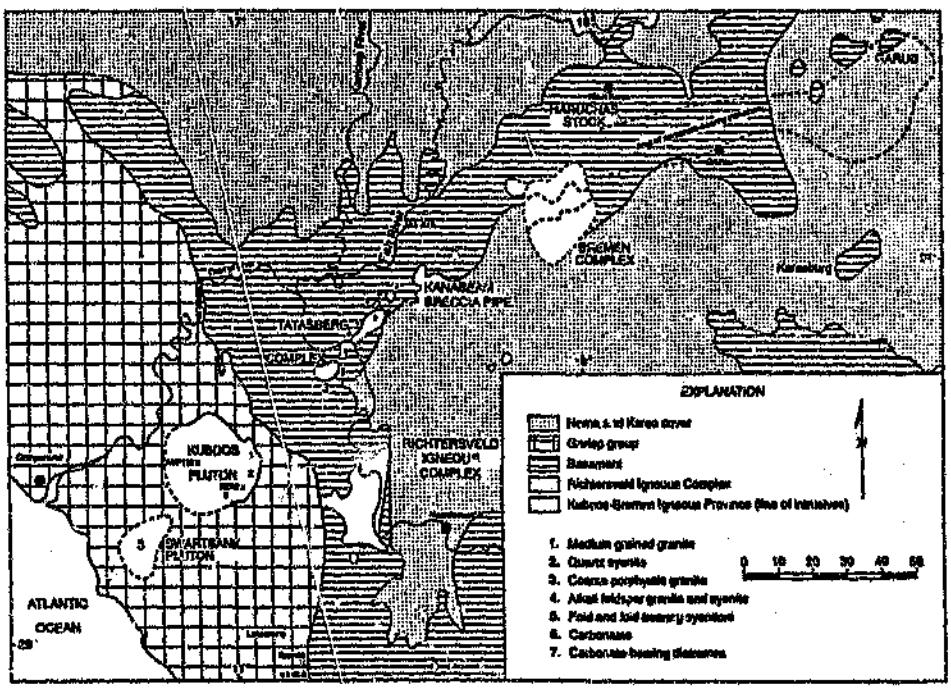


Fig. 2.8: *Simplified geological map of parts of the Richtersveld and southern Namibia (modified after Allsopp et al., 1979).*

2.4), trending in a northerly direction from Dreigratberg to north of Trekpoort Farm, approximately 25 km north of Rosh Pinah.

2.5 RADIOMETRIC AGES OF THE GARIEP GROUP STRATIGRAPHY

Age relationships between the various tectono-stratigraphic and stratigraphic units of the Gariep Belt are not well constrained. All radiometric ages have been derived from pre-, syn-, and post-tectonic magmatic rocks, mostly granites and felsites of the Rosh Pinah Formation. Mineral dates from metasedimentary rocks have not been obtained. The Lekkersink granite, which is intrusive into Stinkfontein lithologies in the Richtersveld, has been dated at 780 +/-10 Ma (Pb-U zircon age), representing the most likely age constraint for the initiation of rifting in the Gariep Belt. This age constraint for the initiation of rifting is supported by the Rb-Sr mineral-isochron age of 717 +/-11 Ma, achieved from basic rocks of the Gannakouriep dyke and sill swarm in the Richtersveld (Ransome and Reid in: Hartnady and Von Veh, 1990), which is intrusive into the Stinkfontein Subgroup and the lower Pickelhaube Formation. A Rb-Sr mineral-isochron age of 719 +/-28 (Welke, *in*: De Villiers, 1968) obtained from the felsites of the Rosh Pinah Formation probably also represents a primary age, rather than the mineral-errorchron age of 686 +/-32 Ma (Allsopp et al., 1979), obtained for the Rosh Pinah felsites.

The lower age for the Gariep Group is constrained from the alkaline granitic members of the Richtersveld Suite (Richterveld Complex and older Bremen granites of Allsopp et al., 1979), which are unconformably overlain by the rocks of the Stinkfontein Subgroup. A maximum age for the initiation of the geodynamic evolution of the Gariep

Belt is sustained from these these lithologies, which produced a U-Pb Zircon age of 920 +/_ 10 Ma and a Rb-Sr whole-rock isochron age of 911 +/_ 39 Ma (Allsopp et al., 1979), as well as an age of 920 +/- 30 Ma (Burger & Coertze, 1973). This would however mean, that rifting took place over a time span of 200 Ma, which is geologically not viable. Allsopp et al. (1979) described the quartzite and lava xenoliths, resembling Stinkfontein lithologies of the Richterveld within the older Richterveld intrusives and implied that the Stinkfontein must be older than 920 Ma. However, because of the strong similarities between the Stinkfontein Subgroup and the Orange River Group, this is very unlikely.

Alsopp et al. (1979) noted two widespread resetting events within the Gariep Belt at about 700 and 500 Ma, that have influenced Rb-Sr whole rock results. Additional evidence for resetting was discovered by Welke et al. (1979), yielding resetting ages of about 480 Ma.

Other ages obtained for the "Gannakouriep dyke and sill swarm" have yielded equivocal ages from 1200 Ma to 200 Ma (40Ar/39Ar; Reid, 1977; 1979) and often fall into the range of 500 to 550 Ma (543 +/- 15 Ma, De Villiers, 1968; 542 +/- 4 Ma, Onstott et al., 1986) and probably represent resetting ages corresponding with the Pan-African metamorphic overprint.

If the correlation of the Numees diamictite with the widespread Varangian Glacial Episode in Europe (Harland, 1983; Hambrey & Harland, 1985) and the Rapitan Glacial Episode of northwest Canada is correct, it was deposited at around 670 Ma.

A minimum age for the Pan-African geodynamic evolution is indicated by the emplacement of the granites, syenites, carbonatites and diatremic intrusives of the multi-phase "Kuboos-Bremen Line" intrusives (Allsopp et al., 1979), which intrude the

rocks of the Gariep Group in the Richtersveld. The entire igneous lineament appears to be post-tectonic (Hartnady & Von Veh, 1990) and transects the Gariep structural trends at a high angle. Hartnady & Von Veh (1990) suggest, that the U-Pb ages ranging between 525 +/- 60 Ma for the Kuboos pluton and 521 +/- 12 Ma for the younger part of the Bremen complex (Allsopp et al., 1979) therefore possibly establish a minimum age for the Adamastor orogeny within the Gariep Belt.

Geochronological data from the Nama Group, which formed as peripheral foreland basins in response to the advancing Khomas orogeny and the Adamastor orogeny (Stanistreet et al., 1991), provides important time constraints to determine a minimum age for the Adamastor orogeny in the southern coastal branch of the Damara Orogen. Geochronological data obtained from shales of the lowermost Schwarzrand Subgroup (lower Nama Group), which was deposited into the Nama foreland basin, situated marginal to the Adamastor orogeny within the Gariep Belt, indicates a K/Ar age of 536 +/_ 12 Ma (Horstmann, 1987). Ages gained from white micas of the Nama Group and compiled by Miller and Grote (1988) yield ages ranging from 547 to 443 Ma, which were previously interpreted as cooling ages, but have been reinterpreted as metamorphic ages by Stanistreet et al. (1991) because of the striking similarity with 40Ar/39Ar metamorphic ages in the Vanrhynsdorp Group (552 to 476 Ma with a maximum at 496 Ma; Gresse et al., 1988), which represents the southern correlative of the Nama Group in Namaqualand, South Africa. Geochronological data obtained from Nama Group sediments in southern Namibia give K/Ar ages between 530 and 500 Ma (Horstmann et al., 1990), suggesting a low grade metamorphic alteration of upper Nama Group sediments in southern Namibia. The 530 to 500 Ma ages may be either indistinguishable from the 496 Ma peak metamorphism of Gresse et al. (1988)

within the limits of experimental error, or may indicate a time trangressive collision from north to south during the final stages of the geodynamic evolution of the Gariep Belt and the associated Nama foreland basins (Stanistreet et al., 1991).

CHAPTER 3

SEDIMENTOLOGY

3.1 INTRODUCTION

No detailed sedimentological studies have been carried out so far in the entire Gariep Belt. In the Richtersveld area and southern Namibia (Fig. 2.8), research work has been restricted mainly to stratigraphic and structural studies and investigations on the geology of Rosh Pinah ore bodies and its immediate vicinity (see section 1.2). One of the aims of this thesis is, therefore, to present data from detailed measured vertical sections at selected localities throughout the Rosh Pinah-Sendelingsdrif and some adjacent areas and to correlate these in order to develop a palaeoenvironmental model. This allow a refinement of the stratigraphy of the Gariep Group of southern Namibia and an insight into the tectonics which controlled its deposition. Sedimentary structures of the Gariep Group lithologies within the study area were affected by upper greenschist/lower amphibolite facies metamorphism and are well preserved. Therefore, the names of the interpreted precursor rocks will be used in this chapter.

The scale of stratification thicknesses of Blatt, Middleton and Murray (1980) was applied in this work.

The positions of localities, referred to in the following text, are presented in Figures 2.4 and 2.8.

3.2 THE ROSH PINAH FORMATION: RIFT SEDIMENTATION WITHIN A FLUVIALLY/LACUSTRINE/FAN DELTA-DOMINATED DEPOSITIONAL SYSTEM WITH VOLCANISM

Within the study area the Rosh Pinah Formation, which was first defined by McMillan (1968) as the Kapok Formation and later renamed Rosh Pinah Formation by SACS (1980), consists of a maximum 2000 m thick clastic and volcanic unit at the base of the Stinkfontein Subgroup. Its stratigraphic relationship to the other formations in the Port Nolloth Zone was the subject of much debate in the older literature. Several authors (De Villiers & Söhnge, 1959; Kröner, 1974; Kröner, 1975; SACS, 1980; Von Veh, 1988) placed the Rosh Pinah Formation into the Hilda Subgroup. Field evidence within the study area, which is the type area of this formation shows, however, that the Rosh Pinah Formation forms the lowermost stratigraphic unit of the Gariep Group north of the Orange River.

Within the following subsections the lithologies and sedimentary structures of the rocks within the Rosh Pinah Formation are described and interpretations of the depositional systems and palaeoenvironments are made. Unfortunately access was denied to the area in the immediate vicinity of Rosh Pinah and Spitskop Farm further to the north (IMCOR Zinc Ltd mine grant area). These are two key areas for the understanding of the evolution of the Rosh Pinah Formation and the early development of the Gariep Belt in southern Namibia. Although no sedimentological and structural work was possible within these areas, nevertheless, existing literature describing the geology of these localities is summarized at the end of this chapter and put into context with the geology of the investigated study areas.

3.2.1 Massive conglomerate/sandstone/mudstone facies association: fan deltas prograding into a lacustrine palaeoenvironment

Nine facies comprise this facies association (Fig. 3.1), namely: (1) massive matrix-supported conglomerate (Cms); (2) massive sandstone (Sms); (3) normally graded sandstone (Sng); (4) inverse graded sandstone (Sig); (5) massive sandstone (Sms); (6) finely interlaminated siltstone and mudstone (Mfl); (7) wave-ripple cross-laminated siltstone/fine sandstone (Swr); and (8) mudstone (Mm).

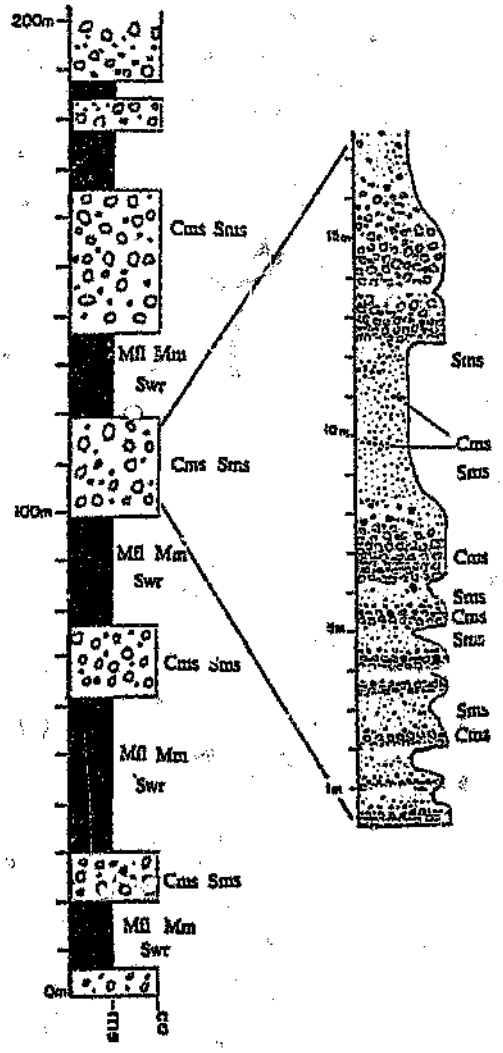


Fig. 3.1: *Measured section through the Rosh Pinah Formation at locality 7, south-east of Pickelhaube (Fig. 2.4).*

(a) Description of lithologies

The grey to dark grey matrix of the matrix-supported massive conglomerate (Cms) consists of medium to coarse grains of quartz, feldspar, and lithic grains including micaschist, with a quartzitic, calcareous and sericitic cement. In handspecimen, the sandstone grains vary from < 0,5 mm to 2 mm and have an angular shape. The conglomerate clasts consist of subangular to subrounded clasts and boulders of vein quartz, gneissic granite, granodiorite, quartzite, micaschist, phyllite, and brown weathered dolomite. The average clast size ranges between 2 to 30 cm, but within some beds, large isolated dolomitic boulders (Fig. 3.2), up to 100 X 5 m in dimension, are present.

The sandstones (Sms, Sng, Sig), which are interbedded with the conglomerates (Cms; Figs. 3.3 & 3.4), consist of quartz, plagioclase, muscovite, biotite, and rock fragments,



Fig. 3.2: *Massive dolomite boulder within the conglomerates of the Rosh Pirah Formation at locality 7, south-east of Pickelhaube (Fig. 2.4).*



Fig. 3.3: *Massive conglomerate (Cms) displaying normal and inverse grading in beds with gradational contacts at locality 7, south-east of Pickelhaube (Fig. 2.4).*

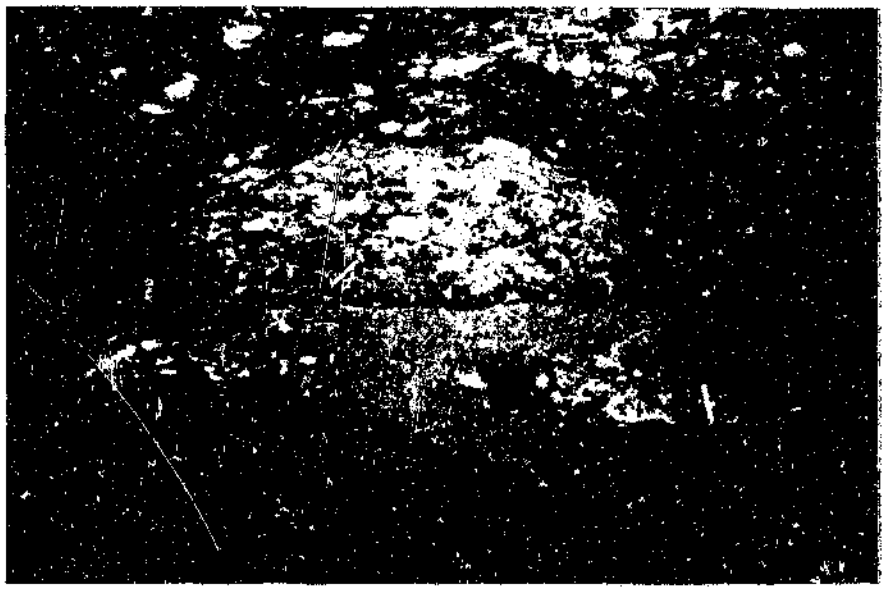


Fig. 3.4: *Sharp scour contact within massive conglomerate (Cms) at locality 7, south-east of Pickelhaube (Fig. 2.4).*

with accessory iron oxide. The sandstones vary from dark grey to dark brown and reddish brown, depending on the amount of iron oxide. The size of the grains varies in handspecimen from < 0,5 mm to 2 mm and they are often joined by granules and pebbles of quartzite. The shape of the grains, granules and pebbles is subangular to subrounded.

The wave-ripple cross-laminated sandstone and siltstone (Swr; Fig 3.5), which is interlaminated with mudstone (Mfl, Mm) and interbedded with the conglomerate/sandstone units (Cms, Sms, Sng, Sig), consists of, in the order of their abundance, quartz, muscovite, biotite and iron oxide. The matrix comprises predominantly quartz and muscovite. The colour of the silt/sandstones (Swr) is light brown to brown. The shape of the grains is angular to subangular.

The mineral composition of the blue-grey-silver to green-grey and dark-grey phyllitic



Fig. 3.5 *Thickly laminated and very thinly bedded wave-ripple cross-laminated sand-/siltstone (Swr), interlaminated with mudstone (Mfl) at locality 7, southeast of Pickelhaube (Fig. 2.4); note penetrative s2 cleavage from bottom left to top right.*

mudstones (Mm, Mfl), which are interlaminated with the fine sand- and siltstones (Sms, Swr; Fig. 3.6), consists of quartz, muscovite and biotite, with a variable amount of carbon, leading to its occasional dark grey colour, as well as smaller amounts of chlorite and feldspar. Iron oxide and tourmaline occur in accessory amounts.

(b) Description of sedimentary facies

The massive conglomerates (Cms) and sandstones (Sms, Sng, Sig; Fig. 3.3) are both bedded and unbedded and contain a variety of well-preserved sedimentary structures. Bed thicknesses of the different sandstones or conglomerates within these units range from several centimetres to 5 m (Fig. 3.1). The overall thickness of the conglomerate/sandstone cycles can vary between 5 to 25 m (Fig. 3.1). Beds are often structureless, but commonly display sedimentary structures such as normal and inverse grading in beds with gradational contacts (Fig. 3.3). Occasionally sharp scour bases are also present (Fig. 3.4). A plane stratification within the massive conglomerates (Cms) is manifested by the weak normal and inverse grading. The sorting of the massive conglomerate and its matix (Cms) and the sandstones (Sms, Sng, Sig; Figs. 3.3 & 3.4) is very poor.

The massive mudstones (Mm) display no sedimentary structures and usually have sharp contacts with the interbedded/interlaminated conglomerate/sandstone lithologies. The overall thicknesses of the massive mudstone units vary between 5 to 40 m (Fig. 3.1).

The laminated mudstones (Mfl) are thinly plane-laminated (< 1 mm to 3 mm; Fig. 3.6) and are interlaminated with massive sandstones (Sms) at the contact to the over- and underlying conglomerate/sandstone units. Towards the contacts with the

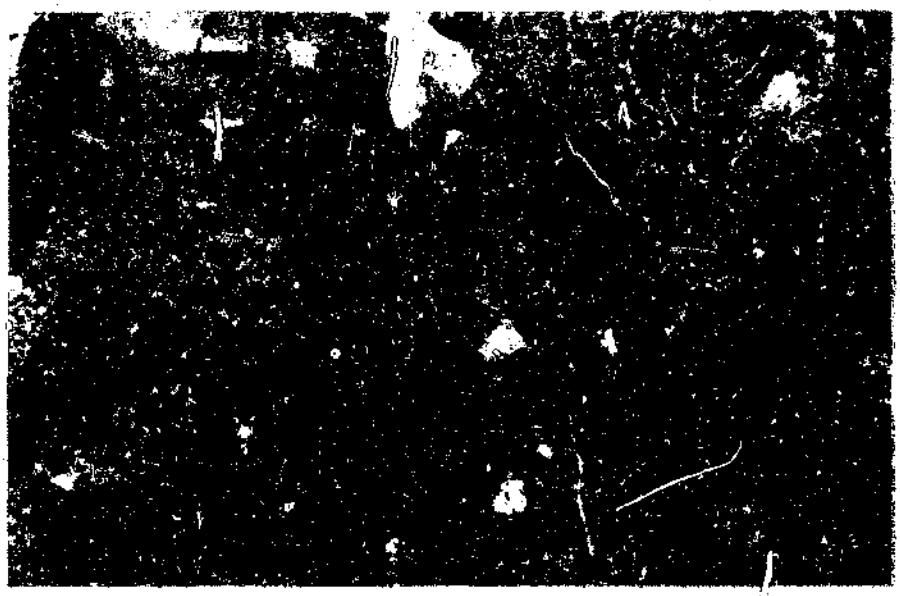


Fig. 3.6: *Thinly laminated mudstone (Mfl) at the transition from sandstone to mudstone lithologies at locality 7, south-east of Pickelhaube (Fig. 2.4); note the penetrative bedding-subparallel cleavage.*

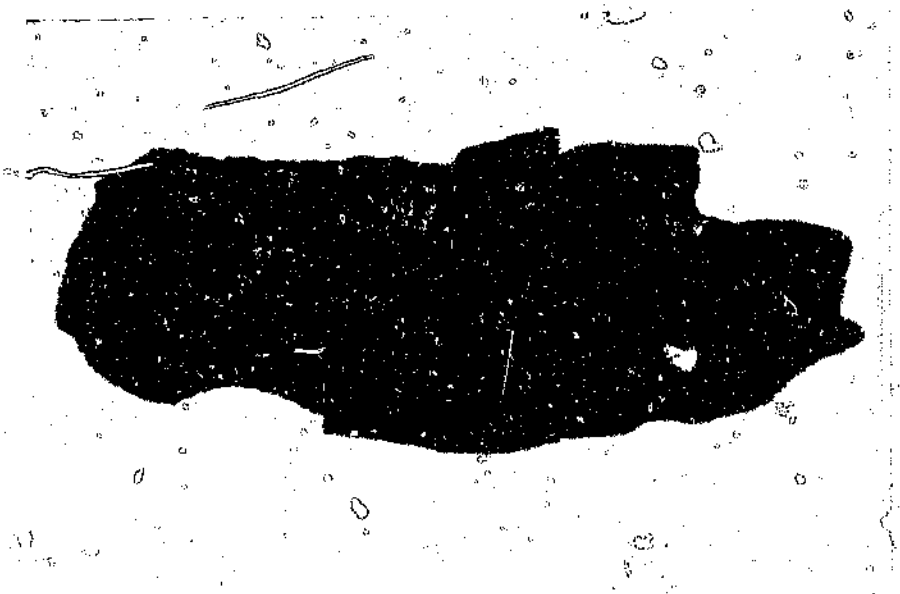


Fig. 3.7: *Wave-ripple marks within the mudstones (Mfl) and sand-/siltstones (Swr) of the Rosh Pinah Formation at locality 9 (Fig. 2.4).*

conglomerate/sandstone units thicknesses of the sandstone beds increase. Contacts with the structureless massive mudstone (Mm) are gradational. In places, the contact zone between the conglomerate/sandstone lithologies (Cms, Sng, Sig, Sms) and the mudstones includes wave-ripple-cross-laminated sand- and siltstones (Swr) with fine mudstone inclusions, interlaminated and interbedded with mudstones (Mm, Mfl; Figs. 3.5 and 3.7).

The sandstone/siltstones (Swr) and mudstones (Mm, Mfl) are thickly laminated to very thinly bedded (1 to 8 cm) and may consist of dark grey carbon-rich mudstone (Mm; Figs. 3.1 and 3.5).

(c) Contact relationships

In the transition zone between mudstone and sandstones a distinctive coarsening and thickening upwards and downwards of the sandstone and mudstone beds is displayed. The thicknesses of the transitional zones from conglomerate/sandstone lithologies to massive mudstones vary between 5 to 25 m, but contacts can also be sharp.

Up to five large scale conglomerate/sandstone/mudstone cycles can be defined within the Rosh Pinah Formation south-west of Rosh Pinah.

(d) Interpretation

Normal and inverse grading within the massive conglomerates (Cms) and sandstones (Sms, Sng, Sig), the presence of sand sheets, the subangular to subrounded shape of clasts, the immature composition of the sandstones and the conglomerate matrix, the extraordinary large size of some dolomite boulders, as well as the presence of

basement-derived clasts indicate a debris-flow-dominated environment, typical for debris-flow-dominated fans. Similar palaeoenvironments have been commonly identified in sedimentary rock strata throughout earth history, e.g in the Archean (Buck, 1980; Kingsley, 1984; Stanistreet and McCarthy, 1991), Proterozoic (McGowen and Groat, 1971; Middleton and Trijillo, 1984; Ruxton and Clemmey, 1986; Master, 1991) and Phanerozoic (Bluck, 1967; Steel and Aasheim, 1978; Schultz; 1984; Hayward, 1983; Wells, 1984; Derbyshire and Owen, 1990). Modern analogues of these debris-flow-dominated fans are the Yallah fan delta in south-east Jamaica (Wescott and Etheridge, 1980), the Gilgit Fans of the Karakoram Mountains (Derbyshire and Owen, 1990), and the Hanaupah Fan in the Death Valley region, USA (Bull, 1963; 1972; Denny, 1965; Hooke, 1967). All of these fans are dominated by debris-flow deposits interbedded with alluvial deposits, particulary those of shallow, braided streams or sheetflows. The abundance of more sandy or conglomeratic material within this facies association indicates sheetflood processes during further distal or proximal deposition within such an environment.

The massive mudstones (Mm) and plane-laminated mudstones (Mfl) and, in places, the highly carbonaceous composition of some mudstones (Mm), indicate deposition within a quiescent subaqueous environment, in which clay particles could settle. The absence of quartz arenites, often developed as a result of wave action in open coastal marine settings, the immature nature of the siltstones/fine sandstones and interlaminated and interbedded sandstones (Swr, Sms), indicate that these sediments formed as debris flows and fan deltas prograding into a lake body. Wave-ripple cross lamination with mudstone inclusions within the fine sandstones/siltstones (Swr) and the interlaminated and interbedded mudstones (Mfl) indicate minor wave reworking

along a shoreline above lacustrine wave base.

Ancient analogues of fan deltas are represented by the Oligocene-Miocene conglomerates of the Meteora monasteries region in Greece (Ori and Roveri, 1987), which were deposited during fluctuations in the water level, which affected both the subaerial and subaqueous facies of fan deltas, and the Tertiary rift basins in the Bohai region of northeastern China (Chen Channing, Huan Jiakuan et al., 1981; Chen Channing, Huang Jiakuan et al., 1982). Within the East-African intracontinental rift system itself, which represents a modern example for environments dominated by alluvial fans prograding as fan deltas into lacustrine environments, clastic sediment is limited to material derived from neighbouring fault scarps and uplifted blocks within the rift and transported through the few river channels that flow along the rift. Therefore, the dominant sediments are those of alluvial fans and fan deltas prograding into lakes (Mitchell and Reading, 1986).

3.2.2 Coarse to fine clastics/carbonate facies association: proximal to distal braid plain, alluvial fan and lacustrine depositional system

The following facies were recognized within this facies association: (1) massive, matrix-supported conglomerate (Cms); (2) massive arkosic sandstone (Sms); (3) normally graded arkosic sandstone (Sng); (4) inverse graded arkosic sandstones (Sig); (5) tabular planar cross-bedded sandstone (Spc); (6) trough cross-bedded sandstone (Stc); (7) ripple marked sandstone (Srm); (8) mudstone (Mm); (9) massive carbonate (Lmd).

(a) Description of lithologies

The sandy matrix of the conglomerates (Cms) and the sandstones and pebbly sandstones (Sms, Sng, Srm) overlying the basal conglomerate are medium to coarse grained and consist of plagioclase, quartz, muscovite, biotite, and chlorite, with accessory titanite, zircon, and tourmaline. Clast sizes vary on average between 2 mm and 5 cm and consist of subrounded white quartzite. The composition of the tabular planar and trough cross-bedded quartzitic sandstones (Spc, Stc) is more mature, containing a higher amount of quartz than the other sandstones within this facies association.

The phyllitic mudstones (Mm) are generally silver-grey to green-grey and consist of quartz, muscovite and biotite. They can also be dark grey to black due to an enrichment of carbon. At locality 22, the mudstones are black and are associated with

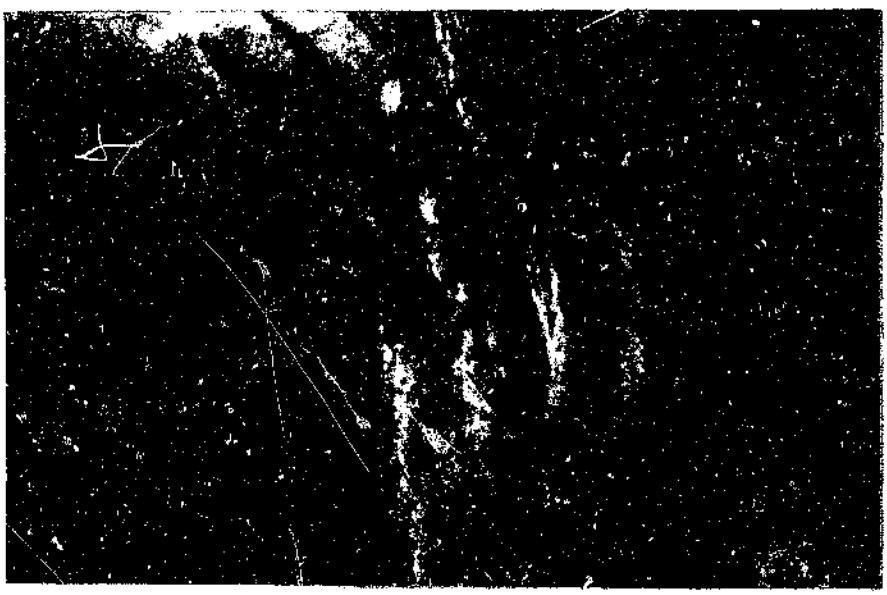


Fig. 3.8: *Black, graphite-rich mudstone (Mm) of the Rosh Pinah Formation displaying sulphur efflorescence (locality 22; Fig. 2.4).*



Fig. 3.9: *Graded beds within arkosic sandstones of the Rosh Pinah Formation in the core of the Anniefontein Anticlinorium near locality 1, immediately north of the Orange River (Fig. 2.4).*

a yellow sulphur efflorescence (Fig. 3.8).

The massive carbonates (Lmd) are light grey to grey and dolomitic in composition.

(b) Description of sedimentary facies

The matrix-supported massive conglomerates (Cms) contain sedimentary structures in the form of upward fining and upward coarsening pebbly beds, with units varying in thickness between 15 cm and 10 m. The matrix comprises medium to coarse and pebbly sandstones. The subrounded pebbles and conglomerate clasts comprise mainly quartzite with average sizes ranging between 2 mm and 5 cm. The base of these beds is usually a sharp scour surface. Some patches of matrix supported conglomerate (Cms) are recognized within the massive sandstone (Sms) units. The

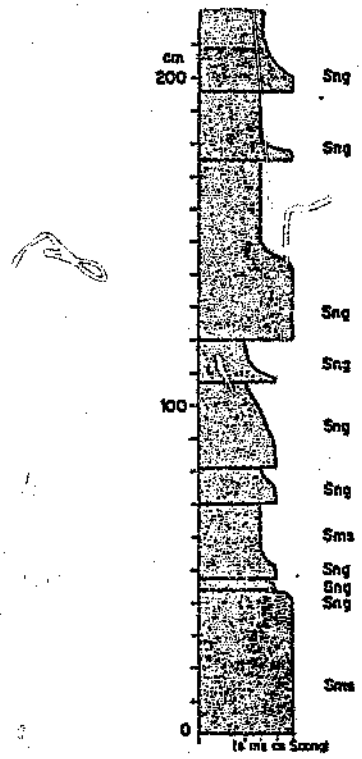


Fig. 3.10: *Measured section through a portion of the Rosh Pinah Formation in the core of the Annisfontein Anticlinorium at locality 1 immediately north of the Orange River (Fig. 2.4).*

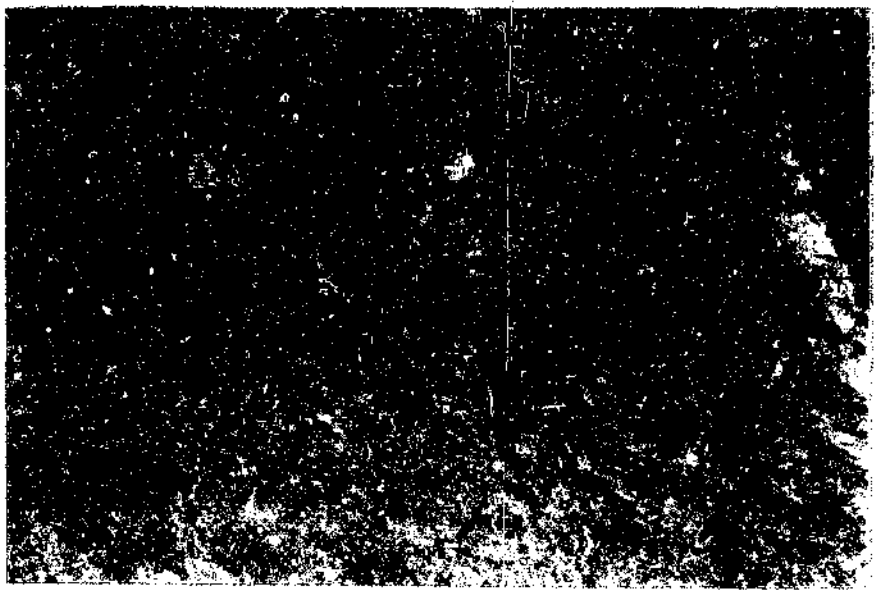


Fig. 3.11: *Linguoid out-of-phase ripple marks within sandstones of the Rosh Pinah Formation, about 2 km south of Gumchavib trigonometrical beacon (Fig. 2.4).*

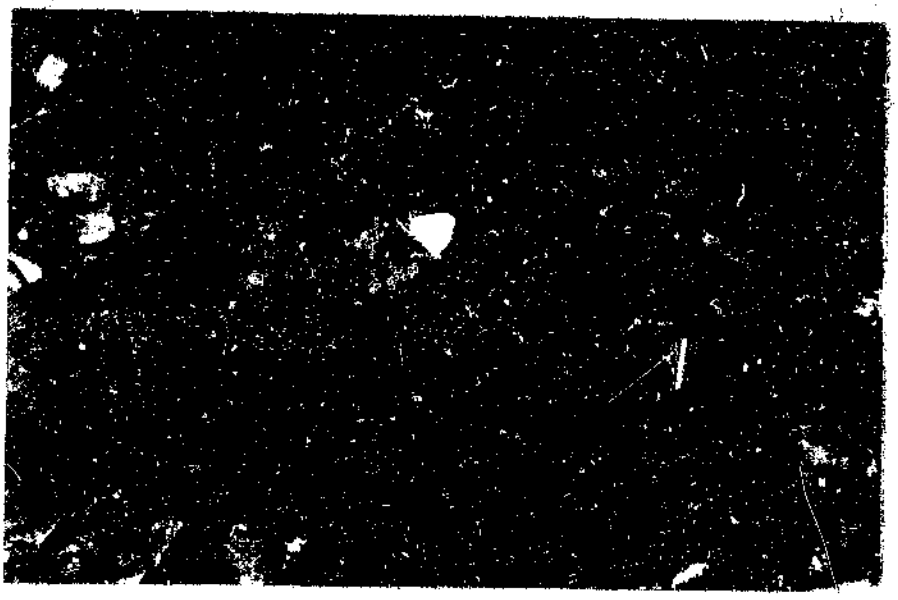


Fig. 3.12: *Sinuous out-of-phase ripple marks within sandstones of the Rosh Pinah Formation, about 2 km south of Gumchavib trigonometrical beacon (Fig. 2.4).*



Fig. 3.13: *Tabular planar cross-bedded quartzitic sandstone (Spc) of the Rosh Pinah Formation at locality 22, about 4 km south of Gumchavib trigonometrical beacon (Fig. 2.4).*

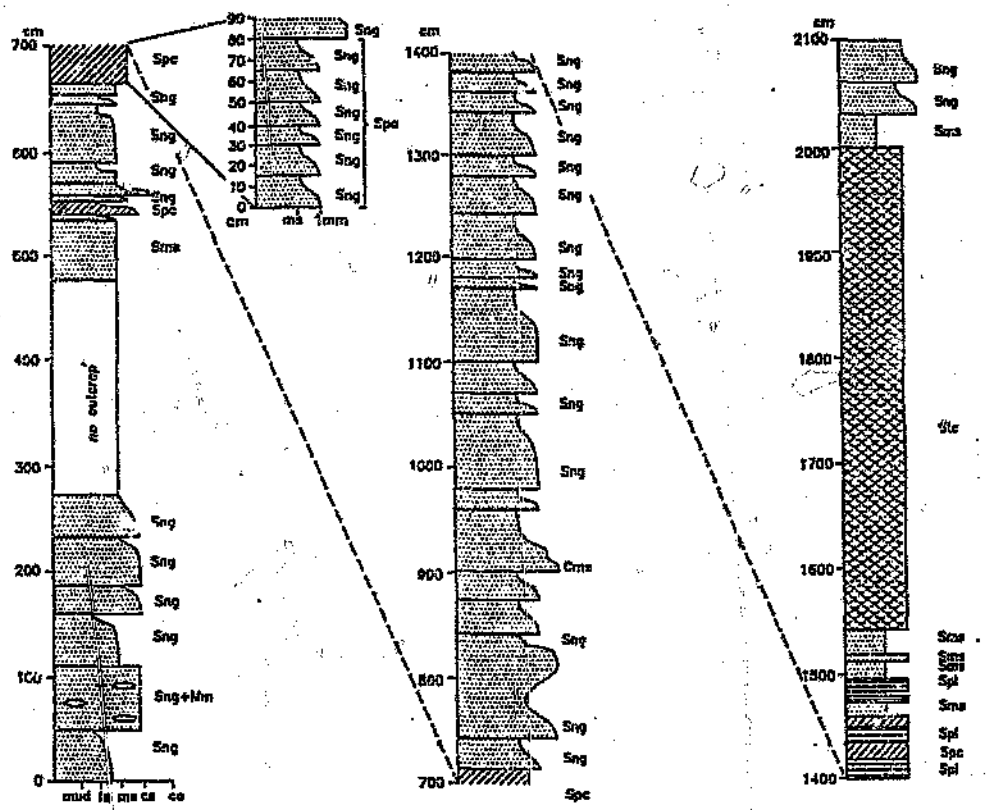


Fig. 3.14: *Measured section through the Rosh Pinah Formation at locality 22, about 4 km south of Gumchavib trigonometrical beacon (Fig. 2.4).*

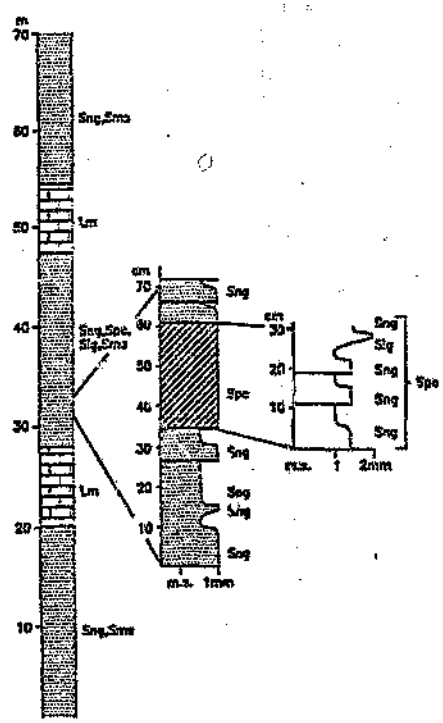


Fig. 3.15: *Measured section through parts of the Rosh Pinah Formation at locality 30, west of Gumchavib Mountain.*



Fig. 3.16: *Trough cross-bedded quartzitic sandstone (Stc) of the Rosh Pinah Formation at locality 22, about 4 km south of Gumchavib trigonometrical beacon (Fig. 2.4).*

conglomerates and their matrix are poorly to moderately sorted.

The feldspathic sandstones (Srns, Srng, Srig, Srm) within this facies association are generally medium to coarse and poorly sorted. Normal grading is common within pebbly arkosic sandstones (Srng) with bed thicknesses varying from 2 cm to 2 m (Figs. 3.9 & 3.10). Asymmetrical linguoid and sinuous out-of-phase ripples are also present (Figs. 3.11 & 3.12). Set thicknesses of graded coarse to medium sandstones of the tabular planar cross-bedded sandstone (Spc) within the Rosh Pinah Formation vary from 10 cm to ~50 cm (Figs. 3.13, 3.14 & 3.15). The troughs of the trough cross-bedded sandstones (Stc; Fig. 3.16) vary from 10 X 5 cm to 150 X 50 cm in width and height. Scarce palaeocurrent directions of the troughs and planar cross beds indicate a westerly drainage. At localities 22 and 30 (Fig. 2.4) the massive sandstones (Srns)

are poorly sorted with bed thicknesses varying from several centimetres to tens of metres. The massive sandstones are interbedded with normal and inverse graded, medium to pebbly sandstones (Sng, Sig) and tabular planar cross-bedded sandstones (Spc). At these localities, bed thicknesses of the normal and inverse graded sandstones (Sng, Sig) range from 5 to 10 cm (Fig. 3.15). Bed thicknesses of interbedded mudstones (Mm) range between 5 cm to over 20 m and display no sedimentary structures.

The interbedded carbonates display no sedimentary structures. The contacts between the carbonates (Lmd) and sandstones are sharp.

(c) Interpretation

The low maturity of the medium to coarse and pebbly sandstones (Sms, Sng, Srm, Spc, Stc) and mudstones (Mm), and the presence of graded beds together with ripple marks, trough cross-bedding and tabular planar cross-bedding indicate a fluvial environment, generated by a braided fluvial system representing both channel and overbank sedimentation. More specifically, the massive and normally graded matrix supported conglomerates (Cms) represent the highest energy environment of deposition and reflect the growth of longitudinal bars at the base of braided channels. The conglomerates (Cms) form the cores of these bars, and tabular planar cross-bedded feldspathic sandstones (Spc) may represent the migration of transverse bars and megaripples (compare Smith, 1971; Boothroyd & Ashley, 1975; Miall, 1978). Each upward fining sequence reflects a single channel body.

The coarser grained feldspathic massive sandstones (Sms) probably represent sands in which sedimentary structures were not preserved, with the mudstones (Mm)

representing overbank deposits. The sedimentary associations suggest a braided fluvial system such as recorded for the South Saskatchewan River and/or the Platte River (Miall, 1978; Harms et al., 1982) for the deposition of this facies association. In particular, the paucity of conglomerates in this facies association suggests the development of a distal fluvial setting analogous to the South Saskatchewan and Platte-type fluvial setting with the continued influx of predominantly sand, rather than an alluvial fan setting, unconformably overlying the basement.

The massive (Sms) and normally and inverse graded sandstones (Sng, Sig) at localities 22 and 30 (Figs. 3.14 & 3.15), which are interbedded with tabular planar cross-bedded sandstones (Spc), probably represent debris flow deposits within a stream dominated alluvial fan. These deposits either prograde into a lake body as a fan delta or represent the earliest marine transgressions, drowning recrystallized algal mats (Lmd) through clastic input during water level changes, which are either tectonic (if lake body) or eustatic (if marine transgression) in origin.

3.2.3 Clastics/carbonate/bimodal volcanic facies association: fluvially, alluvial fan and lacustrine dominated depositional system with volcanism

The following facies occur within this facies association (Figs. 3.17 & 3.18): (1) massive, arkosic sandstones (Sms); (2) normally graded arkosic sandstone (Sng); (3) massive mudstone (Mm); (4) fine laminated mudstone (Mfl); (5) massive carbonate (Lmd); (6) felsic volcanics (Va); and (7) massive sulphides (GoSu).

(a) Description of lithologies

The sandstones (Sms, Sng) are red-brown to grey and consist of subangular to subrounded grains of quartz, plagioclase and carbonate, as well as biotite, muscovite and chlorite. The sandstones are medium to coarse and often pebbly with maximum pebble diameters of 2 cm, with pebbles comprising subangular to subrounded quartzite and plagioclase.

The mudstones (Mm, Mfl) vary from silver-grey to grey-green and black and consist of quartz, biotite and muscovite, and minor chlorite and feldspar, associated with

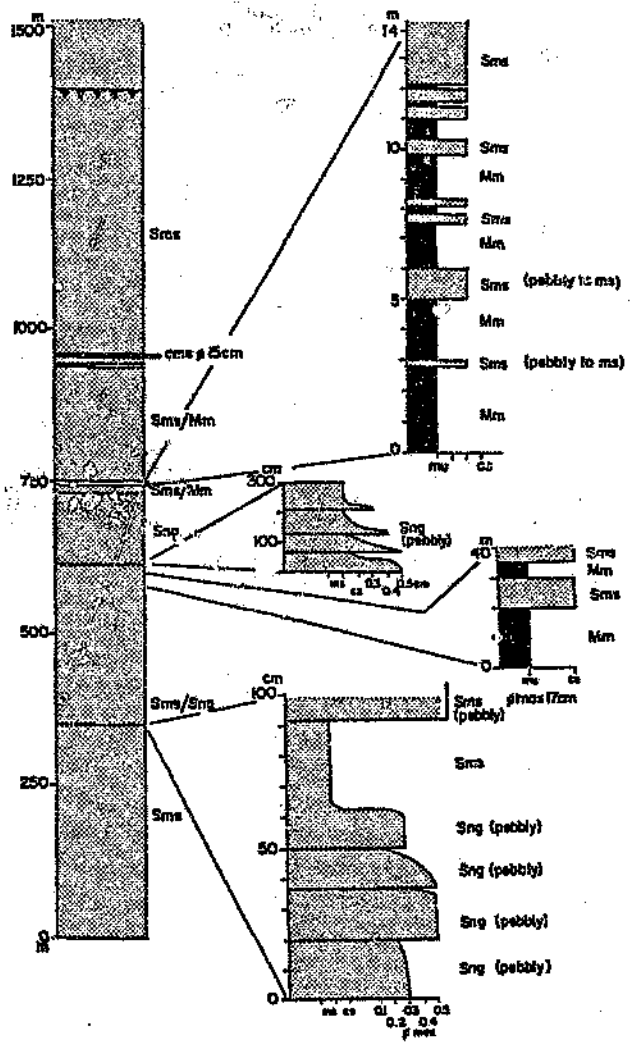


Fig. 3.17: *Measured section through a portion of the Rosh Pinah Formation in the central part of the Rooikat thrust slice (Fig. 2.3).*

varying amounts of carbon, and can be described, depending on their relative composition, as biotite-muscovite schists and be interpreted as carbonaceous or black muds originally.

The carbonates (Lmd) are dark grey, dolomitic in composition with a high amount of carbon, which causes its dark colour.

The volcanics (Va) are white-grey to light brown and light red and consist of approximately 70% quartz and 30% feldspar with a porphyritic texture (see section 3.2.5).

At locality 5 (Fig. 2.4), within the Rooikat thrust slice (Fig. 2.3), a 40 cm gossan (GoSu) indicates the position of massive sulphide and is interbedded with massive feldspathic sandstone (Sms) and mudstone (Mm; biotite schist). The gossan is dark brown, porous and spongy, and is associated with Pb-sulphide mineralization within the Rooikat thrust slice. The overlying sandstone at the contact of the gossan is white to reddish and strongly silicified.

(b) Description of sedimentary structures and facies

Sedimentary structures within the sandstones (Sms, Sng) range from massive structureless (Sms) to normally graded beds of medium to coarse pebbly sandstone. Bed thicknesses range from 10 cm to 70 cm (Fig. 3.17). The grain size within a graded bed can vary from a maximum of 2 cm within pebbly sandstones to fine sandstone or mudstone.

The mudstones (Mm) vary in bedthickness from 80 cm to 9 m. They are interbedded with carbon-rich black carbonates (Lmd; Figs. 3.17 & 3.18).

No sedimentary structures are displayed within the carbonates (Lmd), which have

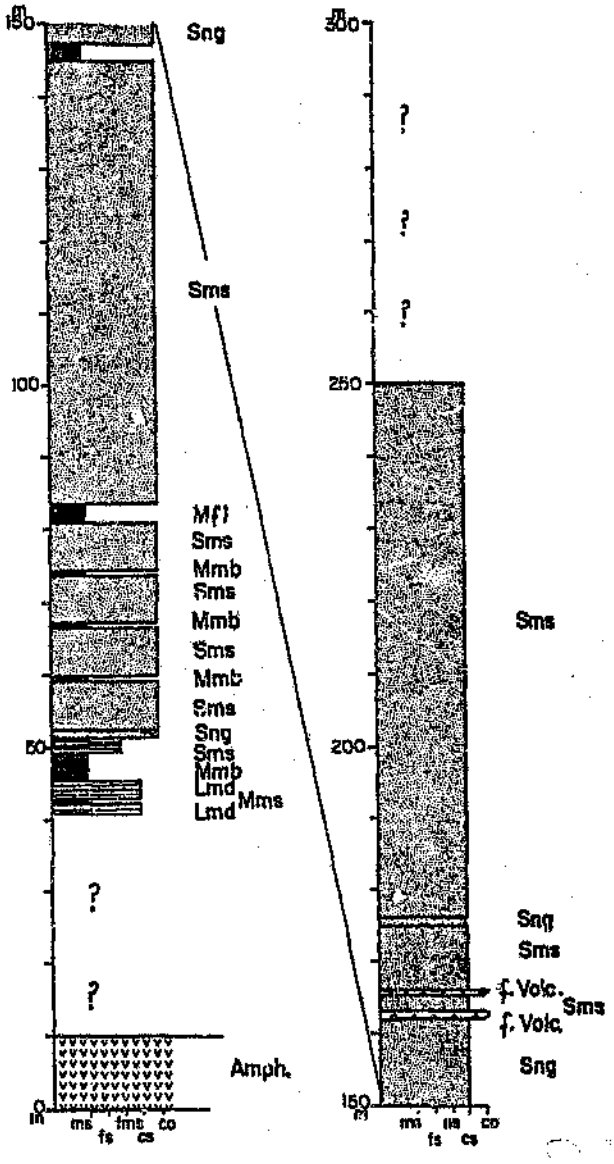


Fig. 3.18: *Measured section through a portion of the Rosh Pinah Formation in the northern part of the Rooikat thrust slice (Fig. 2.3).*

sharp contacts to the under- and overlying lithologies. Up to 2 m thick feldspathic sandstone beds, as well as carbon-rich mudstones are interbedded within the carbonate (Fig. 3.18). Overall thicknesses of these carbonates vary from 1 m to > 15 m.

The thicknesses of the volcanic beds (Va) and sulphides range from 40 cm to 2 m and pinch out laterally within several tens to hundreds of metres. The contact to the under-

and overlying feldspathic sandstones is sharp.

The gossan (GoSu) is interlayered within an underlying massive mudstone (Mm) and an overlying massive feldspathic sandstone (Sms). The contact to the overlying sandstone (Sms) is sharp. The amount of hematitic Fe-oxide within the underlying mudstone appears to increase gradually towards the contact with the gossan (GoSu). The overall thickness of the gossan (GoSu) does not exceed 40 cm and the bed pinches out laterally within tens of metres.

(c) Interpretation

The relatively large thickness of up to 5 m of the massive and laminated mudstone units (Mm, Mfl) and the carbonaceous nature of the mudstones indicate a relatively deep and quiescent depositional environment, in which fines could settle from suspension (Jenkyns, 1986).

The presence of carbonates, which are interbedded with the mudstones (Mm, Mfl) and sandstones (Sms, Sng), indicates a subaqueous deposition of the mudstones (Mm, Mfl), the carbonates (Lmd) and the sandstones (Sms, Sng). The immature composition of the feldpathic sandstones and the absence of quartz arenites, the latter often indicative of marine beach processes operating in open marine settings, indicates a probably lacustrine environment for the deposition of facies Mm, Mfl, Lmd, Sms, and Sng. The massive, structureless pebbly, medium to coarse sandstones (Sms) were deposited as distal fan deltas into the lake body. The graded feldspathic sandstones (Sng) and interbedded massive sandstones (Sms) were deposited in a braided fluvial system within stream-dominated alluvial fans (Collinson, 1986), prograding into a lake body as fan deltas. A modern analogue of stream-dominated fans, which have

probably contributed a great deal to the geological record (Collinson, 1986), is that of the Kosi River, which emerges from the Himalayan foothills to develop a fan prograding into the Ganges Valley (Gole and Chitale, 1966).

The volcanics (Va) were deposited as distal acid volcanic flows into a shallow lacustrine environment, interbedded with alluvial fan deposits.

The origin of the Fe-oxide might be subaqueous, volcanogenic vents near deep reaching fracture and fault zones, associated with volcanic activity in a developing rift system.

3.2.4 Conglomerate facies association: a transgressive basal conglomerate depositional system

This facies association consists only of a matrix-supported conglomerate (Cms).

(a) Description of lithologies

This facies association consists of a matrix-supported conglomerate comprising a light brown, quartz-rich, feldspar and mica bearing, medium grained sandy matrix and is monomictic, containing exclusively angular to subangular, strongly deformed granite clasts with diameters up to 40 cm.

(b) Description of sedimentary structures

The conglomerate at the base of this facies association, overlying the granitic basement unconformably, is approximately 3 m thick and matrix-supported, displaying no sedimentary features.

(c) Interpretation

The massive conglomerate (Cms), overlying the granitic basement unconformably, is interpreted as a transgressive basal conglomerate.

3.2.5 The geology of the Rosh Pinah and Spitzkop area (IMCOR Zinc Ltd. Mine Grant Area)

As access to the Rosh Pinah and Spitskop areas was denied by IMCOR Zinc Ltd., only a summary of already existing literature dealing with the geology and associated stratabound Zn-Pb-Cu-sulphide mineralization of these areas will be given in this chapter. Geological studies of the areas were published by McMillan (1968), Page & Watson (1976), Watson (1980), Van Vuuren (1986), Siegfried (1990), Siegfried and Moore (1990) and Lickfold (1990), but no measured vertical sections have been compiled.

The Rosh Pinah Formation in these areas has been described as essentially consisting of two members, a lower volcanic member and an upper member of mainly sedimentary origin (McMillan, 1968, Page & Watson, 1968; Watson, 1980; Van Vuuren, 1986, Siegfried, 1990).

The lower volcanic member, described by McMillan (1968) as the lower volcanic stage, is restricted to the areas north and north-west of Rosh Pinah and best developed at Spitskop Farm, approximately 15 km north of Rosh Pinah. The upper sedimentary member is confined to the area in the immediate vicinity of Rosh Pinah and north of it.

(a) The lower volcanic member of the Rosh Pinah Formation in the Spitskop Farm area

The lower member of the Rosh Pinah Formation comprises a basal conglomerate, overlain by a succession of felsite and subordinate agglomerate with locally developed beds of quartzite, phyllite, carbon-rich argillite and limestone (Page & Watson, 1976; Watson, 1980). The felsite is often strongly sheared. Agglomeratic felsite occurs as lenses in the felsite near the base of the formation. Lenses of carbon-rich argillite and limestone are interbedded with the felsite. Quartzite, which is underlain by volcanic rocks, probably forms part of the overlying sedimentary member of the Rosh Pinah Formation.

Watson (1980) subdivided the felsites into two major groups, massive felsite and sheared felsite.

The massive felsites are characterized by Watson (1980) by the following features:

1) *Equigranular felsite*, which consists of quartz and feldspar of approximately the same size (average 10 Xm) with a typical felsitic texture. Pyrite can be present in places.

2) *Porphyritic and glomeroporphyritic felsite*, where quartz grains can become larger in places and the rock takes a porphyritic and glomeroporphyritic texture. Phenocrysts are 1 - 2 mm across and consist mainly of quartz, perthite, orthoclase and albite, occurring as sporadic isolated grains in the matrix. The matrix can also be heterogeneous in grain size, with larger grains of quartz and feldspar (50 - 125 μm), that occur as clusters. The rock can contain a reasonable amount of pyrite, subordinate dolomite crystals and occasional mica.

3) *Spherulitic felsite* is characterized by the presence of small to large spherulites (0,5 - 1 mm) and in places by the presence of quartz phenocrystes in a normal felsistic matrix.

4) *Amygdaloidal felsite* comprises the equigranular felsite with large, oval shaped amygdales of quartz and dolomite.

5) *Hypidiomorphic "felsite"* does not display a typical felsitic texture, but is composed essentially of acicular grains of feldspar and roundish grains of quartz, with pyrite as a common accessory.

6) *Felsic tuff and agglomerate* display spherical to angular particles of felsite, set in a normal felsitic matrix.

The intensity of shearing within the sheared felsite can be highly variable. The predominantly low intensity of shearing is characterized by the presence of small amounts of mica. Biotite and chlorite are developed in places in addition to common sericite. Strongly sheared felsite is represented by quartz-mica schist, which can enclose aligned lenses of normal felsite (Watson, 1980).

Chemical analyses and mineral composition of the felsites are in accordance with felsites and rhyolites (Watson, 1980).

(b) The upper volcano-sedimentary member of the Rosh Pinah Formation within the "mine concession area" at Rosh Pinah

No measured vertical sections of the upper sedimentary member of the Rosh Pinah Formation, which was described by McMillan (1968) as the "upper volcano-clastic stage of the Kapok Formation", have been published. It consists mainly of a well to poorly sorted coarse to pebbly feldspathic sandstone, with sedimentary structures

ranging from massive sandstone (Sms) to normal and inverse grading (Sng, Sig), as well as occasional tabular planar cross-bedding (Spc). Inconsistent layers of black argillite (Mm), chert, limestone (Lmd), quartz-muscovite schist (Mm), quartz-biotite schist (Mm), biotite-albite schist (Mm) and amphibolite and felsite (Va) are interbedded with the coarse and pebbly feldspathic sandstones (Sms, Sng, Sig, Spc; Page & Watson, 1976). In the immediate vicinity of Rosh Pinah the eastern part of the Rosh Pinah Formation is underlain by the lower volcanic member, whereas the western and north-western areas consist of the upper sedimentary member including beds of felsic lava and amphibolite sills.

The feldspathic sandstones (Sms, Sng, Sig, Spc) are light to dark grey. Schistose feldspathic sandstone is commonly dolomite-bearing and has a brown weathered surface. They are generally poorly sorted and contain well rounded to angular clasts of granite, feldspar and quartz within a fine grained matrix of quartz and feldspar. Muscovite and sericite is abundant in the schistose sandstones. Towards the north of Rosh Pinah, biotite is, in places, a prominant constituent. Dolomite can appear as a major phase in calcareous sandstones and occurs as interlocking grains with quartz and feldspar. Chemical analyses of some sandstones are, in places, enriched in barium (Page and Watson, 1976; Watson, 1986).

The argillite is dark coloured and appears as lenticular beds within the feldspathic sandstones. At the mine workings it is associated with a similar looking, but harder "microquartzite" (Page and Watson, 1976).

Discontinuous dolomitic carbonate beds (Lmd) and small elongated bodies of dolomitic carbonate (Lmd) occur within the felsites (Va) of the Rosh Pinah Formation. They are grey and dark grey, generally fine grained and carbon-rich. Carbon-rich

dolomitic quartzite can be associated with these beds.

Sulphide-bearing dolomitic carbonate rocks, considered to be primary limestones originally, are developed within the ore horizon of the ore-bodies.

Lenses of quartz-mica schist are present in places and are either related to shearing along fault zones or they are of volcanic origin (Page and Watson, 1976; Watson, 1980).

Porphyritic felsite, which is restricted to the upper part of the upper sedimentary member of the Rosh Pinah Formation, is similar in appearence to the porphyritic felsite of the lower member of the Rosh Pinah Formation.

Dark coloured amphibolites are present as discontinuous zones and small bodies in feldspathic sandstone, and represent either altered basic lava or altered basic intrusions (Page and Watson, 1976; Watson, 1980).

Carbonate hosted Zn-Pb-Cu-sulphide mineralized bodies occur within the upper volcano-sedimentary member of the Rosh Pinah Formation at Rosh Pinah and at the Anglo American Skorpion Exploration Camp in Diamond Area No.1, about 20 km north-west of Rosh Pinah. Sedimentary structures, such as ripple marks, are preserved within the stratiform mineralized ore bodies.

(c) Correlation with facies associations of the study area

The poorly sorted coarse to pebbly feldspathic sandstones (Sms, Sng, Sig, Spc) of the upper volcano-sedimentary member wihthin the "mine concession area" resemble the mixed coarse to fine clastics/carbonate facies association (section 3.2.2) of the study area and were probably deposited in a similar stream dominated alluvial fan depositional system, prograding as a fan delta into a lake body and drowning

recrystallized algal mats (Lmd). Occasional felsic volcanics (Va) of the upper volcano-sedimentary member, which are interbedded with the sandstones (Sms, Sng, Slg, Spc), resemble the rocks which were deposited within a fluvially, alluvial fan and lacustrine dominated depositional system (section 3.2.3), associated with volcanism recorded within the Rooikat thrust slice.

3.2.6 Regional distribution of the facies associations

The various facies associations described in the text in the previous sections are confined to several thrust slices, as shown in Fig. 3.19.

The most widespread facies association within the study area is the coarse to fine clastics/carbonate facies association, described in section 3.2.2. It is confined to several thrust slices, mainly to the Gumchavib thrust slice and parts of the Gemsbok thrust slice, as shown in Fig. 3.19. The carbonates within this facies association are only exposed within the Gumchavib thrust slice and the "mine concession area" within the Rosh Pinah thrust slice. Within the Gumchavib thrust slice this facies association was recognized at Gumchavib Mountain, as well as approximately 1 km northeast of locality 22 and 2 km north of the Orange River within the western limb of the Annisfontein anticlinorium (Fig. 3.19).

The conglomerate/sandstone/mudstone facies association (section 3.2.1), which was deposited in a fan delta/lacustrine dominated environment, is exposed throughout the Gemsbok thrust slice and within several imbricate thrust sheets within the imbricate zone in the eastern parts of the Dreigratberg thrust slice. It is also present at the little outcrop approximately 1 km east of Rosh Pinah, indicating that this facies association



Fig. 3.19: *Regional distribution of the several facies associations developed within the Rosh Pinah Formation; for position of thrust slices and localities, see Figs. 2.3 & 2.4.*

continues in a north-westerly direction into the beds of the Rosh Pinah Formation within the Rosh Pinah Mountain, which host the Rosh Pinah Zn-Pb-Cu-sulfide ore bodies themselves (Fig. 3.19).

The volcano-sedimentary facies association of the Rosh Pinah Formation is only exposed within the Rooikat thrust slice (Fig. 2.3), within the "IMCOR Zinc mine concession area" and at Trekpoort Farm (Fig. 3.19).

Within the "mine concession area" the lower volcanic member, described by McMillan (1968) as the lower volcanic stage, is restricted to the areas north and north-west of Rosh Pinah and best developed at Spitskop Farm, approximately 10 km north of Rosh Pinah. The upper sedimentary member is confined to the area in the immediate vicinity of Rosh Pinah and north of it.

The transgressive conglomerate described in section 3.2.4 is exposed at Obib waterhole and on Trekpoort Farm, where it overlies granitic basement. As the thickness of this facies association does not exceed 10 m, it is not shown in Fig. 3.19.

3.2.7 Vertical sedimentary facies association variations

The recognition of significant vertical facies variations within the Rosh Pinah Formation is rendered difficult by the fact that it is restricted to the several allochthonous tectonic units which generally only consist of one facies association.

The most prominent vertical sedimentary facies association variations were described by McMillan (1968), Page & Watson (1976), Van Vuuren (1986) and Siegfried (1990) from the Rosh Pinah and Spitskop Farm areas, where a lower volcanic and an upper mixed volcano-sedimentary member of the Rosh Pinah Formation is exposed. Within

the upper volcano-sedimentary unit of the Rosh Pinah Formation, a gradational decrease of clast and grain size, as well as an increase of the calcareous component is present towards the top of the succession. At Rosh Pinah Mountain within the "mine concession area", the conglomerate/sandstone/mudstone facies association (section 3.2.1), which was deposited in a fan delta/lacustrine depositional system, is over- and underlain by a several hundreds of metres thick sandstone/mudstone/carbonate facies association of the volcano-sedimentary unit (McMillan, 1968;Page & Watson, 1976; Van Vuuren, 1986; Siegfried, 1990), which was deposited in a similar alluvial fan/lacustrine palaeoenvironment associated with bimodal volcanism.

Within the fan delta/lacustrine facies association itself (section 3.2.1) no vertical variations are recorded.

Within the fluvially/alluvial fan/lacustrine deposited facies association (section 3.2.2), and the volcano-sedimentary facies association (section 3.2.3), interbedded carbonates, probably lacustrine in nature, become more abundant towards the top of each succession. In the volcano-sedimentary facies association within the Rooikat thrust slice, this increase of carbonate deposition is concomittant with the increase of felsic volcanics. A distinct vertical facies variation is recorded at the gradational contact of the Rosh Pinah and the overlying Gumchavib Formation, which records the earliest marine transgression, which will be described in section 3.3.

3.2.8 Lateral sedimentary facies association variations

The recognition of significant lateral facies variations within the Rosh Pinah Formation is made difficult by the fact that most facies associations are restricted to

allochthonous tectonic units with a restricted lateral extension. The strong deformation, caused by thrusting, the presence of imbricate thrust zones and intense folding of the rocks within the study area, also renders the recognition of lateral facies variations difficult.

A prominent lateral facies variation is described from within the "mine concession area" within the Rosh Pinah and Spitzkop beds (Page and Watson, 1976; Van Vuuren, 1986; Siegfried, 1990). The volcanic beds at Spitzkop Farm were described as lateral facies equivalents of the volcano-sedimentary sediments further southeast towards Rosh Pinah. According to Van Vuuren (1986), the volcanic Spitzkop beds were deposited near a volcanic centre situated at Spitzkop Farm, whereas the mixed volcano-sedimentary beds and the sedimentary beds within the same tectonic unit were deposited in a more distal environment further southeast. This observation is supported by reconnaissance mapping at Trekpoort Farm approximately 25 km northwest of Rosh Pinah, which showed a distict increase of felsic volcanics within the same tectonic unit, showing, that these volcanics are a lateral facies equivalent of the Rosh Pinah Formation sediments further south. The conglomerate/sandstone/mudstone facies association (section 3.2.1), which was deposited in a fan delta/lacustrine depositional system, can be followed from a locality approximately 1 km east of Rosh Pinah into the Rosh Pinah Mountain, where it pinches out in a northerly direction (personal communications D. Alchin). At Trekpoort Farm, the fluvially/lacustrine deposited facies association (section 3.2.2) and the transgressive basal conglomerate facies association (section 3.2.4) of the Rosh Pinah Formation are lateral facies association equivalents of the volcanic facies association, showing that all four facies associations recognized within the Rosh Pinah Formation

were deposited concurrently and represent lateral facies equivalents.

3.2.9 Palaeogeographic reconstruction

The dominance of continental sediments, the presence of bimodal volcanics within the rocks of the Rosh Pinah Formation, the tectonic instability recorded by several cycles within the fan delta/lacustrine facies association, and the fact, that this thick continental sequence passes upwards into a marine sequence, is typical for an intracontinental rift depositional system (Fig. 3.20). Palaeocurrent data of the Rosh Pinah Formation, although scanty, indicate sediment transport mainly in a westerly direction. This indicates that the provenance area lay to the east of the present outcrop, being a topographic high. The relative paucity of conglomerates in the western parts of the study area suggests that these areas were an extensive sandy to pebbly braided river system, flowing from a source area in the east, whereas the area immediately west of the topographic high was dominated by lacustrine sedimentation, associated with prograding fan deltas and bimodal volcanism (Fig. 3.20). A volcanic centre was situated northwest of Rosh Pinah near Spitzkop Farm and at Trekpoort Farm.

Fan deltas, prograding into lacustrine environments in the vicinity of the topographic high near the listric, synsedimentary faults in the east of the study area east of Rosh Pinah, stretching in a northerly direction along the reactivated Rosh Pinah thrust fault, can occur over a great range of scales from a few tens of metres to hundreds of kilometres in radius (Collinson, 1986). This is indicated by the widespread fan delta/lacustrine sediments along strike within the study area, which can be traced from the Richtersveld to the area immediately southeast of Rosh Pinah.

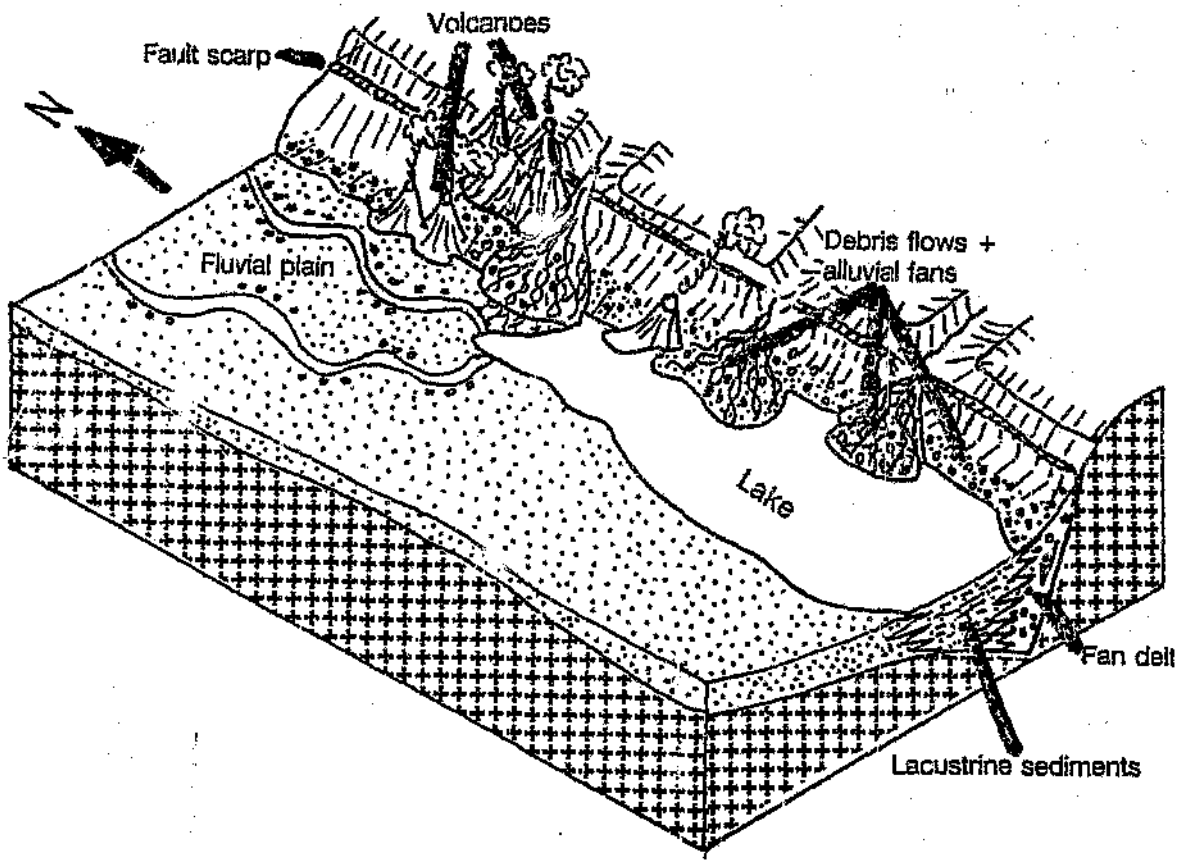


Fig. 3.20: *Schematic reconstruction of the palaegeographic setting present during the deposition of Rosh Pinah Formation rocks within the study area.*

The large thickness of the conglomerates of the fan delta deposits of the Rosh Pinah Formation to the west of the Rosh Pinah thrust fault and the paucity of these sediments to the east of it indicates synsedimentary faulting along the reactivated Rosh Pinah thrust fault, as discussed in section 6.3.2. These synsedimentary fault zones were also used for the implacement of the bimodal volcanics and mineralized brines, which are associated with the Rosh Pinah Formation.

Widening of the lacustrine system as a result of tectonic subsidence caused the finer-grained facies belts to transgress over the coarser-grained ones. Eventually,

subsidence caused marine transgression from the Adamastor Ocean, as recorded by the presence of the Gumchavib Formation (section 3.3), and the first extensive siliciclastic and platform carbonate sediments of the overlying Pickelhaube Formation (section 3.3).

Comparisons with other Damara rift sequences in the inland branch and the northern coastal branch are dealt with in section 6.1.

3.3 THE GUMCHAVIB FORMATION: OPENING OF THE ADAMASTOR OCEAN

The Gumchavib Formation forms the upper part of the Stinkfontein Subgroup north of the Orange River. It comprises several facies associations, representing a transition between the Rosh Pinah Formation and the mainly carbonate Pickelhaube Formation.

3.3.1 Sandstone/mudstone/carbonate facies association: mixed continental and marine carbonate depositional system

The following facies were recognized within this facies association (Figs. 3.21 & 3.22): (1) massive sandstone (Sms); (2) normally graded sandstone (Sng); (3) massive mudstone (Mm); (4) massive carbonate (Lmd); and (5) parallel laminated carbonate (Lfl).

(a) Description of lithologies

The medium to coarse and pebbly sandstones (Sms, Sng) are dark grey to green-grey. They consist of grains of quartz, feldspar, and minor biotite and muscovite. The pebbles of the pebbly sandstones consist of white quartzite.

The mudstones (Mm) are green-grey consisting of quartz, biotite, muscovite and chlorite, and appear only in the lowermost pebbly sandstones, which overly the granitic basement unconformably. The sandstones (Sms, Sng) are similar to those of the Rosh Pinah Formation described in section 3.2.2.

Towards the top of the sequence (Fig. 3.22) the sandstones (Sms, Sng) become more calcareous in composition and consist of grains of quartz, feldspar, carbonate and

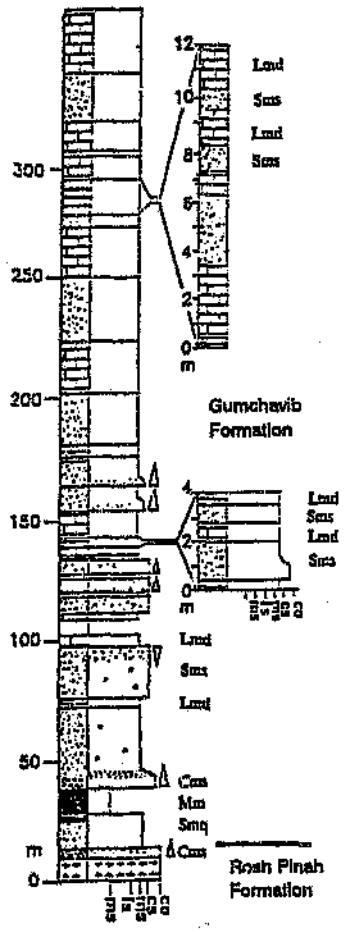


Fig. 3.21: *Measured section through parts of the Gumchavib Formation overlying granitic basement at locality 29, approximately 5 km northwest of Gumchavib Mountain (Fig. 2.4).*

minor muscovite and biotite.

The carbonates (Lmd, Lfl) are light grey to blue-grey and consist of recrystallized cherty dolomitic limestone.

(b) Description of sedimentary facies

Within the sandstones at the base of this sequence (Sms, Sng; Fig. 3.21), some lenses of massive mudstone occur but do not exceed 50 cm in thickness.

Bed thicknesses of the overlying sandstones (Sms, Sng) vary from 1 m to 35 m.

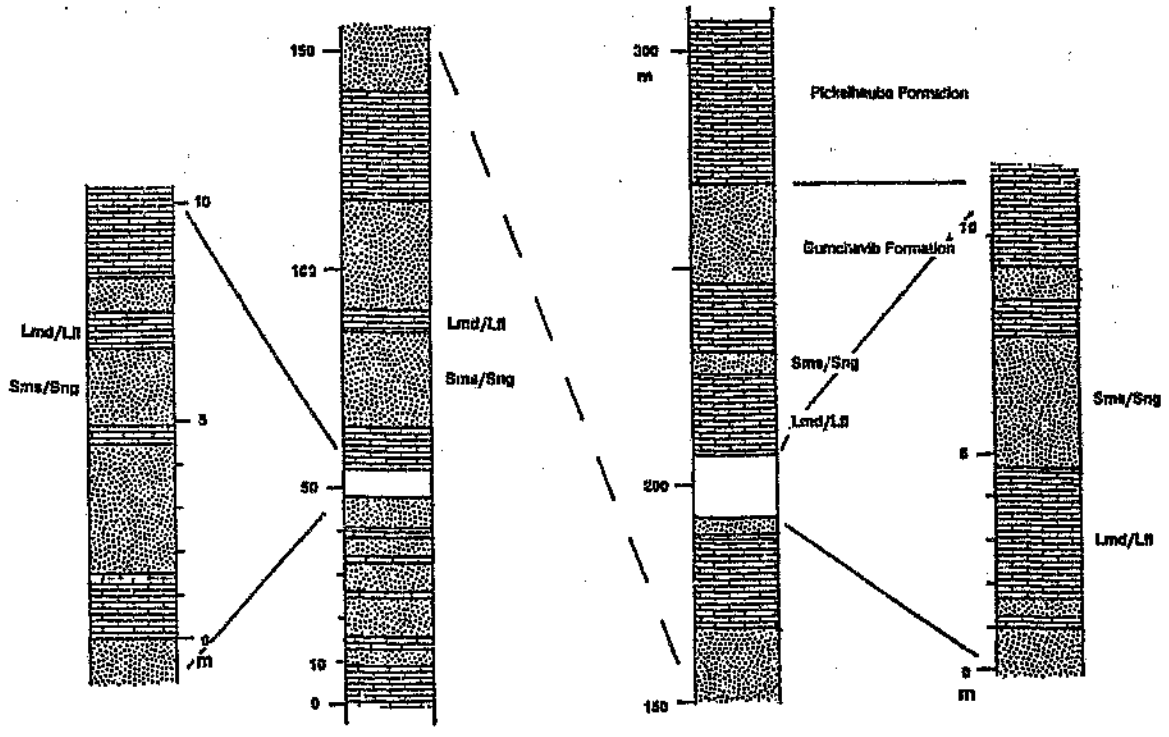


Fig. 3.22: *Measured section through parts of Gumchavib Formation at locality 17, approximately 5 km WNW of Gumchavib Mountain (Fig. 2.4).*

The sandstones grade from pebbly sandstone to coarse or medium sandstone (Fig. 3.21), often grading from up to 5 m thick massive pebbly sandstone to coarse or medium sandstone with sharp contacts with the next overlying graded sandstone bed. Some massive sandstones (Sms) do not display any grading at all and can vary in thickness from 1 m to 25 m (Fig. 3.21). Sorting of both the pebbly and the medium to coarse grained sandstones is poor. The diameter of the pebbles generally does not exceed 1 cm, however, pebbles measuring 5 cm diameter can occur at the base of some beds.

The massive carbonates (Lmd) do not display any sedimentary structures. The contacts between the carbonates with the under- and overlying sandstones are sharp. Towards the top of the sequence (Fig. 3.22), fine parallel-laminated carbonate beds (Lfl) occur occasionally within the massive carbonates (Lmd; Fig. 3.22).

The calcareous sandstones (Sng, Sms) are medium to coarse grained and are generally normally graded from coarse to medium sandstone. They are interbedded with carbonates (Lmd, Lfl) and medium grained structureless sandstones (Sms). Contacts between the different sandstone beds and between sandstones and carbonates are sharp.

(c) Interpretation

The mineralogy of the massive and normally graded feldspathic sandstones and pebbly sandstones (Sms, Sng) and mudstones (Mm) in the lower part of the sequence (Fig. 3.21) and sedimentological structures, indicate a deposition within a fluvially dominated environment, similar to that of the Rosh Pinah Formation. The graded sandstones and graded pebbly sandstones grade into medium sandstones (Sng). The mudstones (Mm) reveal sharp contacts to the overlying pebbly sandstones (Sms, Sng). The sandstones (Sms, Sng) and Mudstones (Mm) may have been deposited in a braided fluvial system, representing both channel and overbank deposits, with the pebbly sandstones being deposited in the most proximal environment of deposition, reflecting the growth of longitudinal bars. Each upward fining sequence within the massive, pebbly sandstones could reflect a single flood cycle. The calcareous composition of the sandstones in the upper Gumchavib Formation (Fig. 3.22), as well as the general lack of sedimentary structures (Sms) within some sandstones, and the presence of normal grading (Sng), might represent braided fluvial reworking of some of the interleaved limestones within stream-dominated fans (Collinson, 1986), which prograde as fan deltas into a shallow marine environment.

The carbonates (Lmd) within this facies association probably represent recrystallized

algal mats, generated during transgressional sea level changes, possibly eustatic in nature, and drowned by clastic input during regressional periods. The laminated carbonates (Lfl) represent storm generated carbonate, deposited near the zone of maximum carbonate production.

The sediments within this facies association represent an interleaving of the underlying Rosh Pinah Formation and the overlying Pickelhaube Formation during the transgression of the Adamastor Ocean and the concomittant retreat of the shoreline.

3.3.2 Quartz arenite/mudstone facies association: foreshore and shoreface depositional system

Five facies are developed within this facies association (Fig. 3.23): (1) massive quartz arenite (Smq); (2) wave-ripple cross laminated quartz arenite (Swq); (3) planar cross-bedded quartz arenite (Spq); (4) plane laminated quartz arenite (Splq); and (5) massive mudstone (Mm).

(a) Description of lithologies

The quartz arenites (Smq, Swq, Spq, Splq) are white to very light brown and consist predominatly of medium, subangular to subrounded quartz grains, with a minor amount of muscovite. The laminated sandstones contain black heavy mineral concentrations, defining the laminations.

The mudstones (Mm) are green-grey and consist of quartz, muscovite, biotite, and chlorite.

(b) Description of sedimentary facies

The quartzitic sandstones are well sorted and, except for the structureless massive quartz arenite (Smq), display a variety of sedimentary features. Bed thicknesses of the quartz arenites vary from 10 cm to approximately 5 m (Fig. 3.23).

The planar cross-laminated sandstones (Spq) vary in thickness from several centimetres to 40 cm. The angle of the laminae is fairly shallow and does often not exceed 20 degrees (Fig. 3.24). These sandstones (Spq) often display intricately interwoven cross-laminations, chevron structures and concave-upward laminae, which are suggestive of wave ripple lamination, as defined by De Raaf et al. (1977), which give them the appearance of trough-cross laminated sandstones. These "troughs" vary in dimension from 1 X 0,2 cm to 20 X 5 cm (Fig. 3.24).

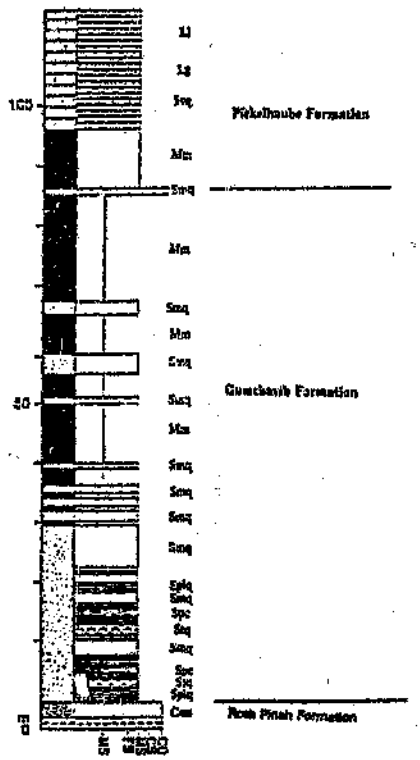


Fig. 3.23: *Measured section through parts of the Gumchavib Formation at Oblb waterhole (Fig. 2.4).*

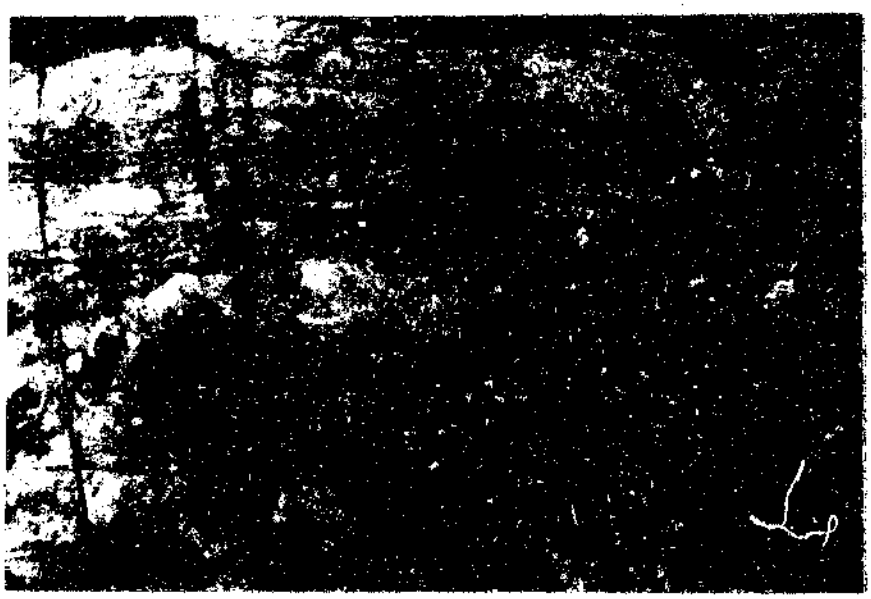


Fig. 3.24: *Wave-ripple cross laminated and low angle plane laminated quartz arenitic sandstones at Obib waterhole (Fig. 2.4).*

The plane-laminated sandstones (Splq), which are interbedded with the other quartz arenitic sandstones (Sms, Swq, Spq), display parallel laminae with distances between the laminae varying from 1 mm to 10 cm. Laminae can be undulating and are, in places, topped by errosive sets. The parallel laminae can also grade into cross-laminae.

The massive mudstones (Mm) do not display any sedimentary structures. They overlie a transgressive basal conglomerate of the Rosh Pinah Formation and are interbedded with massive quartz arenite (Smq) further up this sequence (Fig. 3.23). Towards the top of the sequence the massive mudstones (Mm) become more abundant, with occasional interbedded massive quartz arenites (Smq) (Fig. 3.23).

(c) Interpretation

Few environments are favourable for the formation, deposition and preservation of quartz arenites. These conditions are present in marine environments, in particular shorelines and shelf settings (De Raaf et al., 1977; Elliot, 1986; Johnson and Baldwin, 1986).

The sedimentary structures within the quartzitic sandstones reflect a wide range of energy conditions. Tidal effects could not be determined. The variety of sedimentary structures within the quartzitic sandstones (Splq, Spq; Swq) indicate that they were formed under conditions of considerable wave activity, generated in temporary rough weather, storm and post-storm conditions (De Raaf et al., 1977; Reineck and Singh, 1975; Kumar and Sanders, 1976). A depositional system within the foreshore consisting largely of storm deposits is suggested for these facies, whereas products of longer-lasting fair-weather conditions are found to compose only a minor proportion. The parallel-laminated and interbedded massive sandstones (Splq, Smq) were deposited as suspension fall-out within the shoreface after whirling-up by waves in the foreshore zone, indicating an environment of deposition well beyond wave base, where the mudstone (Mm) was deposited, whilst only incidental catastrophic conditions such as storms could bring in sands (De Raaf et al., 1977). This assumption is also strengthened by the absence of any sedimentary structures related to turbidites. The absence of erosional structures in the mudstone-rich low energy parts of this facies association indicates, that winnowing of the sandstones from the mudstones was inactive (De Raaf et al., 1977).

Similar depositional conditions have been documented from the modern day Gulf of Gaeta, Italy, by Reineck & Singh (1975), from the Late Ordovician Oslo Basin by

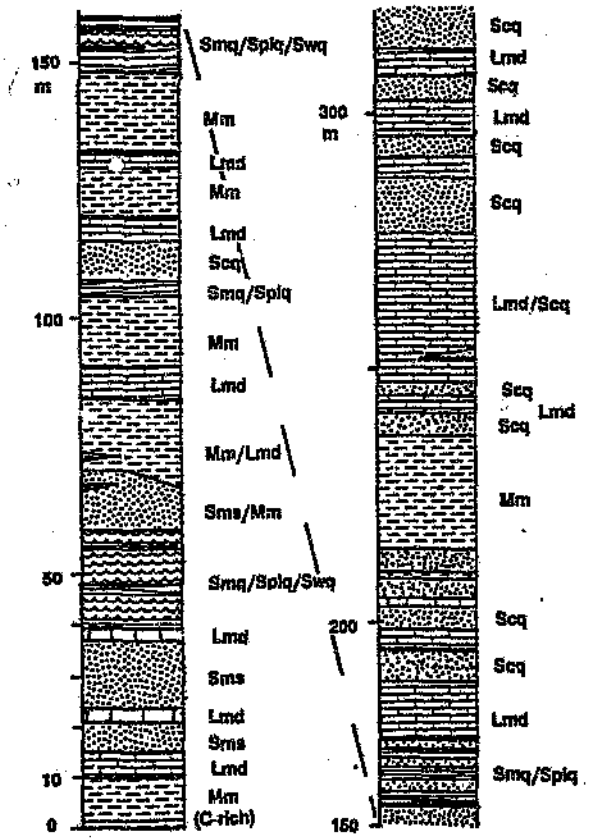


Fig. 3.25: *Measured section through parts of the Gumchavib Formation at locality 28, approximately 1 km northeast of Obib Peak (fig. 2.4).*

Stanistreet (1989), and from the Lower Carboniferous, County Cork, Ireland (De Raaf et al., 1977).

3.3.3 Interleaving of previously defined facies associations

The two facies associations, which are developed in the Gumchavib Formation, interleave at several localities, as shown in Figs. 3.25 and 3.26. They were deposited in a mixed continental/shallow marine depositional system recording a marine transgression.

3.3.4 Regional distribution

Gumchavib Formation lithologies are ony present in the west of the study area (Fig. 3.26). The mixed terrestrial/marine facies association (section 3.3.1) occurs in the southern parts of the Ostrich thrust slice (Fig. 2.3). The interleaved facies associations, as described in section 3.3.3, are developed in the northern parts of the Ostrich thrust slice northeast of Obib Peak. The foreshore/shoreface facies association (section 3.2.2) is present within the Obib thrust slice north of Obib Peak and around Obib waterhole (Fig. 3.26).

3.3.5 Vertical sedimentary facies association variations

The most prominent variations of depositional environments within the study area are rather stratigraphic in nature.

Within the mixed terrestrial/marine facies associations marine sediments, deposited in a foreshore/shoreface and/or a shallow carbonate platform depositional system, become more abundant towards the top of the Gumchavib Formation (Figs. 3.21, 3.22, 3.25), grading into the carbonate dominated Pickelhaube Formation.

Within the foreshore/shoreface facies association, a vertical change from foreshore to shoreface sedimentation is apparent (Fig. 3.23).

The vertical sedimentary facies association variations within the Gumchavib Formation document a transgressive transition from the terrestrially dominated Rosh Pinah Formation to the entirely marine Pickelhaube Formation.

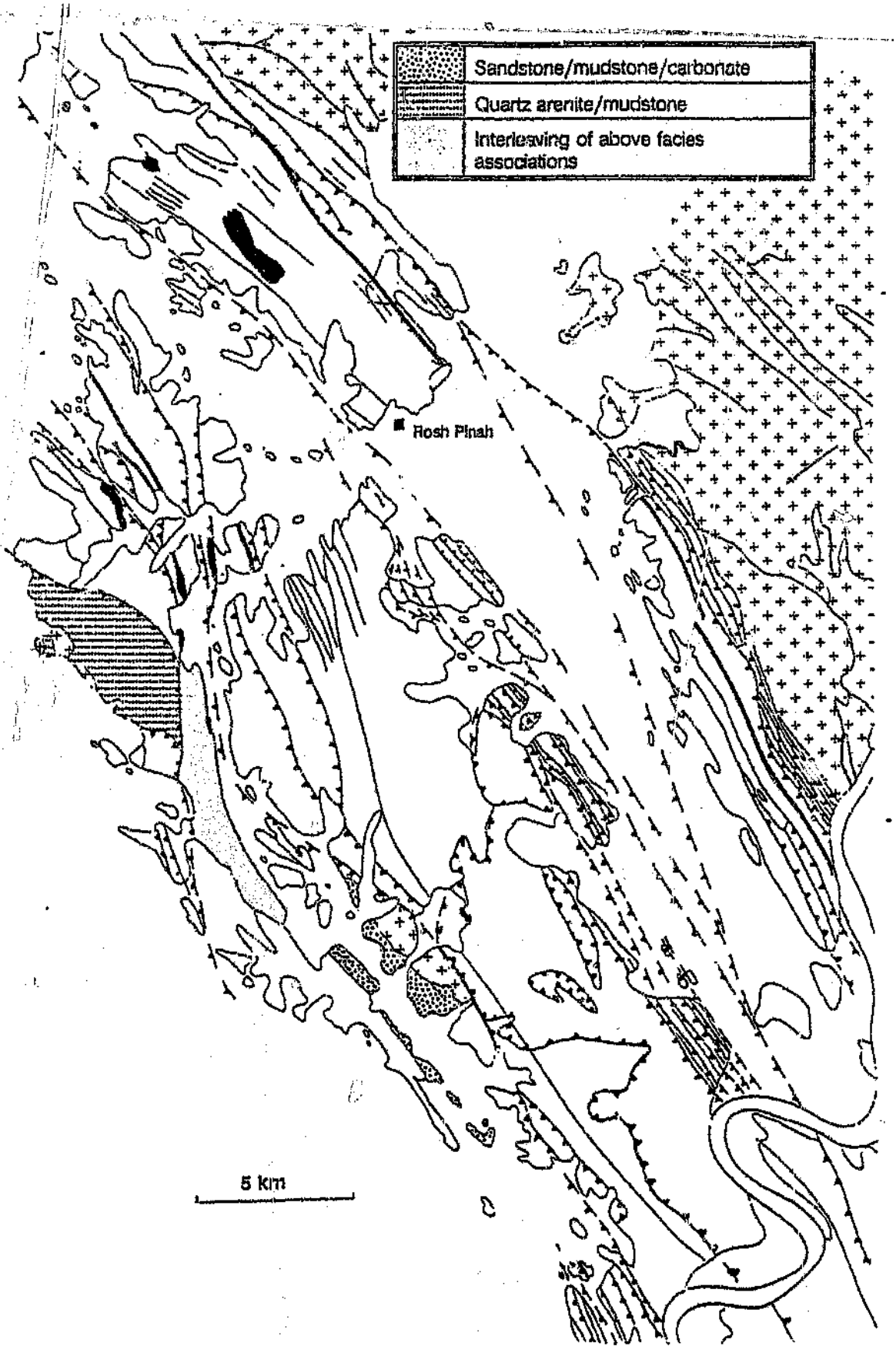


Fig. 3.26: *Regional distribution of the several facies associations developed within the Gumochavib Formation; for position of thrust slices and localities see Figs. 2.3 & 2.4.*

3.3.6 Lateral sedimentary facies association and stratigraphic variations

The only prominent lateral sedimentary facies association variation within the study area is recorded along strike within the Ostrich thrust slice. At locality 28 (Fig. 2.4) in the northern parts of the Ostrich thrust slice, continental sediments are interbedded with beach sediments and platform carbonates, whereas further south within this thrust slice and along strike the continental sediments interleave exclusively with carbonates.

3.3.7 Palaeogeographic reconstruction

The lateral distribution of carbonates and beach deposits along the north- to northwest-trending strike indicates a shoreline, which was dominated by stromatolitic reef growth within a carbonate platform in the southern parts of the Ostrich thrust slice and foreshore to shoreface deposits in the northern parts around Obib waterhole (Fig. 2.4). Fluvial/alluvial fan sediments, prograding into the sea, drowned the marine stromatolitic reefs in the south of the Ostrich thrust slice and are interbedded with beach deposits and associated platform carbonates in the north of it. The area around Obib waterhole, situated within the Obib thrust slice, was dominated entirely by a transgressive foreshore to shoreface depositional system, overlying a transgressive basal conglomerate.

The relative abundance of carbonates towards the top of the Gumchavib Formation indicates the overall evolution of an entirely marine basin and the formation of a carbonate platform and associated clastic carbonate and siliciclastic sedimentation. Palaeocurrent measurements, though scanty, indicate a source area of continental sediments in the east. The assumption of a north-south trending extension of the

shoreline is only indicated by the distribution of the various facies associations along strike and perpendicular to it.

Widening of the continental rift system, into which the Rosh Pinah Formation sediments and volcanics were deposited as a result of tectonic subsidence, caused the shallow marine sediments and carbonates to transgress over a continentally-dominated environment. Thermal cooling of the African continental margin, related to the opening of the Adamastor Ocean (Stanistreet et al., 1991) or proto-South Atlantic Ocean (Porada, 1985), led to further transgression of the sea over continental environments. The tectonic subsidence is recorded by the initial transgression and the deposition of the first shallow marine sediments, whereas the initiation of thermal subsidence is documented by the abundance of marine sediments towards the top of the Gumchavib Formation and the overlying Pickelhaube Formation.

3.4 THE PICKELHAUBE FORMATION: CARBONATE PLATFORM AND CARBONATE SHELF DEPOSITIONAL SYSTEM

The sediments of the Pickelhaube Formation form the lowermost part of the Hilda Subgroup. They consist mainly of carbonates and to a lesser extent of carbonate-dominated clastics and calcsilicidlastics. The Pickelhaube Formation reflects the first appearance of exclusively marine sedimentation within the Gariep Group. Within the study area, no "fundamental break" in the Port Nolloth Zone stratigraphy, as postulated by Von Veh (1988), is recorded by the rocks of the Pickelhaube Formation. This is documented by various cycles involving mixed continental/marine sedimentation during the deposition of the Gumchavib Formation, which gave way gradually to pure marine sedimentation during the deposition of the Pickelhaube Formation.

3.4.1 Carbonate/carbonaceous carbonate facies association: carbonate shelf depositional system

This facies association of the Pickelhaube Formation is the most widespread to be exposed within the study area. It comprises the following facies: (1) plane laminated carbonate (Lpl); (2) massive carbonate (Lmd); (3) graded carbonates (Lg); (4) small scale channel-fill carbonate (Lc); carbonaceous carbonate (Lgi).

(a) Description of lithologies

Facies Lpl, Lmd, Lg, and Lc consist of a fine grained blue-grey dolomitic limestone, consisting of calcite and dolomite with variable minor amounts (< 5%) of carbon, muscovite, biotite, quartz, and plagioclase. The carbonaceous carbonate (Lgi) is dark

grey to black, containining variable amounts of carbon (10 to 70%) and haematitic iron oxide (< 5%). The carbonates consist of medium to fine grained (< 1 mm) recrystallized dolomitic limestone.

(b) Description of sedimentary facies

The massive carbonates (Lmd) do not display any sedimentary structures, which may be due to their relatively high recrystallization.

The plane laminated carbonates (Lpl; Fig. 3.27) and the massive carbonates (Lmd) form the bulk of the Pickelhaube Formation. This formation consists mainly of laterally continuous carbonate units, often associated with 2 to 10 cm thick graded calcareous beds (Lg), and in some rare cases small scale channels (~30 cm width, 3 cm height), containing clastic sandy carbonate (Lc; Fig. 3.28). Slump structures occur occasionally within the laminated carbonates (Fig. 3.27).



Fig. 3.27: *Laminated carbonate of the Pickelhaube Formation about 5 km southwest of Pickelhaube Peak; note the slump structure in the upper right part of the photograph (Fig. 2.4; photo is rotated 90 degrees in an anticlockwise direction).*

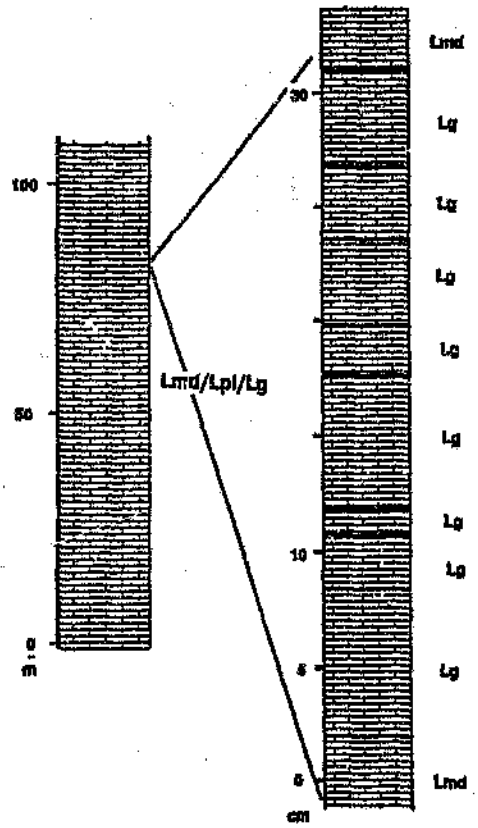


Fig. 3.28: *Measured section through part of the Pickelhaube Formation, showing graded beds of carbonate (Lg) at a locality about 7 km northwest of Pickelhaube Peak (Fig. 2.4).*

Carbonaceous carbonate (Lgi) beds, interbedded with facies Lpl and Lg, are between 1 cm and 5 m thick (Fig. 3.29).

(c) Interpretation

The main difference between carbonate rocks and siliciclastics is, that the former are deposited at or near their site of formation (James, 1984). A variety of chemical and biochemical processes is responsible for the formation of carbonates, and thick sequences can be deposited under favourable conditions. These conditions are fundamentally warm, clear waters with little terrigenous siliciclastic input (Irwin, 1965; Bathurst, 1975; Wilson, 1975; James, 1984; Beukes, 1986; Sarg, 1988; Grotzinger,

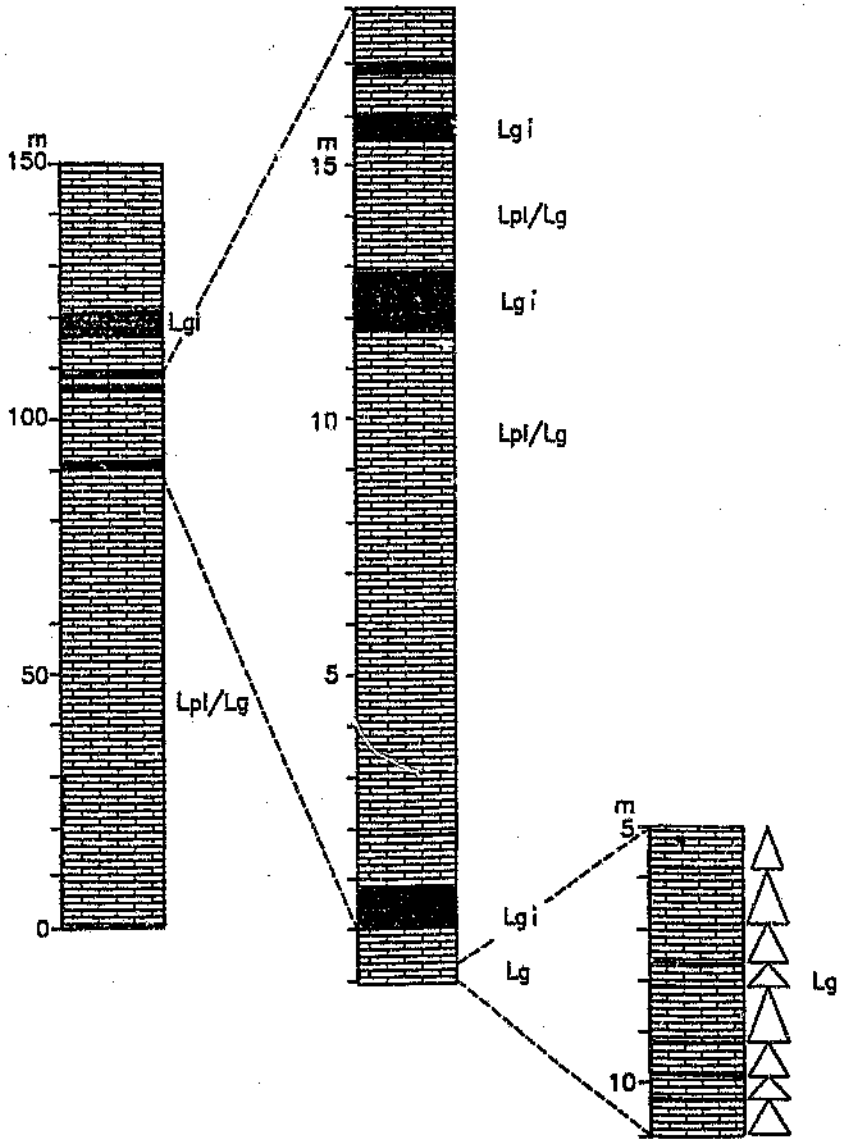


Fig. 3.29: *Measured section through parts of the Pickelhaube Formation at locality 3, about 2,5 km NNW of Obib waterhole (Fig. 2.4).*

1990). Although volumetrically unimportant, carbonates can also form in temperate or even arctic conditions (Rao, 1981a; 1981b; Rao and Green, 1982; Fairchild and Hambrey, 1984; Fairchild et al., 1989).

The laminated and graded carbonates (Lpl, Lg), containing small-scale channels (Lc), were generated in a carbonate shelf environment, landwards or seawards away from the "carbonate factory" by various types of currents, including storm-induced currents and turbidity currents (James, 1984). Slump structures within the laminated carbonates

indicate that these were also deposited within a slope setting. A relatively deep carbonate shelf environment for the deposition of some carbonates (Lgi) is indicated by the carbonaceous composition and relative iron-enrichment. The carbonaceous composition and relative iron-enrichment may, however, also be indicative of the presence of subaqueous volcanogenic brines within a shelf environment.

3.4.2 Carbonate/calcareous clastics facies association: shallow marine sea and prograding distal fan deltas

This facies association forms part of the lower Pickelhaube Formation and comprises the following facies: (1) massive carbonate (Lmd); (2) calcareous quartzitic sandstone (Scq); (3) normally graded calcareous sandstone (Sng); (4) inverse graded calcareous sandstone (Sig); massive mudstone (Mm); and (6) matrix supported conglomerate (Cms).

(a) Description of lithologies

The massive carbonates (Lmd) consist of a blue grey to grey dolomitic limestone, with variable amounts of quartz (10 to 15%) and plagioclase (< 15%). The calcareous sandstones (Scq, Sng, Sig) are light brown and consist of medium to coarse and pebbly quartz, with a variable amount of carbonate (10 to 50%) and plagioclase (< 10%). The pebbles at the base of the sandstone beds consist of white quartzite with diameters ranging from 0,2 to 1,5 cm. The mudstones (Mm) are green-grey and consist of quartz, carbonate, biotite, muscovite, and chlorite. The matrix supported

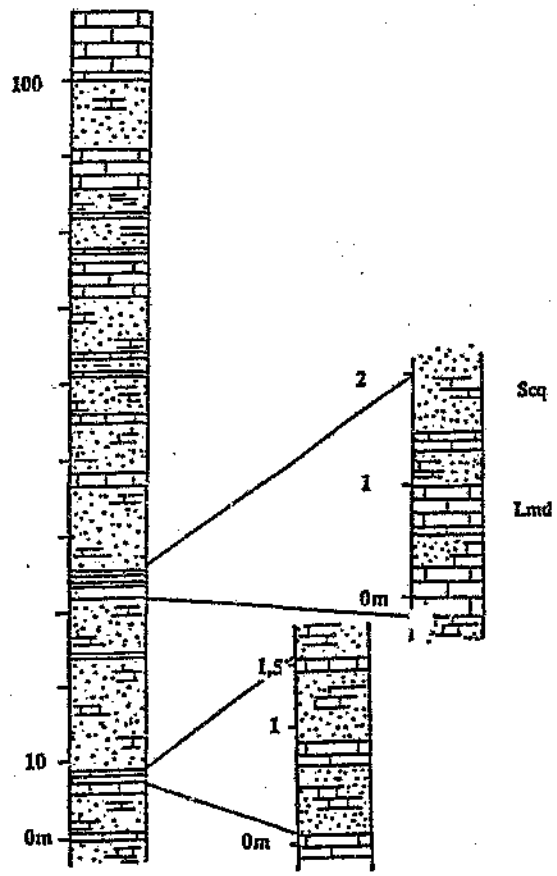


Fig. 3.30: *Measured section through parts of the lower Pickelhaube Formation at locality 4, about 5 km southwest of Rosh Pinah (Fig. 2.4).*

conglomerate (Cms) comprises clasts with diameters of up to 60 cm, consisting of reworked conglomerate, carbonate, quartzite, and mudstone, with a green-grey to grey, pelitic matrix consisting of quartz, carbonate, biotite, muscovite, chlorite and plagioclase.

(b) Description of sedimentary facies

The contacts between the carbonates (Lmd) and the calcsiliciclastics (Scq, Sng, Sig) are generally gradational, with bed thicknesses varying from less than 5 cm to 10 m and varying calcareous composition (Fig. 3.30). At locality 4 (Fig. 2.4), a channel measuring 20m in width and 5m in height has been documented which is erosive into

the underlying massive carbonate (Lmd) and containing calcareous quartzitic sandstone (Scq).

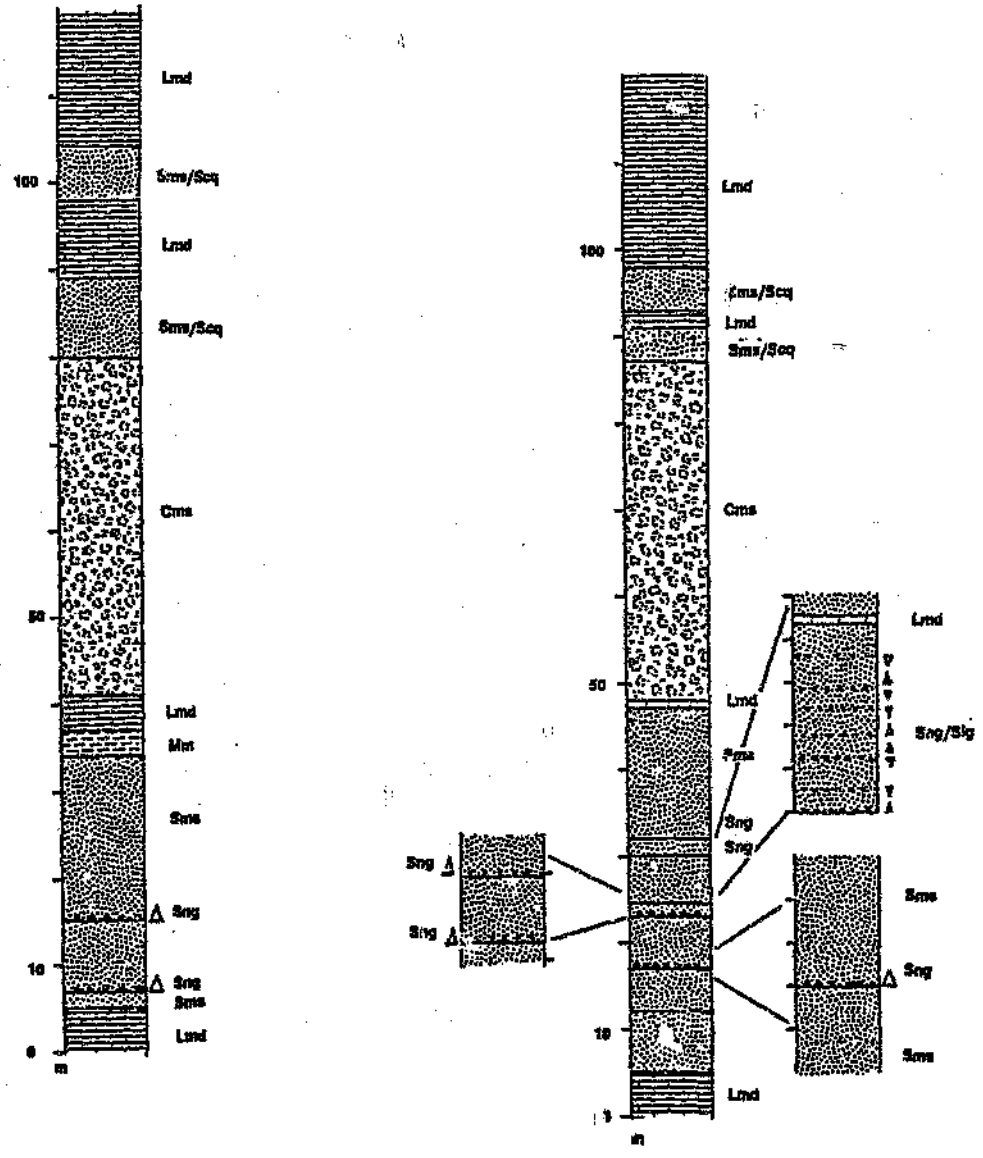


Fig. 3.31: *Measured section through parts of the Pickelhaube Formation at locality 17, about 5 km northwest of Gumchavib Mountain; sections are taken along strike approximately 100 m apart (Fig. 2.4).*

The well sorted calcareous sandstones display several sedimentary features, ranging from structureless coarse to medium, massive sandstone (Scq) to normally and inverse graded pebbly to medium sandstone (Sng, Sig). Bed thicknesses of the well sorted massive sandstones (Scq) range between 2 cm to 1 m. At locality 17, northwest of Gumchavib Mountain (Fig. 2.4), the normally graded sandstones (Sng) generally display sharp contacts to the underlying lithologies, gradational contacts are, however, also common (Fig. 3.31). Bed thicknesses of the normally and inverse graded sandstones (Sng, Sig) vary between 20 cm to 3 m, grading into massive sandstone (Scq; Fig. 3.31). A 3 m thick massive mudstone (Mm) is present within the vertical measured section at locality 17, underlying the carbonate (Lmd) with a sharp contact (Fig. 3.31).

The conglomerate (Cms) is poorly sorted and matrix-supported, displaying sharp contacts with the under- and overlying lithologies. Clasts are subangular and of a polymodal composition. The conglomerate bed (Cms) can be traced for approximately 300 m along strike.

The carbonate (Lmd) and sandstone beds (Sms, Scq, Sng, Sig) pinch out laterally.

(c) Interpretation

The presence of massive carbonates (Lmd) and calcsiliciclastics (Scq), as well as the highly calcareous composition of the sandstones, together with the presence of gradational contacts between these lithologies, implies a deposition within the zone of siliciclastic influx near the zone of optimum carbonate production, indicating a shallow marine shelf setting. Channels containing siliciclastic material (Scq) and conglomerates with intrabasinal clasts (Cms) and sharp erosional contacts indicate periodic influxes

of these sediments, probably related to sealevel changes and possibly eustatic in nature. These channels normally develop at a time of eustatic sea-level fall, when channels can be eroded into the shelf, which allows a mixed siliciclastic and locally eroded fill (Collinson,1986). The normally and inverse graded sandstones (Sng, Sig) and some massive sandstones (Sms) were deposited as distal fan de[illegible]s, prograding into a shallow marine environment (Collinson, 1986).

3.4.3 Carbonate/coarse to fine clastics facies association: mixed carbonate platform/slope apron and deep basin depositional system

This facies association, which is best developed at Dreigratberg in the east of the study area Fig. 2.4), comprises the following facies: (1) interbedded/interlaminated graded sandstone/marlstone (Sng/Ma); (2) massive mudstone (Mm); (3) carbonaceous mudstone (Mg); (4) normally graded sandsto[illegible](Sng); (5) interlaminated carbonate/marlstone (Lmd/Ma); (6) massive carbonate (Lmd); (7) stromatolitic carbonate (Ls); (8) laminated carbonate (Ll); (9) pisolitic carbonate; (10) carbonaceous carbonate (Lgi); (11) matrix-supported conglomerate (Cms); (12) carbonate conglomer[illegible]/carbonate breccia (Cms/Lbr); and (13) gossan (GoSu). A measured section through this facies association at Dreigratberg, where it is best developed, is shown in Figs. 3.32 and 3.33.

(a) Description of lithologies

The sandstone (Sng) of the interbedded and interlaminated graded

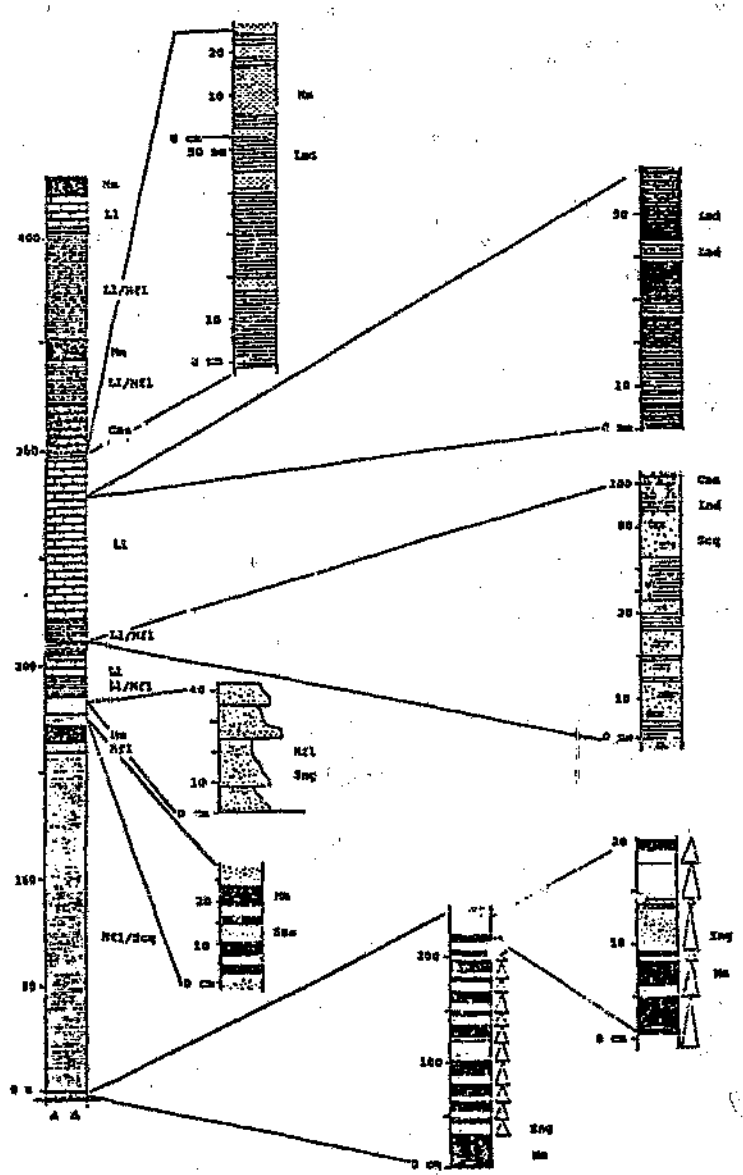


Fig. 3.32: *Measured section through parts of the Pickelhaube Formation at Dreigratberg (Fig. 2.4).*

sandstone/marlstone (Sng/Ma; Fig. 3.34) is a fine grained dark grey, brown weathering calcareous quartz arenite with minor amounts of feldspar, carbonate, and mica (< 5%). It is interbedded and interlaminated with a grey-green calcareous quartz-muscovite-biotite-chlorite schist (Ma).

The carbonaceous mudstone (Mg) is black with an enrichment of hematitic iron oxide, visible in handspecimen by its brown weathering. The carbonaceous mudstone (Mg) is associated with gossan (GoSu), consisting of brown weathering porous-spongy hematite and associated with a yellow sulphur efflorescence.

The interlaminated carbonate/marlstone (Lmd/Ma) consists of a strongly recrystallized pink dolomitic limestone and a grey-green calcareous quartz-muscovite-biotite-chlorite schist (marlstone), overlain by a massive grey dolomitic carbonate (Lmd), grading into a laminated dolomitic carbonate (Ll), which consists of light grey and grey laminae (Fig. 3.32). The grey laminae are caused by the relative enrichment of biotite.

The breccia (Lbr) within the matrix-supported carbonate conglomerate/carbonate breccia facies (Cms/Lbr) at Dreigratberg consists of a calcareous grey matrix with up to 40 cm wide tabular carbonate clasts (Fig. 3.35). Along strike (ca. 500 m north), the thickness increases from 1 m to about 8 m and the clasts change their shape from tabular to subangular to angular round clasts (Lbr). The conglomerates within facies Cms/Lbr can be up to about 20 m thick (Fig. 3.32), consisting of a grey calcareous matrix and clasts and boulders with average diameters of 10 to 30 cm and maximum boulder diameters of 4 m. Clasts consist of dolomitic carbonate and coarse to pebbly quartzitic sandstone, whereas the large boulders consist solely of coarse quartzitic sandstone. At locality 13A the clasts consist of grey dolomitic carbonate (Fig. 3.36) and, although scanty, of pisolitic carbonate (Lpi), resembling the pisolitic carbonate at

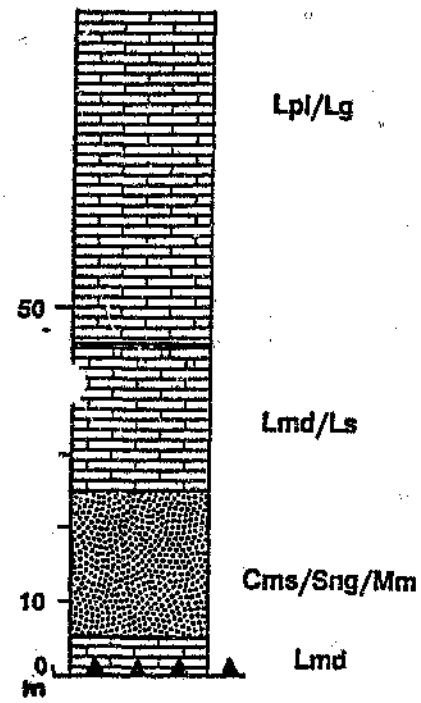


Fig. 3.33: *Measured section through parts of the Pickelhaube Formation at a locality about 5 km north of Dreigratberg (Fig. 2.4).*



Fig. 3.34: *Thickly to thinly laminated sandstone and mudstone (Sng/Mm) of the Pickelhaube Formation at Dreigratberg (Fig. 2.4); every single lamination consists of a normal graded bed.*

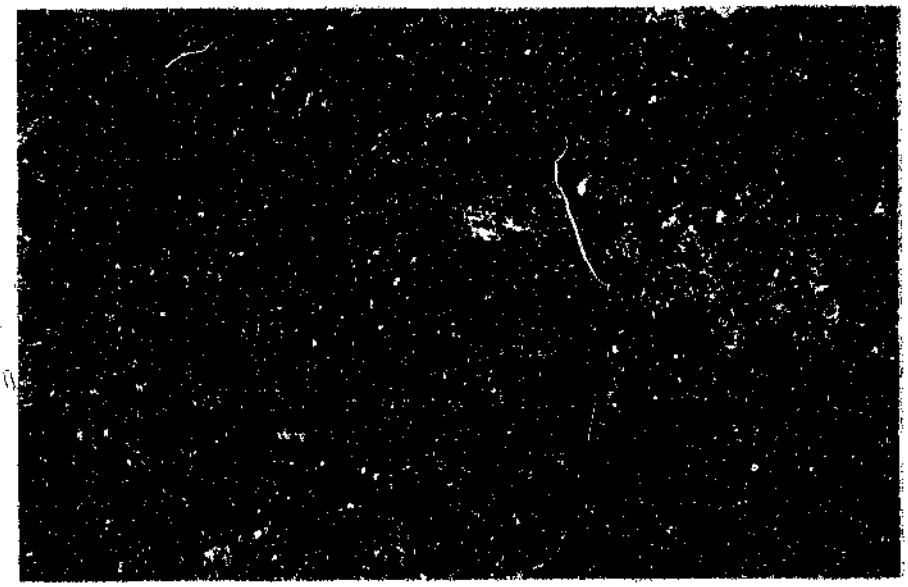


Fig. 3.35: *Tabular carbonate clasts within a calcareous matrix within the mixed carbonate conglomerate/carbonate breccia (Cms/Lbr) of the Pickelhaube Formation at Dreigratberg.*

locality 13B.

At Dreigratberg and approximately 5 km north of it (Fig. 2.4), within the same stratigraphic horizon as the conglomerate-carbonate breccia, a 20 m thick light grey massive dolomitic carbonate bed displaying in places stromatolitic laminae (Ls) is exposed. Immediately west of Oblb Peak, a dark grey carbonaceous carbonate (Lgl) is interbedded with a stromatolitic carbonate (Ls) displaying stromatolitic laminae (Fig. 3.37).

The pisolitic carbonate (Lpi) consists of a blue-grey dolomitic matrix with light grey pisolith spheroids (Fig. 3.38). Angular rock fragments, consisting of brown weathering dolmitic limestone, are present within the pisolite beds. The contact between the sandstones, which can grade into mudstone, with the overlying coarser beds or laminae are sharp (Fig. 3.34).

(b) Description of sedimentary facies

The interbedded and interlaminated sandstone/marlstone (Sng/Ma) is thinly bedded, grading into thickly to thinly laminated sandstone and marlstone towards the top.

The massive mudstones (Mm) and the carbonaceous mudstones (Mg) do not display any sedimentary structures. At Dreigratberg the carbonaceous mudstone (Lg) is closely associated with a several metres thick gossan (GoSu; Fig. 3.32).

The interlaminated carbonates and marlstones (Lmd/Ma) are thinly laminated.

The normally graded sandstones (Sng), overlying carbonaceous mudstone (Mg), are medium bedded and fine to coarse grained, with sharp contacts to the overlying graded beds.

The massive carbonates (Lmd) within this facies association display no sedimentary structures, however, approximately 5 km north of Dreigratberg and at Dreigratberg

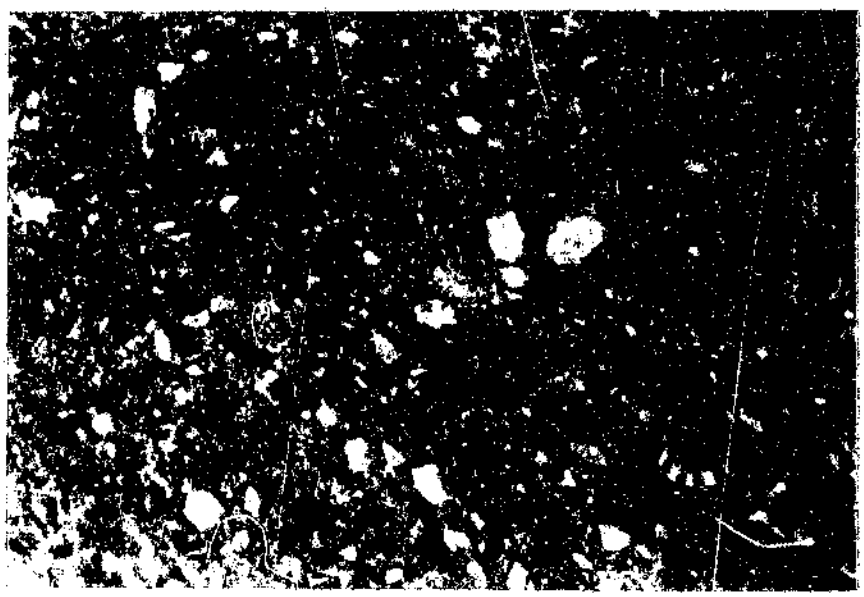


Fig. 3.36: *Massive carbonate conglomerate with carbonate clasts in a carbonate matrix of the Pickelhaube Formation at locality 13 A, about 5 km south-east of Namuskluft Farmhouse (Fig. 2.4).*



Fig. 3.37: *Stromatolitic carbonate of the Pickelhaube Formation at a locality about 1km west of Obib Peak (Fig. 2.4).*

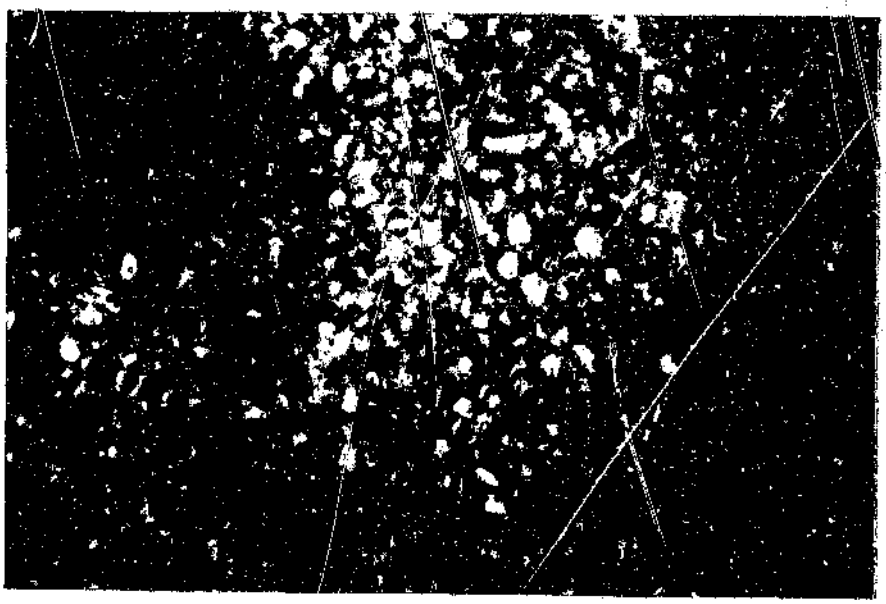


Fig. 3.38: *Pisoliths and carbonate rock fragments within a carbonate matrix at locality 13 A, about 3 km north of Dreigratberg (Fig. 2.4).*

itself, some columnar-layered and cumulate stromatolitic laminae with domal diameters of about 40 cm are exposed. A similar stromatolitic carbonate (Ls) with domal diameters of about 5 cm is exposed west of Obib Peak (Fig. 3.37).

The laminated carbonates (Ll) are thinly laminated.

The carbonate conglomerates/carbonate breccias (Cms/Lbr) are poorly sorted and matrix-supported, with sharp contacts to the under- and overlying lithologies, pinching out laterally after tens or hundreds of metres. The clasts within the breccias are up to 40 cm in diameter and often tabular (Fig. 3.35). At locality 13A, approximately 3 km southeast of Namuskluft Farmhouse, a 30 m thick succession of matrix supported monomictic, poorly sorted carbonate conglomerate (Cms) with subangular dolomitic carbonate clasts measuring up to 40 cm in diameter and averaging about 5 cm, hosted by a dolomitic calcareous matrix (Fig. 3.36), is interbedded with sharp contacts with massive carbonate (Lmd), which displays no sedimentary structures.

The total thickness of the pisolitic limestone, which is best developed at locality 13B, varies between 30 and 50 m. Pisoliths vary in diameter from 1 mm to 2 cm and are well rounded and round to ellipsoidal in shape. Internally, the pisoliths have a concentric, symmetric and continuous pattern of fine laminae (Fig. 3.38). The diameter of the pisolith spheroids varies from 1 mm to 2 cm. The angular rock fragments within the pisolitic carbonate (Lp) have diameters of up to 20 cm.

(c) Interpretation

Stromatolites in carbonates are recorded throughout the geological record, but were particularly abundant in the Late Proterozoic and became less important in the

Phanerozoic (Awramik, 1984). Studies of stromatolites in modern environments show that they can form under a variety of conditions, ranging from tidal flats (e.g. Andros Island, Monty, 1967; 1972) and foreshore environments (e.g. Shark Bay, Logan, 1961) to subtidal environments (e.g. Shark Bay, Playford et al., 1976; and in the Bahamas (Gebelein, 1969; Dill et al., 1986). In the Precambrian, stromatolites developed in basinal to shallow subtidal to supratidal environments (Hoffmann, 1976), but achieved their greatest diversity in the formation of reefs or buildups (Tucker, 1990). Biostroms, laterally persistent over many kilometres, shelf-edge reefs cut through by channels, and bioherms surrounded by oolites have been described throughout the geological record (Tucker, 1990). Within the study area, a carbonate platform setting with shelf-edge reefs is suggested for the deposition of the stromatolitic carbonates (Ls). The massive carbonates (Lmd) may also represent recrystallized stromatolitic carbonate.

Pisoliths (Lpi) can be generated by various mechanisms. They can form by physicochemical precipitation in shallow (< 5m), wave-agitated turbulent water (Illing, 1954; Newell, Purdy and Imbrie, 1960; Rusnak, 1960; Loreau and Purser, 1973; Bathurst, 1971; Fabricius, 1977; Land, Behrens and Frishman, 1979) and are generally round to ellipsoidal in shape (Tucker, 1990). Pisoliths can, however, also be produced by biochemical algal-encrustation processes in relatively calm conditions, with spherical or less well-rounded shapes and diameters, which are normally about 5 mm or smaller. Biochemically formed pisoliths show an asymmetric growth pattern due to stationary growth (Tucker, 1990). The presence of rock fragments within the pisolitic carbonate of the Pickelhaube Formation, their well-rounded and unflattened shape, the relatively large diameters of up to 2 cm, and the concentric and continuous laminae

indicate that they were formed by physicochemical precipitation in a higher energy environment than the biochemically formed pisoliths. An environment, meeting the conditions for the development of inorganic pisoliths can be found within carbonate platform environments, similar to the present day Bahamas (Tucker, 1990), where wave action takes place.

The composition of the matrix of the massive conglomerates (Cms) and the carbonate conglomerates/carbonate breccias (Cms/Lbr), their poor sorting and the absence of any sedimentary structures, as well as the presence and the shape of the intrabasinal clasts, suggests that these facies were deposited as mass gravity flows. The carbonate breccias within facies Cms/Lbr are impressive examples of early sedimentation of carbonate sediments on submarine slopes, which led to the spectacular development of breccias through the secondary movement of the lithified or partially lithified material as mass gravity flows. Breccias made up of tabular clasts, as the ones at Dreigratberg (Fig. 3.35), are especially characteristic (Collinson and Thompson, 1992).

Mudstones, such as facies Mm and Mg, form by suspension settling of very fine sediment under quiescent or waning current conditions (Blatt et al., 1980; Jenkyns, 1986). In marine environments muds may be brought in by rivers and redistributed by marine processes such as sediment gravity flows, which originated from continental margins or platform edges and transport the sediment into the deep sea (Jenkyns, 1986), and are responsible for their deposition as nemi-pelagic to pelagic muds. Subaqueous volcanogenic vents, possibly along extensional fracture zones, are responsible for the enrichment in carbon and iron oxide within the carbonaceous mudstone (Mg) and the presence of gossan (GoSu) and associated sulphur

efflorescence.

The interbedded/interlaminated graded sandstones/marlstones (Sng/Ma), the graded sandstones (Sng), and the laminated carbonates (Ll) were deposited within turbidity currents, representing respectively the AE, the A, and the B or D divisions of classical Bouma sequences (Bouma, 1962). High to low concentration turbididty currents with rapid settling seem to be the predominant depositional processes within these facies, depending on the sandstone/mudstone ratios (Bouma, 1962; Walker, 1976; 1978; Stow and Bowen, 1980).

The carbonate conglomerate/carbonate breccia facies (Cms/Lbr) contains clasts, which were generated in shallow marine environments and were later redeposited. The phenomenon of shallow-water carbonates and other shallow marine sediments in deep-water settings is common throughout the geological record and often associated with platform margins and slope aprons. Examples of resedimented carbonates deposited on slope aprons adjacent to carbonate platforms occur within the Cambrian/Ordovician Whipple Cave Formation and Lower House Limestone of eastern Nevada (Cook and Taylor, 1977), the Cambrian/Ordovician Hales Limestone in central Nevada (Cook and Taylor, 1977), and the middle Cambrian of the southern Rocky Mountains (McIlreath, 1977). Facies models for platform carbonate resedimentation have been developed by Mullins and Neumann (1979) and Mullins (1983) from the modern Bahamas slopes. Eight facies models for the slopes of the Bahamas platform have been suggested, four of which are very relevant to ancient deep-water resedimentation. For an open sea environment the "escarpment model" and the "base-of-slope model" are significant. The escarpment model requires a steep (30 - 60 degrees), high relief escarpment which is mainly a site of resedimentation. Rockfalls,

slides, debris flows, modified grain flows and high density turbidity currents can be expected in this setting, with the sediments being supplied both from the shallow marine platform edge and the slope itself. A narrow talus facies belt passes oceanwards into hemipelagic muds and basinal turbidites (Tbcde divisions and thin graded beds of a classical Bouma sequence within turbidites; Bouma, 1962). This facies model should also be suitable for ancient platform margins, where a steep slope, perhaps fault-bounded, existed.

A palaeoenvironment, similar to the "escarpment model" described above, is suggested for the deposition of this facies association.

3.4.4 Regional distribution

The carbonates and calcsiliciclastics of the Pickelhaube Formation are abundant within the study area, being most conspicuous at Pickelhaube Peak (Fig. 2.4) within the Pickelhaube thrust slice, the type locality of this formation.

The carbonate/carbonaceous carbonate facies association (section 3.4.1) is best developed throughout the Pickelhaube thrust slice, and 3 km south and 7 km south-east of Obib Peak, as well as about 3 km north of Obib waterhole. (Fig. 3.39). It is also developed approximately 3 km south-west of locality 1, north of the Orange River (Fig. 2.4), where it is more recrystallized than in other areas.

The carbonate/calcareous clastics facies association (section 3.4.2) is best developed at locality 15, about 4 km northeast of Obib waterhole, as well as at locality 4, approximately 4 km southwest of Rosh Pinah (Fig. 2.4).

The carbonate/coarse to fine clastics facies association (section 3.4.3) is best developed within the Dreigratberg syncline at Dreigratberg, as well as within some

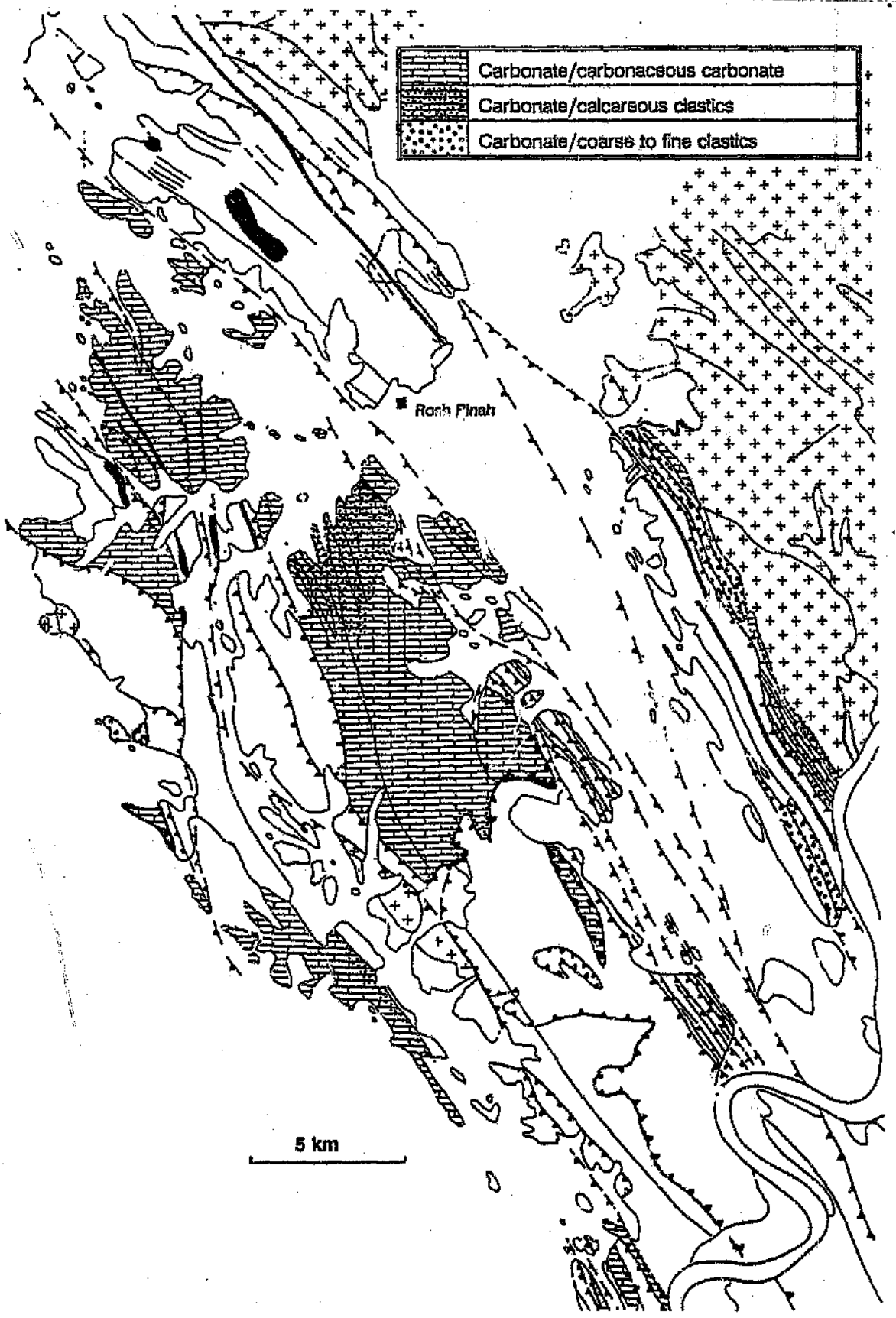


Fig. 3.39: *Regional distribution of the several facies associations recognized within the Pickelhaube Formation in the study area.; for position of thrust slices and localities see Figs. 2.3 & 2.4).*

thrust sheets within the imbricate zone (Rosh Pinah thrust fault) east and southeast of Namuskluft Farmhouse. Parts of this facies association are also developed immediately west of Obib Peak, where stromatolitic carbonate is present (Fig. 3.39).

The pisolitic facies of this facies association is only exposed within the imbricate zone (Rosh Pinah thrust fault; Fig 2.3) approximately 2 km northwest of the Orange River (Fig. 2.4). It is also present within the same imbricate zone, 2 km southeast of Namuskluft Farmhouse.

3.4.5 Vertical sedimentary facies association variations

Within the Pickelhaube Formation itself, a distinct vertical facies association variation from shallow marine interbedded calcsiliciclastics and carbonates at the bottom of the sequence to a calcareous shelf sedimentation towards the top is present, being best developed within the Pickelhaube thrust slice.

Interbedded shallow marine platform carbonates and hemi-pelagic to pelitic muds (section 3.4.3) are exposed towards the top of the Pickelhaube Formation, where carbonates of the Pickelhaube Formation are interbedded with terrestrial sediments of the overlying Obib Peak Formation at Obib Peak, resembling the sandstone/mudstone/carbonate facies association (section 3.3.1) of the Gumchavib Formation.

3.4.6 Lateral sedimentary facies association variations

No major lateral sedimentary facies association variations within the Pickelhaube Formation were recognized within each of the individual thrust slices. Prominent lateral facies association variations are only apparent between the various parautochthonous

thrust slices, indicating that platform carbonate and associated slope and basin sedimentation was active in the southern parts of the study area, whereas shallow marine clastic carbonate deposition with periodic influx of siliciclastics and associated shelf sedimentation dominated in the northern parts of the study area. A similar trend from a sedimentation, which was initially dominated by a carbonate platform in the southern parts of the study area and beach sedimentation in the northern parts of the study area is also recognizable within the underlying Gumchavib Formation.

Minor lateral facies variations were identified within the carbonate conglomerate/carbonate breccia facies (Cms/Lbr) of the carbonate/coarse to fine clastics facies association (section 3.4.3), which pinch out laterally and are substituted by massive (Lmd) and stromatolitic carbonate (Ls).

3.4.7 Palaeoenvironmental reconstruction: synthesis and summary

Overall palaeoenvironmental setting

The sediments of the Pickelhaube Formation were deposited in a variety of palaeoenvironments, ranging from shallow marine platform carbonates with periodic siliciclastic input, to platform edge and associated slope apron sediments and hemi-pelagic to pelagic carbonates and muds. The shelf was dominated by clastic carbonate deposition, generated by storm-induced currents and/or turbidity currents. Sealevel changes, possibly eustatic and/or of tectonic nature, due to reactivation of synsedimentary thrusts, along which iron-rich and sulphidic volcanogenic brines discharge, are recorded by the presence of various cycles within the carbonate/coarse to fine clastics facies association (section 3.4.3).

Palaeogeographic reconstruction

The vertical facies associations within the Pickelhaube Formation indicate that two major depositional systems operated in the area as part of a thermally cooled passive oceanic margin. A marine carbonate platform established itself gradually over the terrestrially-dominated sediments of the Rosh Pinah Formation during the deposition of the Gumchavib and lower Pickelhaube Formations in the southern parts of the study area. The northern parts of the study area were dominated by shallow marine, clastic carbonate deposition with periodic influx of siliciclastics. The change from a carbonate platform in the south to a shallow marine shore, dominated by calcsiliciclastic and clastic carbonate sedimentation in the north of the study area, is also documented within the underlying Gumchavib Formation.

Scanty paleocurrent measurements indicate a topographic high in the east of the study area (Fig. 2.4), along which the shoreline established itself, probably with a north-southerly trend.

The transgression recorded within the Pickelhaube Formation was related to the opening of the Adamastor Ocean (Henry et al., 1988; Von Veh, 1988; Stanistreet et al., 1991). The African continental margin began thermal subsidence during the spreading of the Adamastor Ocean, leading to transgression of the sea over the continental environments. The transgression is initially recorded by the presence of fan delta and siliciclastic sediments, prograding into a shallow marine environment. These sediments are interbedded with massive carbonates, which probably represent recrystallized stromatolitic reefs. Carbonate production then established itself and eventually dominated the deposition in the area. Influx of calcsiliciclastics continued adjacent to the areas of maximum carbonate production.

Fan deltas and debris flows, prograding into a carbonate platform, platform slope, as well as basinal sediments are exposed within the gradational contact of the upper Pickelhaube Formation and the terrestrially-dominated Obib Peak Formation. The Obib Peak Formation records the regression of the Adamastor Ocean during the waning stages of the deposition of the Pickelhaube Formation and is described in the following section. This transgression may be associated with renewed rifting and/or the reactivation of synsedimentary faults, as indicated by the presence of gossans and sulphides, which were precipitated along iron-rich, carbonaceous and sulphidic volcanogenic vents in the vicinity of carbonate platform, slope apron and deep basin environments.

3.5 THE OBIB PEAK FORMATION: REGRESSION OF THE ADAMASTOR OCEAN AND ADVANCE OF FLUVIAL SEDIMENTATION

The rocks of the Obib Peak Formation, which form part of the Hilda Subgroup, overly the carbonates of the Pickelhaube Formation with sharp and gradational contacts, mark a signifdicant change in depositonal system controling the sedimentation ofthese sediments. The Obib Peak Formation comprises only two main facies associations.

3.5.1 Sandstone/carbonate facies association: mixed continental and marine depositional system

This facies association has already been described in section 3.3.1. In the Obib Peak Formation it comprises the following three facies: (1) massive quartzitic calcareous sandstone (Sms); (2) massive carbonate (Lmd); and (3) laminated carbonate (Lfl). Mudstones are not present within this facies association.

3.5.2 Mixed coarse to fine clastics facies association: fluvial braided plain depositional system

This facies association is similar to the facies association described in section 3.2.1. It does, however, not reveal facies Spc, Stc, Srm and Lmd (Figs. 3.40 and 3.41). The conglomerates (Cms) are matrix-supported and display sedimentary structures such as normal grading and erosional channels (Fig. 3.42). At Obib Peak, the conglomerates contain clasts of brown weathered dolomitic limestone, which are absent at other localities.

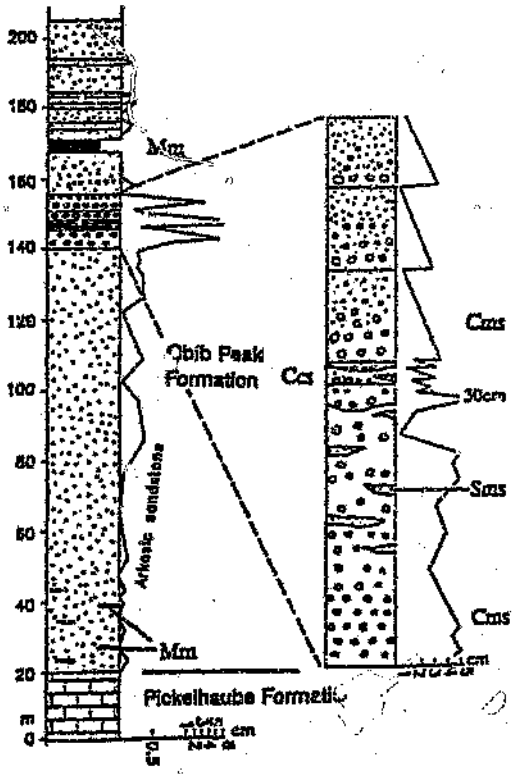


Fig. 3.40: *Measured section through parts of the Obib Peak Formation at locality 3, about 3 km NNW of Obib waterhole (Fig. 2.4); note the sharp contact to the underlying Pickelhaube Formation.*

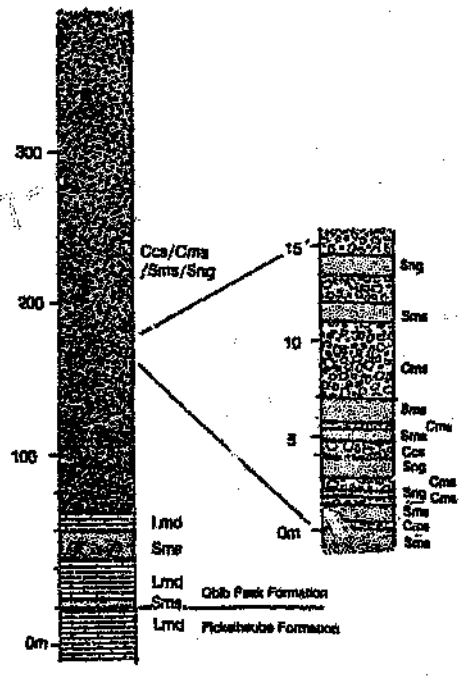


Fig. 3.41: *Measured section through parts of the Obib Peak Formation at Obib Peak (Fig. 2.4); note the gradational contact to the underlying Pickelhaube Formation.*

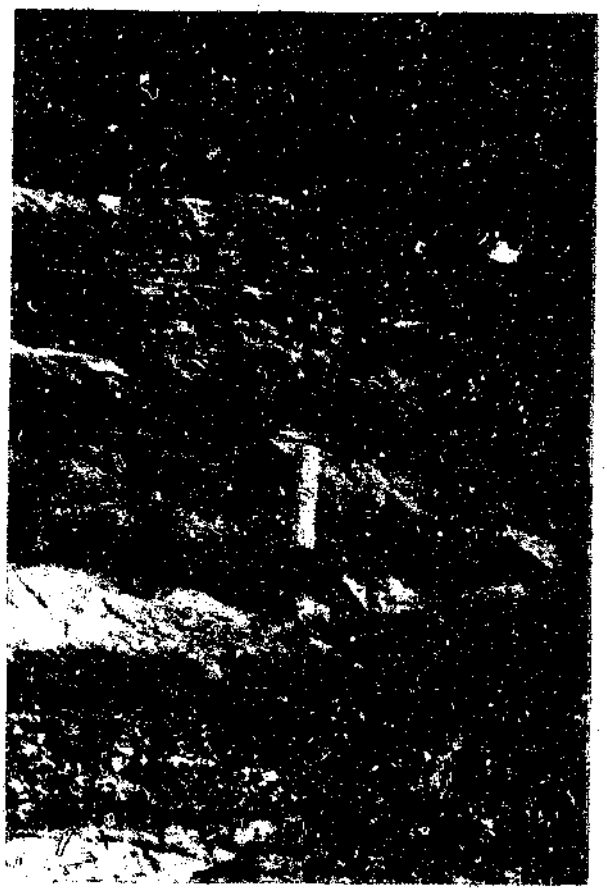


Fig. 3.42: *Erosional channel of conglomerates within arkosic sandstone of the Obib Peak Formation at locality 15, approximately 3,5 km northwest of Obib waterhole (Fig. 2.4).*

3.5.3 Regional distribution

The Obib Peak Formation is only developed at three localities, as shown in Fig. 3.43, namely at locality 3, approximately 3 km NNW of Obib waterhole, at locality 15, about 3,5 km northwest of Obib waterhole, and at Obib Peak, the type locality of this formation (Fig.2.4).

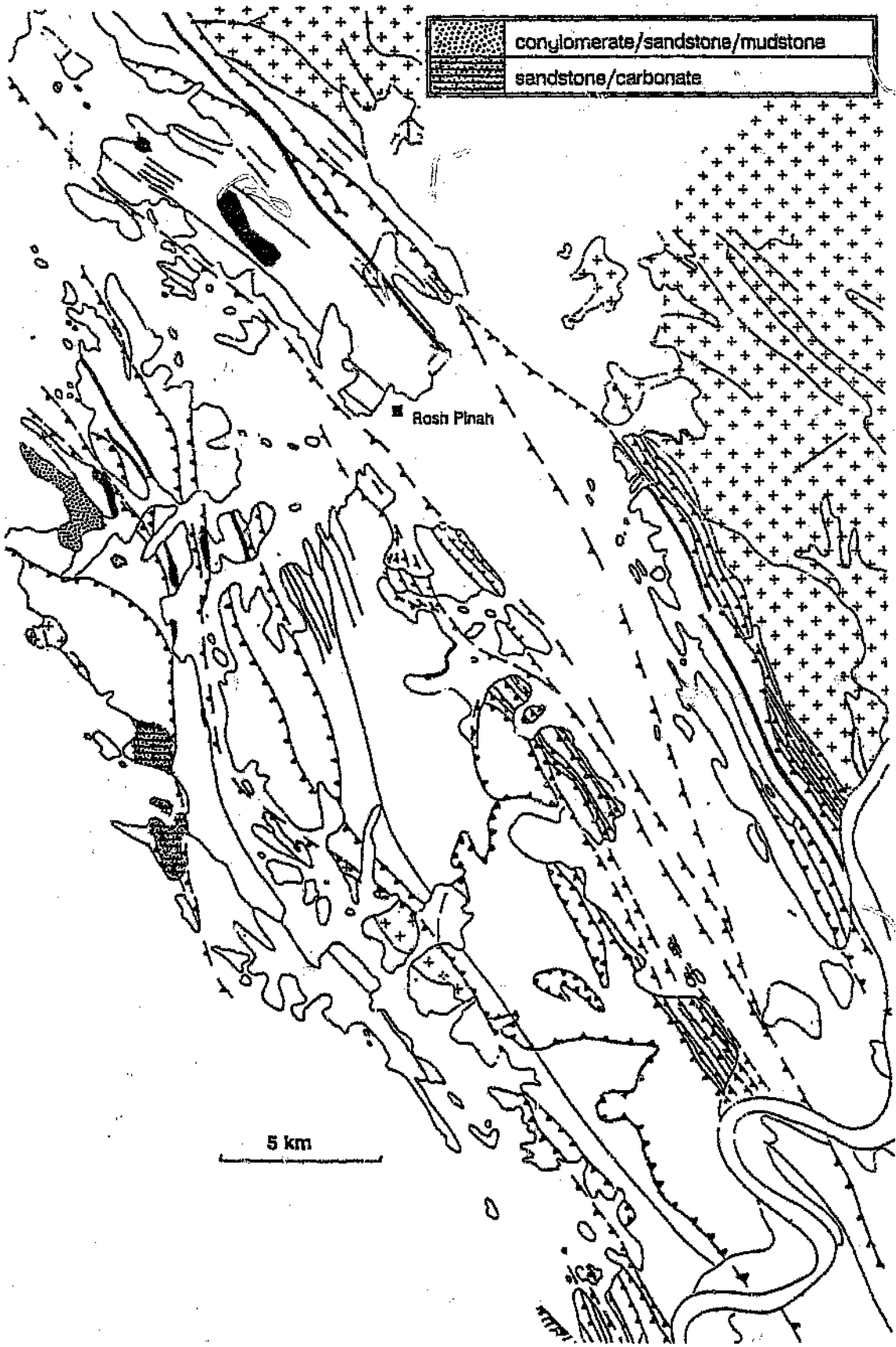


Fig. 3.43: *Regional distributon of the Obib Peak Formation within the study area; for position of thrust slices and localities se Figs. 2.3 & 2.4.*

3.5.4 Vertical and lateral sedimentary facies association variations

Although outcrop of the Obib Peak Formation is very restricted within the study area (Fig. 3.43), vertical facies association variations are apparent, where mixed continental/marine sedimentation changes into exclusively terrestrial sedimentation towards the top of this formation. NNW of Obib water, the fluvial sediments become more proximal towards the top of the Obib Peak Formation.

At Obib Peak the conglomerates contain carbonate clasts, which are conspicuously absent at outcrops further north. Another lateral facies association variation is documented by the contact relationships between the Pickelhaube Formation and the Obib Peak Formation, which is gradational at Obib Peak and sharp at all other localities.

3.5.5 Palaeoenvironmental and palaeogeographic interpretation

The sediments of the Obib Peak Formation document the transition from a shallow marine to a continental environment. Fan deltas prograding into a shallow marine environment, comprising stromatolitic reefs and siliciclastic influx in the vicinity of each other, define the lower part of the Obib Peak Formation around Obib Peak. Fluvially deposited conglomerates, sandstones, and mudstones, the latter representing overbank deposits, which define the upper parts of the Obib Peak Formation, reflect a regression of the Adamastor Ocean, with a seaward moving shoreline. Carbonate clasts within the terrestrial conglomerates indicate that lithified carbonates, probably from a carbonate platform, were present within a provenance area east of Obib Peak, where a topographic high was situated.

The several depositional terrestrial/marine cycles recorded at the gradational contact between the Pickelhaube and the Obib Peak Formations at Obib Peak were probably caused by pulses of tectonic movement along synsedimentary faults. A tectonic nature for the activity of tectonically induced relative sealevel changes at Obib Peak is suggested by the conspicuous absence of cycles at the contact of the Pickelhaube and Obib Peak Formations throughout the rest of the study area. This is furthermore suggested by the presence of the underlying carbonate/coarse to fine clastics facies association (section 3.3.4), which was deposited in the vicinity of synsedimentary faults, which were active during the deposition of the underlying carbonate/coarse to fine clastics facies association (section 3.4.3) of the upper Pickelhaube Formation. Volcanogenic activity during the waning stages of the Pickelhaube Formation and the drastic change from a marine to continental palaeoenvironment, suggests that renewed rifting might have been active during upper Pickelhaube and Obib Peak Formation times.

3.6 THE NUMEES FORMATION: GLACIOMARINE AND INTERGLACIAL SEDIMENTATION

The Numees Formation within the study area, which unconformably overlies the rocks of the Stinkfontein and Hilda Subgroups both in the Richterveld and southern Namibia, was first described by Söhnge and De Villiers (1946), De Villiers & Söhnge (1959), McMillan (1968), Hoffmann (1972), Kröner (1974; 1974a; 1975), Kröner and Germs (1971) and Von Veh (1988). McMillan (1968) subdivided the Numees Formation into a lower diamictite unit and an upper dolomitic unit. The other authors described the presence of a diamictitic Kaigas Formation, which forms part of the lower Stinkfontein Subgroup, and a second diamictitic unit, the Numees Sequence, which is part of the Hilda Subgroup. Von Veh (1988) subdivided the "Numees Sequence" into a basal "Jackalsberg Formation" and an overlying "Sendelingsdrif Formation" (Table 2.2b).

3.6.1 Diamictite facies: glaciomarine sedimentation

A massive diamictite (Dm; Figs. 3.44 & 3.45) forms the bulk of the Numees Formation, with a total maximum thickness of approximately 600 m.

(a) Description of lithologies

The matrix of the bulk of the diamictite (Dm) consists of light grey to blue-grey mudstone, consisting under the microscope of grains of subangular muscovite, quartz, feldspar, and biotite, as well as iron oxide, in highly variable proportions. At Dreigratberg, the lower 100 m of the Numees Formation consists of a brown weathering diamictite, comprising a similar matrix to the light grey to blue-grey

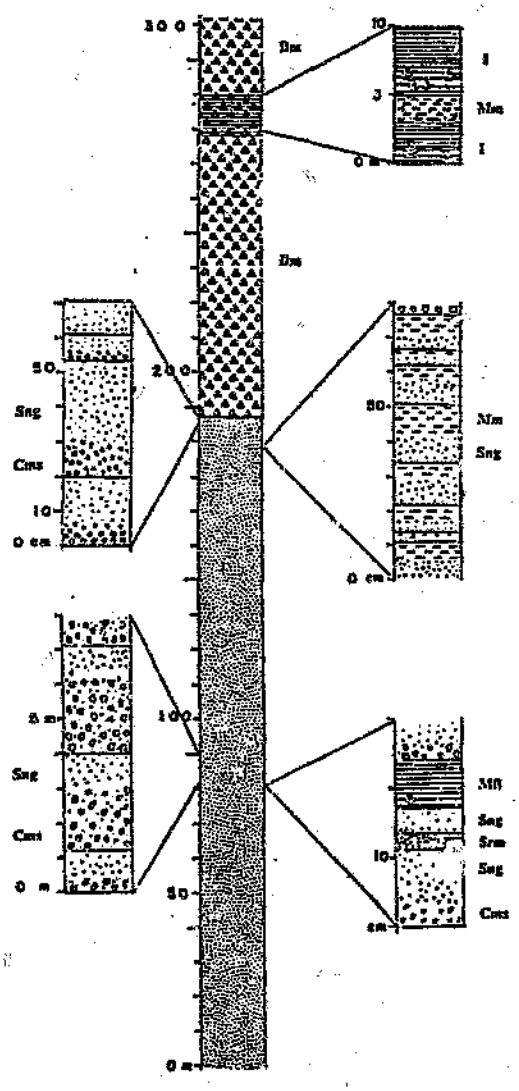


Fig. 3.44: *Measured sections through parts of the Numees Formation at Trekpoort Farm, approximately 25 km northwest of Rosh Pinah.*

diamictite, except for a higher amount of iron oxide, causing the brown colour. The contact between the brown weathering and the light grey to blue grey diamictite (Fig. 3.46) is a normal sedimentary contact. The clasts are in sharp contact with the enclosing matrix and comprise subrounded fragments of basement pegmatite, leucogranite, gneiss, intrabasinal quartzite and brown weathering dolomitic

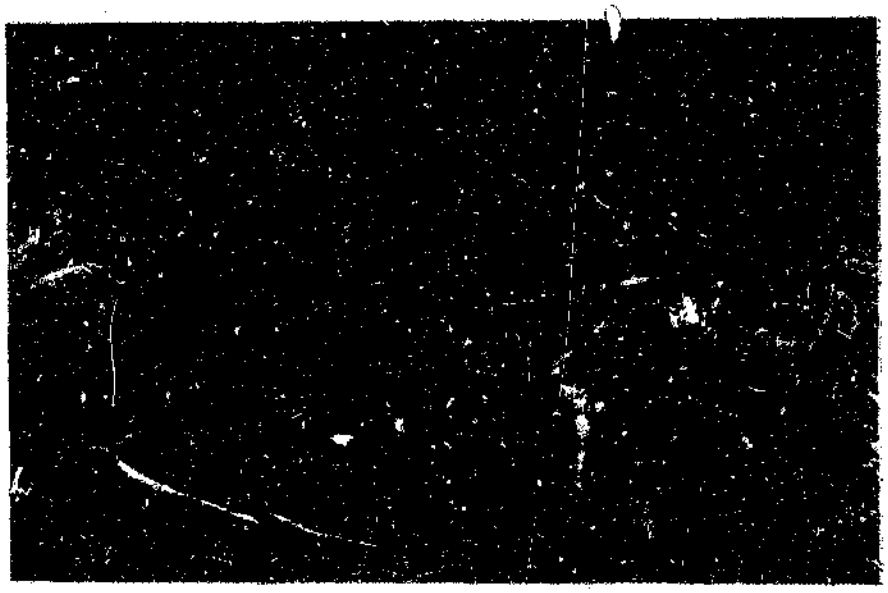


Fig. 3.45: *Massive diamictite of the Numees Formation showing poor sorting and a variety of clasts at Dreigratberg (Fig. 2.4).*

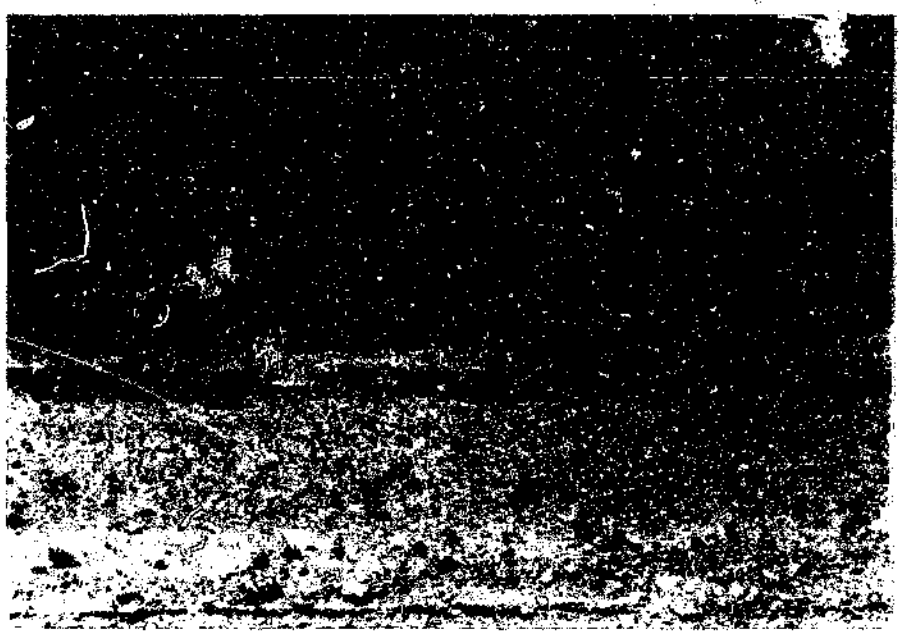


Fig. 3.46: *Brown weathering and light grey to blue-grey diamictite of the Numees Formation 8 km north of Dreigratberg (Fig. 2.4).*

carbonate (Fig. 3.47). Clast sizes range in diameter from small granules to large boulders (10 m), but average 10 to 20 cm. The clasts and boulders may appear in clusters and comprise up to 50% of the whole rock.

(b) Description of sedimentary facies

The massive diamictite (Dm) is matrix-supported with no discernible bedding or other sedimentary structures. Clasts are generally poorly sorted and clusters of clasts of a



Fig. 3.47: *Carbonate clast within massive diamictite of Numees Formation immediately north of Dreigratberg (Fig. 2.4); note alignment of clasts along penetrative s1 foliation from bottom left to top right and s2 cleavage perpendicular to S1.*

particular lithology and/or clast size are present in places.

3.6.2 Iron formation/pebbly sandstone facies association: dropstones in a glaciomarine setting

This facies association is interbedded with the diamictite (Dm). The iron formations are between 10 and 20 m thick and consist of the following facies: (1) banded iron formation with dropstones (Id); and (2) normally graded pebbly sandstone with dropstones (Sng).

(a) Description of lithologies

The iron formation (Id) consists of interlaminated dark-brown magnetite-quartzite and brown bands consisting of quartz, hematite, chlorite, amphibole and carbonate, containing erratics of granite showing sharp contacts with the surrounding matrix (Figs. 3.48 & 3.49).

At Trekpoort Farm, approximately 25 km northwest of Rosh Pinah, magnetite-rich normally graded pebbly sandstones (Sng) are present, containing pebbles consisting of granite and quartzite with 1 cm maximum clast diameters. Granitic dropstones occasionally disrupt these graded beds (Fig. 3.49).

At Dreigratberg, the iron formation is underlain by a diamictite (Dm) about 5 m thick with a mudstone matrix consisting of fine grained chloritic schist with large muscovite and magnetite grains containing clasts of granite and quartzite.

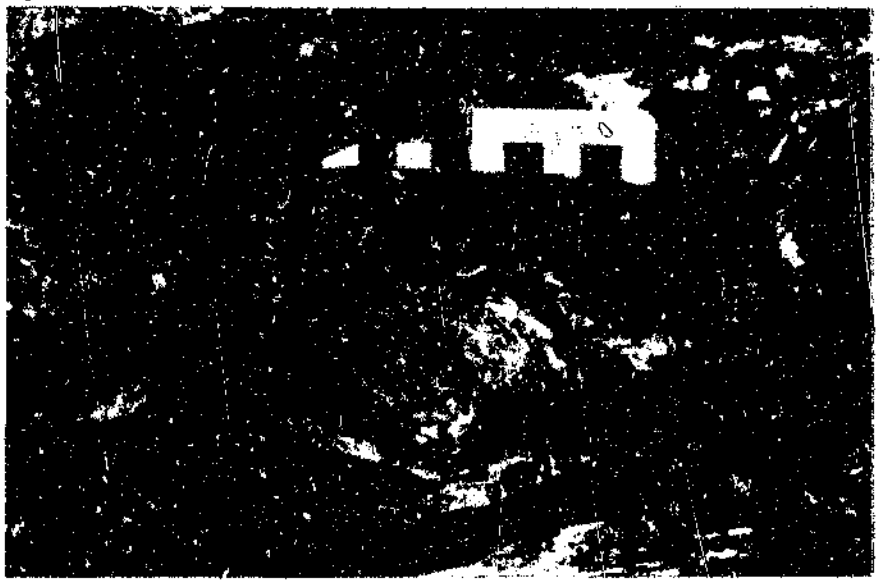


Fig. 3.48: *Granitic dropstone erratic disrupting laminations of the banded iron formation within the Numees Formation at the western flank of Dreigratberg (Fig. 2.4).*



Fig. 3.49: *Magnetite-rich graded pebbly sandstone with granitic dropstone erratics at Trekpoort Farm, approximately 25 km northwest of Rosh Pinah (Fig. 2.4).*

(b) Description of sedimentary facies

The banded iron formations (Id) are fine laminated to very thinly bedded, with dropstones disrupting these laminae (Fig. 3.48). The laminae and bed thicknesses range between 0,1 and 10 mm. The grains of the iron formations measure less than o.01mm.

The normally graded magnetite-rich sandstone beds (Sng) are only present at Trekpoort Farm and have average bed thicknesses of about 15 cm. The iron content within the sandy beds can vary laterally. At the top of one graded sandstone bed asymmetric ripples are present, measuring up to 15 X 2 cm, being overlain by another graded bed containing dropstones within the upper fine grained part of the graded bed.

Several beds of banded iron formation are interbedded with massive diamictite of the Numees Formation in the Richtersveld, pinching out after several tens and hundreds of metres, as revealed by LANDSAT imagery (Newton and Boyle, 1989).

(c) Interpretation of diamictite and iron formation

Diamictite is the lithified product of diamict, a very poorly sorted mixture of mud, sand and gravel (Flint et al., 1960; Eyles and Miall, 1984). Matrix-supported diamictites (Dm) can form by a variety of processes and are by themselves not indicative of a palaeoenvironmental setting. The most common ways of transport and deposition of diamictite are (i) sediment gravity flow processes, in particular mud flows and debris flows (Kuenen and gliorini; 1950; Bouma, 1962; Hampton, 1972; Carter, 1975; Lowe, 1979; 1982; Harms et al., 1982; Vorren et al., 1988; 1991; Vogt et al., 1993) and (ii) direct glacial deposition (Eyles and Miall, 1984; Vorren et al., 1988; 1991). Large

quantities of diamictite can be produced and deposited during glaciation. Studies on modern glaciomarine depositional systems such as off the Antarctica coast (Anderson, 1983; Anderson et al., 1979; 1980; 1984; Kurtz and Anderson, 1979) and of the Bear Island submarine fan in the Svalbard-Barents Sea (Vogt et al., 1993) have shown that the bulk of transport and deposition of sediment occurs by sediment gravity flow processes. Direct evidence of ice activity such as ice rafting is rarely preserved within the study area. Dropstones within the iron formations (Id), disrupting the laminae, are clear evidence for glacial activity.

The origin of iron formation may be associated with volcanic activity (Algoma type) or be purely sedimentary in origin with no apparent volcanic affinities (Lake Superior-type; Trendall and Morris, 1983). Iron formations within the Chuos Formation in the Southern Margin Zone of the Damara Orogen, which is correlatable with the Numees Formation of the southern coastal branch of the study area, are associated with basic volcanism (Breitkopf, 1986; Breitkopf & Maiden, 1987). Bühn et al. (1992) described manganese-rich iron formations of the Chuos Formation in the Otjosondu area about 160 km northwest of Windhoek, relating them to continental break-up and evolution of new spreading ridges, with the main source of metals deriving from the resulting hydrothermal activity, with manganese and iron-rich ocean waters upwelling onto the neighbouring shelf areas. Basic and felsic volcanism, associated with hydrothermal exhalative iron-rich vents within a tectonic environment of rifting may be responsible for the generation of the iron formations of the Numees Formation.

The graded beds and the ripple cross lamination within one of the magnetite-rich sandstone bed (Sng) at Trekpoort Farm strongly resemble the lower "A" and the upper "C" division of a Bouma sequence (Bouma, 1962; Walker, 1984). Even though other

sedimentary processes can be accountable for the formation of graded beds and ripple cross laminae, the studied graded beds are interpreted as turbiditic in origin for the following reasons:

(i) the lateral continuity of the relatively thin (5 to 10 cm) graded beds over outcrop width of several tens of metres;

(ii) the beds have flat bottoms and tops with no evidence for channelling (Walker, 1984).

Assuming a submarine oceanic setting for the deposition of the iron formation within the Numees Formation, the interbedded diamictite must also have been deposited within a submarine environment, with floating ice rafts dropping clasts into fine grained marine sediments and iron formations, as suggested by Henry et al. (1986) for the Chuos Formation in the Central Damara.

3.6.3 Conglomerate/sandstone/mudstone facies association: gravity mass flow within a marine setting

This facies association is interbedded with the light grey to blue-grey massive diamictite of the Numees Formation, with a maximum thickness of about 600 m (Figs. 3.50 & 3.51). It consists of the following facies: (1) normally graded matrix-supported conglomerate (Cms); (2) normally graded sandstone (Sng); (3) massive mudstone (Mm).

(a) Description of lithologies

The groundmass of the conglomerate (Cms) consists of silt and fine grained sand.

Clasts vary in diameter from approximately 3 m to 2 mm, grading into sandstone (Sng) and mudstone (Mm). The clasts consist of subangular boulders and clasts of granite, quartzite, shale and brown weathered dolomitic limestone. The muddy and fine to coarse sandy groundmass of the normally graded conglomerates (Cms), as well as the sandstones (Sng) and the mudstones (Mm), are all light grey to blue-grey and

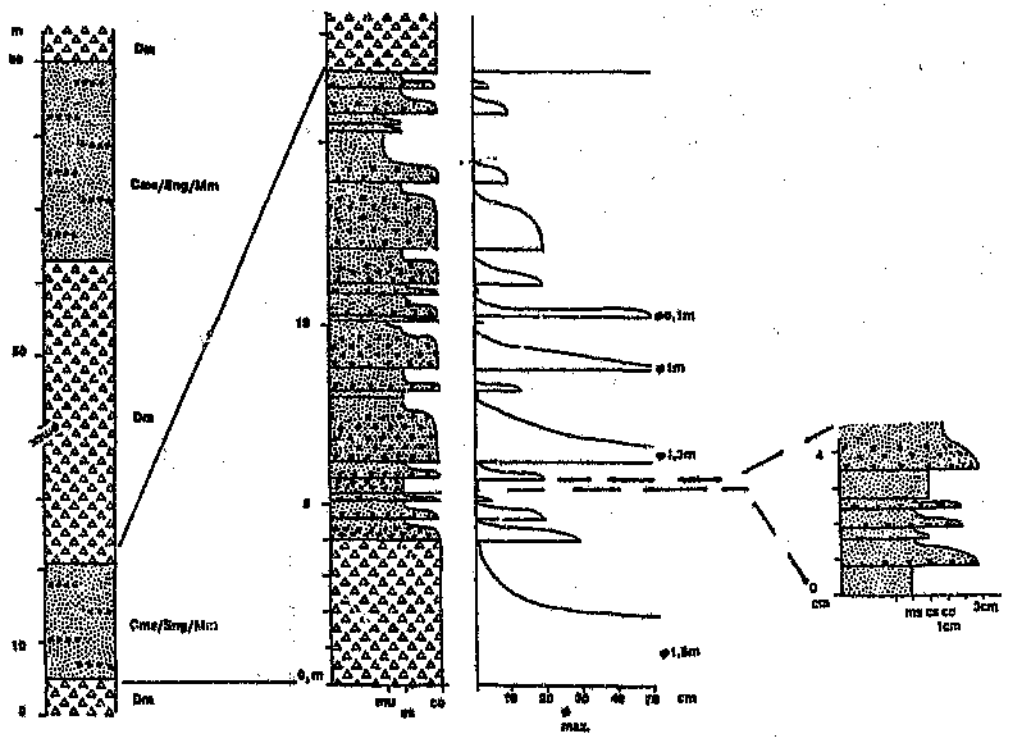


Fig. 3.50: *Measured section through the graded beds of the conglomerate/sandstone/mudstone facies association within the Numees Formation, about 2 km south-east of Namuskluft Farmhouse (Fig. 2.4).*

consist of quartz, feldspar, biotite and muscovite. The grain size of the sandstones varies from medium to fine, often grading into mudstone.

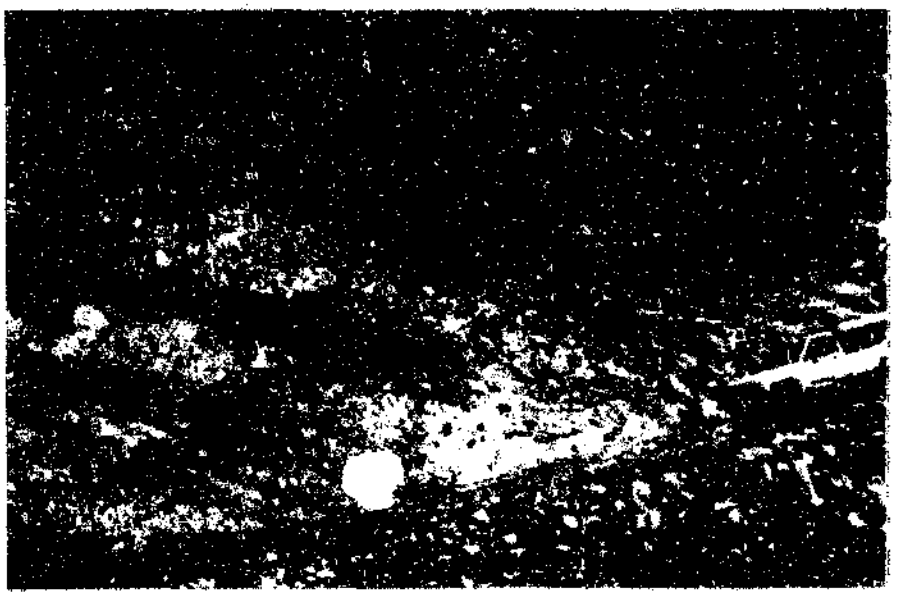


Fig. 3.51: *Graded beds of the conglomerate/sandstone/mudstone facies association within the Numees Formation, about 2 km south-east of Namuskluft Farmhouse (Fig. 2.4).*

(b) Description of sedimentary facies

The beds grade from conglomerate (Cms) with boulders up to 3 m thick to sandstone (Sng), and in some cases to mudstone (Mm; Figs. 3.51 & 3.52). The contacts between the beds are sharp. The beds are consistent over outcrop width, piching out only after tens of metres.

(c) Interpretation

The study of glaciomarine deposition under the Antarctic ice shelf (e.g. Anderson, 1983; Anderson et al.; 1979; 1980; 1984; Kurtz and Anderson, 1979), the Bear Island submarine fan in the Svalbard-Barents Sea (Vogt et al., 1993) and thick diamictite

sequences, which have been interpreted as glaciomarine deposits, such as the Late Cenozoic Yakataga Formation in Alaska (Armentrout, 1983; Eyles and Eyles, 1983) and the Cenozoic environments in the Barents Sea (Vorren et al., 1988; 1991), show that build-ups of sediment at the ice-line result in unstable slopes, where periodic slumping can cause the deposition of mud flows and debris flows. The build-ups of sediment at the ice line comprised mud piles, which were water-rich, rapidly deposited and rich in sand and silt, and, therefore, were prime candidates for gravitational failure (Vogt et al., 1993). Occasionally turbiditic currents are generated and move further downslope to deposit as turbidites.

3.6.4 Carbonate facies association

Normally graded and laminated carbonates (Ll), as well as massive carbonates (Lm) are interbedded with the diamictite (Dm), resembling the carbonates of the Pickelhaube Formation, described in section 3.4.1, in terms of sedimentary structures.

(a) Description of lithologies

The carbonates (Ll; Lm) consist of white and grey dolomitic carbonate with variable minor amounts (<10%) of quartz.

(b) Description of sedimentary facies

The massive carbonates within this facies association display no sedimentary structures.

Normal grading, with thicknesses of graded beds varying from <1cm to about 10cm

is present within some carbonates (Ll). Fine to medium laminations, consisting of white and grey carbonate, are also present within these carbonates (Ll).

The carbonates (Lm; Ll) pinch out against the diamictite within tens and hundreds of metres (Fig. 3.52).

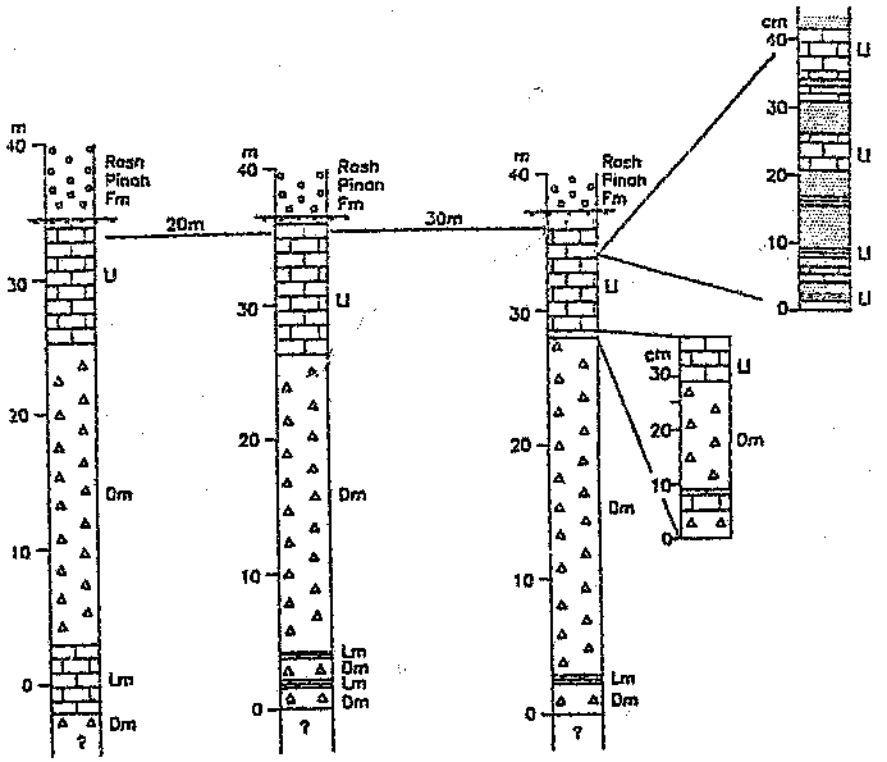


Fig. 3.52: *Measured section through parts of the Numees Formation about 3 km north of Dreigratberg (Fig. 2.4), displaying interbedded carbonate and diamictite.*

(c) Interpretation

The carbonate beds are interpreted as a minor but distinct facies within the diamictite. Several possibilities for the deposition of the carbonates, interbedded with diamictites have been suggested. The sharp contacts and the limited lateral extent of the carbonates do not exclude the possibility that they were deposited as huge boulders or as being huge rafts carried by gravity mass flow processes, since smaller carbonate

clasts commonly occur in the diamictite. They may, however, also have been generated as gravity flows, consisting of redeposited cold water carbonates (Rao, 1981a; 1981b; Fairchild and Hambrey, 1984; Walter and Bauld, 1983). The carbonates may, however, also have developed during interglacial periods, as identified within the Chuos Formation of the central Damara (Bühn et al., 1992), which forms the equivalent of the Numees Formation.

Reworked carbonate deposits from the glacial Varangian Port Askaig Formation in Scotland have been described by Spencer (1981). Other Varangian and Vendian glacial deposits of northern Europe both sandwich and occur within glaciogenic, diamictite beds (Spencer, 1981, 1985; Bjorlykke, 1985; Fairchild & Hambrey, 1984; Nystuen, 1985). Walter & Bauld (1983) described an association of evaporitic sulphate, stromatolitic dolomite and glacial deposits from the Proterozoic of Australia and the Cainozoic of Antarctica. The association of carbonates and glacial deposits is, therefore, not unusual.

3.6.5 Coarse to fine clastics/carbonates/bimodal volcanics facies association: interglacial mixed continental/marine depositional system

The following facies form part of this facies association: (1) matrix-supported conglomerate (Cms); (2) normally graded sandstone (Sng); (3) massive sandstone (Sms); (4) plane-laminated sandstone (Spl); (5) tabular planar cross-laminated sandstone (Stp); (6) ripple-marked sandstone (Srm); (7) calcareous quartzitic sandstone (Scq); (8) massive mudstone (Mm); (9) plane laminated mudstone (Mpl);

(10) cross-laminated mud- and siltstone (MSl); (11) massive carbonate (Lms); (12) plane laminated carbonate (Lpl); (13) stromatolitic carbonate (Ls); (14) carbonate breccia (Lbr); (15) carbonaceous carbonate (Lgl); (16) felsic volcanics (Va); (17) mafic volcanics (Vm).

(a) Description of lithologies

The sandstones (Sms, Sng, Spl, Stp, Srm, Stl) vary from dark-grey and blue-grey to light brown and brown and consist predominantly of quartz (20-65%), mica (25-45%), and feldspar (5-35%), and of lesser amounts of rock fragments (5-10%), iron-oxide (0,5-5%) and calcite (0,5-5%). The feldspar includes both plagioclase and microcline up to 1,5 cm in length. Facies Scq consists of medium grained calcareous quartzitic sandstone.

The mudstones (Mm, Mpl) are green-grey to grey and consist of chlorite, muscovite, quartz, feldspar and calcite.

The conglomerates (Cms) have a matrix similar in composition to the sandstones and contain pebbles and clasts of quartzite, vein quartz, micaceous quartzite, granite, dolomite and felsite.

The carbonates (Lms, Lpl, Ls) vary from rusty brown to blue grey and are dolomitic in composition. The presence of carbon in some of the carbonates (Lgl) changes the colour to blue-black. The presence of a dolomitic breccia (Lbr) within massive carbonate, consisting of a mass of disoriented slabs of extrabasinal material, was described by McMillan (1968) from the Namuskluft area approximately 15 km east of Rosh Pinah (Fig. 2.4).

Basic sills (Vm) are interlayered with sandstones south of Namuskluft waterhole,

consisting of green amphibole, plagioclase, epidoate, quartz, +/-biotite and +/- calcite with accessory ilmenite, hematite and sphene.

Felsic volcanics (Va), interbedded with this facies association at Trekpoort Farm, consist of grey to pink-grey quartz-feldspar porphyry.

(b) Description of sedimentary facies

The conglomerates (Cms) are matrix-supported and are either structureless or normally graded from conglomerate at the bottom to mudstone at the top of the beds. Beds vary in thickness from 2 cm to 3 m. Clasts are subangular to subrounded and average 5 cm in diameter, however, boulders with diameters of 1,5 m are also present. Conglomerate beds pinch out laterally, often displaying erosive structures.

The sandstones are coarse to fine and generally structureless (Sms), occasionally displaying a variety of sedimentary structures, ranging from asymmetric ripples with sinuous out-of-phase to linguoid shape (Srm) to tabular planar cross-bedding (Stp) and normal grading (Sng). Erosive conglomeratic channels (Cms) are developed within some of the sandstone beds.

The conglomerates and sandstones are interbedded with siltstones and mudstones, which are either massive (Mm) or display sedimentary structures, such as wave ripple-laminations and plane laminations, with occasional dropstone erratics, disrupting the laminations. These silt- and mudstones are interbedded with carbonates and structureless calcsiliciclastics (Scq).

Sedimentary structures within the carbonates are either absent (Lms) or include plane laminations (Lpl) or stromatolitic laminations with domal diameters of about 5 cm. The carbonate breccias are poorly sorted, with clast diameters of the tabular to subanguiar

clasts and boulders varying from 2 mm to 50 cm. Bed thicknesses of the carbonates vary between 1 cm and 15 m and contacts between the carbonates and the clastic beds are sharp.

The mafic (Vm) and felsic (Va) volcanics are about 10 to 20 m thick and display sharp contacts with the under- and overlying lithologies. No sedimentary or volcanic structures are discernible within the volcanics (Vm, Va).

(c) Interpretation

The mainly massive, ripple-marked and cross-bedded sandy (Sms, Srm, Spc) and conglomeratic beds (Cms), which form erosional channels in places, are interpreted as fluvial deposits. Some of the massive sandstones (Sms) represent alluvial fans, prograding into a shallow-marine environment.

Asymmetric ripple marks within some fine siltstones and sandstones (Srm) may represent wave ripple-cross lamination, indicating minor wave reworking above wave base. The trough-cross laminated siltstones and mudstones (MSl) possibly represent low energy wave activity and longshore currents generated by storms and waves within a shallow marine environment. The abundance of finely plane laminated siltstone and mudstone (Mpl) indicates a lower shoreface environment. Dropstone erratics disrupting the laminae of some mudstones are evidence of glacial activity deriving from ice rafts. The highly calcareous composition of the quartzitic sandstones (Scq) and interlaminated carbonates (Lms, Lpl, Ls) suggests a deposition within the zone of siliciclastic influx near the zone of optimum carbonate production, possibly indicating a shallow marine shelf setting. The stromatolitic carbonate (Ls) suggests a shallow marine depositional setting within a carbonate platform for the carbonates. The

massive carbonates (Lms) may represent recrystallized stromatolitic carbonates. Carbonate breccias (Lbr) and some graded conglomerates (Cms) may have been deposited as gravity mass flows associated with platform margins and slope aprons (see section 3.4.3).

The presence of carbonaceous shale, locally carbonate, interbedded with felsic volcanics at Trekpoort Farm, and the presence of mafic volcanics interbedded with the continental sediments at Namuskluft, as well as the marked change from a purely marine to continental and mixed shallow marine/continental palaeoenvironment indicates renewed rifting during the deposition of the Numees Formation.

This facies association, which is interbedded with massive diamictites and interbedded iron formations, is interpreted as having been deposited during interglacial periods. This may represent the first time that terrestrial interglacial sediments have been recognized in the Damara Sequence.

3.6.6 Regional distribution

The diamictite within the study area is widespread. The best outcrops are found at Dreigratberg and immediately north of it (Fig. 3.53). The westernmost outcrop exposing Numees diamictite is present 3,5 km south of Obib Peak. Approximately 10 km south of Gumchavib Mountain and west of the the CDM road leading to Oranjemund, Numees diamictite overlies carbonates of the Pickelhaube Formation. Iron formation containing dropstones is present at the western flank of the Dreigratberg syncline, next to the fence to Diamond area No.1. Diamictite, iron formation and magnetite-rich graded sandstone of the Numees Formation are present

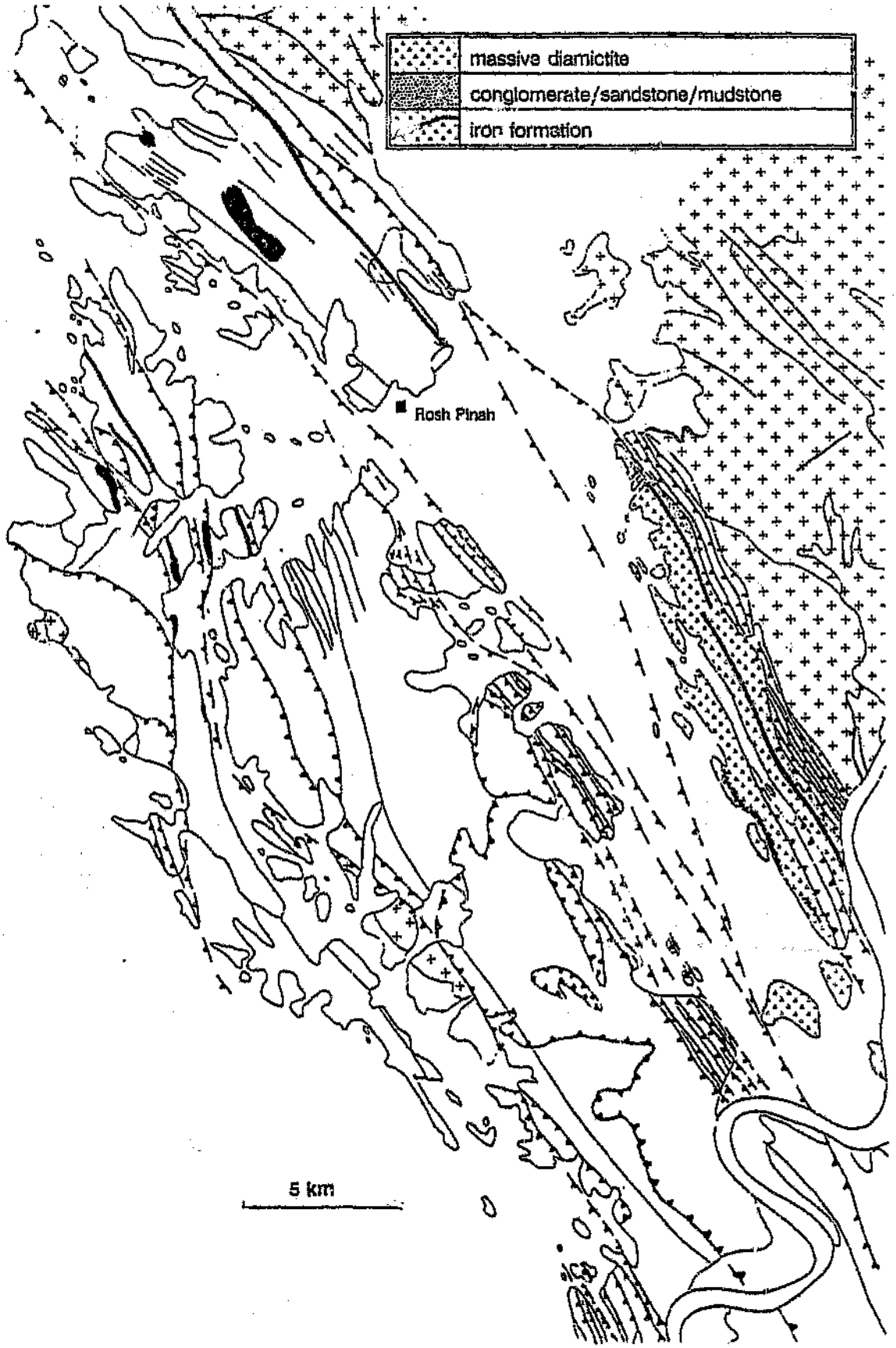


Fig. 3.53: *Regional distribution of the several facies associations of the Numees Formation within the study area; for position of thrust slices and localities see Figs. 2.3 & 2.4.*

at Trekpoort Farm, approximately 25 km northwest of Rosh Pinah, as well as at Witputz Farm, approximately 40 km north of Rosh Pinah. It is underlain by the interglacial clastics/carbonates/bimodal volcanics facies association, which is also well developed at Namuskluft and in the northwestern Richtersveld, where it was attributed to the "Kaigas Formation" (Von Veh, 1988). The carbonate beds within the diamictite are only developed at one locality approximately 3 km north of Dreigratberg within the western parts of the imbricate zone along the Rosh Pinah thrust fault. Numees Formation lithologies are also present north and northeast of Rosh Pinah, within the "IMCOR Zinc mine concession area".

3.6.7 Vertical and lateral facies association variations

The most prominent vertical facies association variations are displayed by the alternation of glacial and interglacial deposits.

At Trekpoort Farm a vertical facies variation from continental to marine deposits is evidence within the interglacial deposits.

Vertical facies association variations are exposed within the massive diamictite at the Dreigratberg syncline, where iron oxide enriched brown diamictite, hosting the iron formation and associated dropstones, is overlain by a light grey to blue-grey diamictite (Fig. 3.46), which hosts coarse to fine clastic beds. The carbonate beds are also interbedded with the lighter coloured diamictite, placing them higher up in the internal Numees Formation stratigraphy than the iron formations.

No significant lateral facies variations are exposed within the massive diamictite itself. The iron formations within the diamictite are laterally not very consistent and pinch out

within several hundreds of metres or several kilometres. The same accounts for the conglomerate/sandstone/mudstone beds and the carbonates, which are interbedded with the massive diamictite within the Numees Formation.

The contact relationships of the Numees Formation with the underlying rocks are unconformable. Within the study area, Numees Formation rocks overly basement rocks and carbonates of the Pickelhaube Formation unconformably, whereas at Trekpoort Farm, approximately 25 km northwest of Rosh Pinah, they overly the Rosh Pinah Formation.

3.6.8 Palaeoenvironmental reconstruction

The Numees Formation lithologies are interpreted as being deposited within a predominantly glaciomarine environment within a passive margin environment (Fig. 3.54). The diamictites were generated within a shelf setting as debris flows which formed from reworking of morainic sediment dumped at the ice-front by glaciers,

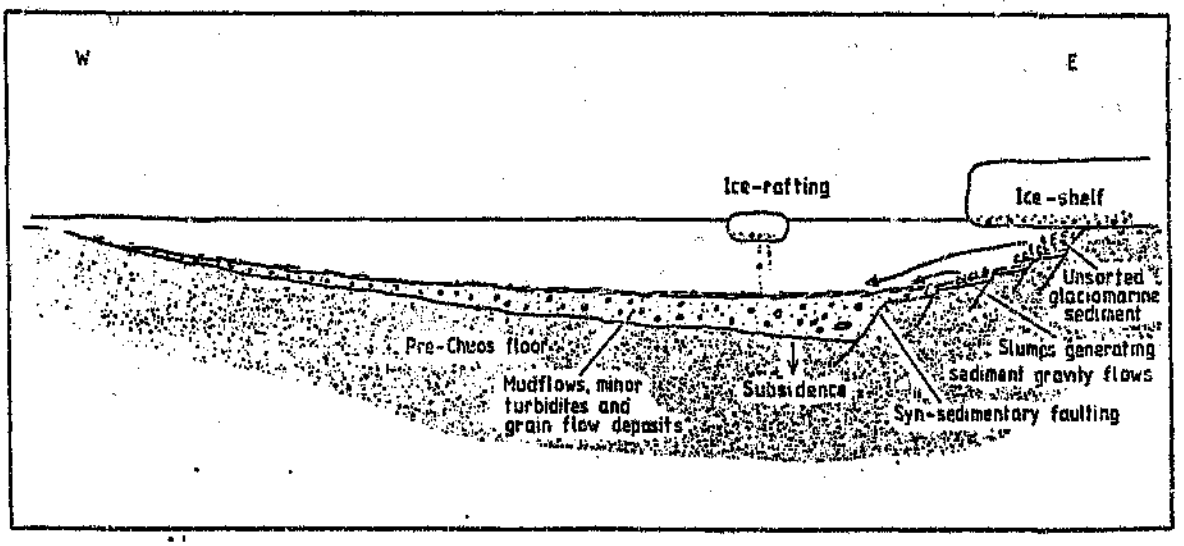


Fig. 3.54: *Model proposed for the origin of the glaciomarine Numees Formation sediments (modified after Henry et al., 1986).*

floating ice sheets and icebergs. The buildup of proximal sediment could have led to gravitational instability of the sediment pile which enabled downslope reworking by sediment gravity processes, as recorded by the presence of normally graded conglomerates, sandstones, mudstones and graded carbonates, deposited as submarine debris flows and turbidites.

Manganese-rich iron formations of the Chuos Formation in the Otjosondu area about 150 km northeast of Windhoek may be related to continental break-up and evolution of new spreading ridges within the Khomas Sea, with the main source of metals deriving from the resulting hydrothermal activity, with manganese and iron-rich ocean waters upwelling onto the neighbouring shelf areas (Bühn et al., 1992). A similar setting, involving the creation of oceanic crust during the opening of the Adamastor Ocean, may have been responsible for the generation of iron formations within of the Numees Formation. The generation of iron formation could, however, also be associated with the generation of amphibolites and felsic volcanics and associated hydrothermal exhalative precipitation during intermittent phases of volcanic activity as a consequence of renewed rifting. A similar origin for the iron formation of the Chuos Formation in the Southern Margin Zone of the inland branch of the Damara Orogen has been suggested by Breitkopf (1986) and Breitkopf and Maiden (1986).

The presence of terrestrially deposited and interbedded shallow marine sediments and platform carbonates, sandwiched between thick successions of massive diamictite, are evidence for the existence of various interglacial periods during the deposition of the Numees Formation. Interglacial periods could account for the source of the redeposited carbonate beds within the glaciomarine diamictite. The source rocks of the carbonates within the Numees Formation diamictites could, however, also be cold

water carbonates.

A model envisaging the deposition of glaciomarine Numees Formation lithologies is presented in Fig. 3.54.

3.6.9 Discussion

Evidence from the study area in Southern Namibia and the Richtersveld shows, that the "Kaigas Formation" and the "Numees Sequence", as subdivided by Von Veh (1988), constitute one stratigraphic unit which has been duplicated by thrusting.

Von Veh (1988) lists the following reasons for a subdivision into two stratigraphic units:

(1) Although both units have unconformable basal contacts, the "Kaigas Formation" rests on basement rocks and Stinkfontein quartzites, whereas the "Numees Sequence" is everywhere underlain by Hilda sediments;

(2) the "Kaigas Formation" diamictite is interbedded with grit, arenite and phyllite, whereas the "Numees Sequence" diamictite is largely unbedded and massive;

(3) the "Kaigas Formation" diamictite does not contain a near-basal iron formation or ferrugeneous zone;

(4) Carbonate erratics are conspicuously absent in the "Kaigas Formation", but present in the "Numees Sequence".

(5) The overlying beds do not resemble each other.

Field evidence shows, that a subdivision into two diamictitic units is not applicable. The "Numees Sequence" of Von Veh (1988) is therefore reclassified as a formation and named Numees Formation in this work. The reasons for a reclassification as a

formation are given in the text below, in direct reply to the above listed argumentation of Von Veh (1988).

To point (1): As the Numees Formation overlies the underlying rocks unconformably, it must be expected that it overlies both Stinkfontein and Hilda Subgroup lithologies, which is the case in Southern Namibia, and also in the Richterveld, if the postulation of only one diamictitic unit is applicable.

To point (2): As described in section 3.6.3, the Numees Formation within the study area is also interbedded with conglomerates/sandstones/mudstones.

To point (3): The fact, that iron formations or ferrugineous zones are absent within the "Kaigas Formation", does not necessarily prove the existence of two different stratigraphic units, as the iron formations pinch out laterally as shown both within the study area and within the correlatable Chuos Formation in the central Damara (Henry, 1992; Henry et al., 1986) and the Kaoko Belt. Debris, consisting of banded iron Formation, was recognized near Numees Prospect in the Richtersveld, where the "Kaigas Formation" is best developed, proving that iron formations are present within the "Kaigas Formation".

To point (4): Carbonate erratics, believed to be conspicuously absent within the Kaigas Formation, were recognized at Numees Prospect in the Richterveld (personal communications Dr. Sharad Master), which was mapped as "Kaigas Formation" by Von Veh (1988).

To point (5): The beds, overlying the "Kaigas Formation" and "Numees Sequence", which do not resemble each other, have contacts to the underlying diamictites which are exclusively tectonic in nature.

Furthermore, the "Kaigas Formation", as defined by Von Veh (1988), is not known to be intruded by the Gannakouriep dyke and sill swarm anywhere in the Gariep Belt, adding further evidence that it postdated the Gannakouriep dyke and sill swarm and is, therefore, younger than the Stinkfontein Subgroup and the lower Pickelhaube Formation.

A subdivision into a lower "Jackalsberg Formation", consisting of a basal iron formation and ferrugineous zone, is not applicable, as this zone is over- and underlain by massive diamictite within the study area and at Trekpoort Farm approximately 25 km northwest of Rosh Pinah (Fig. 3.44), which is also revealed by LANDSAT image interpretation in the Richtersveld (Newton and Boyle, 1989), where several horizons of iron formations are present within the diamictite.

Some controversy has existed concerning the stratigraphic position of the coarse to fine clastics/carbonate/bimodal volcanics facies association, in particular at Namuskluft about 15 km east of Rosh Pinah. McMillan (1968) ascribed this volcano-sedimentary facies association to the Numees Formation. He subdivided the Numees Formation into a basal tillite, overlain by a greywacke and an arkosic stage, representing this facies association, followed by an upper tillite stage and an upper dolomite stage. Hoffmann (1972; 1989) suggested the presence of three distinct stratigraphic units within this area, subdividing the sequence exposed at Namuskluft into a basal diamictitic Kaigas Formation and Stinkfontein quartzites, both being part of the Stinkfontein "Group", and an upper diamictitic Numees Formation, which forms part of the overlying Gariep Group. A correlation of the stratigraphic sequence at

Namuskluft with the Nama Group was suggested by Jasper et al. (1992/1993). New field evidence and metamorphic studies (section 5) revealed however, that these beds are part of the Numees Formation, as first suggested by McMillan (1968).

Reconnaissance mapping at Namuskluft waterhole about 15 km east of Rosh Pinah and previous mapping undertaken by McMillan (1968) and Hoffmann (1972) revealed an approximately 1100 m thick succesion of interbedded conglomerates, quartzitic and feldspathic sandstones, mudstones, carbonates, felsic volcanics and intrusive amphibolites, which are sandwiched between two diamictite units. At Trekpoort Farm, where this facies association only contains felsic volcanics, it is overlain by diamictite and interbedded iron formation. In the Richtersveld, several diamictite beds are interbedded with beds consisting of clastics/carbonate facies associations (Von Veh, 1988), representing glacial/interglacial cycles.

Because of the striking resemblance of the Numees Formation and the Chuos Formation of the Central Damara and the Kaoko Belt in northern Namibia, both in lithological appearance, preserved sedimentary structures, the depositional environment and the underlying stratigraphic units, a correlation between these two formations is proposed. Lithological similarities include the presence of massive diamictite and interbedded iron formation and carbonates, as well as the presence of mafic volcanics. The palaeoenvironmental setting and the tectonic environment of the Numees and Chuos Formations do also resemble each other strikingly, including alternating phases of glaciomarine and interglacial deposition and renewed rifting.

CHAPTER 4

STRUCTURAL GEOLOGY

4.1 INTRODUCTION

Structural studies were undertaken within the study area, as well as reconaissance mapping at Trekpoort Farm, approximately 25 km northwest of Rosh Pinah, and at Bogenfels in the northwestern parts of Diamond Area No.1 (Fig. 1.2), in order to establish an overall deformation pattern to help constrain the tectonic setting of the Gariep Belt in southern Namibia. The first structural analyses within the study area were undertaken by McMillan (1968). Further structural work was later carried out by Siegfried (1990) at Rosh Pinah Mine and around its immediate vicinity. This work represents the first detailed structural analyses within the Obib Berge and the Rosh Pinah-Dreigratberg area. Further detailed structural investigations within these areas are currently being undertaken by Alchin (in prep.) in the course of an M.Sc. project at the University of Stellenbosch.

Within the Richtersveld, south of the present study area, the structural geology of the Gariep Belt was described by Rogers (1916), Kröner (1974), and De Villiers and Söhnge (1959). The first detailed structural analysis of the Gariep Belt south of the Orange River was undertaken by Von Veh (1988). Rogers (1916) described, with only minor detail, the structural complicatio ns associated with the area around Numees Mine and other areas in the northwestern Richtersveld. De Villiers and Söhnge (1959) described some major tectonic structures, neglecting the description of the minor

ones, and interpreted the tectonic evolution of the Gariep Belt in the Richtersveld as a repetition of seven cycles of geosynclinal deposition, orogenesis and associated magmatism along similar, parallel structural trends. Kröner (1974) recognized two main tectonic domains: (1) an eastern "miogeosynclinal" domain; and (2) a western "eugeosynclinal" domain associated with compressional deformation. A "tectogen" model of geosynclinal subsidence with associated gravity folding and a subsequent compressional phase with associated tectonic deformation was suggested by Kröner (1974). The occurrence of these gravity folds was questioned by Von Veh (1988) and in this present study, as most of these features attributed by Kröner (1974) to a "penecontemporaneous gravity deformation" deform an earlier fabric around their fold hinges. Investigations to determine the kinematic history of the Gariep Belt have so far only been undertaken in the Richtersveld (Von Veh, 1988). Von Veh (1988) carried out structural analyses and proposed three kinematic phases for the Richtersveld: (1) a transpressive or convergent wrenching phase, (2) a simple parallel wrenching phase and (3) a transtensive or divergent wrenching phase.

In this work the term "foliation" is used to delineate generally planar surfaces of structural origin. The term "penetrative cleavage" is used for fabrics which are characterized by the preferred alignment (newly crystallized and/or reorientated) of particular minerals (i.e. micas). The nomenclature of Fleuty (1964) is used for fold shapes (i.e. open, close, tight). The terminology of Turner and Weiss (1963) was applied to structural elements, i.e. S1 to Sn for planar, penetrative fabrics, Ln for linear penetrative fabrics, and Fn for folding of fabrics. The relative age of consecutive fabric generations is indicated by suffixes 1, 2, 3. Sedimentary bedding is referred to as So. Identified deformational phases are labelled D1, D2, and D3.

4.1.1 Deformational events

In the study area three phases of deformation, of which the first two are associated with a conspicuous cleavage development, have been distinguished. The most prominent structural features, which form the structural grain of the study area, are north-south- to northwest-southeast-striking, small to large scale D2 folds with northerly and southerly plunging fold axes and major northerly to northwesterly striking thrust faults (Fig. 2.4) with thrust planes dipping towards the west to WSW. Within the study area, the northerly continuation of the Annisfontein anticlinorium of the Richtersveld (Von Veh, 1988) is the most conspicuous fold structure, which occurs in the vicinity of Gumchavib Mountain (Fig. 2.4). These folds deform around their hinge line an earlier, bedding-subparallel fabric, some minor intrafolial isoclinal folds and associated thrust fault planes. The earliest recognized structural features characterize the D1 phase of deformation phase. Subsequently, the D1 and D2 deformational structures were deformed by east-west- to northeast-southwest-trending small to large scale folds, which are classified as representations of the D3 deformational event.

The three recognized deformational events, D1, D2 and D3, are defined by the following main structural characteristics, which are summarized in Table 4.1 and described in more detail in section 4.3: (1) D1 by a bedding-subparallel S1 cleavage, intrafolial F1 folds, and an l1 stretching lineation of grains, clasts, and boulders; (2) D2 by an axial planar cleavage (S2) and north-south- to northwest -southeast-trending F2 folds.; and (3) D3 by east-west- to southwest-northeast-trending F3 folds and a poorly developed axial planar cleavage (S3).

Table 4.1: *Structural elements associated with the deformational events within the Gariep Belt, southern Namibia.*

	D1-deformation	**D2-deformation**	**D3-deformation**
Fold-shape	recumbent, intrafolial (F1)	upright to recumbent, open to isoclinal (F2)	upright, open (F3)
Fold-trend	all degrees	N to NW	W to SW
Fold-size (wavelength)	centimetre scale to 2m	centimetre scale to 5 km	centimetre to >3km
Fold-vergence	southerly	commonly to the east, occasionally to the west	commonly no vergence, occasionally to the south
Foliation	Bedding-subparallel (S1)	axial-planar (S2)	axial-planar (S3)
Lineation	clast- and grain-elongation (l1)	Intersection lineation of S1/S2 (l2)	Intersection lineation of S1/S3 (l3)
Lineation-trend	NNW and WSW (after rotation to horizontal)	N to NW	W to SW
Thrust-trend	N to NW	N to NW	no thrusting

4.2 TECTONOSTRATIGRAPHY

Field evidence indicates the presence of major thrust faults within the study area, defining the boundaries of several tectonosedimentary units and juxtaposing various thrust slices. These thrust faults are associated with the D1 and D2 deformational events and will be described in more detail in section 4.3. Each thrust fault is named after adjacent geographic landmarks or, where these are absent, after indigenous animals within the study area. The recognition of thrust faults and time sequence of thrusting will be dealt with in detail in section 4.3.4.

Changes in fabric and fold morphology can occur between the different parautochthonous thrust slices and the basement-floored sequence east of the Rosh Pinah thrust fault (Figs. 2.3 & 2.4). The thrust slices are parautochthonous, whereas the basement-floored unit is autochthonous. The thrust slices are named after the floor thrust fault of each thrust slice. The structural units (Fig. 2.3) comprise: (1) the autochthonous unit in the east of the study area, immediately east of the Rosh Pinah thrust fault and the associated imbricate thrust zone; and to the west, the parautochthonous (2) Dreigratberg thrust slice, (3) Pickelhaube thrust slice, (4) Gumchavib thrust slice, (5) Rooikat thrust slice, (6) Ostrich thrust slice, (7) Obib thrust slice and (8) Gemsbok thrust slice.

The autochthonous and framework parautochthonous units within the study area will be described briefly in this chapter. As most structural fabrics, associated with the various deformational phases, are well developed throughout the study area, only the main structural elements characterizing the different tectonic units, together with the stratigraphy, will be portrayed.

4.2.1 The autochthonous unit

Unconformable sedimentary relationships are recognized between the basement and carbonates of the Pickelhaube Formation, overlying granitic basement east of Namuskluft Farmhouse (Fig. 2.4), as well as sediments of the Numees Formation, overlying the basement unconformably north and NNE of Rosh Pinah (Fig. 2.4; Van Vuuren, 1986). Numees Formation lithologies also overlie the basement at Namuskluft waterhole, approximately 10 km northeast of Rosh Pinah (Fig. 1.2).

Structurally, the autochthonous unit is characterized by NNW-trending reverse faults and small scale to medium scale open F2 folds (<50 m wavelength). Shear zones and the effect of shearing can be observed in the fine-grained units (carbonates and phyllite) at several places near the basement contact.

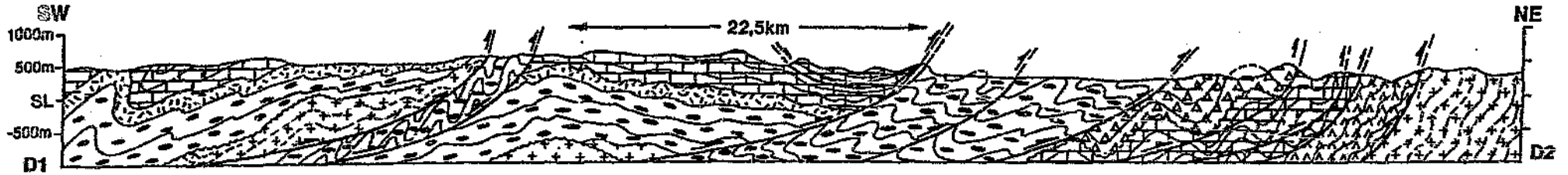
4.2.2 Parautochthonous units

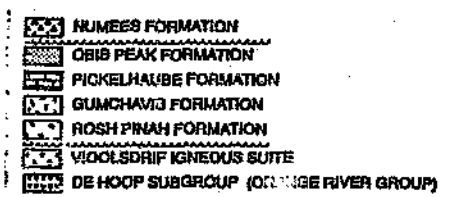
The Dreigratberg thrust slice

The Dreigratberg thrust slice is located in the east of the study area, extending from north of Octha along the basement contact to about 4 km north of Namuskluft Farmhouse (Fig. 2.4). To the east, this thrust slice is bound by an imbricate thrust zone, which is situated immediately east of the basement. This imbricate thrust zone forms the southerly continuation of the Rosh Pinah thrust fault and defines the floor thrust fault of the Dreigratberg thrust slice. The western boundary of this thrust slice is defined by the Sendelingsdrif thrust fault, forming the roof thrust fault of this thrust slice. The floor and the roof thrust faults link with each other north of Namuskluft

Farmhouse, restricting the northerly extension of the Dreigratberg thrust slice. West of the Sendelingsdrif thrust fault, the vergence of F2 folds is generally easterly, whereas to the east of it the folds generally verge in a westerly direction. In a southerly direction, the Dreigratberg thrust slice extends into the Richterveld.

The Dreigratberg thrust slice comprises diamictite and iron formation of the Numees Formation, structurally overlain by a clastic/calcareous succession of the Pickelhaube Formation. The northwest-trending Dreigratberg syncline forms the core of this thrust slice, which also folds the thrusted contact between the Numees Formation and the overlying Pickelhaube Formation lithologies (Figs. 2.4, 4.1 and 4.2C). The Dreigratberg syncline, whose fold limbs dip in an easterly direction and have a wavelength of at least 3 km, has a westerly vergence. The fold hinge plunges at a shallow angle in a southerly direction, explaining the pinching-out of the Pickelhaube lithologies towards the north. A prominent imbricate zone with steeply, generally west-dipping faults (65 to 89 degrees) is situated to the east of the Dreigratberg syncline, near the thrust contact with the autochthonous unit (Figs. 2.4, 4.1, 4.2 and 4.3). Field evidence shows that these thrust planes are overturned in the vicinity of the highly competent basement and underwent a south-southeasterly-and easterly-directed thrust movement. The various thrust slices within this imbricate zone are each uniform in their lithological composition comprising either sandstones and conglomerates of the Rosh Pinah Formation, massive carbonates of the Pickelhaube Formation, pisolitic carbonates of the Pickelhaube Formation, or massive diamictite of the Numees Formation. Towards the north, in an area ranging from southeast to northeast of Namuskluft Farmhouse, the Dreigratberg thrust slice comprises massive diamictite of the Numees Formation and carbonate and calcareous conglomerate of the


SW
NE
1000m
500m
SL
-500m
D1
22,5km
D2


NUMEES FORMATION
OBIB PEAK FORMATION
PICKELHAUBE FORMATION
GUMCHAVIB FORMATION
ROSH PINAH FORMATION
VIOOLSDRIF IGNEOUS SUITE
DE HOOP SUBGROUP (OI GE RIVER GROUP)

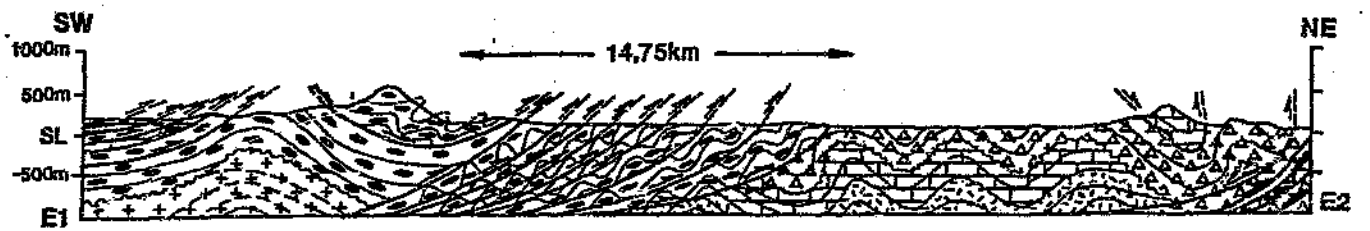

SW
NE
1000m
500m
SL
-500m
E1
14,75km
E2

Fig. 4.1: *(opposite page); A) Structural SW to NE cross-section D1-D2 cutting through parts of the Obib thrust slice south of Obib Peak in the SW, and parts of the Ostrich, Rooikat, Pickelhaube, Gemsbok, and Dreigratberg thrust slices, as well as the parautochthonous zone in the NE.*
B) Structural SW to NE cross-section E1-E2, cutting through the Ostrich thrust slice approximately 8 km S of Gumchavib in the SW, and parts of the Gumchavib, Gemsbok, and Dreigratberg thrust slices, as well as the parautochtonous zone in the NE.
Position of cross-sections is shown in Fig. 2.4.

Pickelhaube Formation. At the easternmost exposure the carbonates of the Pickelhaube Formation have a thrusted contact with the autochthonous unit (Figs. 2.4 and 4.2B). Towards the east an F2 synclinal box fold measuring about 100 m from one fold limb to the other, with a steeply westerly dipping axial plane, folds the sediments of the Pickelhaube Formation. East of this syncline the basement and the lithologies dip towards the west. About 1,5 km northeast of Namuskluft Farmhouse, 5 m thick granitic basement, overlain by Pickelhaube carbonate, is thrust over a thick succession of similar Pickelhaube lithologies, thus emphasizing the parautochthonous nature of this thrust slice.

Structural cross sections (Figs. 4.1, 4.2 and 4.3) taken along the Dreigratberg thrust slice (Fig. 2.4) show how the several imbricate thrust slices pinch out laterally. The only continuous thrust fault within the imbricate thrust zone, which does not splay, is the westernmost thrust fault, juxtaposing the Numees diamictite and the imbricate thrust slices (Figs. 2.4, 4.1, 4.2 and 4.3). Stereonet projections of structural data from the Dreigratberg thrust slice are shown in Fig. 4.4, showing the random dispersion of D1-related structural features, the north to northwesterly trend of F2 folds. Stereonet data in Fig. 4.4 also portray a generally westerly dip of S2 and D2 axial planes, as well as an occasional dip of S2 and D2 axial planes towards the east, caused by backfolding. F3 folds trend in a northeast-southwesterly direction with associated axial planes

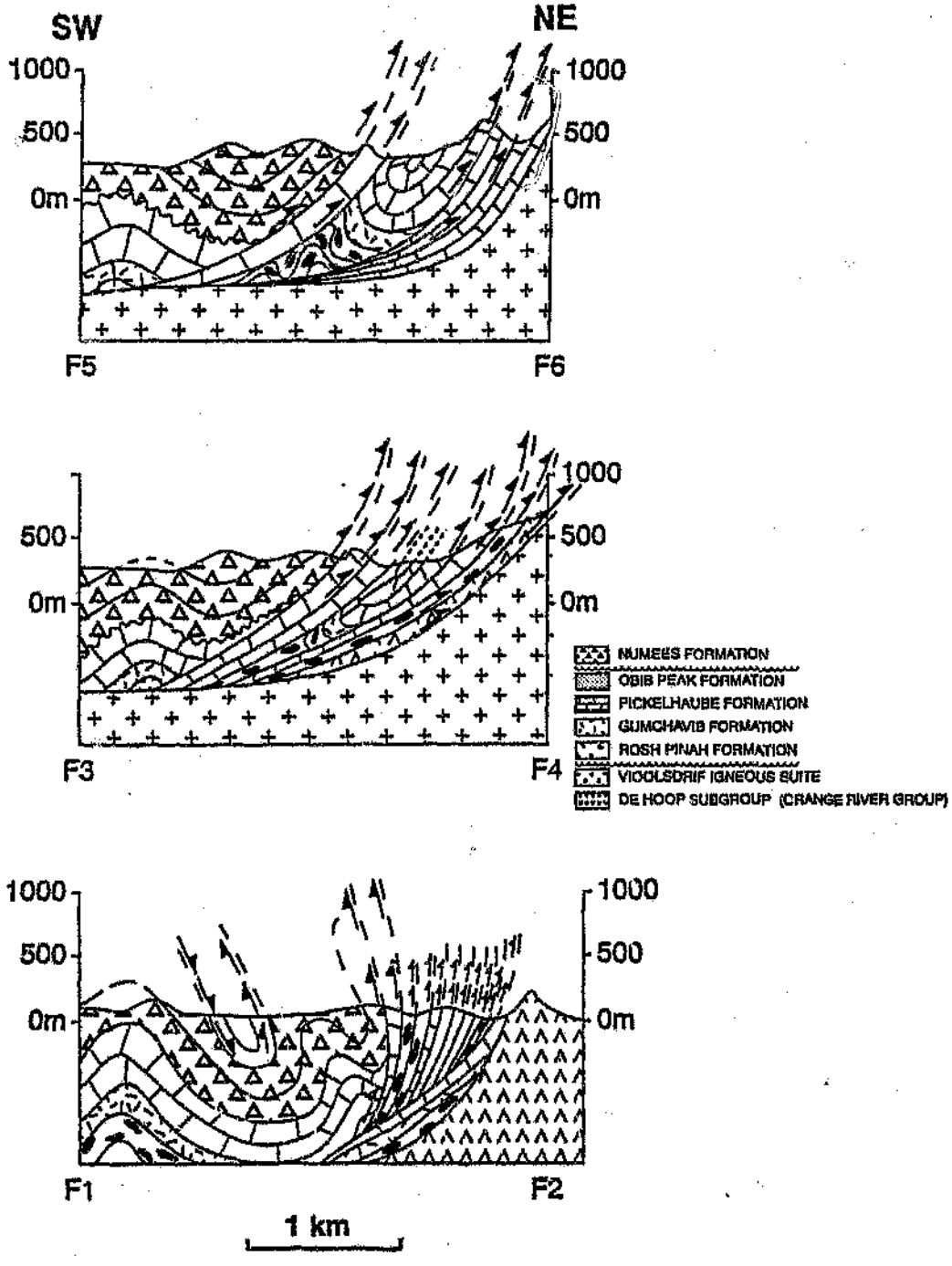


Fig. 4.2: *Structural SW to NE cross-sections A) F5-F6; B) F3-F4; and C) F5-F6, situated within the imbricate zone in the east of the Dreigratberg thrust slice. Positions of cross-sections are shown in Fig. 2.4.*

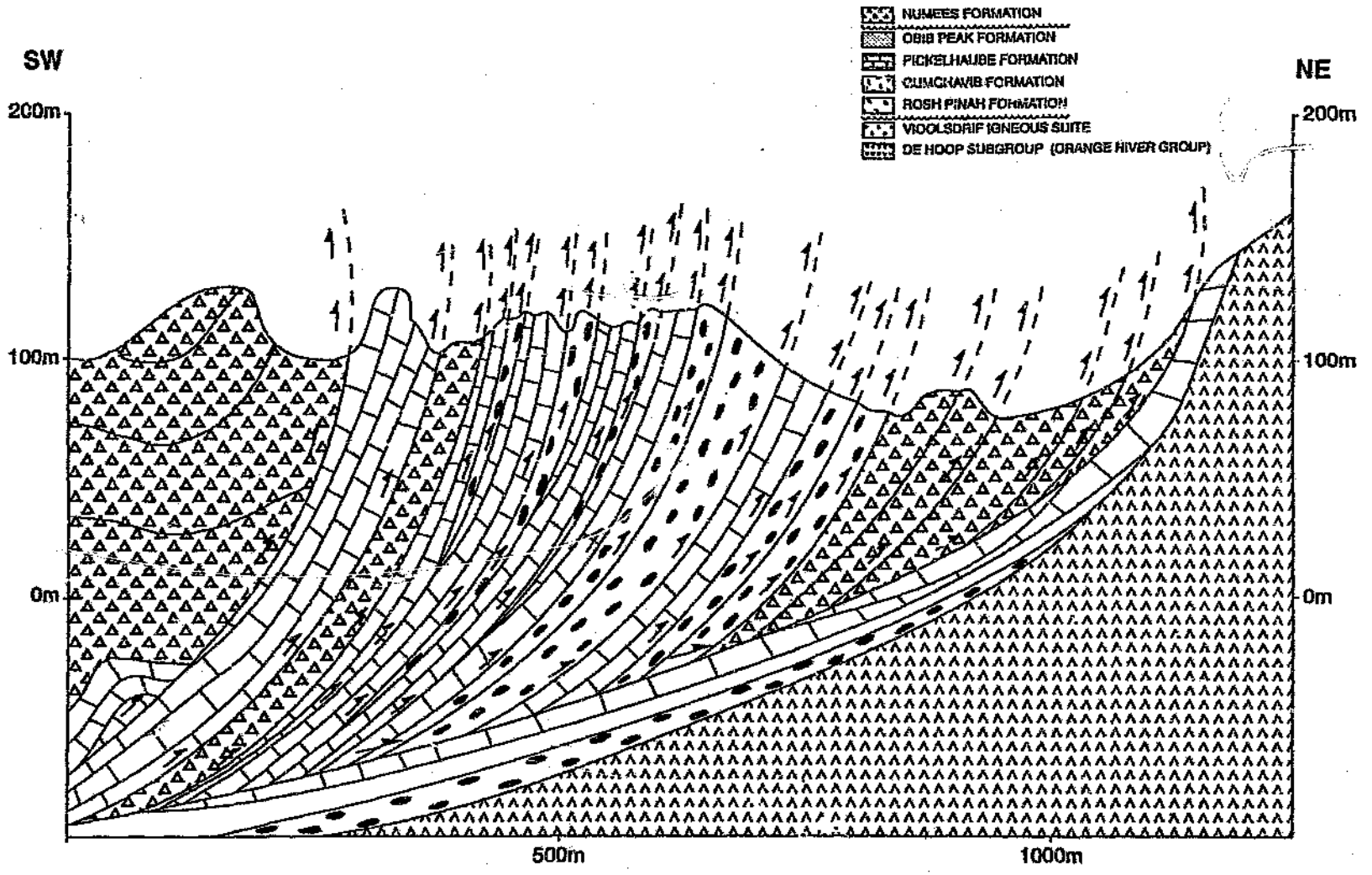

NUMEES FORMATION
OBIB PEAK FORMATION
PICKELHAUBE FORMATION
CLIMCHAMB FORMATION
ROSH PINAH FORMATION
VIOOLSDRIF IGNEOUS SUITE
DE HOOP SUBGROUP (ORANGE RIVER GROUP)
SW
NE
200m
100m
0m
200m
100m
0m
500m
1000m

Fig. 4.3: *opposite page; Structural SW to NE cross-section H1-H2 situated within the imbricate zone in the east of the Dreigratberg thrust slice about 4 km north of Dreigratberg. Positions of cross-section is shown in Fig. 2.4.*

occasionally dipping gently towards the southwest.

A later, Phanerozoic tectonic phase, which has affected the area, is indicated by the presence of two NNW-trending dolerite dykes of Karoo age, which cut through the sediments of the Numees Formation along the eastern limb of the Dreigratberg syncline.

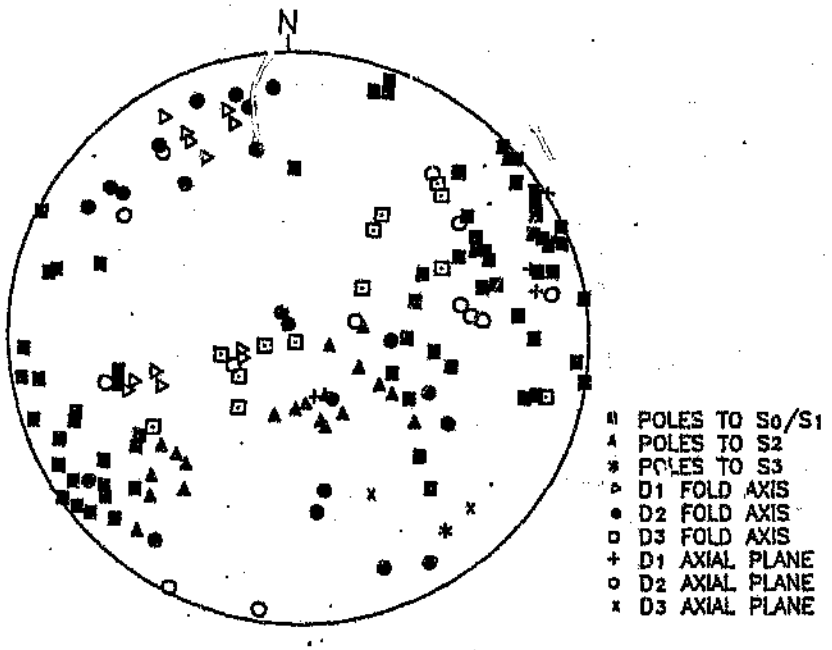


Fig. 4.4: *Stereonet projections of structural data for the Dreigratberg thrust slice.*

The Rosh Pinah thrust slice

The Rosh Pinah thrust slice is located about 5 km northwest of the Dreigratberg thrust slice. The Rosh Pinah thrust fault forms the floor thrust fault of this thrust slice defining the eastern boundary of this tectonostratigraphic unit, whereas the Aus road thrust

fault forms the roof thrust fault and defines its western extensions (Figs. 2.3 and 2.4). The Rosh Pinah thrust slice extends from south of Rosh Pinah Mountain to northwest of Spitskop Farm, which is situated approximately 15 km north of Rosh Pinah (Fig. 1.2). West of the Aus road thrust fault, F2 folds generally verge in an easterly direction, whereas east of it, the fold vergence is directed towards the west.

At Spitzkop Farm, the Rosh Pinah thrust slice comprises a mixed succession of volcanic and sedimentary rocks of the Rosh Pinah Formation (Page and Watson, 1976; Watson, 1980; Davies and Coward, 1982; Van Vuuren, 1986; De Kock, 1987; Siegfried, 1990 and Lickfold, 1991). In the Rosh Pinah area, the Rosh Pinah thrust slice consists of a mixed conglomerate/arkosic sandstone/mudstone/carbonate succession and bimodal volcanics of the Rosh Pinah Formation associated with a massive Zn-Pb-Cu-Ag-(+Ba) sulphide mineralization. The contact between the basement and the volcanics with the sediments of the Rosh Pinah Formation and the Numees Formation north and northwest of Rosh Pinah is thrusted. In the Rosh Pinah area, large scale northwest-trending open F2 backfolds are recognized with axial planes dipping in a north-easterly direction (Figs. 2.4 and 4.5). Southwest trending F3 folds (Fig. 4.6), deforming earlier structures, were described by Siegfried (1990). Thrust faults, trending in a northwesterly direction with northeasterly dipping thrust planes, were recognized. The northeasterly dip of the thrust fault planes is related to overturning of thrust faults in the immediate vicinity of the highly competent basement. Stereonet projections of structural data from the Rosh Pinah thrust slice are shown in Fig. 4.6, showing a wide dispersion of F2 fold axes from generally SSE to east within the Rosh Pinah thrust slice, as well as a random dispersion of S0/S1 at all bearings. F3 folds have a westerly trend and only occasionally display a southerly vergence.

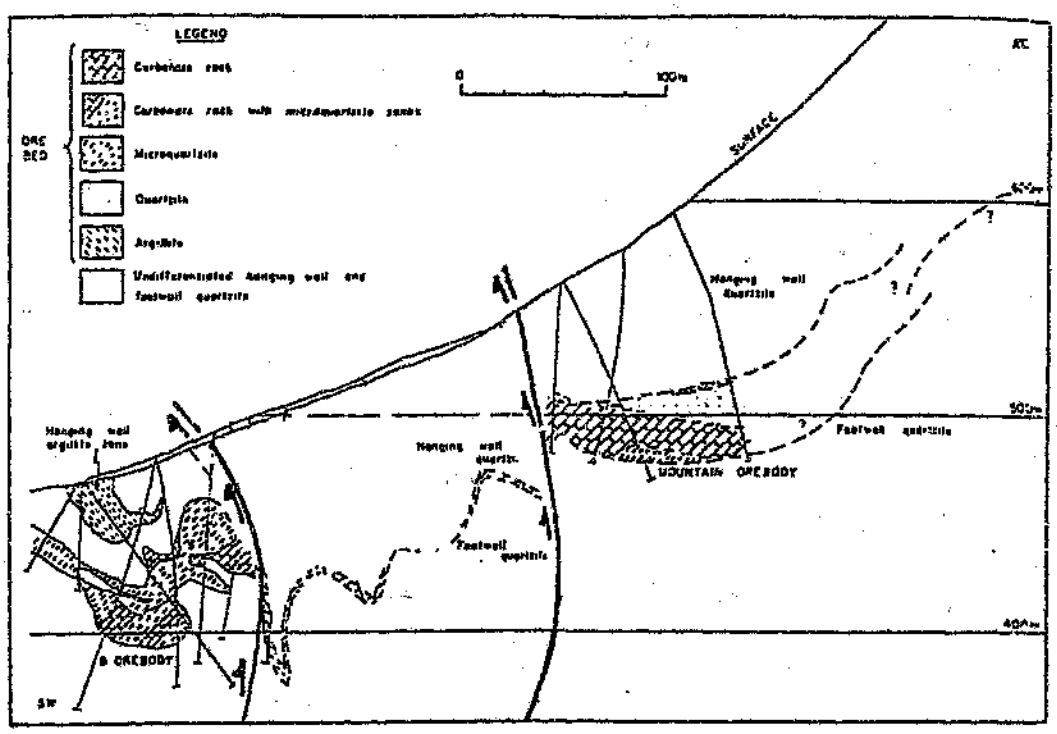


Fig. 4.5: *Structural profile G1-G2 through parts of the Rosh Pinah thrust slice (modified after Van Vuuren, 1986). Position of cross-section is shown in Fig. 2.4.*

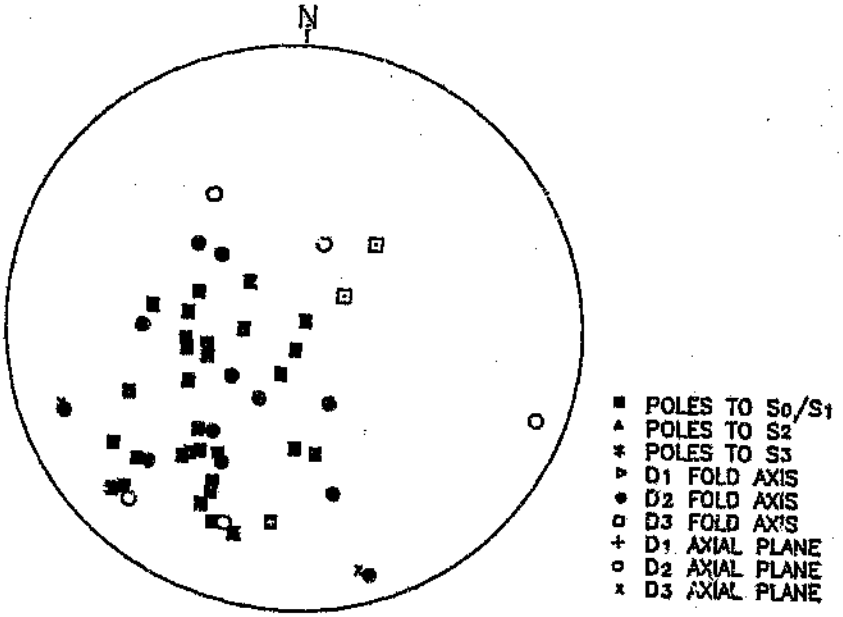


Fig. 4.6: *Stereonet projections of structural data for the Rosh Pinah thrust slice.*

A later, phanerozoic tectonic phase, which has affected the area, is also indicated within the Rosh Pinah thrust slice by the presence of a northwest-trending Karoo dolerite dyke, which links with the dolerite dykes in the Dreigratberg thrust slice, cutting through rocks of the Rosh Pinah Formation at Rosh Pinah Mountain. This dolerite dyke can be followed to Trekpoort Farm, situated approximately 25 km northwest of Rosh Pinah (Figs. 1.2 and 2.4).

The Pickelhaube thrust slice

The Aus Road thrust fault, which changes its trend from northwest in the area north of Rosh Pinah to NNW south of Rosh Pinah, separates the Rosh Pinah thrust slice to the east from the Pickelhaube thrust slice to the west (Fig. 2.3), forming the floor thrust fault and eastern boundary of this tectonostratigraphic unit. The Rooikat thrust fault forms the roof thrust fault, which defines the western boundary of the Pickelhaube thrust slice, linking with the Ostrich thrust fault further south (Fig. 2.3). Along the Aus Road thrust fault the dip of axial planes of F2 folds changes drastically from a generally easterly direction west of the thrust fault to a westerly direction east of it.

Lithologically, the Pickelhaube thrust slice comprises calcareous quartzitic sandstones, laminated carbonates and graphitic black shale of the Pickelhaube Formation.

The Aus Road thrust fault links with the Sendelingsdrif thrust fault about 7 km north of the Orange River, where it was delineated by Von Veh (1988) in the Richtersveld. South of Rosh Pinah, the Pickelhaube thrust slice and the continuation of the Gemsbok thrust slice are juxtaposed along northwest- to NNW-trending thrust faults with steep westerly dipping fault planes, and in some cases overturned fault planes. The most prominent fold structure is the northerly continuation of the F2 Annisfontein

anticlinorium, delineated by Von Veh (1988) in the Richtersveld, which folds pre-existing D1 fabrics and thrust planes. The F2 folds in this area trend NNW to northwest and range from small to large scale (> 200 m). They are open and upright folds and verge towards the east. Pickelhaube trigonometrical beacon (Fig. 2.4) is situated in the centre of a conspicuous thrust slice, which consists of carbonates and calcareous quartzitic sandstones of the Pickelhaube Formation and in turn is thrusted over

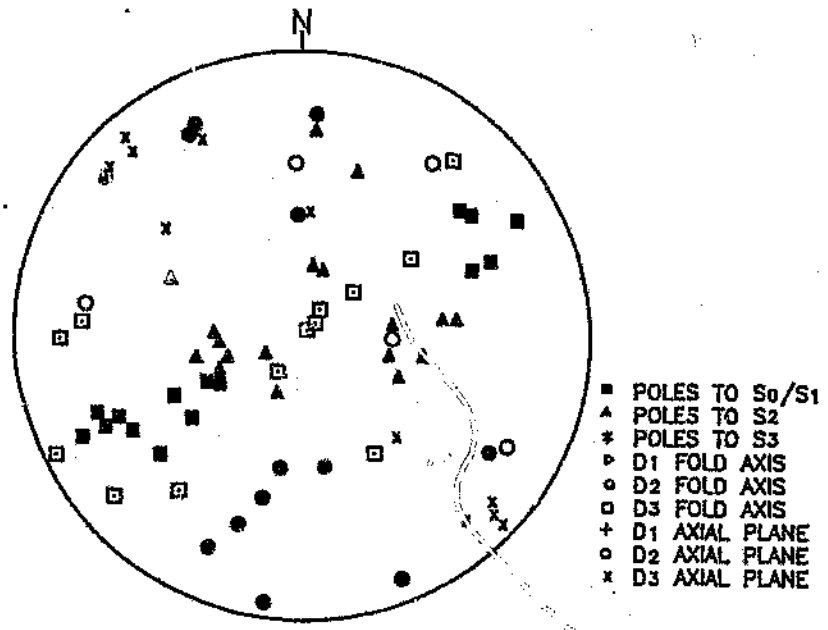


Fig. 4.7: *Stereonet projections of structural data for the Pickelhaube thrust slice.*

carbonates of the Pickelhaube Formation and conglomerates and sandstones of the Rosh Pinah Formation (Fig. 4.1A). North of Pickelhaube, at localities 9 and 19 (Fig. 2.4), carbonates of the Pickelhaube Formation are duplicated by steep easterly dipping, overturned thrust faults. Stereonet projections of structural data from the Pickelhaube thrust slice are shown in Fig. 4.7, showing the north-northeasterly to

northwesterly trend of F2 folds and associated westerly to easterly dipping axial planes and S2 cleavages. F3 fold trends range from west to southwest and associated D3 axial planes dip steeply in northerly and southerly directions.

The Gemsbok thrust slice

The Gemsbok thrust slice can be traced from the Orange River in the south of the study area to about 5 km southeast of Rosh Pinah in the north (Fig. 2.3). The Aus road thrust fault and an associated conspicuous imbricate zone, as well as the Sendelingsdrif thrust fault immediately north of the Orange River form the floor thrust fault in the east of the Gemsbok thrust slice. The roof thrust fault in the north of this thrust slice is defined by thrust faults, thrusting the Pickelhaube thrust slice over the Gemsbok thrust slice (Figs. 2.3, 2.4 and 4.1A). The western boundary of the Gemsbok thrust slice in the area south of Pickelhaube is marked by the Gumchavib thrust fault, which can be traced southwards into the Richtersveld, where it was delineated by Von Veh (1988), and northwards to Gumchchavib Mountain and southwest of Pickelhaube (Fig. 2.3 and 2.4).

Lithologically, the Gemsbok thrust slice consists of conglomerates, arkosic sandstones, and mudstones of the Rosh Pinah Formation. At locality 8, recumbent F2 folds with wavelengths of 100 to 200 m and an easterly vergence are present just east of the imbricate thrust zone associated with the Aus road and the Sendelingsdrif thrust faults. Within the different thrust sheets of this imbricate thrust zone, asymmetric folds, climbing up steepening thrust faults and therefore changing their vergence from a generally easterly to a westerly vergence, are present (Fig. 4.8). These folds are referred to as "backfolds" in this study. Near locality 23, NNW of Gumchavib, two small

thrust slices, the one comprising laminated carbonates of the Pickelhaube Formation and the other consisting of diamictite of the Numees Formation, are thrust over conglomerates, sandstones and mudstones of the Rosh Pinah Formation. At locality 7, large scale overturned to recumbent isoclinal F2 folds with wavelengths of over 100 m are situated immediately west of the imbricate thrust zone in the east of Pickelhaube trigonometrical beacon (Figs. 4.1B and 4.9). Large scale (>200 m) box folds are developed about 2 km NNW of Pickelhaube and southwest of Pickelhaube small scale chevron folds and medium to large scale (< 200 m) folds were recognized. In the vicinity of listric thrust faults, the F2 folds change their vergence from an easterly to a westerly direction due to backfolding (Figs. 4.1A and 4.1B).

Stereonet projections of structural data from the Gemsbok thrust slice are shown in Fig. 4.10 and show a generally north-northwesterly trend of F2 folds and a westerly and easterly vergence of associated D2 axial planes and S2 foliations. The trend of F3

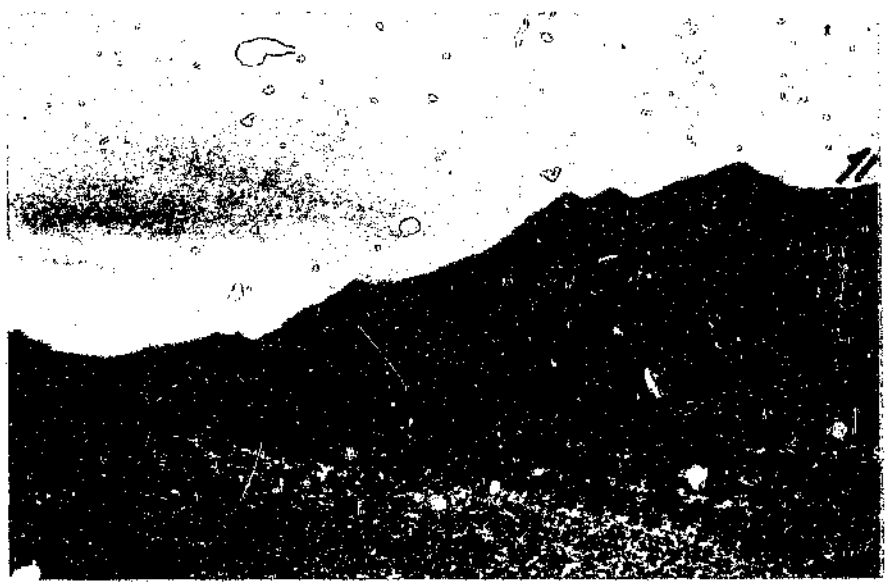


Fig. 4.8: *F2 backfolds within the imbricate thrust zone immediately south of Pickelhaube at locality 7 (Fig. 2.4), showing the change from an easterly to a westerly vergence caused by backfolding.*

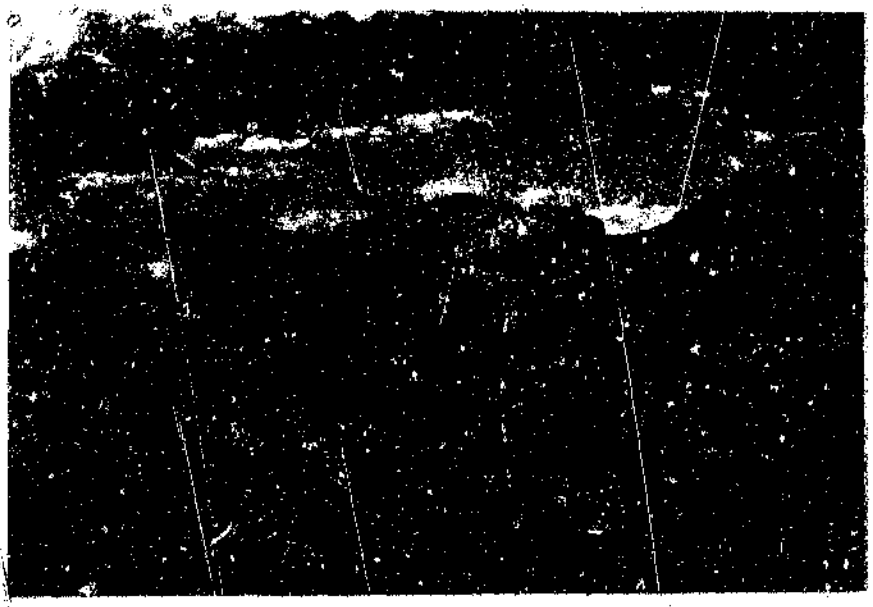


Fig. 4.9: *Large scale isoclinal overturned to recumbent F2 fold within the imbricate thrust zone west of Pickelhaube, at locality 7, south of Pickelhaube (Fig. 2.4).*

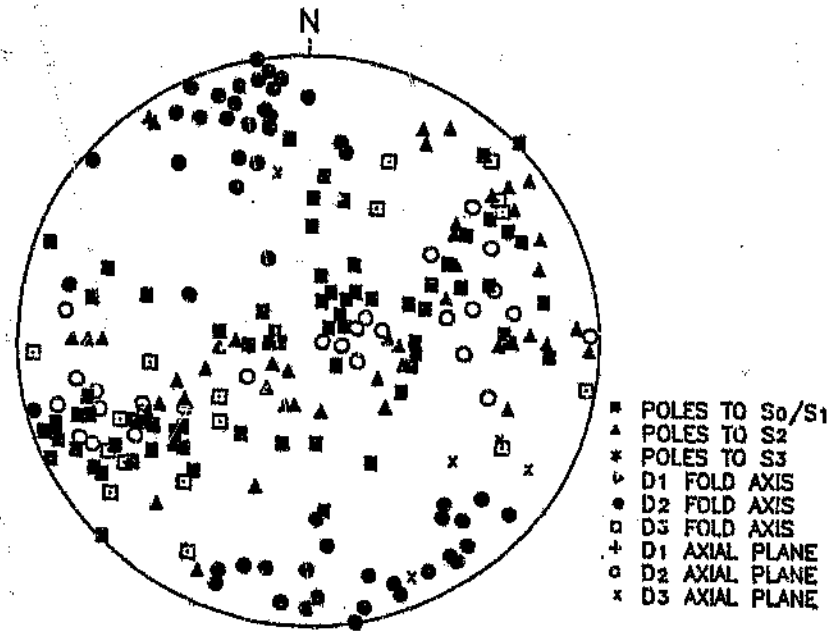


Fig. 4.10: *Stereonet projections of structrural data for the Gemsbok thrust slice.*

folds ranges from ESE to southwest, with associated axial planes only occasionally verging in a generally southerly direction. S0/S1 strikes on all bearings, due to the later deformation by the D2 and D3 deformational events.

The Gumchavib thrust slice

The Gumchavib thrust slice stretches from north of the Orange River to northwest of Gumchavib Mountain. In the east it is bounded by the Gumchavib thrust fault. The roof thrust fault to the west of this thrust slice is defined by a northwest-trending thrust fault, which splays the Ostrich thrust fault into the Gumchavib thrust fault and the southerly continuation of the Ostrich thrust fault about 3 km northwest of Gumchavib Mountain (Figs. 2.3 and 2.4). The Gumchavib thrust slice comprises a mixed succession of conglomerates, sandstones, mudstones and isolated carbonate beds of the Rosh Pinah Formation, as well as carbonates and calcareous sandstones of the Pickelhaube Formation. Immediately south of Gumchavib trigonometrical beacon carbonates and calcareous quartzite are interbedded within the Rosh Pinah Formation.

The most conspicuous structural feature within this thrust slice is the northwest-trending continuation of the Annisfontein anticlinorium, which was delineated by Von Veh (1988) in the northwestern Richtersveld (Figs 2.4 and 4.1B). West of the central parts of the thrust slice, sediments of the Rosh Pinah Formation are juxtaposed to each other along the a northwest-trending roof thrust fault of the Gumchavib thrust slice (Figs 2.3, 2.4 and 4.1B).

Stereonet projections of structural data from the Gumchavib thrust slice are shown in Fig. 4.11 and display a similar pattern of distribution of structural elements associated with the D1, D2 and D3 deformational phases as within the Gemsbok thrust slice.

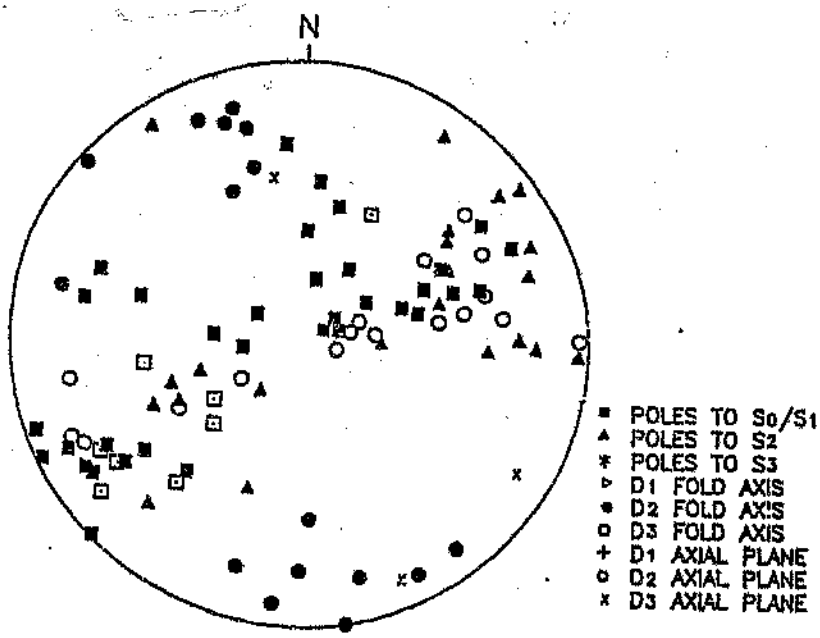


Fig. 4.11: *Stereonet projections of structural data for the Gumchavib thrust slice.*

The Ostrich thrust slice

The Ostrich thrust slice changes its trend from northwest in the south to a northerly trend north of the area situated about 3 km northeast of Obib Peak. It can be traced from the Orange River in the south of the study area to the area northeast of Obib waterhole (Fig. 2.3). In the northern parts of the Ostrich thrust slice a northerly trending thrust fault, named Ostrich thrust fault, juxtaposes the Ostrich and Rooikat thrust slices and defines the floor thrust fault of this tectonic unit. About 3 km southeast of Obib Peak, the Ostrich thrust fault continues in a southeasterly direction, where it thrusts granitic basement over sandstones and conglomerates of the Rosh Pinah Formation (Fig. 2.4). The Ostrich thrust fault can be followed further to the southeast, where it links with an imbricate thrust zone west of locality 1, immediately north of the Orange River. The roof thrust fault in the west of this thrust slice is

delineated by the Obib thrust fault and the Obib dunes, which conceal the geology of this thrust slice further south.

Lithologically the Ostrich thrust slice cosists of a thick succession of conglomerates, arkosic and quartzitic sandstones, mudstones and carbonates of the Rosh Pinah and Gumchavib Formations, and carbonates, calcareous sandstones and conglomerates of the Pickelhaube Formation. In the central parts of the thrust slice, in a south-westerly direction perpendicular to strike, carbonates of the Pickelhaube Formation are abundant. Several tens of metres thick basic sills of the Gannakourlep dyke and sill swarm, which also underwent metamorphism of the upper greenschist facies, are interbedded with the sediments of the Gumchavib Formation (Fig. 2.4). A mixed succession of arkosic sandstones, mudstones and carbonates unconformably overly the granitic basement northwest of Gumchavib Mountain (Fig. 2.4). The granitic basement structurally overlies sediments of the Rosh Pinah Formation along a thrust fault and thus emphasizes the parautochthonous nature of this thrust slice. The beds within this thrust slice change their strike from north in the northern parts of the thrust slice to northwest further south and dip in a westerly and southwesterly direction. Minor small to medium scale F2 folds are present throughout the thrust slice. At locality 6 (Fig. 2.4) and south of it, a large scale (approximately 200 m wavelength), isoclinal and overturned F2 fold is exposed (Fig. 4.12C), folding sediments of the Gumchavib Formation.

The fold hinges of the F2 folds plunge gently (< 10 degrees) in various directions due to the refolding of the fold hinges by the D3 deformational event. Immediately north of the Orange River the Ostrich thrust slice is characterized by an imbricate thrust zone (Fig. 4.2B). The thrust slices within this imbricate thrust zone consist of

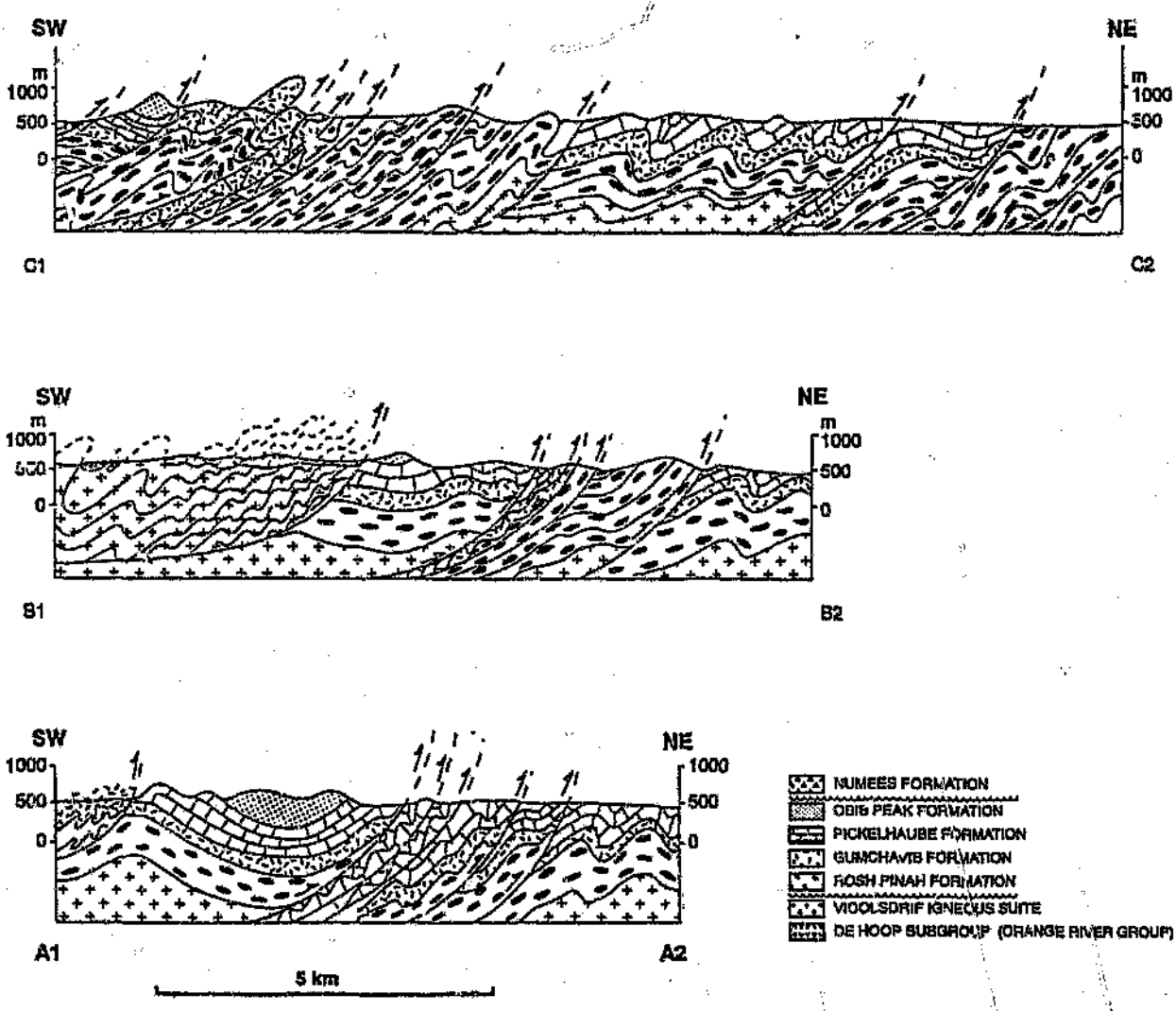


Fig. 4.12: *A) Structural SW to NE cross-sections A1-A2 through parts of the Obib and Pickelhaube thrust slices.*
B) Structural SW to NE cross-section B1-B2 through parts of the Obib, Ostrich, Rooikat, and Pickelhaube thrust slices.
C) Structural SW to NE cross-section C1-C2 through parts of the Obib, Ostrich, Rooikat, Pickelhaube, and Gemsbok thrust slices. Position of cross-sections are shown in Fig. 2.4.

arkosic sandstones of the Rosh Pinah Formation, carbonates of the Pickelhaube Formation, diamictite of the Numees Formation and carbonate of the Pickelhaube Formation. The Numees Formation sediments, which overlie carbonates of the Pickelhaube Formation, form the southernmost outcrop of Numees diamictite in southern Namibia. Stereonet projections of structural data showing from the Ostrich

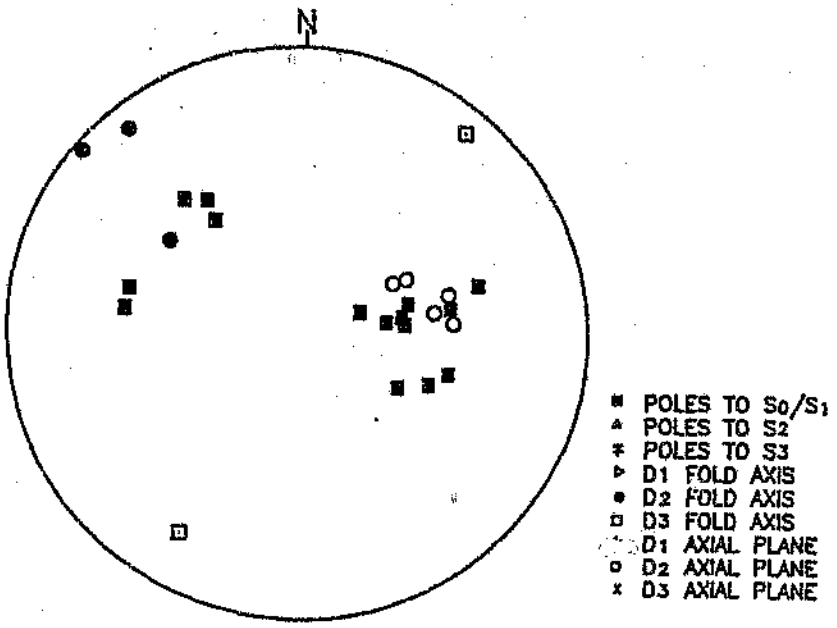


Fig. 4.13: *Stereonet projections of structural data for the Ostrich thrust slice.*

thrust slice are shown in Fig. 4.13, displaying a northwesterly trend of F2 folds and associated easterly verging axial planes. F3 folds, though scarce, show a southeasterly trend and do not display any vergence of associated axial planes.

The Rooikat thrust slice

The boundaries of the Rooikat thrust slice are defined by the Rooikat thrust fault in the east of this tectonic unit, which forms the floor thrust fault, juxtaposing the Rooikat and Pickelhaube thrust slices, and by the Ostrich thrust slice in the west, delineating the roof thrust fault of this tectono-stratigraphic unit (Fig. 2.3).

The Rooikat thrust slice comprises an approximately 1000 m thick succession of arkosic sandstone, mudstone, carbonates, basic volcanics and minor acid volcanics associated with mineralized gossans and collectively constitutes the Rosh Pinah Formation. The Rosh Pinah Formation is duplicated by a NNW-trending thrust fault,

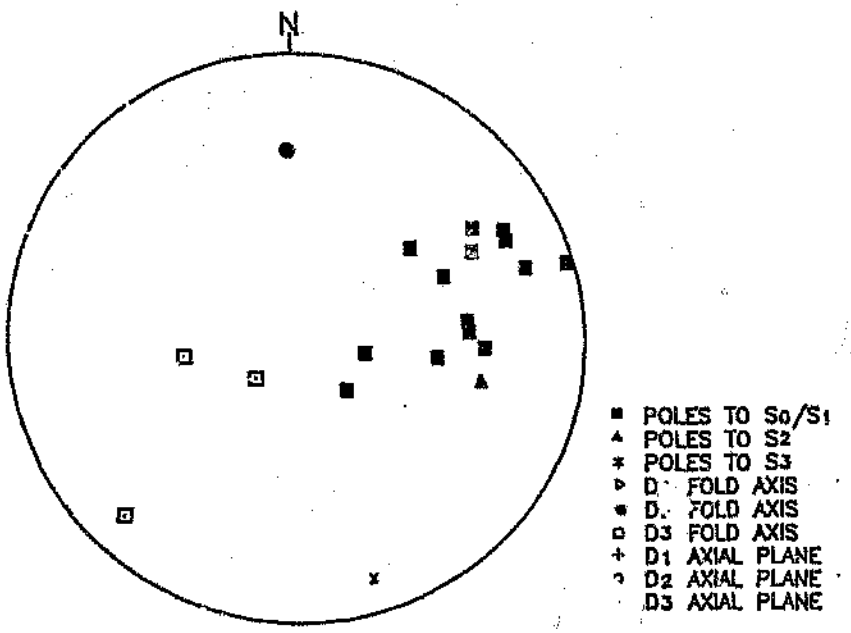


Fig. 4.14: *Stereonet projections of structural data for the Rooikat thrust slice.*

which splays from the Ostrich thrust fault (Figs. 2.4 and 4.12C). Towards the top of the succession several limestone beds are interbedded with ir · osic sandstone. Up to 30 m thick amphibolite sills of the Gannakouriep dyke and sill swarm have been intruded into the sediments of the Rosh Pinah Formation in the northern parts of the Rooikat thrust slice (Fig. 2.4). Bedding generally strikes NNW and dips to the west, but is folded in the south of the Rooikat thrust slice (Fig. 4.12C and 4.2A). Small to medium scale (1 to 10 m), open asymmetric folds trending NNW with axial planes dipping to the WSW are observed in some places (Fig. 4.12C). Approximately 1 km west of the Rooikat thrust fault, a large scale, tight and east-vergent F2 fold with a wavelength of about 100 m is displayed (Fig. 4.12C). Stereonet projections of structural data from the Rooikat thrust slice are shown in Fig. 4.14. The scarce F2 folds trend in a northerly direction and display a easterly vergence. F3 folds are generally upright and occasionally south vergent with the trend of fold axes ranging

from west to southwest. Bedding (S0) and bedding-subparallel S1 foliation dip to west to southwest (Fig. 4.14).

The Obib thrust slice

The floor thrust fault to the east of the Obib thrust slice is defined by the Obib thrust fault, which strikes north immediately east of Obib Peak, and which changes its strike to northwest about 6 km northeast of Obib waterhole where it links with the Ostrich thrust fault.

Around Obib waterhole and towards Obib Peak, the Obib thrust slice comprises interbedded quartzarenites and mudstones of the Gumchavib Formation, which are thrust over carbonates of the Pickelhaube Formation along a northwest striking thrust fault north of Obib waterhole. This thrust fault links with the Obib thrust fault about 4 km east of Obib waterhole. The Pickelhaube carbonates are overlain by arkosic sandstones and conglomerates of the Obib Peak Formation. The westernmost granitic outcrop near Obib waterhole is overlain by intensely sheared basal conglomerate of the Rosh Pinah Formation and interbedded quartzarenites and mudstones of the Gumchavib Formation in the west. Towards the east, the contact of Rosh Pinah and Gumchavib Formation beds and the granitic basement is intensely folded by isoclinal overturned F2 folds with wavelengths of several tens of metres. F2 folds with wavelengths of up to 150 m change their easterly vergence to a westerly vergence due to backfolding in the vicinity of a northwest-striking thrust fault, situated about 2 km northeast of Obib waterhole. This thrust fault juxtaposes the quartz arenites and mudstones of the Gumchavib Formation and the carbonates of the Pickelhaube Formation. At Obib Peak, arkosic sandstones and conglomerates of the Obib Peak

Formation are thrusted over sandstones and mudstones of the Gumchavib Formation. The westernmost Numees Formation diamictites crop out about 3 km south of Obib Peak, where they reveal thrusted contacts with carbonates of the Pickelhaube Formation and arkosic sandstones of the Obib Peak Formation. Structural cross-sections through parts of the Obib thrust slice are presented in Figs. 4.1A , 4.12A,

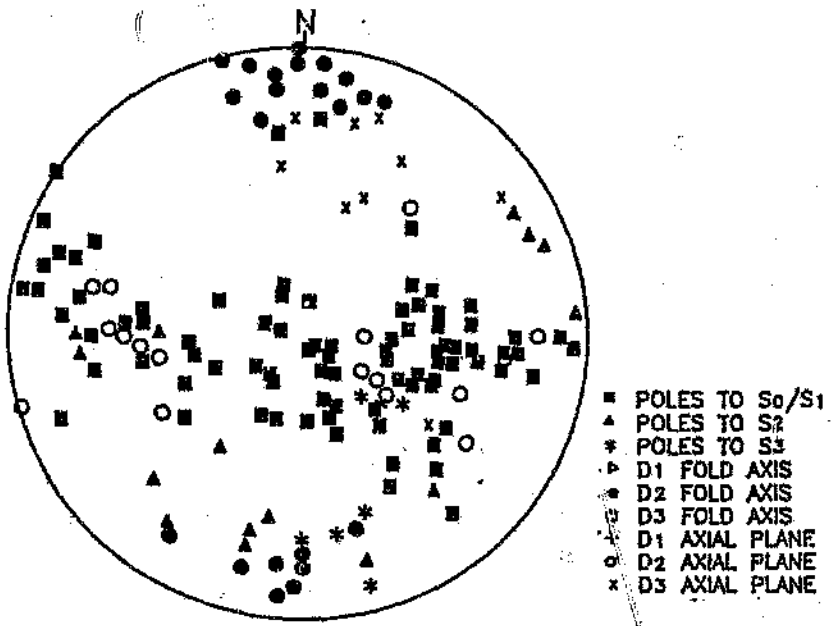


Fig. 4.15: *Stereonet projections of structural data for the Obib thrust slice.*

4.12B and 4.12C. Stereonet projections of structural data from the Ostrich thrust slice are shown in Fig. 4.15. The trend of F2 fold axes ranges from north to northwest. The D2 axial planes generally verge towards the east to northeast, but can also verge in the opposite directions due to backfolding. The trend of F3 folds within this thrust slice ranges from west to southwest and axial planes and the associated axial planar cleavage (S3) occasionally verge in a southerly direction. S0/S1 has been deformed by the D2 and D3 deformational events, as displayed by the distribution of the poles to S0/S1.

4.3 TIME SEQUENCE OF DEFORMATIONAL EVENTS

Three phases of deformation, D1, D2, D3, have been identified within the study area. The most conspicuous structural elements developed throughout are associated with D2, which therefore serves as a structural datum or benchmark. The relationships and the occurrences of planar and linear elements and folds within the study area are plotted on stereonets and described in the following sections. The deformation phases are described in their deduced chronological order.

4.3.1 D1 phase of deformation

The most important feature associated with the earliest recognized D1 deformational event are F1 folds. They are typically small scale (1 cm to 2 m wavelength), recumbent and isoclinal in form, and intrafolial with respect to the sedimentary bedding and a bedding-subparallel cleavage. The F1 folds are best developed in the laminated carbonates of the Pickelhaube Formation (Fig. 4.16).

A bedding-subparallel to -parallel D1 fabric (S1), which is dispersed by subsequent deformations to strike on all bearings and dips variably, has a highly variable strike and dip (Fig. 4.17A) and is well-developed throughout the study area. In mica schist and siltstones the S1 fabric is characterized by a penetrative slaty cleavage, associated with the growth of mica, and is developed subparallel to parallel to bedding planes (Fig. 4.18). In coarser sediments, the D1 deformation is characterized by the preferred orientation and elongation of boulders, pebbles and grains, whose long axes plunge by variable amounts, defining the L1 stretching lineation (Fig. 4.19). The preferred orientation of clasts is best developed within conglomerates of the Rosh Pinah Formation (Fig. 4.20) and in pisolitic limestone of the Pickelhaube Formation (Fig.

3.38).

Associated with the D1 deformational event are bedding-subparallel D1 thrust faults, which are closely associated with F1 folds and the S1 foliation and cleavage. These

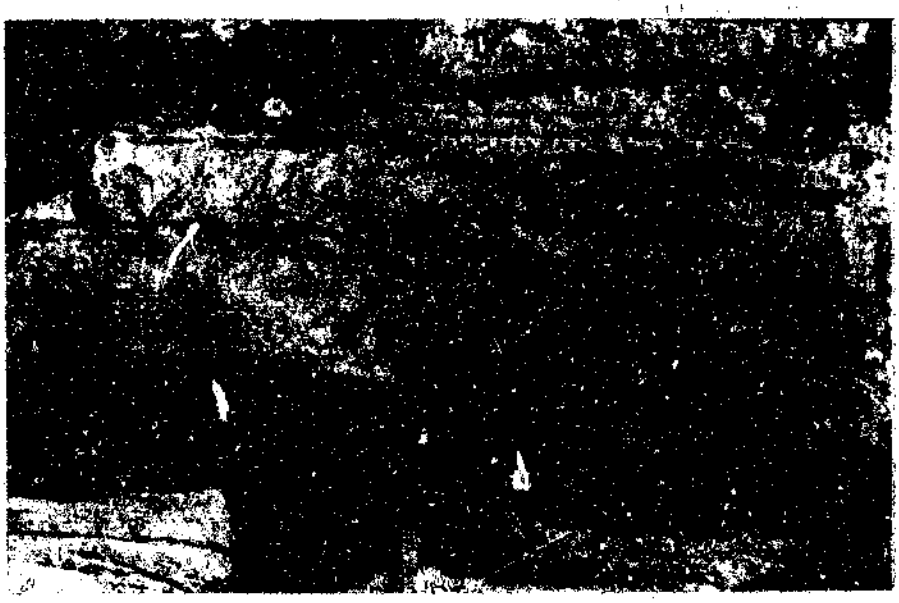


Fig. 4.16: *Intrafolial, southerly verging F1 folds within dolomitic carbonate at locality 13A, approximately 5 km southeast of Namuskluft Farmhouse (Fig. 2.4).*

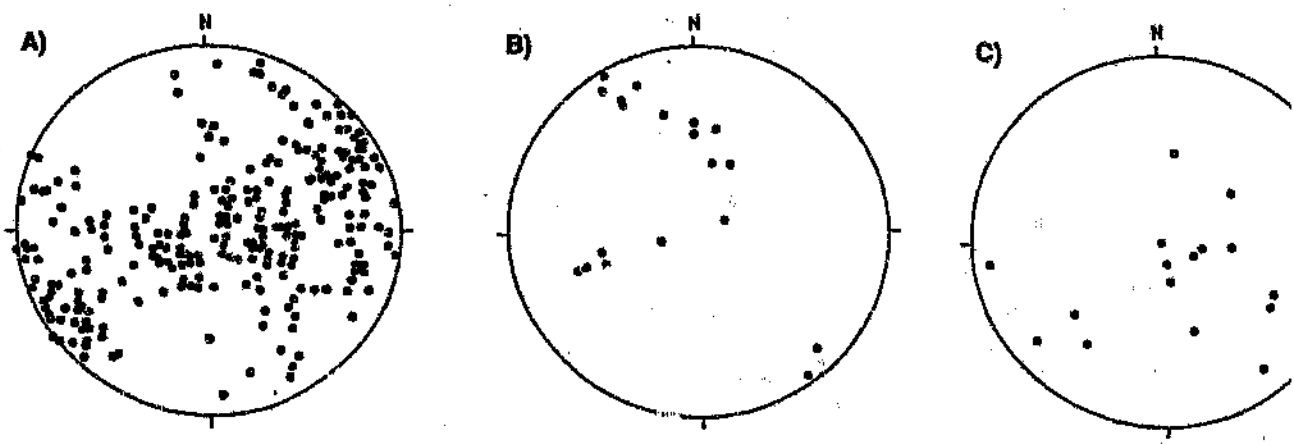


Fig. 4.17: *Stereonet projections of data associated with D1 throughout the study area; A) poles to S0/S1; B) F1 fold axes; C) poles to F1 axial planes.*



Fig. 4.18: *Bedding subparallel penetrative S1 cleavage developed within mudstones of the Rosh Pinah Formation south of Pickelhaube (Fig. 2.4).*

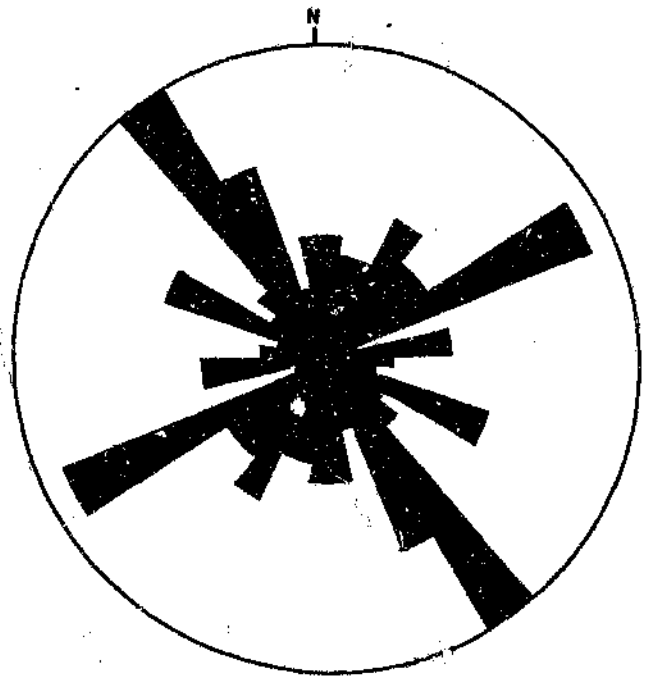


Fig. 4.19: *Rose diagram showing the main trend elongation of clasts of the Rosh Pinah Formation and pisoliths of the Pickelhaube Formation from throughout the study area during D1.*



Fig. 4.20: *Elongation of clasts of a Rosh Pinah Formation conglomerate associated with D1 at locality 13B, approximately 3 km north of Dreigratberg (Fig. 2.4). Flattening and stretching of clasts parallel to subparallel to bedding and S1 cleavage. Note the cigar-like shape of clasts.*

D1 thrust faults preferably use contacts between lithologies with contrasting competency, i.e. sandstones being thrust over mudstones or carbonates. Thrust faults are dealt with in more detail in section 4.3.4.

4.3.2 D2 phase of deformation

The most conspicuous features characterizing the D2 deformation are very small to large scale folds, with fold axes trending at about 140 to 190 degrees and plunging moderately at various amounts in northerly and southerly directions (Fig. 4.21). Axial planes generally dip in a westerly direction. The thrust planes of some thrust faults,

which have a listric appearance, steepen in an easterly direction to the point, that they can even be overturned. F2 folds with an originally easterly vergence, which occur together with some of these steepened or overturned thrust faults, change their vergence towards a westerly direction as they "climb up" the thrust planes and are referred to as "backfolds". East of the Aus road thrust fault and the Sedelingsdrift thrust fault (Fig. 2.3), F2 folds generally verge in a westerly direction, which is caused by backfolding in the proximity of the basement and the presence of steep and overturned thrust faults (Figs. 4.3, 4.5 and 4.8).

F2 folds vary in scale from small scale (<5 cm wavelength) to large structures with wavelengths of up to about 5 km (Annisfontein anticlinorium; Fig. 2.4). The F2 folds which refold among others the earliest D1 thrust faults, display a variety of fold shapes. Folds are symmetric to assymmetric, upright to recumbent and vary from open, tight, to isoclinal in form, harmonic to disharmonic and may be polyclinal (box folds and parasitic folds; Figs. 4.22 and 4.23). Small scale chevron folds are present at one locality 10 about 2 km south of Pickelhaube (Fig. 2.4).

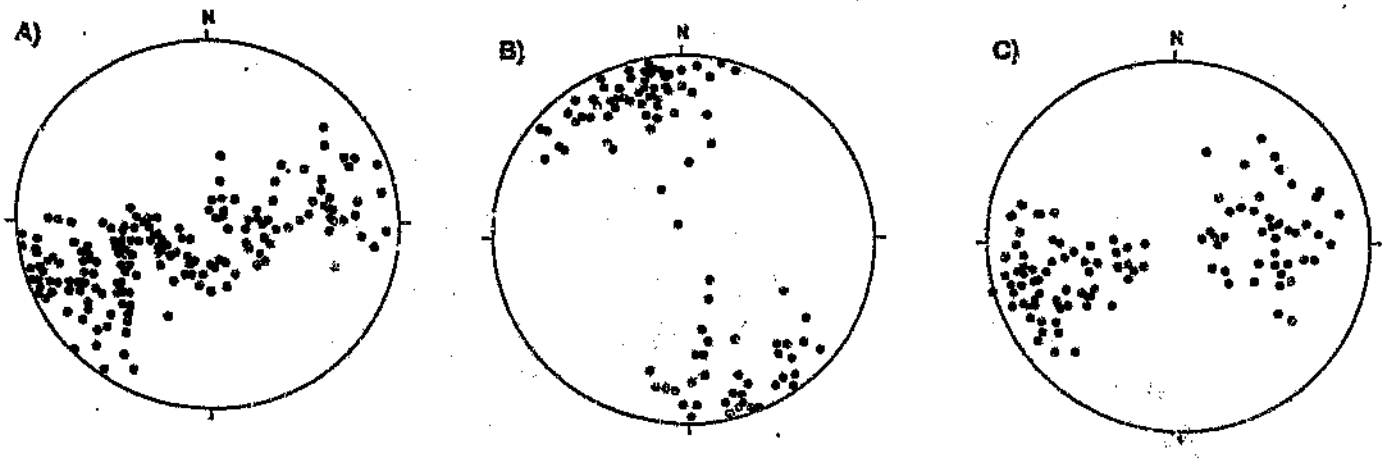


Fig. 4.21: *Stereonet projections of data associated with D2 throughout the area; A) poles to S0/S1; B) F2 fold axes; C) poles to F2 axial planes.*



Fig. 4.22: *Disharmonic F2 fold within arkosic sandstones of the Rosh Pinah Formation at Trekpoort Farm (Fig. 1.2).*

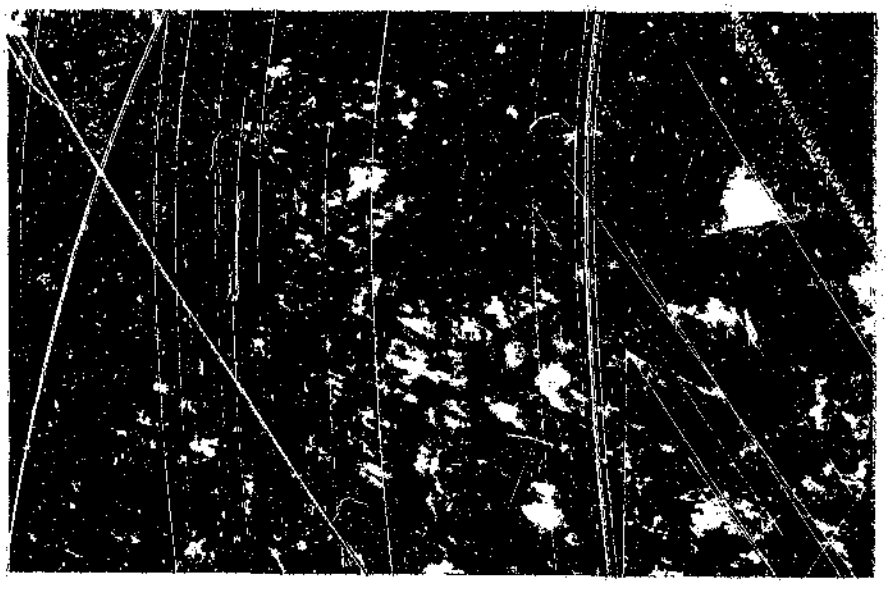


Fig. 4.23: *Penetrative S2 axial planar cleavage within a northwest-trending, overturned tight F2 fold near Daberas, about 30 km NW of the Oranjemund road (Fig. 1.2).*

Throughout the study area an S2 axial planar penetrative cleavage is developed within pelitic rocks and an axial planar foliation within psammitic rocks (Figs. 4.23 and 4.24). The S2 axial planar cleavage is defined by a penetrative slaty cleavage within argillaceous units (Figs. 4.24 and 4.26) and by an axial planar fracture cleavage or a preferred orientation of grains in arenites (Figs. 4.23, 4.24 and 4.25). The S2 axial planar cleavage and associated axial plane strike at about 140 to 190 degrees and dip



Fig. 4.24: *Refraction of S2 cleavage around folded layers of of different competencies within folded mudstone and sandstone of the Rosh Pinah Formation at locality 7, south of Pickelhaube (Fig. 2.4); note the characteristic flattening of the cleavage in the pelitic layers and the higher angle between cleavage and bedding in the psammitic layers.*

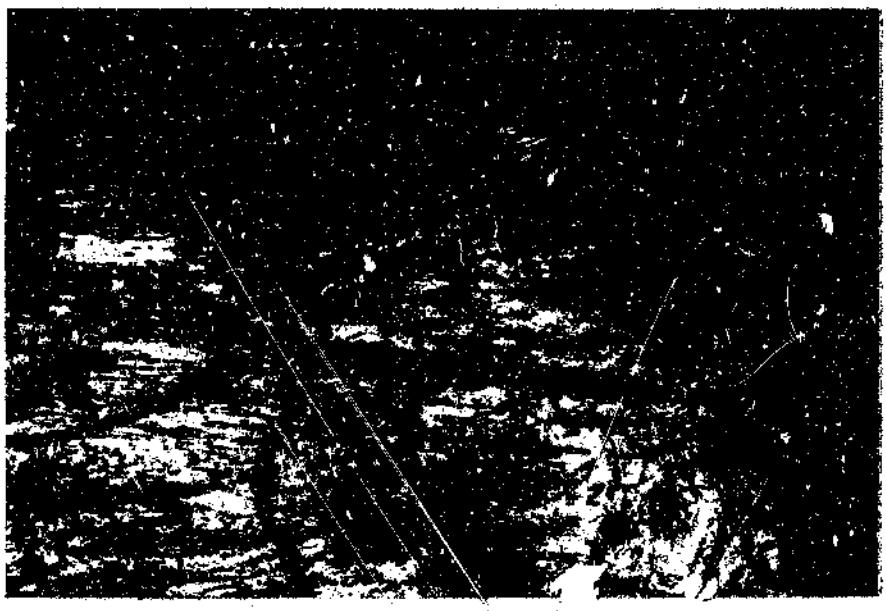


Fig. 4.25: *S2 crenulation lineation l2 within phyllite of the Gumchavib Formation, about 3 km northwest of Obib waterhole; crenulation lineation l2 is parallel to pencil and developed on the bedding plane.*

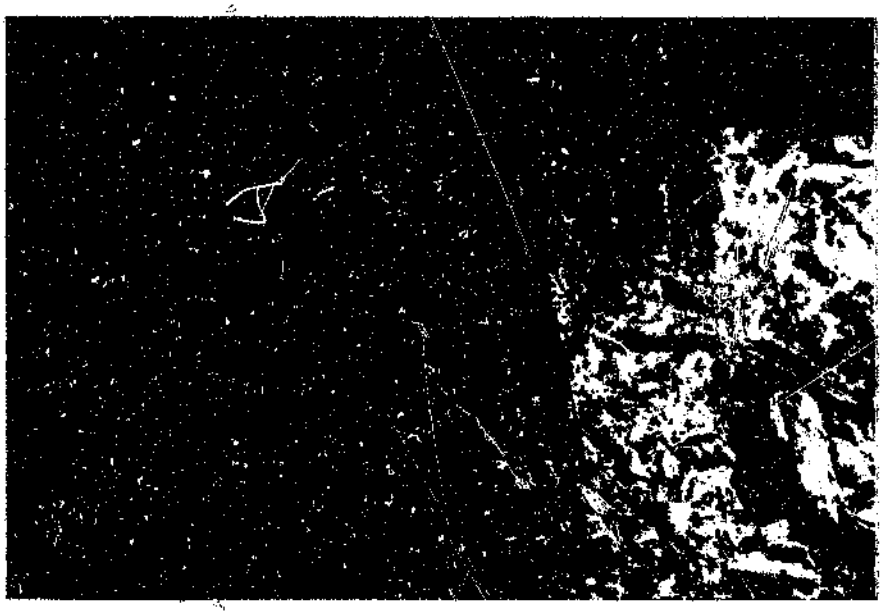


Fig. 4.26: *Axial planar S2 cleavage deforming So-subparallel S1 cleavage within mudstones of the Rosh Pinah Formation at locality 7, east of Pickelhaube (Fig. 2.4).*

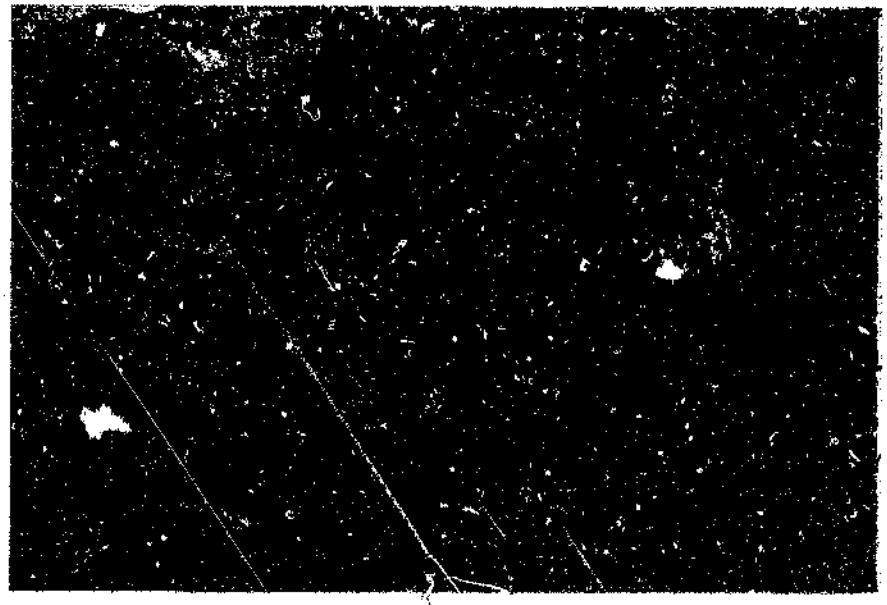


Fig. 4.27: *D2 thrust fault at locality 1 (Fig. 2.4); note the fold limb of the F2 fold is cut-off by thrust fault.*



Fig. 4.28: *D2 thrust fault immediately south of Pickelhaube Peak (Fig. 2.4), carbonates of the Pickelhaube Formation are thrust over sandstones and conglomertaes of the Rosh Pinah Formation. Note the relatively undeformed carbonate in the upper thrust slice overlying folded sandstones and conglomerates with a clearly developed S2 axial planar foliation beneath the thrust fault.*

with variable amounts in a westerly or easterly direction (Fig. 4.21A and B).

An S2 intersection crenulation cleavage, deforming the pre-existing S1 bedding-subparallel cleavage, is present throughout the study area. The intersection cleavage (S1/S2), which defines the l2 crenulation lineation IFig. 4.25), plunges in various directions with up to 20 degrees and trends at 140 to 190 degrees.

In places F2 fold limbs are cut-off by associated thrust faults at high angles (Fig. 4.27). At Pickelhaube (Fig. 2.4) relatively undeformed carbonate of the Pickelhaube Formation is thrust over sandstones and conglomerates of the Rosh Pinah Formation (Fig. 4.28). The lithologies of the Rosh Pinah Formation are folded and display a clear axial planar S2 foliation, which is defined by the elongation of grains, pebbles and clasts. Thrusting, associated with D2, will be described in more detail in section 4.3.4.

4.3.3 D3 phase of deformation

A D3 deformation phase has been recognized throughout the study area. Stereonet projections of data associated with this deformational phase are shown in Fig. 4.29, displaying a trend of F3 fold axes ranging from WNW to southwest. F3 axial planes generally show no vergence. They may, however, verge in a northerly and, more commonly, in a southerly direction.

The most conspicuous features of this phase of deformation are open, upright small-scale to large scale cross folds, referred to as F3 folds, ranging from small scale folds (<5 cm wavelength), mainly developed in argillaceous rocks, to medium scale (Fig. 4.30) and large scale folds with wavelengths of several kilometres. Open, small scale chevron-like folds are also present (Fig. 4.31).

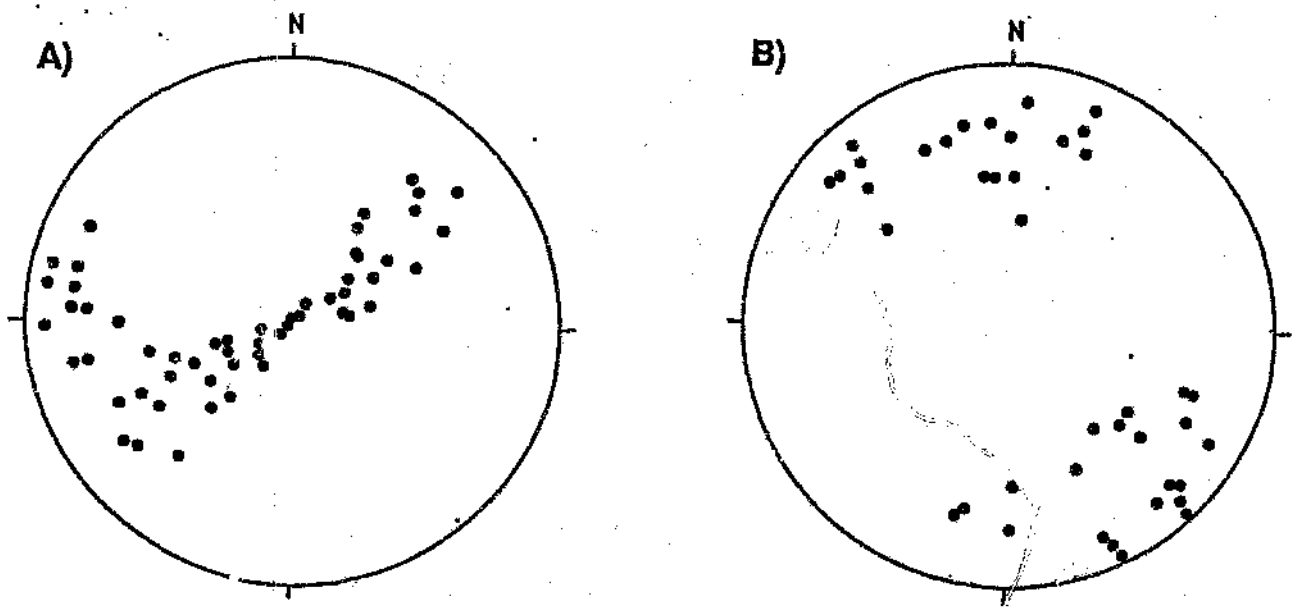


Fig. 4.29: *Stereonet projections of data associated with D3 throughout the area; A) F3 fold axes (n=68); B) poles to F3 axial planes (n=46).*



Fig. 4.30: *F3 open fold developed within carbonates of the Pickelhaube Formation at locality 17 (Fig. 2.4).*

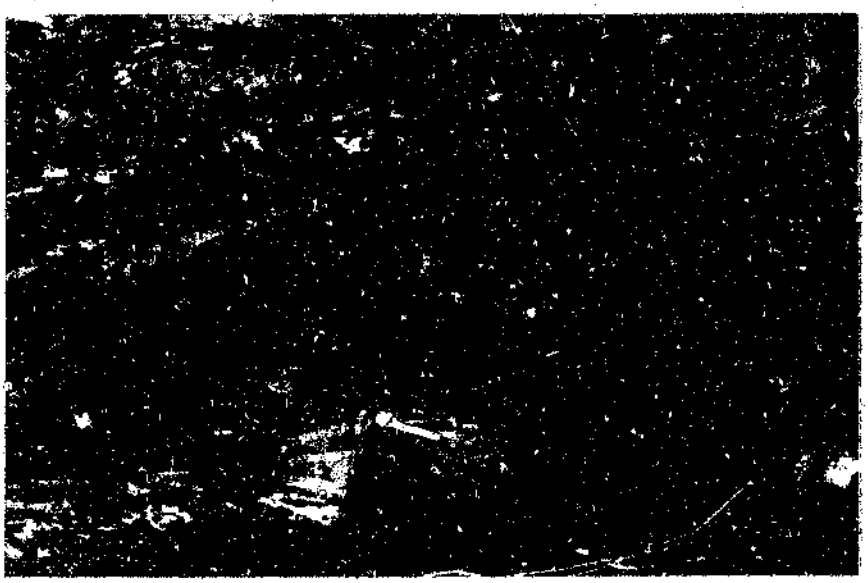


Fig. 4.31: *F3 open chevron fold developed within carbonates of the Pickelhaube Formation at locality 17 (Fig. 2.4) in the Ostrich thrust slice.*



Fig. 4.32: *Fold interference structure caused by a F3 fold deforming the fold hinge of a F2 fold at Dreigratberg (Fig. 2.4).*

The F3 folds form fold interference structures due to refolding of the pre-existing F2 folds (Fig. 4.32). The interference structure is dome-like in form and the superposition of the F3 folds on F2 folds is responsible for the variable plunge directions of the F2 folds. An S3 crenulation cleavage, associated with the development of F3 folds, was observed at locality about 2 km northeast of Obib waterhole (Fig. 2.4), and could only be recognized where the S1 cleavage was overprinted by a weak axial planar S3 cleavage, defining the l3 intersection lineation. Except for the S3 crenulation cleavage, no D3 associated foliation was recognized.

4.3.4 Recognition of thrust faults and time sequence of thrusting

Thrust faults, associated with the D1 and D2 deformational events, are amongst the most important structural elements within the study area. Their recognition and the understanding of the time sequence of the activity of these thrust faults is most important for the understanding of the structural evolution and kinematic interpretation of the Adamastor orogenesis in the Gariep Belt, as well as for the establishment of a correct stratigraphy.

The major thrust faults within the study area generally trend north-south to northwest-southeast (Fig. 2.4) with thrust planes dipping in a westerly direction. Thrust planes are in some cases steeply inclined towards the east as a result of intense compression in the vicinity of the basement or within imbricate thrust zones. Thrust planes, formed during D1, are in places refolded by the D2 deformational event, thus dipping with variable angles in an easterly direction.

The thrust faults are marked by: (1) intrafolial F1 folds, shear zones, the presence of

quartz veins and feldspar pegmatoids in the vicinity of thrust faults; (2) mylonite zones; (3) stratigraphic discordances associated with ramping; (4) a conspicuously developed foliation within and in the vicinity of shear and thrust zones; (5) the presence of an intense silicification of sandstones; (6) the alteration of limestones to marbles; (7) the occurrence of actinolite schist in association with amphibolite sills; (8) the presence of tight to isoclinal and recumbent F2 folds; and (9) the change of fold vergence from east to west.



Fig. 4.33: *D2 thrust fault cutting through the stratigraphy at a locality south of Gumchavib trigonometrical beacon, probably caused by the failure of the footwall ramp.*

The most common thrust faults generated during D1 are bedding parallel to subparallel, often steepening with a westerly dip in an easterly direction taking the shape of listric thrust faults. The listric thrust faults occasionally form ramps, which cut

across the stratigraphy and may be caused by successive failure in the footwall (Fig. 4.33). Imbricate zones, present at various locations throughout the study area, may be a subsequent result of the progressive failure of footwall ramps. Intrafolial F1 folds, a bedding-subparallel S1 cleavage and the elongation of grains and clasts (l1) are associated with bedding-parallel thrusting in the vicinity of thrust contacts. In the east of the study area, within imbricate thrust zones and in the immediate vicinity of the competent basement, the westerly dip of thrust planes steepens and can even be steeply inclined towards the east (Figs. 4.1 and 4.2). Subsequently, after a maximum amount of bedding-parallel compression and the formation of duplexes, the rocks were folded during the D2 deformational event. D1 thrust planes, as shown within the Dreigratberg syncline (Figs 4.1B and 4.2C), were folded around fold hinges during D2. Folding and the development of a penetrative axial planar S2 cleavage and foliation is intimately associated with thrusting during D2, with the thrust faults cutting folded beds at high angles (Fig. 4.27). Thrusting continued during the late stages of D2, as shown at a locality immediately south of Pickelhaube, where relatively undeformed sediments are thrust over folded rocks, which also display a penetrative axial planar S2 foliation (Fig. 4.28).

As demonstrated above, thrusting occurred from the early stages of D1, through the main phases of D2 until the late stages of the D2 deformational event, showing that D1 and D2 took place progressively.

4.4 KINEMATIC INTERPRETATION

Within the study area three kinematic phases were identified from the analysis of finite strain ellipsoids, slickensides, dip and strike directions of D1 and D2 thrust faults, the

sense of vergence of the F1, F2 and F3 folds, the trend of fold hinges, their shape along strike over long distances and the variations in strain ellipsoid shape from prolate to oblate within the entire Gariep Belt. The two earliest kinematic phases took place progressively. The earliest recognized kinematic phase is related to convergent, southeast to SSE directed tectonic transport, which is related to the closure of the Adamastor Ocean and the accretion of the Marmora Superterrane and the Port Nolloth Zone. The second kinematic phase is associated with eastward directed tectonic transport during the D2 deformational phase, which took place during the collision of proto-South America and the Kalahari Craton. The latest kinematic phase within the study area is related to a sinistral strike-slip phase during the D3 deformational event.

4.4.1 Transpressive phase

The analyses of several structural features, which led to the recognition of an early transpressional phase, are associated with the D1 and D2 deformational events. Rigid body analyses and finite strain analyses were carried out in order to define the first kinematic phase of the tectonic evolution of the Gariep Belt.

Finite strain analysis

Von Veh (1988) obtained a total amount of 89% shortening for the Gariep Belt in the northwestern Richtersveld. Unfolding of F2 folds within the study area with the help of balanced cross-sections amounted to an approximate shortening of about 90%. Because of the paucity of marker horizons within the Gariep Belt, it is not possible to delineate the exact amount of displacement which took place along the thrust faults.

Using the bow and arrow method of Elliott (1976) for the prominent Schakalsberge thrust fault, which juxtaposes the Marmora Superterrane and the Port Nolloth Zone, the displacement is more than 100 km in an easterly direction. Applying the rule of Elliott and Johnson (1980), stating that the displacement of a thrust fault is equal to the length of the thrust fault multiplied by the factor 0.07, a displacement of 16 km results for the Schakalsberg thrust fault.

Within the Gariep Belt north of the Orange River, X (long)-, Y (intermediate)-, and Z (short)-axes of clasts and boulders of conglomerates of the Rosh Pinah Formation and pisoliths of the Pickelhaube Formation were measured. The plunge of the X-axes were measured and rotated back into the horizontal. Figure 4.19 shows two main trends of strain ellipsoids at two oblique angles. The main trend strikes NNW, and the second trend at WNW, showing that differential movement took place. The main tectonic transport component of the differential movement is towards the southeast to SSE, whereas the minor component is directed towards the east. The X/Y and Y/Z ratios of the measured ellipsoids were plotted on a Flinn diagram (Fig. 4.34). This diagram shows the field of flattening and the field of constriction, assuming that no volume changes took place and that the measured objects were initially spherical. The plots in Fig. 4.34 show that the measurements at localities 13B and 7 (Fig. 2.4) plot in both the flattening and the constrictional fields, i.e. averaging with plane strain. At locality 8 (Fig. 2.4), which lies further westsouthwest and perpendicular to strike, measurments plot in the constrictional field. A trend is recognizable, displaying a change from a flattening strain field in the vicinity of the basement in the east to the constrictional strain field to the west of the study area away from the basement.

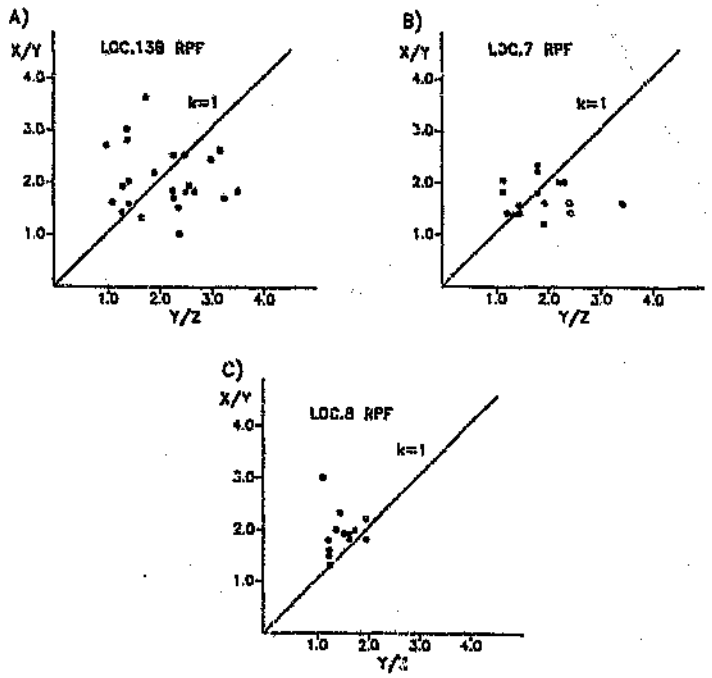


Fig. 4.34: *Flinn plots of strain data from (A) locality 13B; (B) locality 7; and (C) locality 8 (localities are shown in Fig. 2.4).*

Rigid body analysis

The structural limits of the Gariep Belt outline an arcuate form in relation to the present coastline of southern Namibia and the northern Cape Province of South Africa (Fig. 2.1). In southern Namibia, the Gariep Belt and associated deformation is restricted to the area southwest of a line from Lüderitz to Dreigratberg at the Orange River. South of Lüderitz and in the vicinity of Bogenfels the structural trend of the main structural elements such as thrust faults and F2 folds ranges from north-south to NNW-SSE. In the Witputs-Dreigratberg area, which also includes the study area, the general trend of thrust faults and F2 folds ranges from north-south to northwest-southeast, changing to NNW immediately south of the Orange River and swinging to northeast-southwest in the coastal outcrops from Cape Voltas to the mouth of the Holgat River further

south (Von Veh, 1988). The arcuate shape of the Gariep Belt could not have developed as a late bending event on a regional scale, as basement rocks southeast of the arc provide no evidence for such bending strains (Davies and Coward, 1982). The post-Gariep Kuboos and Swartbank plutons (Fig. 2.7) may be partially responsible for a change in structural trends in their immediate vicinity as a result of diapiric activity, however, it seems highly unlikely that they have caused the present arcuate shape of the entire Gariep Belt. Differential movement, detected within several thrust sheets, can only be partially liable for the concave form of the structural features within the Gariep Belt. On the grounds of the bow and arrow method of Elliott (1976) it has therefore to be concluded, that an eastward directed tectonic transport during D2 was mainly responsible for the concave form of the structural features within the Gariep Belt and for the arcuate shape of the Gariep Belt as a whole.

4.4.2 Strike-slip phase

The latest tectonic event within the study area is recorded by D3, which is responsible for small to large scale east-west to southwest-northeast trending open folds. A sinistral strike-slip phase localized along existing zones of weaknesses is responsible for these structural features. Plane sinistral wrenching may have continued until after the deposition of the upper Schwarzrand Subgroup of the Nama Group, as indicated by the presence of warping of Schwarzrand Subgroup lithologies, shown in a N-S section through the Nama Group by Germs and Gresse (1991).

4.4.3 Interpretation

The results of the finite strain analyses of D1 related strain ellipsoids show the presence of differential movement with two main components during the D1 deformational event (Fig. 4.19). The main tectonic transport was directed southeast to SSE, associated with a second easterly directed component. Extreme compression in the vicinity of the basement, associated with the difference in ductility of the compressed lithologies and the basement itself, is thought to be responsible for the presence of differential movement.

Subsequent eastward directed tectonic transport during the D2 deformational phase is liable for the concave shape of tectonic features such as the trend and vergence of F2 folds, the trend and dip of the thrust faults throughout the Gariep Belt and for the arcuate shape of the Gariep Belt as a whole.

The tectonic evolution of the Gariep Belt terminated with a sinistral strike-slip movement along existing weakness zones, ceasing only after the deposition of the Schwarzrand Subgroup of the Nama Group.

Strain ellipsoids in the Richtersveld have very variable shapes, ranging from strongly deformed prolate ellipsoids in the northern parts of the Richtersveld to oblate ellipsoids in the south, with the average strain ellipsoid trending NNW (Von Veh, 1988). Considering the swing in structural trend and the presence of prolate and oblate ellipsoids deformed during the D1 deformational phase in the area immediately north of the Orange River the study area was situated in the transitional zone between the frontal and the lateral edge of a southeast- to SSE- directed tectonic unit during the D1 deformational event (Fig. 4.35). Davies and Coward (1982) recognized no effects of Gariep deformation within the granites of the Aurus Mountains approximately 60 km

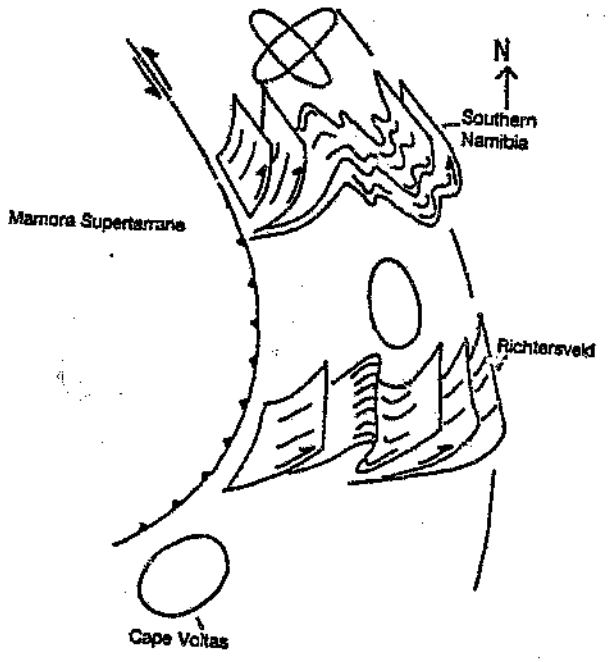


Fig. 4.35: *Schematic diagram summarizing the structural variations and change of strain ellipsoids during the earliest kinematic phase (D1) in the central and southern parts of the Port Nolloth Zone (modified after Von Veh, 1988).*

northwest of Rosh Pinah and concluded that the deformation associated with thrusting dies out not only to the north along the strike of the thrusts, but also to the northwest. Therefore, Davies and Coward (1982) suggested that the movement of thrusts increases to the south and southeast, giving rise to extensional flow in the area southeast of the Aurus Mountains (Fig. 1.2). Field evidence in the Bogenfels area and the area immediately south of Lüderitz shows, however, that early D1 related southeast- to SSE-directed thrusting, as well as eastward directed tectonic transport during the D2 deformational event, did also take place in the north-western parts of the Sperrgebiet. Field evidence from the study area shows, that the direction of tectonic movement in the Gariep Belt was not restricted towards the SSE, as postulated by Von Veh (1988), but that it changed from SSE during D1 to east during D2, and to southerly directed strike-slip movement during D3.

CHAPTER 5

METAMORPHISM

5.1 INTRODUCTION

No detailed work has so far been undertaken to constrain the metamorphic evolution of the Port Nolloth Zone of the Gariep Belt. Studies on the metamorphic evolution of the Gariep Belt were first undertaken by De Villiers and Söhnge (1959), who postulated an older dynamic event, which gave rise to phyllites and chlorite-rich schists, and a younger contact thermal event forming spotted slates and hornfelses. Kröner (1974; 1975) recognized only one Barrovian-type regional metamorphism, increasing from low grades in the "miogeosynclinal shelf" in the eastern parts of the Gariep Belt (Port Nolloth Zone) to intermediate grades in the "eugeosynclinal realm" (Marmora Terrane) to the west of the Schakalsberge thrust fault (Fig. 2.1). "Granitization" and "feldspathization" are terms frequently used in older literature (Martin, 1965; McMillan, 1968). These phenomena have, however, been resolved by the recognition that many of the "granitized" rocks represent tectonically emplaced granitic basement (Joubert and Kröner, 1972; Kröner, 1974a; Von Veh, 1988; Jasper, 1992/1993). Von Veh (1988) recognized two metamorphic events for the Gariep Belt lithologies in the Richtersveld. The M1 regional metamorphic event (Kröner, 1974) comprises greenschist facies metamorphism with temperatures assumed to be consistently low across the Gariep Belt, possibly not exceeding ~450 degrees C. Pressures during M1 were assumed to increase in a westerly direction, ranging between 6 and 7 kbar. The M1 metamorphic

event is suggested to be related to the closure of the Adamastor Ocean and the collision between the South American and the Kalahari Cratons. The M2 contact metamorphic event (Von Veh, 1988) is related to the emplacement of the Kuboos Pluton and occurred after the M1 metamorphic event.

Detailed metamorphic studies in the Marmora Superterrane to the west of the study area (Fig. 2.1) were undertaken by Frimmel and Hartnady (1992) and indicated a multiphase metamorphic history for this superterrane. The first metamorphic event, M1, was interpreted as a very low-pressure hydrothermal oceanic metamorphism that affected the igneous protoliths up to amphibolite facies temperatures. The subsequent M2 metamorphism was syntectonic, being characterized by temperatures similar to those reached during M1 but with higher pressures, indicating burial to 10 to 15 km. This event is interpreted as being related to a subduction process. A third metamorphic event, M3, was low grade and of regional nature. These results indicate that subduction and subsequent obduction have occurred in the Gariep Belt, although blueschist facies metamorphism has not been reached (Frimmel and Hartnady, 1992).

5.2 METHODS OF STUDY

This work represents the first detailed studies of the metamorphic evolution of the Port Nolloth Zone of the Gariep Belt (Fig. 2.1). Phase relations within the amphibolites and metasediments and the P-T estimates for these rocks are discussed. Sedimentary structures within the Gariep Group lithologies of the Port Nolloth Zone in southern Namibia, although affected by upper greenschist to lower amphibolite facies metamorphism, are still well preserved.

5.2.1 Selection of samples

In order to investigate the metamorphic conditions throughout the study area, selected sampling was undertaken. Geothermometry and geobarometry within this study is based on the investigation of the critical mineral assemblages hornblende-plagioclase-epidote-chlorite-quartz within amphibolites, plagioclase-microcline-biotite-phengite-quartz within psammites, and garnet-chlorite-muscovite-plagioclase-ilmenite-quartz within pelites. To determine the mineral content and the phase relations and to estimate the metamorphic peak conditions, five amphibolites, three psammites and two garnet-chlorite schists were investigated (Table 5.1). The amphibolite samples A1, A2 as well as the psammite gneiss sample 35 were taken from the Rosh Pinah Formation in the northern part of the study area (Fig. 2.4). The garnet-chlorite schists P1 and P2, as well as the psammite 235 originate from the Rosh Pinah Formation from the southern part of the study area north of Gumchavib Mountain (Fig. 2.4). Psammite sample RP185 is part of the Obib Peak Formation near Obib Peak. The amphibolites RP60 and A5 were taken from the lower Pickelhaube Formation (Fig. 2.4). Sample AN originates from Namuskluft waterhole in the easternmost parts of the study area and is part of the Numees Formation.

5.2.2 Mineral chemistry analyses methods

Mineral analyses were performed using a CAMECA SX 50 microprobe with four spectrometers at the University of Würzburg, Germany. Instrument conditions were: 15 kV acceleration potential, 10 nA specimen current and, depending on the measured element, 10, 20 or 30 seconds counting time. The CAMECA standard set was used

Table 5.1: *Mineral assemblages of investigated samples.*

Sample	Formation	Rock type	Mineral assemblages
AN	Numees	basic volcanic	green amphibole, plagioclase, epidote, chlorite, quartz ±biotite ±calcite. Accessories are tables of ilmenite, hematite and sphene. In sample RP60 relics of magmatic pyroxenes occur
A1	Rosh Pinah	basic volcanic	
A2	Rosh Pinah	basic volcanic	
A5	Lower Pickelhaube	basic volcanic	
RP60	Lower Pickelhaube	basic volcanic	
35	Rosh Pinah	Psammite	plagioclase, microcline, white mica, biotite, quartz, minor amounts of retrograde chlorite and opaques
235	Rosh Pinah	Psammite	
RP185	Obib Peak	Psammite	
P1	Rosh Pinah	Pelite	garnet, plagioclase, chlorite, muscovite, ilmenite, quartz. Accessory minerals are opaques and rare zircon
P2	Rosh Pinah	Pelite	

for reference; correction procedures were carried out using the PAP program. The Fe3+/Fe2+-ratios in the analysed amphiboles were estimated by the method of Papike et al. (1974), modified by Franz & Häussinger (1990), assuming the Fe3+ content as the midpoint between the maximum and the minimum Fe3+ contents. The Fe3+/Fe2+-ratios in the analysed garnets and ilmenites were estimated using charge balance criteria (Appendices 7 & 8).

5.3 PETROGRAPHY AND PHASE RELATIONS OF THE SELECTED SAMPLES

Amphibolites: The distinctly foliated amphibolites are of volcanic origin, which is indicated by magmatic relics in the form of pyroxene. They all display the paragenesis green amphibole-plagioclase-epidote-chlorite-quartz ± biotite ± calcite. Accessory

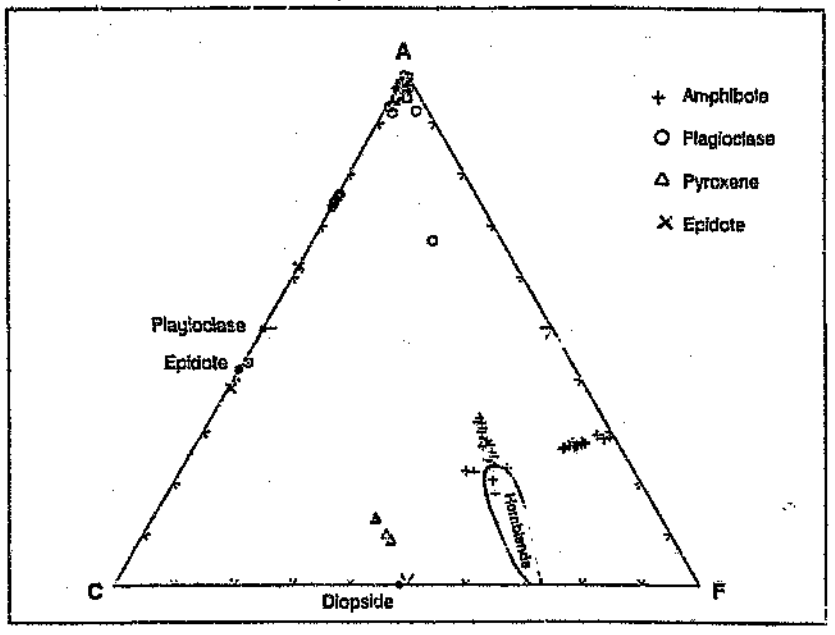


Figure 5.1: *ACF diagram showing mineral compositions within the amphibolites.*

minerals include tabular ilmenite, hematite and sphene. In sample RP60, relics of magmatic pyroxenes were detected. The pale brownish pyroxenes are strongly retrograded and rimmed by hornblende and epidote. The mineral compositions within the amphibolites are documented within the ACF diagram of Fig. 5.1.

Psammites: The psammites consist of the paragenesis plagioclase-microcline-white mica-biotite-quartz and minor amounts of retrograde chlorite and opaques. The mineral compositions within the paragneisses are shown in the A'KF diagram in Fig. 5.2. The psammites generally display a foliation, which is often disturbed by detrital fragments and best developed in mica-rich layers.

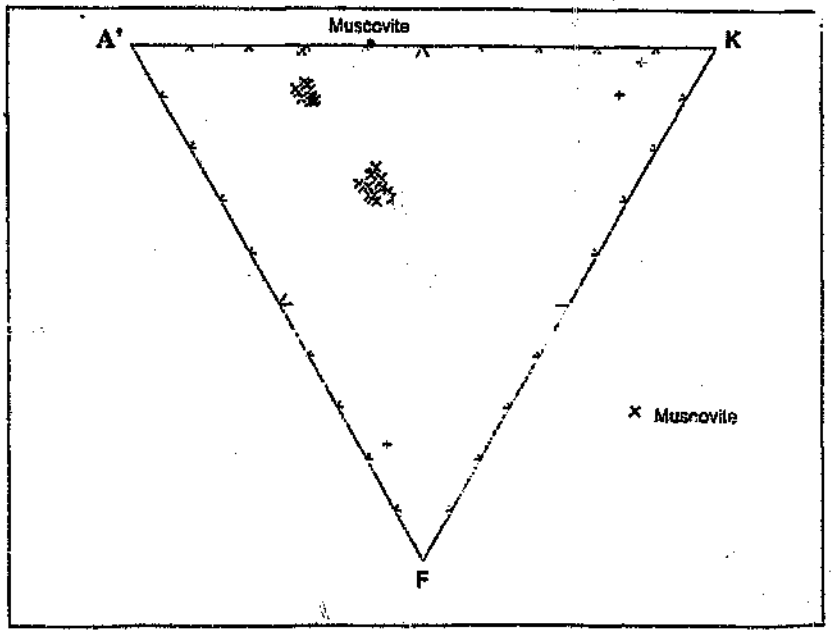


Figure 5.2: *A'KF diagram showing mineral compositions within the paragneisses.*

Garnet-chlorite schist: The garnet-chlorite schists were derived from a Ca- and Mn-rich pelitic protolith. The garnets and the ilmenites in particular reveal high amounts of Mn.

The critical mineral assemblage is garnet-plagioclase-chlorite -muscovite-ilmenite-quartz. Accessory minerals are opaques and rare zircon. Two cleavages are clearly visible in the garnet-chlorite schists: the S1 cleavge is subparallel to the compositional layering S0 and the less penetrative S2 cleavage cuts S1 at an angle of about 20°. The growth of the mineral phases can be well correlated with the fabrics. Garnet as well as muscovite and chlorite schistosities define S1 and indicate their growth during the D1 deformation. A static phase after S1 led to the growth of idioblastic garnet rims and postdeformational mica and chlorite. The S2 foliation led to a preferred orientation of muscovite and chlorite. The growth of garnet also continued during D2.

5.4 MINERAL CHEMISTRY

Pyroxenes:

Microprobe analyses of several grains of pyroxene from sample RP60 reveal high diopside contents of 96-98 mol % (Appendix 1). Microprobe analyses reveal a weak

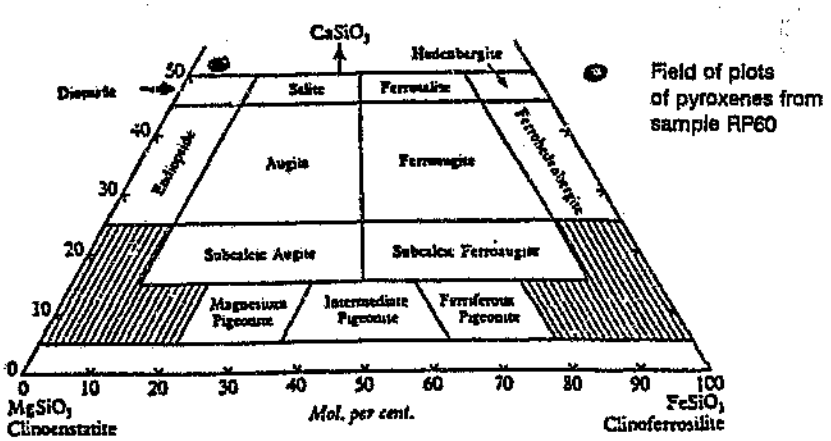


Figure 5.3: *Nomenclature of Clinopyroxenes in the system $CaMgSi_2O_6$-$CaFeSi_2O_6$-$Mg_2Si_2O_6$-$Fe_2Si_2O_6$ (after Poldervaart & Hess, 1951).*

zonation within the pyroxene with a slight increase of the jadeite component from 0.5-2 mol % and a decrease of diopside from the core to the rim. The acmite component is relatively constant at about 2 mol %. The high Ca-content of the diopsides (Fig. 5.3) may be a product of plagioclase inclusions and the analytical error. The precursor minerals of the diopsides at the time of emplacement were prbably augites.

Amphiboles: The amphiboles of the amphibolites are all Ca-amphiboles using the classification of Leake (1978). A distinct zoning could not be observed in any sample. The bluish-green amphiboles from samples A2 and A5 mainly plot into the fields of pargasitic and edenitic hornblende, whereas the brownish Si-poor amphiboles from

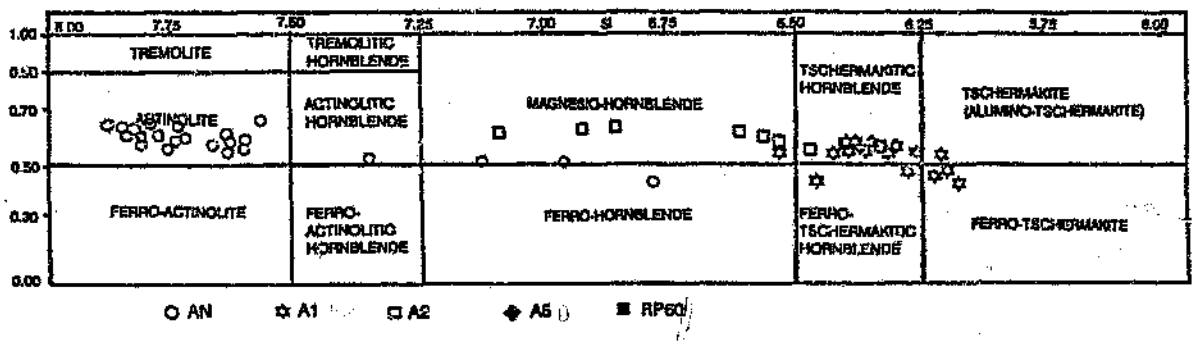


Figure 5.4: *Leake (1978) amphibole nomenclature of calcic amphiboles: $(Na + K)_A \geq 0.50$; $Ti < 0.50$; $Fe^3 \leq Al^{VI}$.*

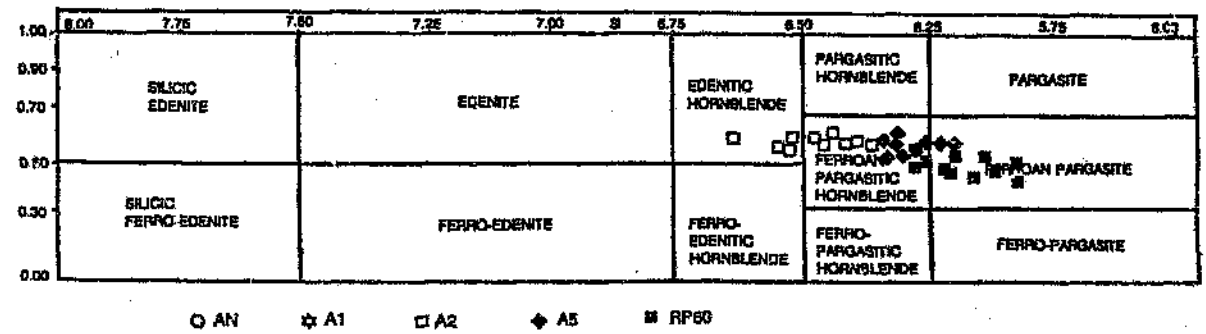


Figure 5.5: *Leake (1978) amphibole nomenclature of calcic amphiboles: $(Na + K)_A < 0.50$; $Ti < 0.50$.*

sample RP60 are commonly ferroan pargasites (Fig. 5.4). Almost all amphiboles from sample A1 are (ferro-) tschermakites and (ferro-) tschermakitic hornblendes (Fig. 5.5 and Appendix 2).

Plagioclases: The plagioclases coexisting with the amphiboles are albites and oligoclases. Representative microprobe analyses of the plagioclases are listed in Appendix 3. All plagioclases of sample A1 display An contents of 19-26 mol %. Relics of oligoclase (An_{17}) are also present in sample A2, which mainly contains albite (An_{0-8}). This is probably due to retrograde processes. The amphibolites A5, AN and RP60 are all albite-bearing with An contents of 0-8 mol %. The plagioclases of the garnet-chlorite schists are oligoclases and andesines with An-contents of 29-33 mol %.

Epidotes: The pistacite contents of the epidotes are quite similar in all amphibolite samples. They range from 18-32 mol % and are virtually unzoned. Microprobe analyses of the epidotes are listed in Appendix 4.

White micas: Microprobe analyses of the white micas from the gneisses show distinct differences in the Si content. The highest Si contents were found in sample 35, where they range between 6.4 and 6.62 p.f.u. The paragonite content of the micas varies between 3 and 5 mol %. Compared to the micas of the other gneisses, the XFe is relatively high, ranging between 0.45 and 0.57 (Fig. 5.6). The phengites in sample RP185 reveal distinctly lower celadonite contents with Si ranging between 6.35 and 6.5 p.f.u. and a paragonite component of 3-5.3 mol %. Even lower Si contents were found

in the micas of sample 235. They vary within a wide range from 6.15-6.43 p.f.u. and reveal a paragonite content between 3.7-9 mol %. The lowest celadonite contents and the highest paragonite contents are observed in muscovites of the garnet-chlorite schist (sample P1; Fig. 5.6). This is probably due to the absence of K-feldspar in the rock. The Si-contents of the micas range between 6.15 and 6.3 p.f.u., while the paragonite component lies between 15 and 25 mol %. It is remarkable that there are no significant chemical differences between micas which formed during the

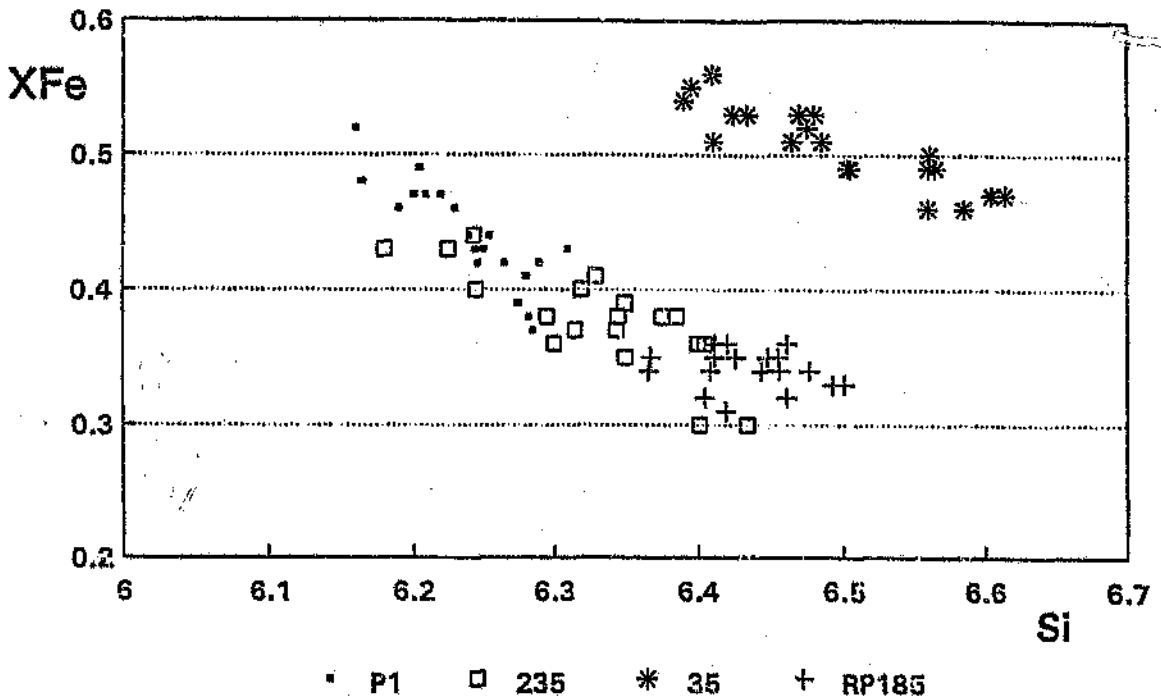


Figure 5.6: *Diagram showing the Fe-Si composition of samples P1, 235, 35, RP 185.*

development of S1 and S2. Selected microprobe analyses of white micas are listed in Appendix 5.

Chlorites: Like the muscovites, the chlorites from the garnet-chlorite schist (sample P2)

show a rather homogeneous chemistry. They are classified as ripidolites after Hey (1954), with slightly elevated MnO-contents of up to 0.9 wt.-%. Microprobe analyses are listed in Appendix 6.

Ilmenite: The ilmenites from the garnet-chlorite schists are strongly altered to a brownish mass of leucoxene. Unaltered ilmenites are only preserved as inclusions in the cores of the garnets. These ilmenites have extremely high Mn-contents with pyrophanite components of up to 52 mol.-%. The geikielith component never exceeds 0.1 mol %. Microprobe analyses are listed in Appendix 7.

Garnets: The garnets from the garnet-mica schists (samples P1 and P2) show no zonation. Microprobe profiles parallel and perpendicular to the S1 foliation reveal a rather homogeneous chemistry with $Spess_{40-43}$ $Gross_{11-15}$ Alm_{40-42} Pyp_{4-5}. The same applies to garnets which show a growth on the S2 schistosity planes. Microprobe analyses of selected garnets are listed in Appendix 8.

5.5 METAMORPHIC EVOLUTION

The mineral parageneses of the basic volcanic rocks of the study area indicate P-T conditions of the epidote amphibolite facies grading into the lower amphibolite facies. Plyusnina (1982) calibrated a geothermometer based on the reaction of

hornblende + epidote + H_2O + CO_2 <==> plagioclase + chlorite + calcite + quartz,

which can also be observed in the amphibolites from the Gariep Belt. A plot of coexisting amphiboles and plagioclases from the basic volcanics within the study area shows a great variability concerning pressures and temperatures (Fig. 5.7). The amphibolite samples A1 and A2 from the Rosh Pinah Formation reveal elevated pressures of 7-8 kbar. The temperatures range between 450 and 550°C. The relatively low temperatures of sample A2 result from the strong retrograde overprint of the plagioclases. Sample RP60 from the lower Pickelhaube Formation shows a pressure

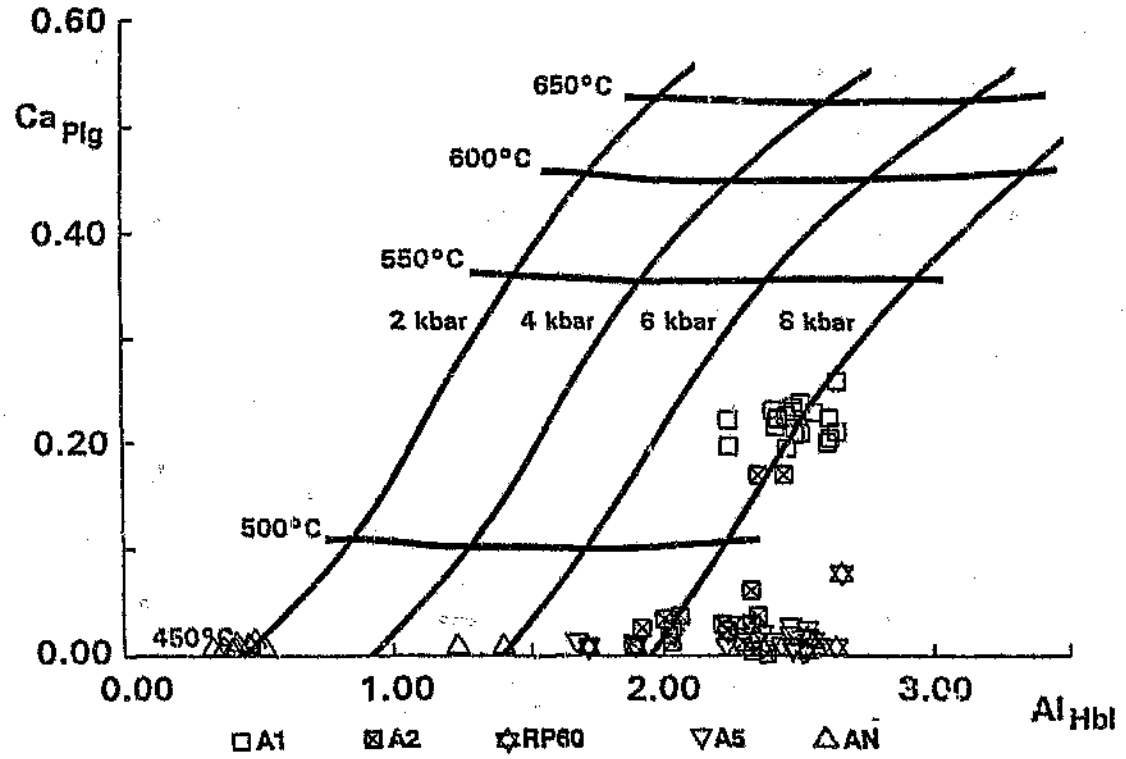


Figure 5.7: *Plagioclase-hornblende thermobarometry after Plyusnina (1982) showing plot of coexisting amphiboles and plagioclases from amphibolite samples; note the great variability of pressures and temperatures.*

range between 7 and more than 8 kbar and temperatures between 450 and 500°C. For this sample, an upper temperature limit can be calculated using the retrograde reaction of magmatic clinopyroxene and plagioclase to hornblende, clinozoisite and

quartz. The divariant curve for the reaction

4 diopside + 10 plagioclase (An_{50}) + 4 H_2O <==>

hornblende + 6 clinozoisite + 3 quartz

was calculated with the THERMOCALC program (Powell & Holland, 1988; see Fig. 5.8). Similar pressures and temperatures to sample RP60 can be estimated for sample

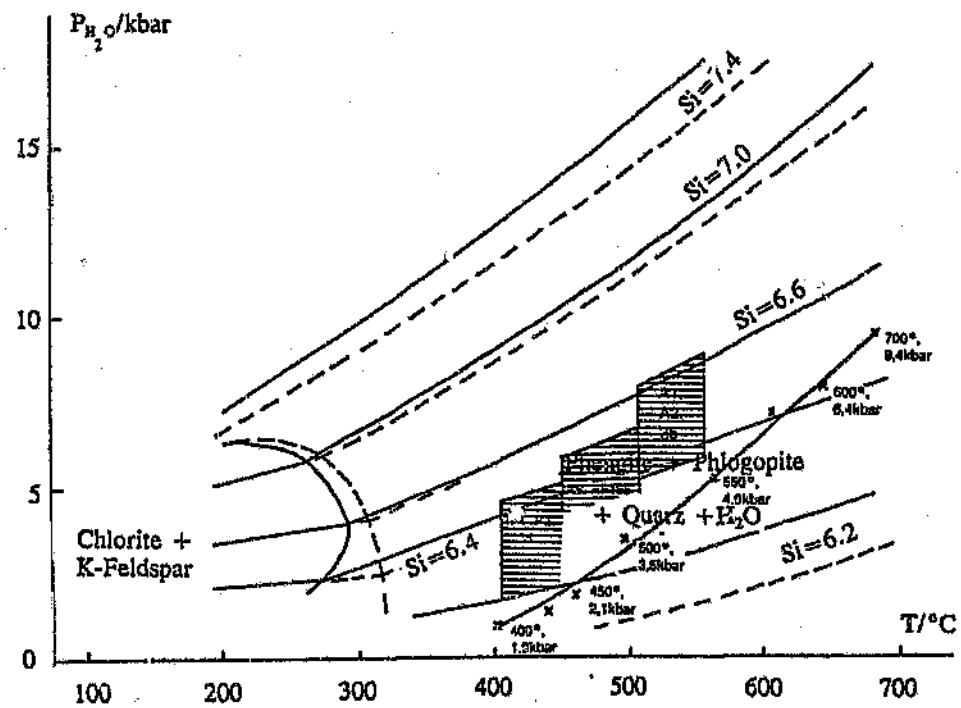


Figure 5.8: *P-T diagram with "isoplethes" for Si-contents of phengites after Massone (1991); note great variability of pressures and temperatures of the investigated samples.*

A5 from the lower Pickelhaube Formation. The lowest P-T conditions of about 2 kbar and 450°C are represented by sample AN of the Numees Formation.

The pressures determined from some of the amphibolite samples can also be

constrained using the Si contents of the micas in gneisses from the same units. Application of the phengite geobarometer of Massonne (1991) yields the following pressures: for samples A1, A2 and the coexisting gneiss sample 35 from the northern Rosh Pinah Formation, pressures of up to 8 kbar were estimated, assuming a temperature range of 500-550°C. Assuming pressure range of 7 to 8 kbar, the gneiss sample RP185 from the Obib Peak Formation indicates temperatures of 450-500°C (Fig. 5.8).

The resulting facies fields of the metabasites are shown in Fig. 5.9 (after Laird & Albee, 1981).

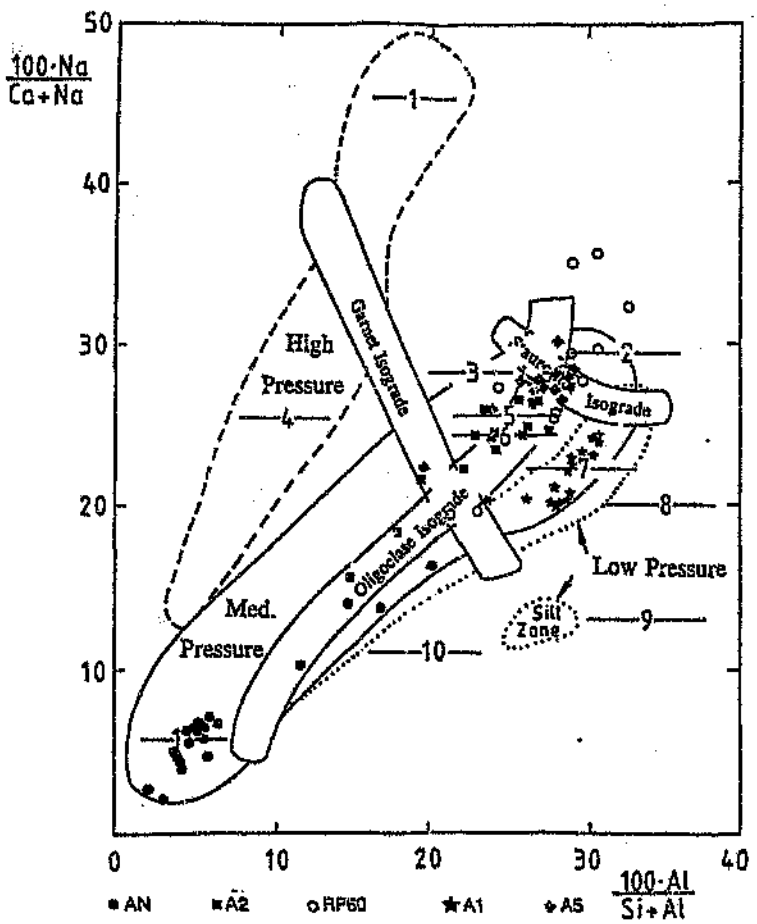


Figure 5.9: *Facies fields of metabasites and coexisting pelites after Laird & Albee (1981).*

The parageneses of the garnet chlorite-schists P1 and P2 as well as the gneiss sample 235 allow a well constrained P-T estimate for the Rosh Pinah Formation in the southern parts of the study area. The garnet-chlorite geothermometres of Dickenson & Hewitt (1986) and Ghent et al. (1987) both indicate temperatures between 400 and 450°C (Appendix 9) assuming a pressure of 5 kbar. The garnet-muscovite geothermometer of Hynes & Forest (1988) points to slightly higher temperatures of 450-500°C (Appendix 10). However, these results are maximum values because no Fe3+-estimate was performed for the white micas. It is remarkable, that there are no significant differences in the temperatures determined from syn-S1, post S1 and syn-S2 micas, chlorites and garnets. A pressure constraint is possible using the phengites of the gneiss sample 235. For temperatures between 400 and 450°C, pressures of up to 6 kbar can be deduced (Fig. 5.8).

5.6 CONCLUSIONS

The critical mineral assemblage in the amphibolites from the northern Rosh Pinah Formation is hornblende-plagioclase-epidote-chlorite-quartz, while the psammites consist of plagioclase-microcline-biotite-phengite-quartz. Microprobe data shows, that many of the plagioclases are albites. These assemblages testify to the lower amphibolite-facies with peak metamorphic temperatures at 500-550°C and pressures of more than 8 kbar. In the Obib Peak Formation, geothermometry and barometry reveal P-T conditions of the epidote-amphibolite facies with temperatures of 450-500°C and pressures of up to 7 kbar. In the southern Rosh Pinah Formation, a Mn-rich pelite with the mineral assemblage garnet-chlorite-muscovite-plagioclase-ilmenite-quartz was

detected. Geothermometry of this sample, as well as geobarometry of coexisting psammites, point to P-T conditions of the greenschist facies at about 400-450°C and 4-6 kbar. In the Pickelhaube Formation, geothermometry and -barometry reveal a pressure range between 7-8 kbar and temperatures between 450-500 degrees C. Textural evidence shows that these P-T conditions were consistant during the D1 and D2 deformation. All these P-T estimates reveal a Barrovian-type metamorphism with a geothermal gradient of about 20°C/km. Very low pressures (about 2 kbar) were recorded in an amphibolite of the Numees Formation with the mineral assemblage actinolite-albite-epidote-chlorite-quartz from the easternmost parts of the study area, substantiating further field evidence for the fact that these sediments are part of the Numees Formation and not of the Rosh Pinah Formation as suggested by Hoffmann (1989).

CHAPTER 6

TECTONICS AND SEDIMENTATION OF THE SOUTHERN COASTAL BRANCH OF THE DAMARA OROGEN (GARIEP BELT)

6.1 INTRODUCTION

One of the main aims of this study was to develop a more highly resolved geodynamic model for the evolution of the Gariep Belt, which forms the southern part of the coastal branch of the Damara Orogen. The understanding of the tectono-sedimentary evolution of the Gariep Belt might be a valuable help for the development of geodynamic models for other parts of the Damara Orogen.

In order to be able to understand the tectono-sedimentary evolution of the Gariep Belt, it is important to look through the tectonic deformation and metamorphism, which affected the rocks of the Gariep Group. The understanding of the tectonic deformation, together with detailed sedimentological studies, has enabled the establishment of a stratigraphy for the Gariep Group. In terranes that have undergone substantial extension, any geodynamic model must take into account the role of syn-sedimentary fault systems.

6.2 PREVIOUS GEODYNAMIC MODELS FOR THE EVOLUTION OF THE SOUTHERN COASTAL BRANCH OF THE DAMARA OROGEN (GARIEP BELT)

Several geodynamic models have been proposed for the evolution of the southern coastal branch of the Damara Orogen (Gariep Belt).

Previous workers related the development of the Gariep Belt to the growth and closure of a Late Proterozoic ocean, which was tied in with the evolution of the inland branch of the Damara Orogen (Kröner, 1974, 1975; Hartnady, 1978; Frasch, 1983, 1983a; Porada, 1983). In this regard, several authors (Martin & Porada, 1977; Porada, 1979, 1983; Martin, 1983; Miller, 1983) regarded the Gariep Belt and the other parts of the coastal branch of the Damara Orogen as recording the development of an ocean with substantial width, while the inland branch of the Damara Orogen formed as an aulacogen or failed rift. A weakness of these models is, that they are not based on detailed work in the coastal branch of the Damara Orogen, but rather on inferred and generalized relationships between the well-studied inland branch and the reconnaissance picture we previously had of the coastal branch in general. In this regard an understanding of the Gariep Belt is crucial for the development of a geodynamic model of the coastal branch of the Damara Orogen.

The first detailed geodynamic models for the evolution of the Gariep Belt were presented by Martin (1965), McMillan (1968), and Kröner (1972), who described it as a geosynclinal assemblage, comprising an eastern "miogeosynclinal" accumulation of terrigenous clastic shelf sediments, carbonates, diamictites, and subordinate volcanic rocks, flanked by a western "eugeosyncline" filled with volcanic rocks overlain by fine terrigenous clastics, which were subjected to higher degrees of deformation and more

intense metamorphism. Stratigraphically, the "eugeosyncline" comprised the Grootderm, Holgat, and Oranjemund Formations, whereas the "miogeosyncline" consisted of the Stinkfontein, Hilda, and Numees Formations.

Kasch (1981, 1983) suggested that subduction of oceanic material along a coastal extension of the inland branch of the Damara Belt continued after the collision of the Kalahari and Congo Cratons and proposed that the pre-Gariep subduction complex

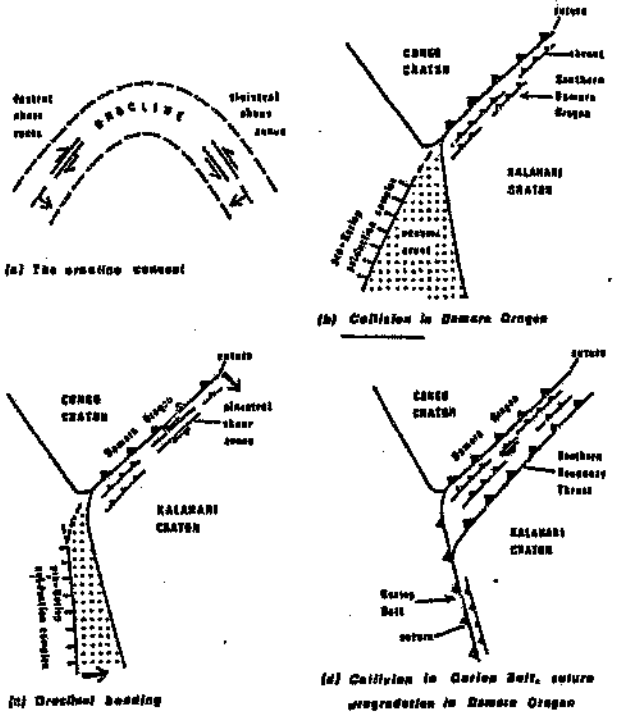


Fig. 6.1: *Oroclinal bending model as suggested by Kasch (1983).*

rotated relative to the inland branch of the Damara Belt prior to its collision in the southern coastal branch (Fig. 6.1).

Davies and Coward (1982) first recognized the important role of large scale thrusting within the Gariep Belt. They presented a model of differential movement in a thrust regime for the origin of the arcuate structures, which were possibly caused by

localized spreading of an obducted thick dense mass of basic volcanic rocks to the southeast. Gravitational instabilities were held responsible for the collapse of the dense mass. Associated spreading caused imbricate faulting in previously undeformed sediments (Fig. 6.2).

Geochemical analyses of basalts of the Grootderm Formation, which are obducted along the Schakalsberge thrust fault within the Marmora Superterrane (Hartnady et al., 1985), indicate a tholeiitic affinity for most of the pile, but in the upper sequences of

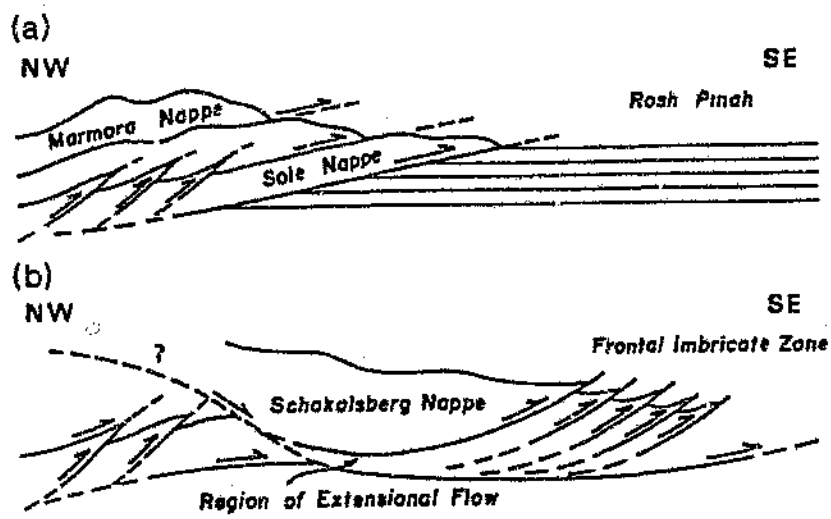


Fig. 6.2: *Cross-sections showing the gravitational collapse model of Davies & Coward (1982).*

the Grootderm Formation, alkali basalts occur (Smith and Hartnady, 1984). Smith & Hartnady (1984) and Hartnady et al. (1985) interpreted a within-plate ocean-floor setting with strong hot-spot or plume-type magmatic source affinities of the ophiolitic Grootderm Formation of the "eugeosynclinal assemblage" in the west of the Gariep Belt of southern Namibia. Hartnady et al. (1985) described the metavolcanics of the Grootderm thrust sheet as being created by an enriched magmatic source distant from any nearby terrigenous sedimentary provenances. He concluded that it could be an accreted upper part of an oceanic island-seamount chain, as suggested by Kröner

(19[illegible], or an aseismic ridge or small oceanic plateau.

The subsequent subdivision of the Gariep Belt into a western Marmora Terrane and an eastern Port Nolloth Zone (Von Veh, 1988; Hartnady & Von Veh, 1990) is based on the facies distinction of the "eugeosyncline" and the "miogeosyncline" described by previous authors, and the recognition of a major tectonic discontinuity, the Schakalsberge thrust fault, within the belt (Davies & Coward, 1982; Stowe et al., 1984; Hartnady et al., 1985). Von Veh (1988) proposed that the Port Nolloth Zone evolved as a rifted, Atlantic-type, passive continental margin on the western edge of the Kalahari Craton. He concluded that the rifting stage with its associated alkaline acid volcanics, tuffs, and agglomerates was followed by a sea-floor spreading stage when the continental margin cooled and subsided as it moved away from a spreading centre, followed by a period of tectonic instability associated with glacial activity. The unconformably overlying Numees Formation diamictites and ferruginous sediments were interpreted as having been deposited in a "continental slope" palaeo-environment. Continuing subsidence is suggested to have caused the deposition of the overlying Holgat sediments in a distal slope or basin environment, while the uplifted hinterland was largely eroded away and shallow water Kuiseb and lower Schwarzrand clastics and carbonates of the Nama Group transgressed onto the adjoining craton. An approaching orogenic front was incorporated in the distal parts of the depositional basin (Von Veh, 1988). Subsequent oceanic closure, which culminated in the collision of the Port Nolloth Zone continental margin with a subduction zone (Hartnady & Von Veh, 199[illegible] and led to the accretion of the Marmora Terrane as an allochthonous block, was suggested to have predated the final closure of the inland branch of the Damara Orogen (Von Veh, 1988). Von Veh (1988) proposed a southward migrating

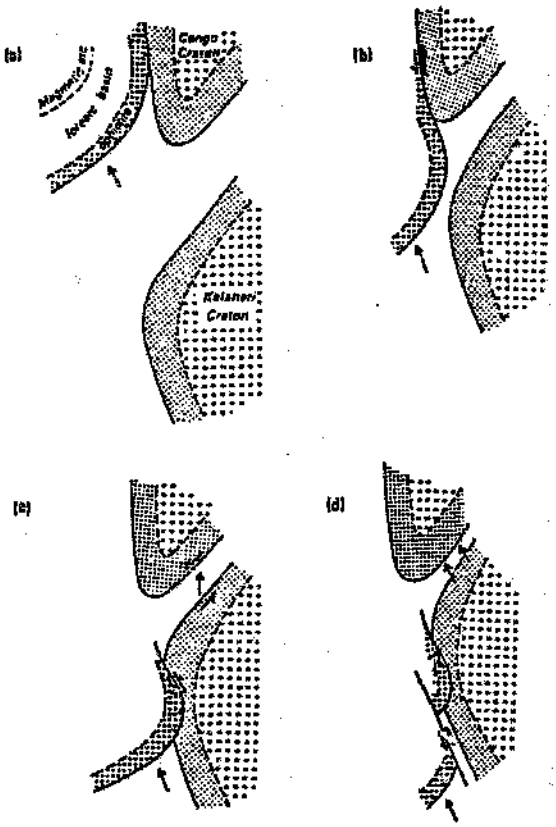


Fig. 6.3: *Schematic diagram showing the proposed southward migrating subduction zone, responsible for the development of the arcuate shape of the Gariep Belt (Von Veh, 1988).*

subduction zone in a direction roughly parallel to the western margin of the Kalahari Craton (Fig. 6.3). Because the obducted Marmora Terrane had become sutured to the Port Nolloth Zone, a major sinistral transform fault is proposed to have developed in an off-shore position at or near the interface between the continental and oceanic lithosphere (Fig. 6.3d). Von Veh (1988) concluded that the Pan-African evolution terminated with the emplacement of the Kubcos-Bremen line of plutons prior to or during the final stages of the closure of the inland branch of the Damara Orogen. This model implies that the orogeny within the inland branch did not predate the orogeny of the coastal branch of the Damara Orogen.

The most recent model proposed for the geodynamic evolution of both the inland and

the coastal branches of the Damara Orogen was proposed by Stanistreet et al. (1991), who described the basinal-sedimentary responses to the opening of the Adamastor Ocean along the coastal branch and the subsequent opening of the Khomas Sea in the inland branch of the Damara Orogen. The model suggests that the Khomas Orogeny involved the subduction of hot young oceanic crust associated with a relatively short residence time of the Khomas Sea, which can be dated at just before the Proterozoic-Cambrian boundary, whereas, in contrast, the Adamastor Ocean had a residence time of about 200 Ma suggesting, therefore, that convergence involved the subduction of cooled oceanic crust and incorporation of exotic terranes (Marmora Superterrane). In this model, the temporal separation of the Khomas and the subsequent Adamastor Orogenies is distinguished (Fig. 6.4). Furthermore, it is proposed that the Nama Group sediments were deposited into peripheral foreland basins, which developed adjacent to the approaching Khomas and Adamastor orogenic fronts.

Global geodynamic models have been proposed by Dalziel (1991), Hoffman (1991) Hartnady (1991) and Moores (1991). The evolution of the Adamastor Ocean and Adamastor Orogeny and their position in regard to a global geodynamic model, in particular, was discussed by Dalziel (1991), Hartnady (1991) and Hoffman (1991), who described the existence of a Late Proterozoic supercontinent (pre-750 Ma), analogous to Pangaea, called Rodinia (McMenamin and McMenamin, 1990). The Late Proterozoic fragmentation of Rodinia centred on Laurentia, followed by rapid fan-like collapse of the present southern continents and the eventual consolidation of East and West Gondwanaland, with a pole of rotation near the Weddell Sea (Hoffman, 1991; Dalziel, 1991), thus explaining the the dominance of wrench tectonics in present west-east

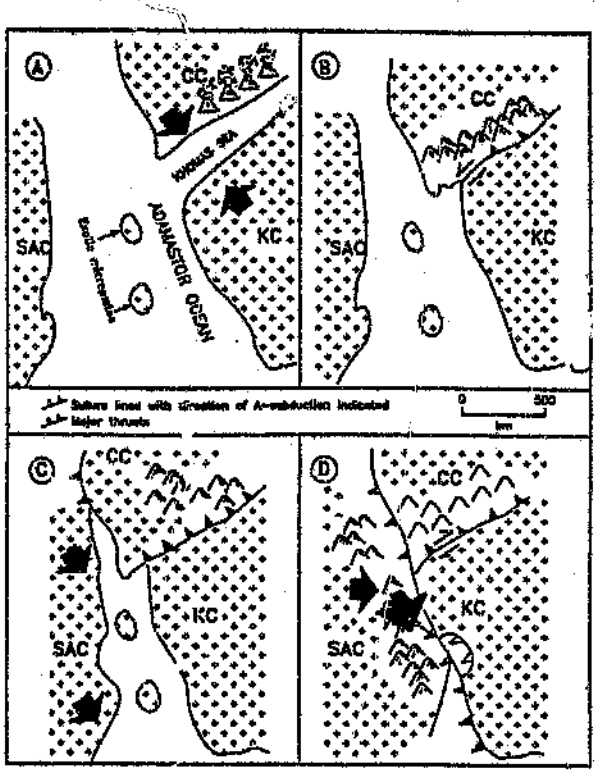


Fig. 6.4: *Schematic diagram showing the cratonic motions during the closure and collisional phases of the Khomas Sea and Adamastor Ocean (modified after Stanistreet et al., 1991). KC= Kalaha· raton; CC= Congo Craton; SAC= South American Continent.*

trending and subduction-accretion tectonics in north-south trending Pan-African mobile belts (Hoffman, 1991). During fragmentation, rifts originating in the interior of the Rodinia supercontinent became the external margins of Gondwanaland, while the exterior margins became landlocked within the interior of Gondwanaland (Hoffman, 1991). Hartnady (1991) also suggested that Laurentia was the centre of the Rodinia supercontinent, flanked by "East proto-Gondwanaland" to the west of it, and "West proto-Gondwanaland" to the east of it. In this model, the southern African block is situated in a hinge position between "East proto-Gondwanaland" and "West proto-Gondwanaland" (Fig. 6.5A). Rodinia was then turned "inside out" around the southern African block, which also rotated in an anti-clockwise sense, giving rise to the opening of the proto-Pacific Ocean and concomitantly the Adamastor Ocean, which forms an

arm of the new proto-Pacific Ocean. The inside out movement of "East proto-Gondwanaland" away from Laurentia in an anti-clockwise sense gave rise to the convergence of "East proto-Gondwanaland" and "West proto-Gondwanaland" and the closure of the Mozambique Ocean, which subsequently resulted in their collision and the formation of the Mozambique metamorphic belt (Hartnady, 1991; Fig. 6.5B).

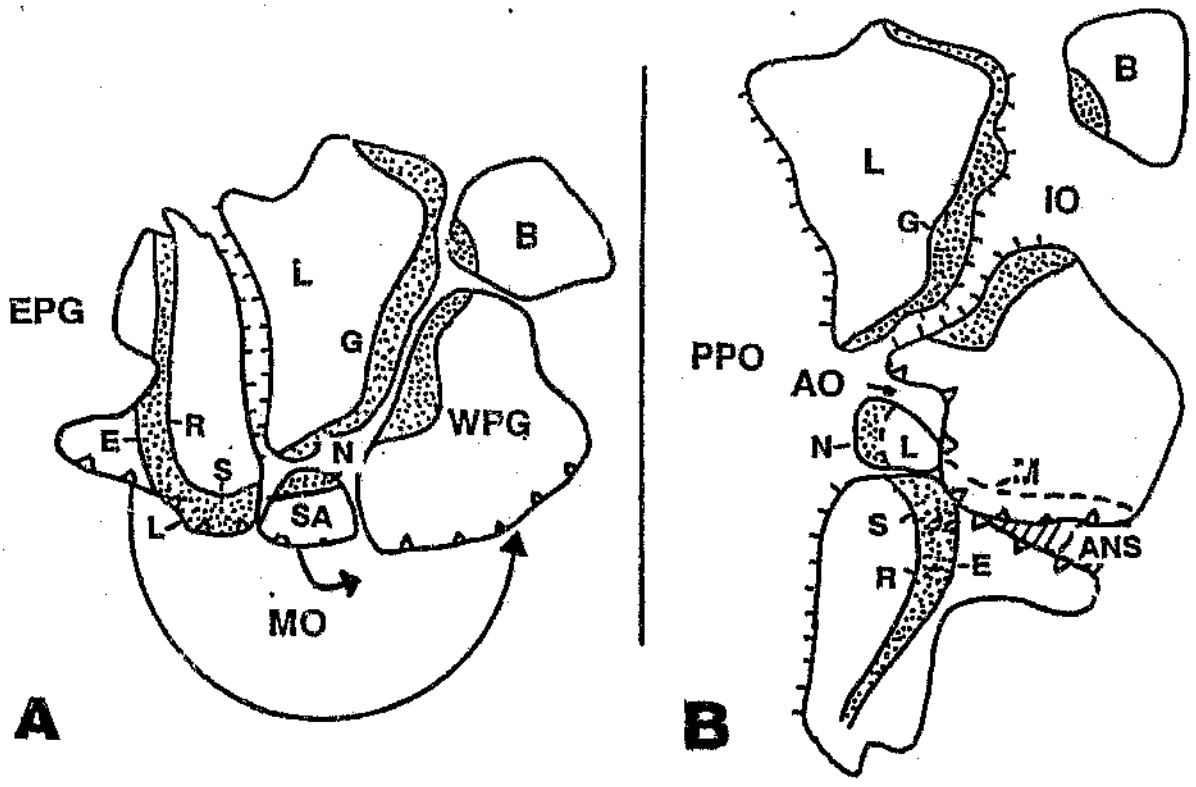


Fig. 6.5: *A) - (modified from Hoffman, 1991; and Hartnady, 1991): Rodinia in its pre-750 Ma old configuration with Laurentia.*
B) - (modified after Hartnady, 1991): the 650-600 Ma old configuration of Rodinia after it has been turned inside out. EPG= East proto-Gondwanaland; WPG= West proto-Gondwanaland; L= Laurentia; B= Baltica; SA= southern African block; G= Grenville belt; N= Namaqua belt; Lu= Lurio belt; S= Sverdrupfjella belt; V= Vijayan belt, E= Eastern Ghats belt; R= Rayner belt; AO= Adamastor Ocean; MO= Mozambique Ocean; PPO= protp-Pacific Ocean; IO= Iapetus Ocean; M= Mozambique metamorphic belt; ANS= Arabian-Nubian Shield.

6.3 TECTONIC INVERSION WITHIN THE GARIEP BELT IN SOUTHERN NAMIBIA

6.3.1 Location of inverted faults

Within the study area an autochthonous area in the east has been differentiated from a parautochthonous area in the west (Fig. 2.4), which comprises a set of basement-cored thrust slices. The major structural boundary between the two is the Rosh Pinah fault, which can be followed over a total distance of about 85 km. It can be delineated from an area situated about 40 km northwest of Rosh Pinah and about 15 km northwest of Trekpoort Farm southeastwards into the Richtersveld, where it splays into the Klipneus, the Grasvlakte and the Vandersterrberg faults (Von Veh, 1988).

In the northern part of the study area, the Rosh Pinah thrust slice and the autochthonous unit to the east of it are juxaposed along the Rosh Pinah thrust fault. In the southern parts of the study area the Dreigratberg thrust slice is juxtaposed with the autochthonous assembledge to the east (Fig. 2.4).

6.3.2 Stratigraphic thickness variations along inverted faults

The untelescoping of thrust faults within the study area reveals considerable lateral thickness variations of stratigraphic sequences, providing direct evidence for faulting during the extensional phase of the evolution of the Gariep Belt.

The important structural boundary represented by the Rosh Pinah fault is coincident with the major stratigraphic break which occurs in the study area. To the east of this

fault, rocks of the Pickelhaube and Numees Formations unconformably overlie basement rocks, to the west of it most of the entire sequence, comprising the Rosh Pinah, Gumchavib and Pickelhaube Formations, unconformably overlie basement (Fig. 6.6).

Because more complete sequences are only preserved to the west of the Rosh Pinah fault, it is obvious that the fault acted with a normal sense of throw with down-to-the-west movement during the sedimentary history. Because this is the most major stratigraphic break, it suggests that the Rosh Pinah fault was the master low angle fault controlling extension in the study area (Fig. 6.7). It is not surprising that the thickest and best developement of the intracontinental rift sequence represented by the Rosh Pinah Formation is preserved just to the west of this major extensional structure.

6.3.3 Tectono-sedimentary history of the study area

Lateral variations in stratigraphic thickness along the Rosh Pinah thrust fault have shown that it has an older history prior to the compressional phase, which affected the sedimentation of almost the entire Gariep Belt. During subsequent compression, inversion took place along the extensional fault to produce an eastward directed low-angle reverse fault, presently exposed as the Rosh Pinah thrust fault zone.

The basin architecture within the Gariep fold and thrust belt has exerted a profound influence on the contractional tectonics in the study area. The geometries of the extensional faults controlled the level of detachment and apparent thrust fault sequences. The example of the Rosh Pinah basin, situated west of the inverted extensional Rosh Pinah fault, demonstrates the extent to which the early basin

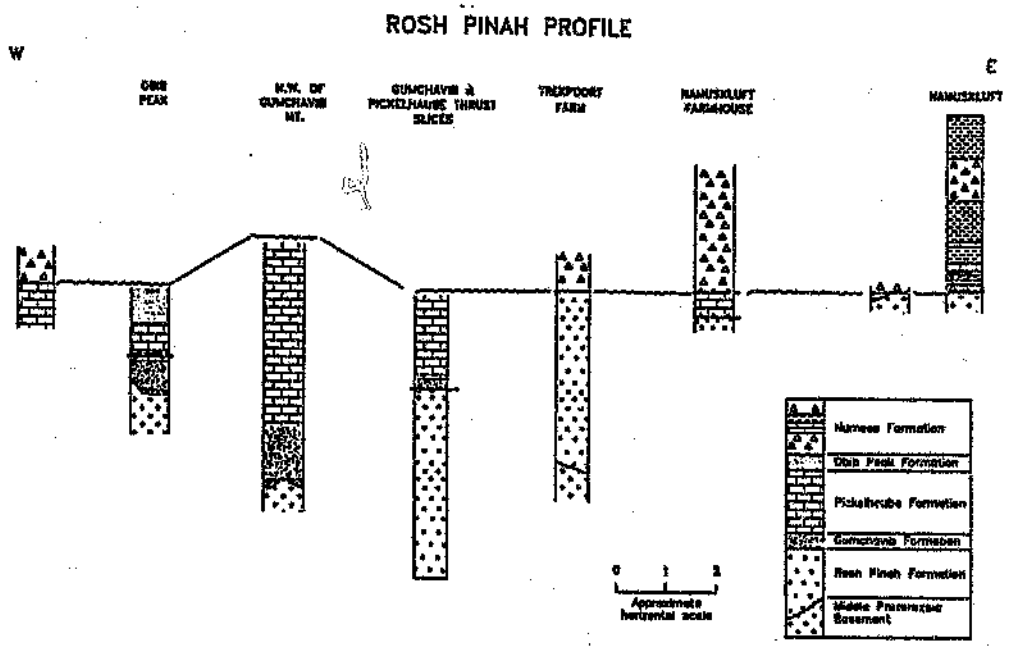


Fig. 6.6: *Schematic diagram showing stratigraphic thickness variations within the study area (for locations see Figs. 1.2 and 2.4).*

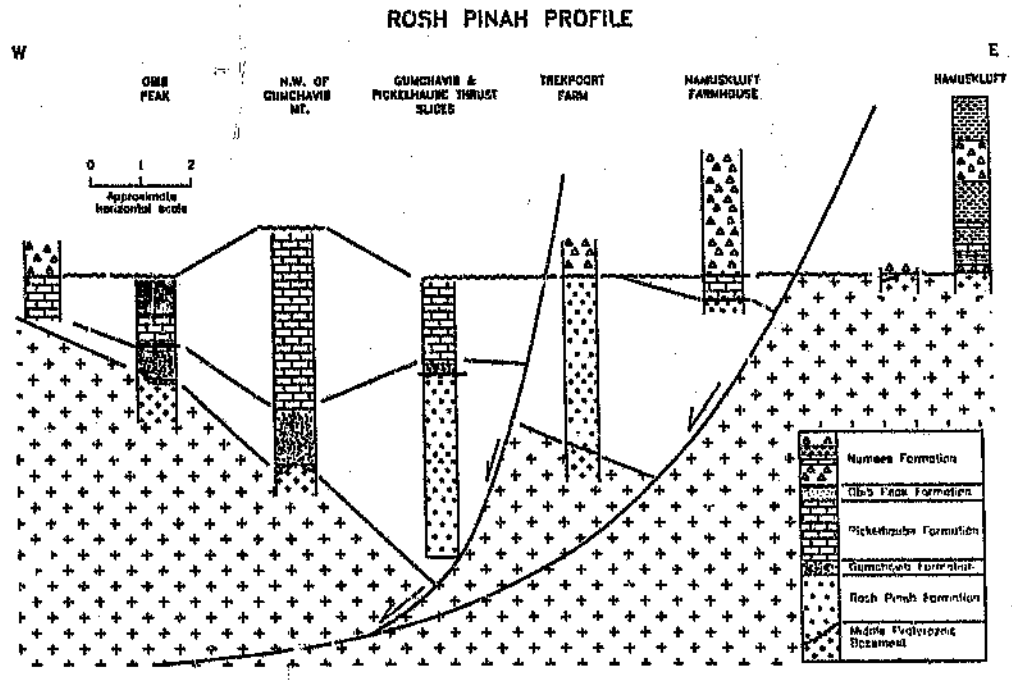


Fig. 6.7: *Interpretation of Fig. 6.6, showing the proposed position of syn-sedimentary faults, which controlled the deposition of the Gariep Group sediments within the study area.*

architecture and characteristics of the associated syn-rift sediments and volcanics shaped this section of the Gariep fold and thrust belt. The Rosh Pinah thrust fault represents a most conspicuous inversion structure. A model that illustrates the sequential contraction and inversion of the Rosh Pinah half-graben system is shown in Fig. 6.8. Another key aspect for the recognition of inversion structures is the identification of a syn-rift (or passive infill) sequence (Cooper et al., 1989). The sediments and volcanics of the Rosh Pinah Formation represent syn-rift deposits and, therefore, add further evidence for the possible presence of structural inversion. The extensional thrust plane (Fig. 6.8a) is reactivated during the early stages of contraction (Fig. 6.8b). During continued contraction lithological boundaries both along the basement contact and within the synrift and post-rift cover sequences are used as thrust planes during the D1 deformational phase (Fig. 6.8c). Further contraction along the same thrust fault planes leads to intense folding and associated thrusting during the D2 deformational phase (Fig. 6.8d). Intense folding and imbrication of the half-graben sediments is attributed to the space problem generated by shortening of the half graben during inversion. In addition, high cut-off angles of faults suggest that imbrication did not only take place during the D1 deformational event, but also during and after folding (D2). Duplex structures are a common feature within the inverted Rosh Pinah half graben.

6.3.4 Inversion tectonics within other fold and thrust belts

The basin architecture of several fold and thrust belts, as shown by the example of the Kechika Trough in the western Rocky Mountains of northern Canada (McClay et al.,

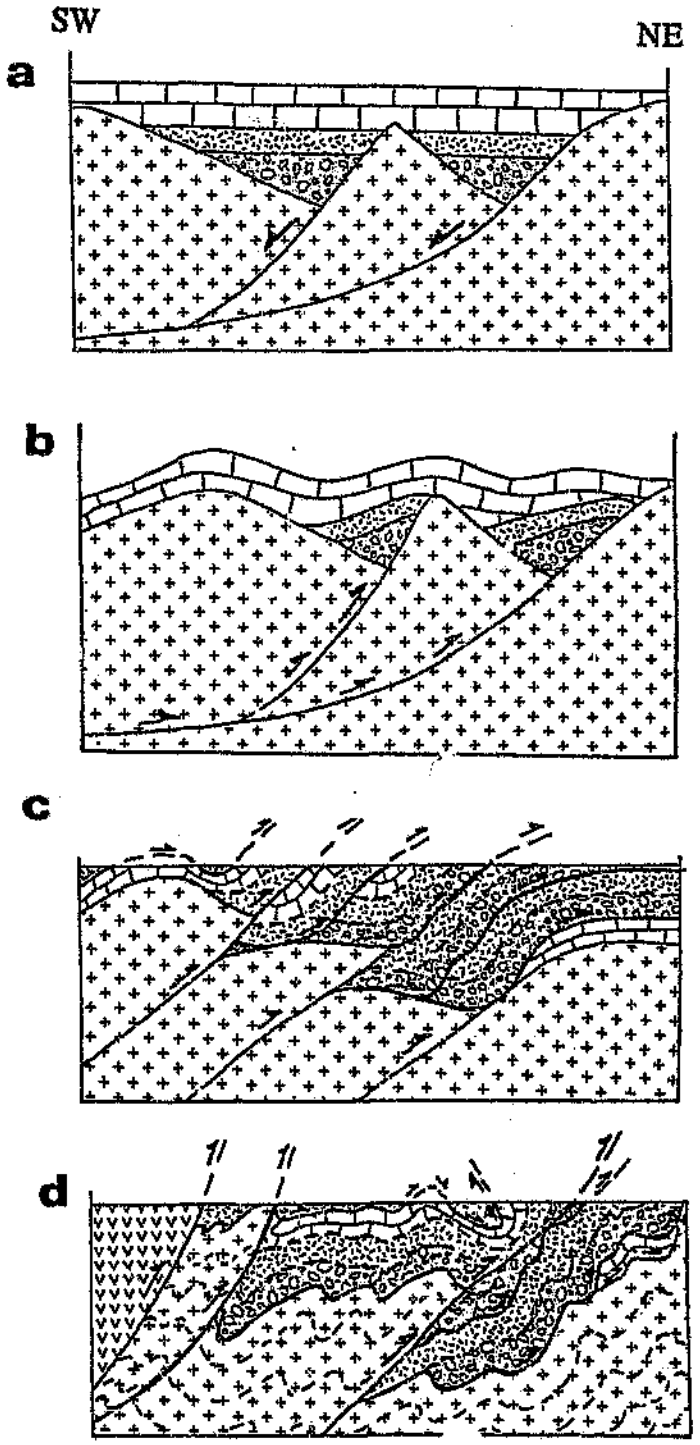


Fig. 6.8: *Schematic model for the inversion of the Rosh Pinah half graben; (a) Pre-inversion geometry of the half graben with deposition of syn-rift sediments and volcanics; (b) Initial inversion showing reactivation of the listric normal fault which bounds the half graben; (c) Continued deformation with ramping and bedding sub-parallel thrusting along the extensional listric fault plane (D1); (d) Subsequent folding and associated thrusting (D2) along the reactivated extensional fault plane.*

1989), can exert a distinct influence on the contractional tectonics. The reactivation of extensional structures during compressional tectonics has been noted in various thrust and fold belts, e.g. the Cordilleran Fold and Thrust Belt (Taylor and Stott, 1973; Thompson et al., 1987; McClay et al., 1989). The recognition of fault inversion and lateral asymmetries of thicknesses of stratigraphic sequences on either side of reversed faults and the presence of syn-rift sediments and volcanics is therefore of great importance as direct proof for extensional faulting.

6.4 TECTONICS AND SEDIMENTATION

The Damara Orogen, of which the Gariep Belt forms part, is one of several orogenic provinces collectively referred to as the Pan-African (Cahen et al., 1984). It has traditionally been divided into an inland branch and a coastal branch. The coastal branch consists of a northern coastal branch, the Kaoko Belt, and a southern coastal branch, which extends southwards to the Gariep Belt. The coastal branch possibly links in a northerly direction with the West Congolian Belt, and in a southerly direction with the Saldanian Belt in the Cape Province of South Africa (Clifford, 1967; Stowe et al., 1984). Because of good outcrop conditions within the Gariep Belt, the relatively low metamorphic grade in its eastern parts (Port Nolloth Zone), and the good preservation of primary sedimentary structures, the Gariep Belt represents a crucial area in interpreting the geodynamic evolution of the coastal branch of the Damara Orogen and its relationship with the inland branch. The synthesis of conclusions from the detailed sedimentological and structural studies within the study area helps to discriminate between the various interpretations given for the geodynamic evolution of the Gariep

Belt. The information gathered in this study, together with information of previous work undertaken by various authors throughout the Gariep Belt, is combined in a model which involves the sedimentary-basinal responses to the opening of the Adamastor Ocean, and the convergence and collision of the Kalahari and South American Cratons associated with the accretion of several exotic terranes. The model proposed in this work adds to the growing evidence, that a supercontinent, analogous to Pangaea, accreted during the Middle to Late Proterozoic (Bond et al., 1984; Dalziel, 1991; Hartnady, 1991; Hoffman, 1991; Moores, 1991; Piper, 1987). This supercontinent subsequently fragmented during the Late Proterozoic/Early Palaeozoic, as testified within southern Africa by early rifting and spreading both along the coastal and the inland branches of the Damara Orogen. The subsequent Khomas and Adamastor Orogenies were integral components of the processes which resulted in eventual reassembly of the previously rifted- and spread-apart crustal fragments to produce western Gondwanaland (Hoffman, 1991).

Several stages of development of the coastal branch have been proposed by Stanistreet et al. (1991) in a model, which includes the geodynamic evolution of both the inland and the coastal branches of the Gariep Belt, as well as the Nama foreland basin. Detailed study of sedimentation, stratigraphy and structure of the Gariep Belt within the study area supports the main features of the model presented by Stanistreet et al. (1991) for the develoment of the southern coastal branch during its extensional phase. Various stages of geodynamic evolution of the Gariep Fold and Thrust Belt will be presented in this section, adding to the understanding of the so far poorly understood Gariep Belt. Four stages of geodynamic development could be distinguished: (i) rifting phase; (ii) supercontinental breakup: opening of the Adamastor

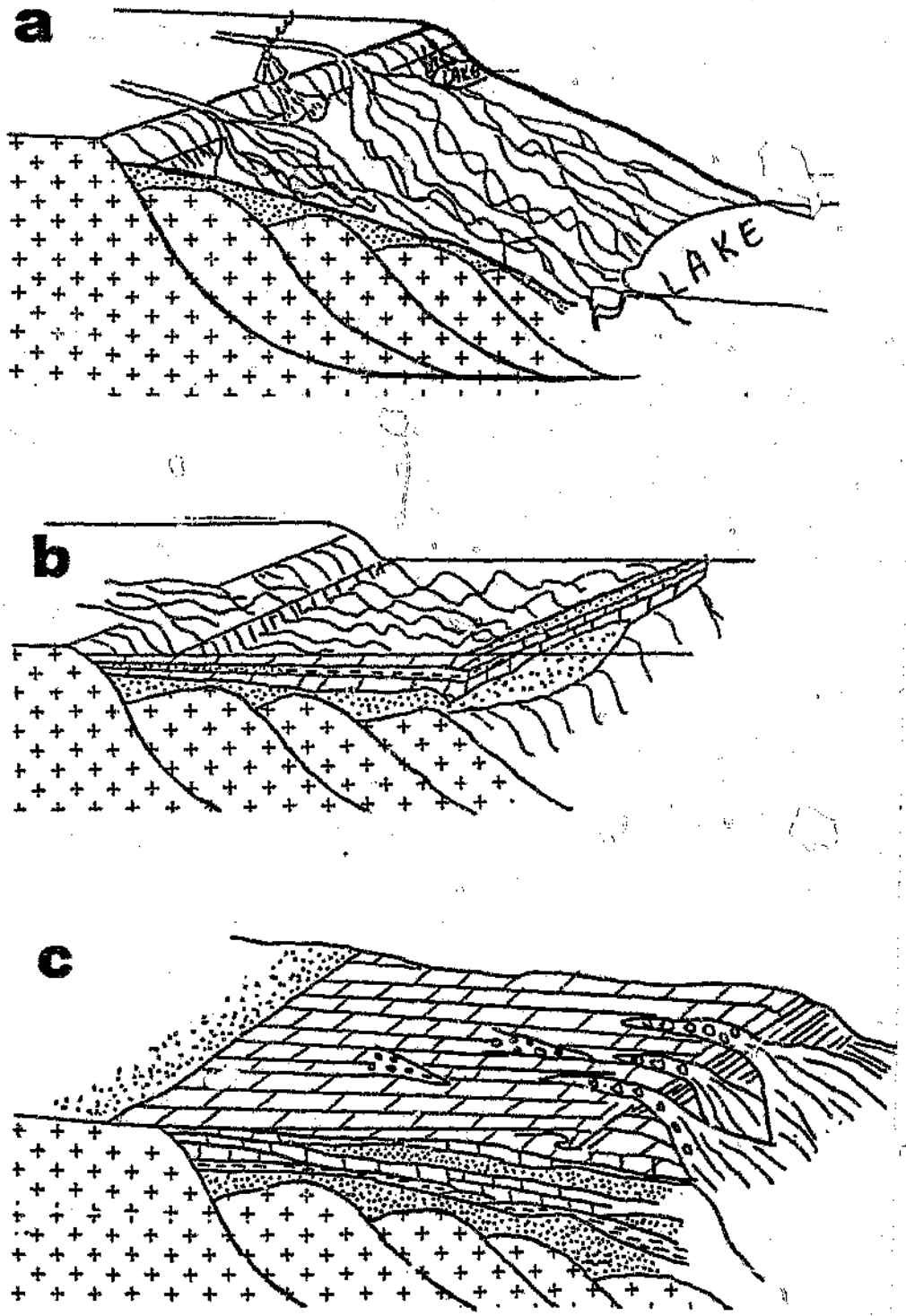
Ocean; (iii) closure of the Adamastor Ocean; (iv) continental collision.

6.4.1 Tectonic framework and evidence of rifting

The evolution of the Gariep Belt in southern Namibia commenced with an initial rift system, recorded by the deposition of immature fluvial and lacustrine sediments and the emplacement of bimodal volcanics. The rift sediments and volcanics were produced by activation of a linked fault system, which may have followed older lines of tectonic weaknesses in the crust, controlled by the Middle Proterozoic Sinclair Belt (Stanistreet et al., 1991), which has been suggested to have developed in association with oceanic closure and orogenesis (Hoal, 1990).

6.4.2 Sedimentary response to intracontinental rifting

The synrift sediments of the Rosh Pinah Formation were deposited in several fault-controlled asymmetric extensional basins. North of the Orange River, the Rosh Pinah Formation forms the lowermost stratigraphic unit of the Stinkfontein Subgroup. The sediments of the Rosh Pinah Formation were deposited within a continental environment, associated with syn-sedimentary faulting and bimodal volcanism. Coarse conglomerates and sandstones, derived by sub-aerial erosion of uplifted fault blocks and dominated by large extra- and lesser intrabasinal clasts, poured westwards into the Rosh Pinah trough, which was dominated by fluvial and lacustrine sedimentation (Fig. 6.9a). The coarse conglomerates and sandstones were deposited as subaqueous


a
LAKE
b
c

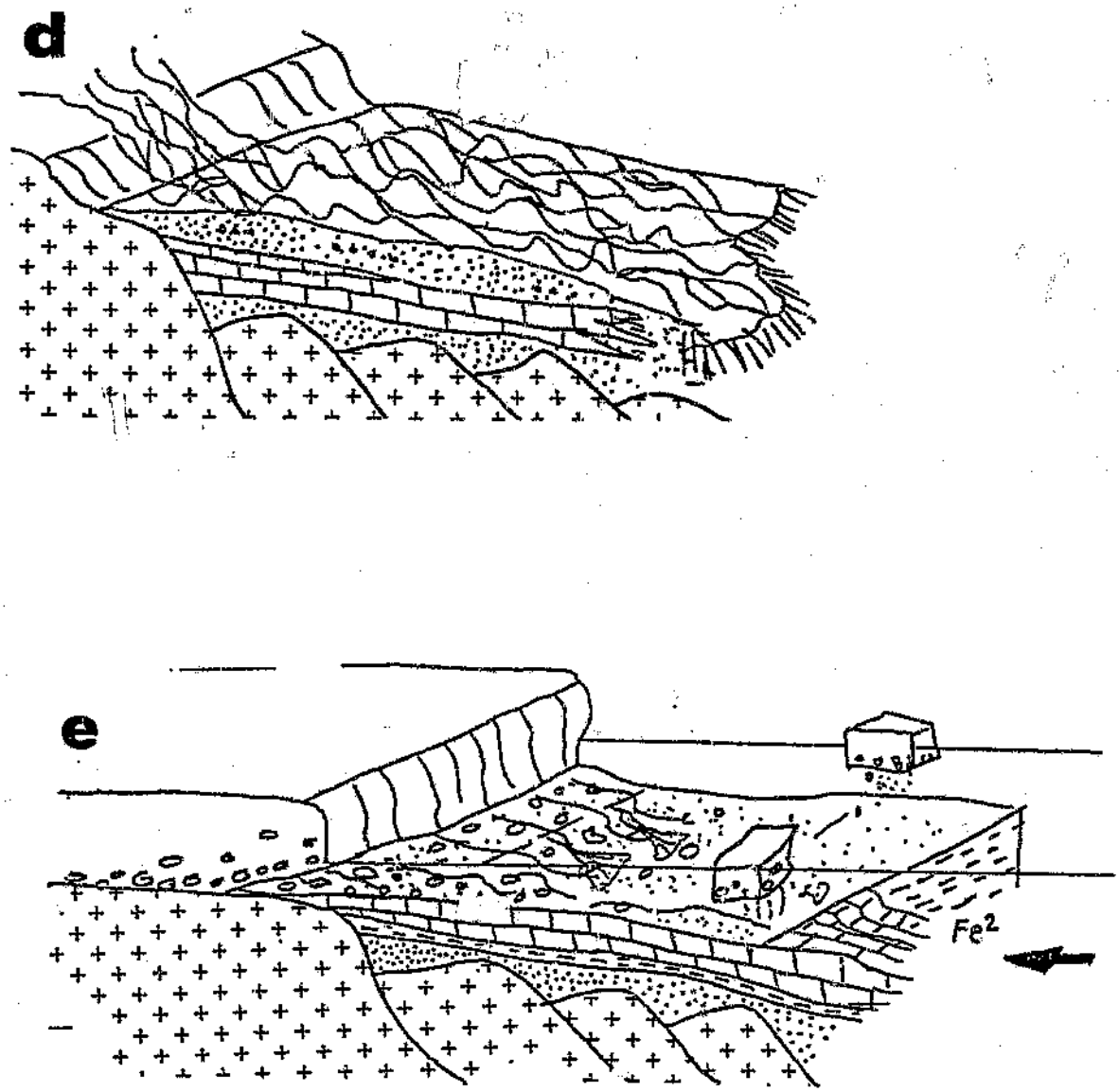


Fig. 6.9: *(Fig. 6.9a, b and c on opposite page) Summary diagrams showing stages during the deposition of the sedimentary and volcanic rocks of the Garlep Group. (a) Deposition of Nosh Pinah fluvial, lacustrine, and alluvial fan sediments associated with volcanism during the rift stage. (b) First marine transgressions characterized by interbedded distal fluvial and shallow marine carbonates and beach deposits, indicating continued rifting. (c) Marine transgression accompanied by influx of siliciclastic sediments and the formation of a carbonate platform, a carbonte shelf, and deep sea deposition of the Holgat beds during Pickelhaube times, indicating that the Kalahari Craton and South America separated, and sea floor spreading began in the Adamastor Ocean. (d) Regression of marine sediments and deposition of continental sediments. (e) Deposition of mainly glaciomarine sediments during Numees glaciation, associated with the development of a major unconformity prior to Numees sedimentation.*

fans and fan deltas, prograding into lake bodies within the half grabens. The debris flow nature and the lack of mud matrix and coarse average clast size of the conglomerates indicates that they were deposited rapidly, associated with the marked extension and rapid subsidence of the rift system as a series of half-graben and sub-basins.

The various depositional cycles, recorded within these sediments, were probably triggered by pulses of synsedimentary faulting along the extensional fault systems. At Spitskop and at Trekpoort Farms, which are situated in the east of the Garlep Belt, the volcanics were extruded as fissure eruptions which were conducted along the major syn-sedimentary fault zones. Several isolated volcanic cones probably developed. Basinal subsidence causing rapid erosion of the basement rocks at the same time as the cyclic volcanic eruptions were responsible for the complex stratigraphic relationships between the volcanics and the sedimentary rocks. Simultaneous with the pronounced volcanic activity in the north of the study area, volcanic activity appears to be less intensive further south from Spitskop Farm towards Rosh Pinah.

South of the Orange River, the Stinkfontein Subgroup comprises a considerably thicker succession of clastics of a more mature composition.

Continued rifting, which subsequently led to initiation of oceanic spreading of the Adamastor Ocean, is indicated by the transgression represented by the mixed continental/shallow marine Gumchavib Formation, which records the earliest marine transgressions (Fig. 6.9b).

6.4.3 Dating of rifting and oceanic opening

The Lekkersing granite, which is intrusive into Stinkfontein lithologies in the Richtersveld, has been dated at 780 +/-10 Ma (Pb-U zircon age; Allsopp et al., 1979), representing the most likely age constraint for the initiation of rifting in the Gariep Belt. This age constraint for the initiation of rifting is supported by the Rb-Sr mineral-isochron age of 717 +/-11 Ma, achieved from basic volcanics of the Gannakouriep dyke and sill swarm in the Richtersveld (Ransome and Reid *in*: Hartnady and Von Veh, 1990), which is intrusive into the Stinkfontein Subgroup and the lower Pickelhaube Formation. A Rb-Sr mineral-isochron age of 719 +/-28 (Welke, in: De Villiers, 1968) obtained for the Rosh Pinah Formation felsites probably also represents a primary age, rather than the mineral-errorchron age of 686 +/-32 Ma (Allsopp et al., 1979), obtained for the Rosh Pinah felsites. The Richtersveld Complex and the older Bremen granites, which are unconformably overlain by Stinkfontein lithologies, yielded ages of ages of 920 +/- 10 Ma and 911 +/- 30 Ma respectively (Allsopp et al., 1979). These were suggested by Von Veh (1988) and Hartnady and Von Veh (1990) as representing the oldest possible age bracket for the initiation of rifting. If rifting did, however, initiate at around 900 Ma, then the period between initiation and cessation of rifting would range at about 200 Ma, which is geologically not viable for continuous rifting processes assumed for the Gariep Belt rift system. If a duration of 200 Ma was postulated for rifting within this rift system, it would have to have occurred in several pulses separated by tectonically quiescent periods, as described from the North Sea (Sclater & Christie, 1980). There is, however, no direct evidence to support this in the southern coastal branch of the Damara Orogen and these dates are more likely to represent ages of the Middle Proterozoic basement (Hoal, 1990).

6.4.4 Oceanic opening and thermal subsidence

The Pickelhaube Formation, which conformably overlies the Gumchavib Formation, records a continuous transgression, which was related to thermal subsidence after the initiation of oceanic spreading of the Adamastor Ocean (Stanistreet et al., 1991). The absence of any apparent regional break-up unconformity separating the rift deposits from the post-rift deposits might indicate that rifting was unaccompanied by doming (Miller, 1987). A carbonate platform and carbonate shelf developed sediments of the Pickelhaube Formation (Fig. 6.9c).

6.4.5 Renewed rifting and/or glacial outwash? - the Obib Peak Formation

The Obib Peak Formation, which overlies the Pickelhaube Formation conformably within the study area, reflects a marked change from the marine sedimentation of the Pickelhaube Formation to continental sedimentation (Fig. 6.9d). The preservation of Obib Peak Formation lithologies west of the Rosh Pinah fault and the absence of these lithologies to the east of the fault suggests that syn-sedimentary faulting was clearly operative during Obib Peak Formation sedimentation.

Various processes might be called on to account for this sudden break in marine sedimentation:

(i) renewed rifting,

(ii) glacial outwash heralding the advance of the Numees glaciation and associated dropping sealevel changes and

(iii) a combination of these two processes.

6.4.6 Glaciation

The deposition of the Obib Peak Formation was followed by the Numees glaciation, which is contemporaneous with the 670 Ma old Varangian glacial episode in Europe and the Rapitan glacial episode in northwest Canada (Harland, 1983; Hambrey & Harland, 1985).

The Numees Formation was deposited within a predominantly glaciomarine setting, although the sedimentary record indicates interruption by several interglacial phases. The diamictites were deposited on the shelf as a debris flow, which comprises reworked sediments, dumped at the ice-front. Floating ice sheets and icebergs caused dropstone formation (Fig. 6.9e). Interglacial periods account for the redeposited carbonate beds and the deposition of deltaic and fluvial sediments, which are interbedded with the glacio-marine diamictites. Felsic volcanics and amphibolite sills, which intruded into the interglacial sediments, suggest the possibility of renewed rifting during the deposition of the Numees Formation, possibly associated with the opening of the Khomas Sea (Henry et al., 1988). Iron formations within the glaciamarine diamictites of the Numees Formation may also be related to renewed rifting and associated spreading ridges.

Because of the absence of sediments overlying the Numees Formation, in contrast with the case in the inland branch, where the Karibib Formation carbonates overlie Chuos Formation diamictites, the 670 Ma age serves only as a minimum age for the end of deposition of Gariep Group lithologies.

6.5 MINERALIZATION AND VOLCANISM IN THE WESTERN VICINITY OF THE INVERTED ROSH PINAH FAULT

A thick pile of intermediate to felsic volcanics of the Rosh Pinah Formation has been deposited within the Gariep Belt in southern Namibia. The most prominent outcrops of mainly felsic volcanics are situated at Spitskop Farm about 10 km northwest of Rosh Pinah, and at Trekpoort Farm, about 25 km northwest of Rosh Pinah (Fig. 1.2). The formation of carbonate- and shale-hosted synsedimentary, stratiform Zn-Pb-Cu-Ag-(+Ba)-sulphide mineralization (SEDEX) was associated with volcanism during the deposition of the Rosh Pinah Formation. Several basemetal-sulphide deposits have been discovered so far. The most prominent deposit is situated at Rosh Pinah Mountain, where 11,5 tons of ore have been mined since 1969, leaving about 11 tons of proven ore with about 6,5% Zn, 1,8% Pb and 0,1% Cu to be mined in the future (personal communications R.P. Randell). An oxidized Zn-Pb-Cu-Ag-(+Ba)-sulphide deposit at Skorpion exploration camp, situated within Diamond Area No.1, approximately 17 km northwest of Rosh Pinah, revealed ore reserves of about 8,3 million tons at about 10,9% Zn. This deposit is, however, exceptionally deeply oxidized, locally exceeding 800m below surface (Corrans, 1983). Geochemical stream sampling of watercourses draining volcano-sedimentary rock ridges at Trekpoort Farm revealed strong geochemical anomalies, indicating the presence of a further major Zn-Pb-Cu-Ag mineralization (personal communications J. Dean).

All these deposits, as well as the intermediate to felsic volcanics are situated in the immediate western vicinity of the Rosh Pinah thrust fault.

The sulphide-mineralization is considered to have formed from metalliferrous brines which ponded in local extensional basins during crustal extension during the rift stage.

The acid to intermediate volcanics of the Rosh Pinah Formation also discharged along these active growth faults.

The fact that the volcanics and the sulphide mineralization were all discharged in the western vicinity of the Rosh Pinah thrust fault adds further indirect evidence to the suggestion, that the Rosh Pinah thrust fault had an extensional history prior to its inversion.

A minor sulphide mineralization and associated gossan was found on surface within the Rooikat thrust slice. West of the Rooikat thrust fault and east of the Ostrich thrust slice (Figs. 2.3 and 2.4), an approx. 1000 m thick succession of Rosh Pinah sediments is interbedded with acid volcanics and minor Zn-Pb-sulphide mineralisation. The absence of any volcanics east of the Rooikat thrust fault, the great thickness of the Rosh Pinah Formation within this thrust slice, as well as the fact that the Rooikat thrust slice links in a southerly direction with the prominent Ostrich thrust fault, which thrusts granitic basement ov a thin sequence of Rosh Pinah Formation sediments, suggests the existence of a restricted extensional subbasin within the Rosh Pinah basin.

6.6 EFFECTS OF OCEANIC CLOSURE AND CONTINENTAL COLLISION

Rifting and spreading was followed by the closure of the Adamastor Ocean, associated with a northwestward directed subduction of oceanic crust under the Kalahari Craton (Fig. 6.4). Subduction was associated with the development of tectonic melanges and the accretion of three allochthonous exotic terranes, namely the Chamais, Oranjemund, and Schakalsberge terranes, which form the Marmora Superterrane (Hartnady et al., 1990). The Marmora Superterrane and the Port Nolloth Zone are

juxtaposed along the Schakalsberg thrust fault (Fig. 2.1). Oceanic closure culminated in the collision of the Port Nolloth Zone continental margin and the accreted Marmora Superterrane as an allochthonous tectonic block. The collision of the South American Craton with the Port Nolloth Zone continental margin was associated with the obduction of ophiclitic material on top of the Schakalsberge thrust fault. The collisional event was accompanied by intense southeastward and susequently eastward directed tectonic transport (D1 and D2), resulting in intense folding and thrusting of Port Nolloth Zone sediments and volcanics during the Adamastor Orogeny. Associated with the Adamastor orogenic event is the development of a peripheral retroarc foreland basin to the east, into which sediments of the Schwarzrand and Fish River Formations Formations of the Nama Group were deposited (Stanistreet et al., 1991). Folding and thrusting, associated with the D2 deformational event, also affected Nama Group sediments in the eastern parts of the Nama basin. After the collision of South America and the Kalahari Craton, a sinistral movement developed along the defined fault zones, deforming both Gariep and Nama Group sediments as far east as Vioolsdrif, approximately 50 km east of the easternmost Gariep Belt outcrop in the Richtersveld. The collisional event was accompanied by a Barrovian Type metamorphism with a geothermal gradient of about 20 degrees C/km. The tectonic evolution of the Gariep Belt continued with the emplacement of the granitoids of the "Kuboos-Bremen-line" (525 +/- 60 Ma; 521 +/- 12 Ma) and the younger part of the Bremen complex intrusives (521 +/- 12 Ma; Allsopp et al., 1979) during the deposition of upper Nama Group sediments. The Nama Group sediments were shed into a foreland basin, marginal to the advancing Adamastor orogeny. Ages gained from Nama Group sediments range from 547 to 443 Ma (compiled by Miller & Grote, 1988) and were

reinterpreted by Stanistreet et al. (1991) as metamorphic ages. Similar metamorphic ages from the Vanrhynsdorp Group sediments, which represent the southern correlative of the Nama Group in Namaqualand, South Africa, range from 552 to 476 Ma with a peak at 496 Ma (Gresse et al., 1988) and also indicate that the Adamastor orogeny within the Gariep Belt only ceased at about 500 Ma. Horstmann et al. (1990) reported K/Ar ages of upper Nama Group sediments from southern Namibia, which may be indistiguishable from the 496 Ma peak metamorphism of Gresse et al. (1988) within the limits of experimental error. These ages may, however, also indicate that a time trangressive collision from north to south occurred during the final stages of the geodynamic evolution of the Gariep Belt and the associated Nama foreland basins (Stanistreet et al.; 1991).

6.7 CORRELATION OF THE GARIEP BELT WITH OTHER PARTS OF THE DAMARA OROGEN

Various models have been proposed for the geodynamic evolution of the Damara Orogen. The latest model, proposed by Stanistreet et al. (1991), differentiates between the tectonosedimentary evolution of the inland and the coastal branches, proposing that the extensional history of the coastal branch took place prior to that of the inland branch. According to this model, the Khomas Sea closed prior to the closure of the Adamastor Ocean. If this is the case, the temporal difference of geodynamic evolution would mean that a direct stratigraphic and tectonic correlation of the inland and the coastal branches is only applicable to a certain extent. On the other hand, comparisons with other areas of the coastal branch would allow a test of whether the

concept of an Adamastor Orogeny is valid.

6.7.1 Stratigraphic correlation of the Gariep Belt with other parts of the Damara Orogen

Correlation within the Gariep Group Zone

Correlations of stratigraphic units of the Bogenfels area with stratigraphic units of the Gariep Belt immediately north of the Orange River have so far not been attempted. Reconnaissance mapping of the Bogenfels area in the north-western parts of the Sperrgebiet and reconaissance work undertaken by Davies and Coward (1982) reveals the presence of a banded dolomite overlain by massive blue-grey dolomite, referred to as the lower and upper dolomite units of the Bogenfels Formation (Davies & Coward, 1982). These dolomite units bear a striking resemblance to the dolomitic carbonates of the Pickelhaube Formation in the study area. In the district of Pomona, situated south of Bogenfels (Fig. 1.2), a discontinuous conglomerate unconformably overlies granitic gneisses, augengneisses and schists assigned to the Namaqualand Metamorphic Complex. The conglomerate forms the base of a sequence and is followed by feldspathic grit, arkoses, thin interbanded yellow dolomites and massive, cross-bedded sandstones and quartzites, which comprise the base of the Bogenfels Formation (Davies & Coward, 1982). This "basal clastic member' of the Bogenfels Formation resembles the Gumchavib Formation in the area north of the Orange River, both in lithological composition, and in terms of its interpreted depositional palaeoenvironment.

Reconnaissance mapping carried out in the area immediately south of Lüderitz, revealed the presence of a several tens of metres thick succession of interbedded quartz-arenitic sandstones and interbedded dolomites, which was previously mapped as basement (SWA/Namibia Geosurvey Map, 1982). This formation, which has not been described previously, will be referred to as the Lüderitz Formation and can be correlated with the Gumchavib or the lowermost Pickelhaube Formation within the study area, reflecting deposition within a shallow marine shelf environment.

The Diaz Point Formation (Greenman, 1966; Siegfried, 1992/1993) consists of a sedimentary mixtite bordering the coastline of Namibia from Lüderitz southwards to Atlas Bay. Greenman (1966) first interpreted these metasediments, which are conspicuously different from the gneissic basement ascribed to the Namaqua Metamorphic Complex, as being part of the Gariep Group. Kröner and Jackson (1974) reinterpreted the Diaz Point Formation as refoliated basement, but present consensus is that they represent Gariep age lithologies that have been highly tectonized (SACS, 1980; SWA/Namibia Geosurvey Map, 1982; Siegfried, 1992/1993). Siegfried (1992/1993) correlates the Diaz Point Formation with the Numees Formation of the Gariep Group, because of the gross similarities in mineral and clast composition.

The latest attempt to correlate stratigraphic units throughout the Damara Belt was undertaken by Hoffmann (1989). His correlation of the Gariep Group stratigraphy with other parts of the Damara Sequence is mainly based on stratigraphic and structural work presented by Von Veh (1988) for the Gariep Belt in the Richtersveld. The present sedimentological and structural investigations within the study area have, however, revealed, that the stratigraphic subdivision of the Gariep Belt, as proposed by Von Veh (1988), has to be partly revised for southern Namibia (Table 2.2), as structural

repetition and lateral and vertical sedimentary facies variations in the structurally highly complex Richtersveld have not always been recognized correctly. In southern Namibia, the Rosh Pinah Formation forms the lowermost stratigraphic unit in the southern parts of the Gariep Belt, overlying the basement unconformably at several localities. The Wallekraal Formation, integrated by Von Veh (1988) into the Hilda Subgroup, forms part of the Rosh Pinah Formation. Stratigraphic correlations of the Gariep Group lithologies within Diamond Area No.1 in southern Namibia are summarized in Table 6.1.

Table 6.1: *Stratigraphic correlation of Gariep Group lithologies of southern Namibia.*

Southern Diamond Area No.1 (this work)	Bogenfels and Pomona areas (Davies & Coward, 1982)	Lüderitz and Diaz Point areas (this work; Siegfried, 1992/1993)
Numees Formation		Diaz Point Formation
Obib Peak Formation		
Pickelhaube Formation	"lower and upper dolomite unit" of Bogenfeld Formation	
Gumchavib Formation	"basal member" of Bogenfels Formation	Lüderitz Formation
Rosh Pinah Formation		

Correlation with the inland branch

The Kaigas, Jakkalsberg, and Numees Formations, described by Von Veh (1988) as independent lithostratigraphic units, form one stratigraphic unit, defined here as the Numees Formation. The Holgat Formation is a distal lateral facies equivalent of the Pickelhaube Formation, and therefore underlies the Numees Formation

stratigraphically. The absence of a lower diamictitic unit, the Kaigas Formation (Von Veh, 1988), is of great importance for the correlation of stratigraphic units of the Gariep Group with other parts of the Damara Sequence. Hoffmann's (1989) attempt to correlate the Gariep Group stratigraphy with other parts of the Damara Sequence was based on the presence of two distinct diamictitic units, the lower Kaigas Formation of the Stinkfontein Sungroup, and the upper Numees Formation. Hoffmann (1989) also included the Rosh Pinah Formation in the Hilda, and not the lower Stinkfontein Subgroup. The Stinkfontein Subgroup, comprising cross-bedded arkoses, feldspathic quartzites, conglomerates, and minor intercalated acid to intermediate volcanics, was described by Hoffmann (1989) as "virtually identical to the Nosib Group in the southern Damara Belt (inland branch) and elsewhere in the central and northern Damara Belt". As the Rosh Pinah Formation forms the bulk of the Stinkfontein Subgroup in southern Namibia, a correlation of the Rosh Pinah Formation with the Nosib Group of the inland branch, as well as the Nosib Group of the northern coastal branch of the Damara Orogen, is applicable.

As the inclusion of the Wallekraal Formation (part of the Rosh Pinah Formation) into the Hilda Subgroup is not correct, the striking resemblance between the Pickelhaube and Dabie River Formations, described by Von Veh (1988) from the Richtersveld, allow their correlation as a single stratigraphic unit, in a similar fashion to the sequence defined here north of the Orange River. This carbonate unit, referred here to as the Pickelhaube Formation, also incorporates the more distal "Holgat Formation", and was correlated by Hoffmann (1989) with the Kudis and lower Vaalgras Subgroup and their stratigraphic equivalents in the Naukluft Nappe Complex and foreland sequence, respectively.

Correlation with the northern coastal branch

A striking similarity exists between the Rosh Pinah Formation of the Gariep Belt and the Nosib Group in the northern coastal branch, both in lithology and palaeoenvironmental setting (Table 6.2). The pelites and carbonates of the Omuhiva Formation in the Kaokoveld, which were deposited in a lacustrine depositional setting, may also be correlatable with the Rosh Pinah Formation, which was deposited in a mixed fluvial/lacustrine depositional setting (Table 6.2). The Omuhiva Formation may, however, also form part of the Gumchavib Formation of the Gariep Belt. The Omuhiva and Outuwo Formations of the Ugab Subgroup in the northern coastal branch (Kaoko Belt) of the Damara Orogen (Henry et al. 1992/1993) were deposited within a playa lacustrine or/and shallow marine environment and resemble the sediments of the Gumchavib Formation in the study area, which were deposited in a similar palaeoenvironment, representing the transition from a predominantly continental to a marine environment. The overlying Okarondokavi, Otjorongwari, and Okovikuti Formations, which comprise a sequence of pelites, psammites, diamictites and meta-basaltic volcanics, interbedded with carbonate beds, were interpreted as being deposited within a marine environment, including submarine turbidite fan and debris flow deposition (Henry et al., 1992/1993). A within-plate alkaline signature for the basalts of the Okovikuti Formation is indicated by major and trace element plots (Henry et al., 1992/1993). The Okarondokavi and Otjonrongwari Formations can possibly be correlated with the deepsea Holgat beds of the Pickelhaube Formation (Table 6.2).

Table 6.2: *Lithostratigraphic correlation of the northern and southern coastal branches of the Damara Orogen.*

Southern coastal branch	Lithologies	Northern coastal branch (Henry et al., 1992/1993)
Numees Formation	Diamictite (Glacio-marine)	Chuos Formation
Obib Peak Formation Pickelhaube Formation	Pelites/siliciclastics/carbonates/ meta-basalts (marine -> fluvial)	Okovikuti Formation Otjorongwari Formation Okarondokavi Formation
Gumchavib Formation	Orthoquartzites (shallow marine)	Cutuwo Formation
Rosh Pinah Formation	Pelites/carbonates (lacustrine) Arkoses/conglomerates (alluvial fan/fluvial)	Omuhiva Formation Nosib Group

The Numees Formation of the Gariep Belt is correlated with the Chuos Formation of the inland and the northern coastal branches of the Damara Orogen for several reasons:

(1) both consist mainly of diamictites, which were deposited within a glacial palaeoenvironment and resemble each other lithologically;

(2) both were deposited within similar palaeoenvironments during an extensive glaciation;

(3) both include laterally inconsistent banded iron formations with dropstones disrupting lamination;

(4) both contain interbedded, laterally inconsistent carbonate beds; and

(5) both were deposited after the deposition of carbonate dominated shelf, and in the case of the northern coastal branch, associated deep marine environments.

6.7.2 Correlation of tectonic events of the Gariep Belt and other parts of the Damara Orogen

Three progressive deformational events (D1, D2, D3), associated with the closure of the Adamastor Ocean and associated collision between proto-South America and the Congo and Kalahari Cratons, were recognized in this study in the southern coastal branch (Gariep Belt).

Correlation within the Gariep Zone

A structural pattern similar to that developed in the study area, is present in the Richtersveld, where an early, bedding sub-parallel cleavage was folded around the fold hinges of north- to northwest-trending small to large scale (>4 km wavelength) folds with a generally easterly vergence, changing to a westerly vergence in the vicinity of the basement outcrop to the east. The latest deformational event also forms open west- to southwest-trending folds (Von Veh, 1988). The intrusion of the Kuboos Pluton generated a radial fold trend of minor folds, which is not recognizable in southern Namibia and is therefore only of minor importance (Von Veh, 1988).

In the Bogenfels area, in the north-western part of the Sperrgebiet, the earliest deformational event is characterized by a bedding sub-parallel cleavage and foliation, which was folded around fold hinges of north- to northwest-trending small to large scale (up to several hundreds of metres) open to isoclinal folds with an easterly vergence. These structural features reflect a similar tectonic history to that in the areas adjacent to the Orange River. The warping of the D2 related folds may be related to the presence of approximately west-east-trending folds, similar to the F3 folds in the study area and the northwestern Richtersveld.


m W
2000
1000
0
WKZ
Mudorid River
CKZ
Hoanib River
EKZ
E

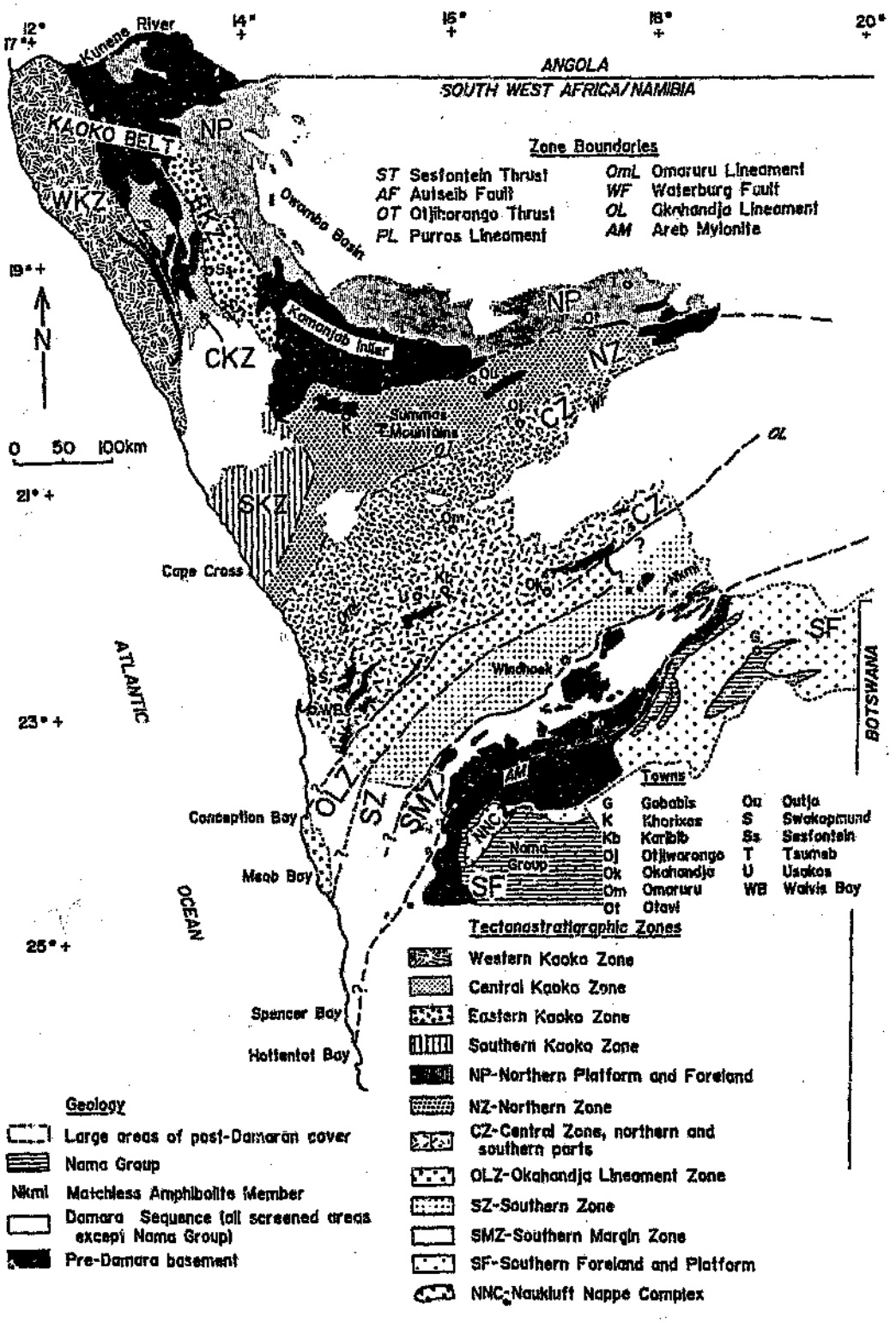


Fig. 6.10: *Tectonostratigraphic zones of the Damara Orogen (from Miller, 1983)*

Fig. 6.11: *(opposite page) Structural E-W cross-section across the Kaoko Belt, Sesfontein area (from Miller, 1983).*

Structural investigations undertaken by Siegfried (1992/1993) south of Lüderitz revealed that two deformational events are preserved. These are characterized by the presence of north-south trending thrust faults, northwest-southeast trending normal faults, and a dominant bedding parallel foliation striking at 240 degrees with a northwesterly dip of 16 degrees, associated with an intense mineral lineation trending at 15 degrees on a bearing of 330 degrees, which have been generated as the result of continued unidirectional compression from north-northwest. Siegfried (1992/1993) correlates these structural features with the D1 deformational event of the Gariep Belt at the Orange River. A crenulation cleavage, trending 04 degrees on a bearing of 230 degrees is concordant with folds developed towards the end of D1 or during a less well-developed D2 deformational event (Siegfried, 1992/1993), which correlates with the D2 deformational event developed in the southern Sperrgebiet and the Richtersveld.

Correlation with the northern coastal branch

The northern coastal branch of the Damara Orogen (Kaoko Belt) is subdivided into a Western Kaoko Zone, a Central Kaoko Zone, and a Southern Kaoko Zone (Figs. 6.10 & 6.11), which are all characterized by contrasting structural styles (Miller, 1983). In the Western Kaoko Zone bedding and fold closures are rarely seen. However, a strongly penetrative foliation with a N-S to NW-SE trend and a moderate westward dip (Guj, 1970) is displayed. Several strike-parallel shear zones (Guj, 1970; Miller, 1983) mark the eastward transition into the domain of steep, narrow, westerly inclined,

basement cored antiforms (Gui, 1970), which straddle the Purros Lineament (Figs. 6.10 & 6.11). A strong bedding parallel foliation is associated with tight to isoclinal folds within this domain of anticlines (Coward, 1983). The Central Kaoko Zone is bounded by the Purros Lineament in the west and the Sesfontein thrust in the east (Figs. 6.10 & 6.11). This zone is characterized by N-S trending folds and thrust faults, and NW plunging lineations and axes of small-scale folds (Coward, 1983). The N-S trending folds have an easterly vergence, which changes into a westerly direction in the vicinity of the Sesfontein thrust fault in the east of the Central Kaoko Zone (Fig. 6.11). These structural features were ascribed to a D2 deformational event, caused by southeastward directed thrusting (Coward, 1983). The change from a predominantly easterly to a westerly vergence near to the Sesfontein thrust fault can be ascribed to backfolding near the Sesfontein thrust fault (Coward, 1981). The latest deformational event in the Central Kaoko Zone is characterized by upright, southeast verging folds with a SW-NE trend and large wavelengths (Coward, 1983), which were probably generated by a late sinistral movement along existing fault systems. The Eastern Kaoko Zone, which is situated east of the Sesfontein thrust fault (Figs. 6.10 & 6.11), is, similar to the eastern parts of the Central Kaoko Zone, characterized by west-vergent backfolding. Large wavelength, low amplitude folds with a ENE-WSW trend, warp the earlier N-S trending structures.

Reconnaissance mapping in the Sesfontein-Hoanib River area in the northern coastal branch (Kaoko Belt) by I.G. Stanistreet, E.G. Charlesworth and the author showed the presence of a pervasive bedding-sub-parallel fabric (D1), which probably is caused by SSE-directed tectonic transport. This D1 fabric is deformed by a prominent phase of folding, which forms the main north-south structural grain and is polyphase in parts

of the Kaokoveld (D2 and D3). Small to large scale (>1km) open, east-trending folds (D4) interfere with folds of the previous deformational phases (D1 to D3) to form dome and basin structures.

Throughout the coastal branch of the Damara Orogen penetrative bedding parallel to sub-parallel foliation and thrust faults (D1 of this work), related to a SSE-directed tectonic transport, are associated with the first deformational event. North to NW

Table 6.3: *Correlation of deformational events of the Gariep Belt (southern coastal branch) and the Kaoko Belt (northern coastal branch) of the Damara Orogen.*

Southern coastal branch (this work)	**Structural features**	**Northern coastal branch - Western Kaokoveld (Guj, 1970; Miller, 1983; Coward, 1983; this work)**
D1	Pervasive bedding-sub-parallel fabric: tectonic transport to SSE	D1
D2	Prominent phase of folding forming main ~N-S structural grain: polyphase in parts of the Kaokoveld	D2 progressive D3
D3	Small to large scale (>1km) open folds with easterly trend forming interference structures with previous deformation to form domes and basins	D4

trending folds with a generally easterly vergence (D2 of this work), associated with an easterly directed tectonic transport, and deforming the bedding parallel to sub-parallel foliation, are developed throughout the southern coastal branch (Gariep Belt) and within the northern coastal branch (Kaoko Belt). The correlation of deformational

events in the northern and southern coastal branches of the Damara Orogen is summarized in Table 6.3.

The change of vergence from an easterly to a westerly direction in the eastern parts of the respective belts is a feature observed both in the Gariep and Kaoko Belts. West to SW trending folds (D3 of this work), related to sinistral tectonic movement along older fault zones, were observed in the entire coastal branch of the Damara Orogen. The strikingly similar tectonic history of the southern and the northern coastal branches appear to validate the concept of an Adamastor Orogeny along the entire coastal branch after the closure of the Khomas Sea.

REFERENCES

Alexander, Capt., J.E., 1838. *An Expedition of Discovery into the Interior of Africa*, London (2 Vols.).

Allsopp, H.L., Köstlin, E.O., Welke, H.J., Burger, A.J., Kröner, A. and Blignault, H.J., 1979. Rb-Sr geochronology of Late Precambrian-Early Palaeozoic igneous activity in the Richtersveld (South Africa) and southern South West Africa. *Trans. geol. Soc. S. Afr.*, **82**, 2185-204.

Anderson, J.B., 1983. Ancient glacial-marine deposits: their distribution in time and space. 3-92. *Molnia, B.F. (Ed.). Glacial-marine sedimentation. Plenum, New York, 844pp.*

Anderson, J.B., Kurtz, D.D. and Weaver, F.M., 1979. Sedimentation on the Antarctic continental slope. 61-73. *Doyle, L.J. and Pilkey, O.H. (Eds.). Geology of continental slopes. Spec. Publ. Soc. Econ. Paleon. Miner.*, **27**, *374pp.*

Anderson, J.B., Kurtz, D.D., Domack, E.W. and Balshaw, K.M., 1980. Glacial and glacial marine sediments of the Antarctic continental shelf. *J. Geol.*, **88**, 399-414.

Anderson, J.B., Brake, C.F. and Myers, N.C., 1984. Sedimentation on the Ross Sea continental shelf, Antarctica. *Marine Geol.* **57**, 295-333.

Armentrout, J.M., 1983. Glacial lithofacies of the Neogene Yakataga Formation, Robinson Mountains, Southern Alaska Coast Range, Alaska. 629-665. *In: Molnia, B.F. (Ed.). Glacial-marine sedimentation. Plenum, New York, 844pp.*

Awramik, S.M., 1984. Ancient stromatolites and microbial mats; 1-22. *In: Cohen, Y., Castenholz, R.W. and Halvorson, H.O. (Eds.). Microbial Mats: Stromatolites.* A.R. Liss. Inc., New York.

Badenhorst, F.P., 1988. The lithostratigraphy of the Chuos mixtite in part of the southern Central Zone of the Damara Orogen, South West Africa. *Communs. geol. Surv. S.W. Africa/Namibia*, 4, 103-110.

Bathurst, R.G.C., 1975. *Carbonate sediments and their diagenesis.* 2nd enlarged edition, Elsevier, Amsterdam, 658pp.

Beetz, P.F.W., 1926. On a great trough valley in the Namib. *Trans. geol. Soc. S. Africa*, **27**, 1-38.

Beukes, N.J., 1986. *Introduction to the sedimentology of the Precambrian carbonates.* Short course notes, Rand Afrikaans Univ., Johannesburg, 193pp.

Bertrand, J.M., 1976. Granitoids and the deformation sequence in the Goodhouse-Henkries area. A new interpretation of the relationship between rocks in the Vioolsdrif-Goodhouse area and the Namaqualand and Bushmanland gneisses. *A. Rep. Precambr. Res. Unit, Univ. Cape Town,* **13**, 61-70.

Bjorlykke, K., 1985. Glaciations, preservation of their sedimentary record and sea level changes - A discussion based on the Late Precambrian and Lower Plaaeozoic sequence in Norway. *Palaeogeog., Palaeoclim., Palaeoecol.,* **51**, 197-207.

Blatt, H., Middleton, G.V., and Murray, R., 1980. *Origin of sedimentary rocks.* 2nd. ed. Prentice-Hall, Englewood Cliffs, New Jersey, 782p.

Blignault, H.J., 1974. Aspects of the Richtersveld Province. In: Kröner, A. (Ed.). Contributions to the Precambrian geology of Southern Africa. *Bull. Precambr. Res. Unit, Univ. Cape Town*, **15**, 49-56.

Bluck, B.J., 1967. Deposition of some Upper Old red Sandstone conglomerates in the Cycle area: A study in the significance of bedding. *Scott. J. Geol.*, **3**, 139-167.

Blundy, J.D., and Holland, T.J.B., 1990. Calcic amphibole equilibria and a new amphibole-plagioclase geothermometer. *Contr. Mineral. Petrol.*, **104**, 208-224.

Bond, G.C., Nickeson, P.A. and Kominz, M.A., 1984. Breakup of a supercontinent between 625 Ma and 555 Ma: New evidence and implications for continental histories. *Earth planet Sci. Lett.*, **70**, 325-345.

Boothroyd, J.C., and Ashley, G.M., 1975. Processes, bar morphology and sedimentary structures on braided outwash fans, north-eastern Gulf of Alaska, In: *Jopling, A.V., and McDonald, B.C. (eds.), Glaciofluvial and glaciolacustrine sedimentation: Society of*

Economic Palaeontologists and Mineralogists Special Publication, **23**, 193-222.

Borg, G., 1988. The Khoras-Sinclair-Ghanzi rift in southern Africa. Volcanism, sedimentation, age relationships and geophysical signature of a late Midlle Proterozoic rift system. *Precambrian res.*, **38**, 75-90.

Bouma, A.H., 1962. *Sedimentology of some flysch deposits: a graphic approach to facies interpretation*. Elsevier, Amsterdam, 168p.

Breitkopf, J., 1986. *Iron Formations and associated amphibolites in the southern part of the Damara Orogen of SWA/Namibia.* PhD thesis (unpubl.) Univ. Witwatersrand, Johannesburg, 350pp.

Breitkopf, J.H. and Maiden, K.J., 1987. Volcanogenic-exhalative iron formations in the Southern Margin Zone of the Damara Orogen. *Communs. geol. Surv. SWA/Namibia*, **2**, 131-144.

Breitkopf, J.H. and Maiden, K.J., 1987. Geochemical patterns of metabasites in the southern part of the Damara Orogen, SWA/Namibia: applicability to the recognition of tectonic environment. 355-361. *In*: Pharaoh, T.C., Beckinsale, R.D., and Rickard, D. (Eds.). Geochemistry and mineralization of Proterozoic suites. *Spec. Publ. geol. Soc. Lond.*, **33**.

Bühn, B., Stanistreet, I.G. and Okrusch, M., 1992. Late Proterozoic outer shelf manganese and iron deposits at Otjosondu (Namibia) related to Damara oceanic opening. *Econ. Geol.* .

Buck, S.G., 1980. Stromatolite and ooid deposits within the fluvial and lacustrine sediments of the Precambrian Ventersdorp Supergroup of South Africa. *Precambrian Res.*, **12**, 311-330.

Bull, W.B., 1963. Alluvial fan deposits in western Fresno country, California. *J. Geol.*, **71**, 243-251.

Bull, W.B., 1972. Recognition of alluvial-fan deposits in the stratigraphic record. *In: Rigby, K.J. and Hamblin, W.K. (Eds.). Recognition of Ancient Sedimentary Environments; Spec. Publ. Soc. econ. Paleont. Miner.*, **16**, 68-83.

Burger, A.J. and Coertze, F.J.,1973. Radiometric age measurements on rocks from Southern Africa to the end of 1971. *Bull. geol. Surv. S. Afr.*, **58**, 46pp.

Cahen, L., Snelling, N.J., Delhal, J. and Vail, J.R., 1984. *The geochronology and evolution of Africa.* Clarendon Press, Oxford, 512pp.

Carter, R.M., 1975. A discussion and classification of subaqueous mass-transport with particular application to grain-flow, slurry-flow and fluxoturbidites. *Earth-Sci. Rev.*, **11**, 145-177.

Chen Channing, Huan Jiakuan, Chen Jingshan, Tian Xingyou, Chen Ruijun, and Li Li, 1981. Evolution of sedimentary tectonics of Bohai rift system and its bearing on hydrocarbon accumulation. *Sci. Sin. Peking*, **24**, 521-529.

Chen Channing, Huan Jiakuan, Chen Jiagshan, and Tian Xingyou, 1982. Depositional models of tertiary rift basins, eastern China, and their application in oil and gas prediction. *Inst Geol. Acad. Sin., Res. Geol.*, **1982**, 141-148.

Clifford, T.N., 1967. The Damaran episode in the Upper Proterozoic-Lower Palaeozoic structural history of Southern Africa. *Spec. Pap. genl. Soc. Am.*, **92**, 100pp.

Collinson, J.D., 1986. Alluvial sediments. In: *Reading, H.G.. Sedimentary environments and facies.* Blackwell, Oxford, 615pp.

Collinson, J.D. and Thompson, D.B. 1992. *Sedimentary structures.* Chapman and Hall, London, 207pp.

Cook, H.E. and Taylor, M.E., 1977. Comparisons of continental slope and shelf environments in the Upper Cambrian and lowermost Ordovician of Nevada. 51-81. *In: Cook, H.E. and Enos, P. (Eds.). Deep-water Carbonate Environments, Spec. Publ. Soc. econ. Paleont. Miner.*, **25.**

Cordani, U,G., Figueiredo, M.C.H., Teixeira, W., Basei, M.A.S., and Soliani jr., E., 1990. Geotectonic evolution of the Dom Feliciano Belt in South America. *Abstr Geocongress '90, Geol. Soc. S. Afr.*, 111.

Corrans, R.D., 1983. Internal report Anglo American Prospecting Services (Pty) Ltd. Skorpion Prospect - Sperrgebiet S.W.A.: Summary report covering exploration and

results for the period June 1976 to September 1982. 36pp.

Coward, M.P., 1981. The junction between Pan African mobile belts in Namibia: its structural history. *Tectonophysics*, **76**, 59-73.

Coward, M.P., 1983. The tectonic history of the Damaran Belt. 409-421. *In: Miller, R.McG. (Ed.). Evolution of the Damara Orogen of South West Africa/Namibia. Spec. Publ. geol. Soc. S. Afr.*, **11**, 515pp

Dalziel, I.W.D., 1991. Pacific margins of Laurentia and east Antarctica-Australia as a conjugate rift pair: Evidence and implications for an Eocambrian supercontinent. *Geology*, **19**, 598-602.

Davies, C. and Coward, M.P., 1982. The structural evolution of the Gariep Arc in southern Namibia. *Precambr. Res.*, **17**, 173-198.

De Raaf, J.F.M., Boersma, J.R. and van Gelder, A., 1977. Wave-generated structures and sequences from a shallow marine succession, Lower Carboniferous, County Cork, Ireland. *Sedimentology*, **24**, 451-483.

De Villiers, J., 1968. *A. Rep. Precambr. Res. Unit, Univ. Cape Town*, **6**, 16pp.

De Villiers, J. and Söhnge, P.G., 1959. The geology of the Richtersfeld. *Geol. Surv. of S.A., Memoir* **48**

De Kock, N.J., 1987. *Die veranderinge van die wandgesteentes in die omgewing van die ertsliggame van Rosh Pinah.* Msc thesis (Unpubl.), Univ. Pretoria, 115pp.

Derbyshire, E. and Owen, L.A., 1990. Quaternary alluvial fans in the Karakoram Mountains. *In: A.H. Rachocki and M. Church (Eds.), Alluvial Fans: A Field Approach.* Wiley, Chichester, pp. 27-53.

Denny, C.S., 1965. Alluvial fans in Death Valley Region, California and Nevada. *Prof. Pap. U.S. geol. Surv.*, **466**, 62pp.

Dickenson, M.P. & Hewitt, D., 1986. A garnet chlorite geothermometer. *GSA abstracts*

with programs, **18**, 584.

Dill, R.F., Shinn, E.A., Jones, A.T., Kelly, K. and Steinen, R.P., 1986.Giant subtidal stromatolites forming in normal salinity waters. *Nature*, **324**, 55-58.

Dunn, E.J., 1872. *On the country traversed by the "Gold Prospecting Expedition" Namaqualand. Cape of Good Hope Parl. Rep.*, **G 21**, Cape Town.

Elliot, T., 1986. Siliciclastic shorelines. 155-188. *In*: Reading, H.G. (Ed.). *Sedimentary environments and facies*. (2nd ed.), Blackwell, Oxford, 615pp.

Elliott, D., 1976. The motion of thrust sheets. *J. Geophys. Res.*, **81**, 949-963.

Elliott, D. and Johnson, M.R.W., 1980. Structural evolution in the northern part of the Moine thrust belt, NW Scotland. *Trans. R. Soc. Edinburgh: Earth Sciences*, **71**, 69-96.

Eyles, N. and Miall, A.D., 1984. Glacial facies. 15-38. *In*: Walker, R.G. (Ed.). *Facies models*. 2nd ed. Geosci. Can. Reprint Series 1, 317pp.

Eyles, C.H. and Eyles, N., 1983. Glaciomarine model for upper Precambrian diamictites of the Port Askaig Formation, Scotland. *Geology*, **11**, 692-696.

Fabricius, F.H., 1977. Origin of marine ooids and grapestones. *Contr. Sedimentol.*, **7**, 113pp.

Fairchild, I.J. and Hambrey, M.J., 1984. The Vendian succession of northeastern Spitsbergen: Petrogenesis of a dolomite - tillite association. *Precambrian Res.*, **26**, 111-167.

Fairchild, I.J., Hambrey, M.J., Spiro, B. and Jefferson, T.H., 1989. Late Proterozoic glacial carbonates in northeastern Spitsbergen: new insights into the carbonate-tillite association. *Geol. Mag.*, **126**, 469-490.

Fleuty, M.J., 1964. The description of folds. *Proc. Geol. Assoc. Lond.*, **75**, 461-492.

Flint, R.F., Sanders, J.E. and Rodgers, J., 1960. Diamictite: a substitute term for symmictite. *Geol. Soc. Am. Bull.*, **71**, 1809-1910.

Franz, L. and Häussinger, H., 1990. Die Anwendung interaktiver Programme in der Mineralogie am Beispiel des Programms "Amphibol". *Eur. J. Mineral.*, **2**, Beih. 1, 68.

Frimmel, H.E. and Hartnady, C.J.H., 1992. Blue amphiboles and their significance for the Pan-African Gariep belt, Namibia. *J. metamorphic Geol.*, **10**, 651-669.

Gebelein, C.D., 1969. Distribution, morphology and accretion rate of recent subtidal algal stromatolites, Bermuda. *J. sedim. Petrol.*, **39**, 49-69.

Germs, G.J.B. and Gresse, P.G., 1991. The foreland basin of the Damara and Gariep orogens in Namaqualand and southern Namibia: stratigraphic correlations and basin dynamics. *S. Afr. J. Geol.*, **94 (2/3)**, 159-169.

Ghent, E.D., Stout, M.Z., Black, P.M. and Brothers, R.N., 1987. Chloritoid bearing rocks with blueschists and eclogites, northern New Caledonia. *J. Metam. Petrol.*, **5**, 239-254.

Gole, C.V. and Chitale, S.V., 1966. Inland delta building activity of Kosi River. *J. Hydraul. Div., Proc. Am. Soc. civ. Engrs*, **92**, 111-126.

Greenman, L., 1966. *The geology of area 2515C, Lüderitz, South West Africa.* Unpubl. M.Sc. thesis, Univ. Cape Town.

Gresse, P.G., Fitch, F.J. and Miller, J.A., 1988. $^{40}Ar/^{39}Ar$ dating of the Cambro-Ordovician Vanrhynsdorp tectonite in southern Namaqualand. *S. Afr. J. Geol*, **91**, 257-263.

Grotzinger, J.P., 1990. *Principles of carbonate platform development.* Short course notes, Rand Afrikaans University, Johannesburg, 42pp.

Guj, P., 1970. The Damara mobile belt in south-western Kaokoveld, South West Africa. *Bull. Precambrian Res. Unit, Univ. Cape Town*, **18**, 168pp.

Hambrey, M.J. and Harland, W.B., 1985. The Late Proterozoic Glacial Era. *Palaeogeogr., Palaeoclimatol., Palaeoecol.*, **51**, 255-272.

Hampton, M.A., 1972. The role of subaqueous debris flow in generating turbidity currents. *J. sedim. Petrol.*, **42**, 775-793.

Harland, W.B., 1983. The Proterozoic glacial record. *In:* Medaris, L.G., Byers, C.W., Michelson, D.M. and Shanks, W.C. (Eds.). Proterozoic geology. *Bull. geol. Soc. Am. Mem.*, **161**, 279-286.

Harms, J.C., Southard, J.B. and Walker, R.G., 1982. *Structures and sequences in clastic rocks.* Soc. Econ. Palaeont. Miner. Short Course **9**, Calgary.

Hartnady, C.J.H., 1978.The stratigraphy and structure of the Naukluft nappe complex. *14th and 15th a. Reps. Precambrian Res. Unit, Univ. Cape Town, 163-170.*

Hartnady, C.J.H., 1991. About turn for supercontinents. *Nature*, **8**, 476-478.

Hartnady, C.J.H., Joubert, P. and Stowe, C.W., 1985. Proterozoic crustal evolution in southwestern Africa. *Episodes,* **8**, 236-244.

Hartnady, C.J.H. and Von Veh, M.W., 1990. Tectonostratigraphic and structural history of the Late Proterozoic-Early Palaeozoic Gariep Belt, Cape Province, South Africa. *Guidebook Geocongress '90, Geol. Soc. S. Afr.,* PO1: 1-49.

Hartnady, C.J.H., Ransome, I.G.D. and Frimmel, H., 1990. Accreted Composite Terranes-An example from the Gariep Orogenic Belt. *Abstracts, Geocongress 1990, Cape Town*, 218-221.

Haughton, S.H., 1961. Discussion of "The Gariep System" by J. De Villiers. *Publ. C.C.T.A.*, 80, 89.

Haughton, S.H., 1963. *Stratigraphic history of Africa south of the Sahara.* Oliver and Boyd, Edinburgh, 365pp.

Hayward, A.B., 1983. Coastal alluvial fans and associated marine facies in the Miocene of southwest Turkey. *In: J.D. Collinson and J. Lewin (Eds.), Modern and Ancient Fluvial Systems. Int. Assoc. Sedimentol., Spec. Publ.,* **6**, 323-336.

Henry, G., Osborne, M.A. and Schmerold, R.K., 1992/1993. Proposed lithostratigraphic subdivision of the Ugab Subgroup (Damara Sequence) in Kaokoland, Namibia. *Communs. geol. Surv. Namibia*, **8**, 143-146.

Henry, G., Stanistreet, I.G. and Maiden, K.J., 1986. Preliminary results of a sedimentological study of the Chuos Formation in the Central Zone of the Damara Orogen: Evidence for mass flow processes and glacial activity. *Communs geol Surv. S.W. Africa/Namibia*, **2**, 75-92.

Henry, G., Stanistreet, I.G. and Maiden, K.J., 1988. Timing of continental breakup in the Damara Orogen - A review and discussion. *Ext. Abstr., Geocongress '88 Geol Soc. S. Afr., Durban, 267-270.*

Hey, M.T., 1954. A new review of the chlorites. *Mineralogical Magazine*, **30**, 274-292.

Hoal, B., 1990. Tectonomagmatic evolution of the Proterozoic Awasib Mountain Terrain, southern Namibia. *Ext. Abstr. Geocongress '90.* Geol. Soc. S. Afr., Cape Town, 246-249.

Hoffman, P., 1976. Environmental diversity of Middle Precambrian stromatolites. 599-611. *In: Walter, M.R. (Ed.). Stromatolites.* Elsevier, Amsterdam.

Hoffman, P., 1991. Did the breakout of Laurentia turn Gondwanaland inside-out? *Science*, **252**, 1049-1412.

Hoffmann, K.-H., 1972. *Geological report on an area north-east of Rosh Pinah in South West Africa*. B.Sc. (Hons) Proj. (unpubl.), Univ. Cape Town.

Hoffmann, K.-H., 1989. New aspects of lithostratigraphic subdivision and correlation of late Proterozoic to early Cambrian rocks of the Damara Belt and their correlation with the central and northern Damara Belt and the Gariep belt. *Communs. geol. Surv. S.W.Afr./Namibia*, **5**, 59-67.

Hooke, R. Le B., 1967. Processes on arid-region alluvial fans. *J. Geol.*, **75**, 438-460.

Horstmann, U.F., 1987. Die metamorphe Entwicklung im Damara Orogen, Südwest Afrika/Namibia, abgeleitet aus K/Ar-Datierungen an detritischen Heliglimmern aus

Molassesedimenten der Nama Group. *Göttinger Arbeiten zur Geologie und Paläontologie,* **32**, 1-95.

Horstmann, U.E., Ahrendt, H., Clauer, N. and Porada, H., 1990. The metamorphic history of the Damara Orogen based on K/Ar data of detrital white micas from the Nama Group. *Precambrian Res.*, **48**, 41-61.

Hynes, A. and Forest, R.C., 1988. Empirical garnet-muscovite geothermometry in low grade metapelites, Selwyn Range (Canadian Rockies). *Metamorphic Geol.*, **6**, 297-309.

Illing, L.V., 1954. Bahamian calcareous sands. *Bull. Am. Ass. petrol. Geol.*, **38**, 1-95.

Irwin, M.L., 1965. General theory of epeiric clear water sedimentation. *Assoc. Petrol. Geol. Bull.*, **49**, 445-459.

James, N.P., 1984. Shallowing-upward sequences in carbonates. 213-228. *In*: Walker, R.G. (Ed.). *Facies models*. 2nd Ed. Geosci. Can. Reprint Series 1, 317pp.

Jasper, M.J.U., Stanistreet, I.G. and Charlesworth, E.G., 1992/1993. Preliminary results of a study of the structural and sedimentological evolution of the Late Proterozoic/Early Palaeozoic Gariep Belt, southern Namibia. *Communs. geol. Surv. Namibia,* **8**, 99-118.

Jenkyns, H.C., 1986. Pelagic environments. 343-397. *In*: Reading, H.G. (Ed.). *Sedimentary environments and facies*. 2nd ed. Blackwell, Oxford, 615pp.

Johnson, H.D. and Baldwin, C.T., 1986. Shallow siliciclastic seas. 229-282. *In*: Reading, H.G. (Ed.). *Sedimentary environments and facies*. 2nd ed. Blackwell, Oxford, 615pp.

Joubert, P. and Kröner, A., 1972. The Stinkfontein Formation south of the Richtersveld. *Trans. geol. Soc. S. Afr.*, **75**, 47-54.

Joubert, P., Hartnady, C.J.H. and Von Veh, M.W., 1986. *The geology of the Alexander Bay area. Explanation of Sheet 2816 (Scale 1 : 250 000)*, Open file rep. geol. Surv. Dep. Min., 28pp.

Kaiser, E., 1926. Die Eruptivgesteine der Chloritschieferstufe, der Konkip- und Namaformation und die Amphibolitisierung in diesen Stufen. *In: Kaiser, E. (Ed.). Die*

Diamantenwüste Südwest- Afrikas. D. Reimer Verlag, Berlin, 190-208.

Kasch, K.W., 1980. The Damara metamorphic traverse. *17th a. Rep. Precambrian Res. Unit, Univ. Cape Town, 118-129.*

Kasch, K.W., 1981. The structural geology, metamorphic petrology and tectonothermal evolution of the southern Damara belt around Omitara, SWA/Namibia. *Bull. Precambrian Res. Unit, Univ. Cape town,* **27**, 333pp.

Kasch, K.W., 1983. Continental collision, suture progradation and thermal relaxation: A plate tectonic model for the Damara Orogen in central Namibia. 423-429. *In: Miller, R.mcG. (Ed.). Evolution of the damara Orogen of South West Africa/Namibia. Spec. Publ. geol. Soc. S. Afr.,* **11**, 515pp.

Kingsley, C.S., 1984. Dagbreek fan delta: an alluvial placer to prodelta sequence in the proterozoic Welkom Gold fields, Witwatersrand. *In: E.H. Koster and R.J. Steel (Eds.), Sedimentology of Gravels and Conglomerates. Mem. Can. Soc. Pet. Geol.,* **10**, 321-330.

Knetsch, G., 1937. Übersicht über die Geologie des südlichen Lüderitzlandes. *Geol. Rdsch.*, **28**, 208-223.

Kröner, A., 1972. Preliminary resume of the geology of the Gariep geosyncline in the Orange River area. 7-9, 51-57. *In: De Villiers, J. (Ed.). A. Rep. Precambrian Res. Unit, Univ. Cape Town,* **13**.

Kröner, A., 1974. The Gariep Group, Part I: Late Precambrian formations in the western Richtersveld, northern Cape Province. *Bull. Precambr. Res. Unit, Univ. Cape Town,* **13**, 115pp.

Kröner, A., 1974a. Reports on research activities - The Gariep Group. *A. Rep. Precambr. Res. Unit, Univ. Cape Town*, 10-11, 73-74.

Kröner, A., 1975. Late Precambrian formations in the western Richtersveld, northern Cape Province. *Trans. R. Soc. S. Afr.*, 41, 375-433.

Kröner, A., 1977. Non-synchroneity of late Precambrian glaciations in Africa. *J. Geol.*,

85, 289-300.

Kröner, A., 1979. Pan-African mobile belts as evidence for a transitional tectonic regime from intraplate orogeny to plate margin orogeny. *In: Al-Shanti, A. (Ed.). Evolution and mineralization of the Arabian-Nubian Shield. Pergamon Press, Oxford,* 21-27.

Kröner, A. and Blignault, G.J.B., 1976. Towards a definition of some tectonic and igneous provinces in western South Africa and southern South West Africa. *Trans. geol. Soc. S. Afr.*, **79**, 232-238.

Kröner , A. and Germs,G.J.B., 1971. A re-interpretation of the Numees-Nama contact at Aussenkjer, South West Africa. *Trans. geol. Soc. S. Afr.*, **74**, 69-74.

Kröner, A. and Hawkesworth, C.J., 1977. Late Pan-African emplacement ages for Rössing alaskitic granite (Damara belt) and Rooi Lepel bostonite (Gariep belt) in Namibia and their significance for the timing of metamorphic events. *A. Rep. res. Inst. Afr. Geol., Univ. Leeds*, **20**, 14-17.

Kröner, A. and Jackson, M.P.A., 1974. Geological reconnaissance of the coast between Lüderitz and Marble Point, South West Africa. *Bull. Precambrian Res. Unit, Univ. Cape Town,* **15**, 35pp.

Kröner, A., McWilliams, M.O., Germs, G.J.B., Reid, A.B. and Schalk, K.E.L., 1980. Paleomagnetism of Late-Precambrian mixtite-bearing formations. *Am. J. Sci.*, **280**, 942-968.

Kröner, A. and Rankama, R., 1972. Late Precambrian sedimentary rocks in southern Africa: a compilation with definitions and correlations. *Bull. Precambr. Res. Unit, Univ. Cape Town*, **11**, 37pp.

Kröner, A. and Welin, E., 1973. Evidence for +500 my old thermal episode in southern South-West africa. *Earth Planet Sc. Lett.*, **21**, 149-152.

Kuenen, Ph. and Migliorini, C., 1950. Turbidity currents as a cause of gradded bedding. *J. Geol.*, **58**, 91-127.

Kumar, N. and Sanders, J.E., 1976. Characteristics of shoreface storm deposits: modern and ancient examples. *J. sedim. petrol.*, **46**, 145-162.

Kurtz, D.D. and Anderson, J.B., 1979. Recognition and sedimentoogical description of recent debris flow deposits from Ross and Weddell Seas, Antarctica. *J. Sed. Petrol.*, **49**, 1159-1170.

Laird, J. and Albee, A.L., 1981. Pressure, temperature, and time indicators in mafic schists: Their application to reconstructing the polymetamorphic history of Vermont. *Am. J. Sci.*, **281**: 1269-1278.

Land, L.S., Behrens, D.A. and Frishman, S.A., 1979. The ooids of Baffin Bay, texas. *J. sedim. Petrol.*, **49**, 1269-1278.

Leake, B.E., 1978. Nomenclature of amphiboles. *Am. Miner.*, **63**, 1023-1053.

Lickfold, V., 1990. *A geological study of the Rosh Pinah Zn-Pb-Cu-Ag mine, Namibia.* BSc (Hon) report (Unpubl.), Univ. of the Witwatersrand, 70pp.

Logan, B.W., 1961. Cryptozoon and associated stromatolites from the Recent, Shark Bay, Western Australia. *J. Geol.*, **69**, 517-617.

Loreau, J.P. and Purser, B.H., 1973. Distribution and ultrastructure of Holocene ooids in the Persian Gulf. 279-328. *In: Purser, B.H. (Ed.). The Persian Gulf.* Springer Verlag, Berlin.

Lowe, D.R., 1979. Sediment gravity flows: their classification and some problems of application to natural flows and deposits. 75-82. *In*: Doyle, L.J. and Pilkey, O.H. (Eds.). *Geology of continental slopes*. Spec. Public. Soc. Econ. Palaeont. Miner., **27**, 374.

Lowe, D.R., 1979. Sediment gravity flows: their classification and some problems of application to natural flows and deposits. 75-82. *In: Doyle, L.J. and Pilkey, O.H. (Eds.). Geology of continental slopes. Spec. Publ. Soc. Econ.Paleont. Miner.*, **27**, 374pp.

Lowe, D.R., 1982. Sediment gravity flows: **II**. Depositional models with special reference to the deposits of high density turbidite currents. *J. Sed. Petrol.*, **52**. 279-297.

Martin, H., 1983. Overview of the geosynclinal, structural and metamorphic development of the intracontinental branch of the Damara Orogen, 473-502. *In: Martin, H. and Eder, F.W. (Eds.). Intracontinental Fold belts.* Springer, Berlin, 945pp.

Martin, H., 1965. The Precambrian geology of South West AFrica and Namaqualand. *Precambrian Res. Unit, Univ. Cape Town*, 159pp.

Martin, H. and Porada, H., 1977. The intracratonic branch of the Damara Orogen in South West Africa. I. Discussion of geodynamic models. *Precambrian Res.*, **5**, 311-338.

Massonne, H. J., 1991. *High pressure, low temperature metamorphism of pelitic and other protoliths based on experiments in the system K2O-MgO-Al2O3-SiO2-H2O.* Habilitation thesis, Univ. Bochum, Germany, 172p.

Master, S. 1991. *The Origin and Control on the Distribution of Copper and Precious Metal Mineralization at the Mangula and Norah Mines, Mhangura, Zimbabwe.* Ph.D. Thesis (unpubl.), Univ. of the Witwatersrand, Johannesburg, 385 pp.

McClay, K.R., Insley, M.W. and Anderton, R., 1989. Inversion of the Kechika Trough, Northeastern British Columbia, Canada. 235-257. *In: Cooper, M.A. and Williams, G.D. (Eds.). Inversion Tectonics.* Geol. Soc. Spec. Publ., **44.**

McGowen, J.H. and Groat, C.G., 1971. Van Horn Sandstone, west texas: an alluvial fan model for mineral exploration. *Report of Investigations,* **72**, 57 pp. Bureau of Economic Geology, Univ. of Texas, Austin.

McIlreath, I.A., 1977. Accumulationof a Middle Cambrian, deep-water limestone debris apron adjacent to a vertical submarine carbonate escarpment, southern Rocky Mountains, Canada. *In: Cook, H.E. and Enos, P. (Eds.). Deep-water Carbonate Environments. Spec. Publ. Soc. econ. Paleont. Miner.*, **25**, 113-124.

McMenamin, M.A.S. and McMenamin, D.L.S., 1990. *The Emergence of Animals: The Cambrian Breakthrough.* Columbia University Press, New York.

McMillan, M.D., 1968. The geology of the Witputs-Sendelingsdrif area. *Bull. Prec. Res. Unit, Univ. Cape Town*, **4**, 177pp.

Miall, A.D., 1978. Lithofacies types and vertical profile models in braided river deposits:

a summary. 597-604. *In*: Miall, A.D. (Ed.). *Fluvial sedimentaology. Can. Soc. Petrol. Geol. Mem.*, **5**, 859pp.

Miall, A.D., 1984. *Principles of sedimentary basin analysis*. Springer, New York, 490pp.

Middlemost, E.A.K., 1964. Petrology of the plutonic and dyke-rocks of the south-eastern Richtersveld. *Trans. geol. Soc. S. Afr.*, **67**, 227-261.

Middleton, L.T. and Trijillo, A.P., 1984. Sedimentology and depositional setting of the Upper Proterozoic Scanlan Conglomerate, Central Arizona. *In: E.H. Koster and R.J. Stee! (Eds.), Sedimentology of Gravels and Conglomerates. Mem. Can. Soc. Pet. Geol.* **10**, 189-201.

Miller, J.M.G., 1987. Palaeotectonic and stratigraphic implications of the Kingston Peak - Noonday contact in the Panamint Range, Eastern California. *J. Geol.*, **95**, 75-86.

Miller, R.McG., 1983. The Pan-African Damara Orogen of South West Africa/Namibia. 431-515. *In: Miller, R.mcG. (Ed.). Evolution of the Damara Orogen of South West Africa/Namibia. Spec. Publ. geol. Soc. S. Afr.*, **11**, 515pp

Miller, R. McG. and Grote, W., 1988. (Compilers) *Geological map of the Damara Orogen South West Africa/Namibia 1:5000 000.* Geol. Surv., Windhoek, Namibia.

Mitchell, A.H.G. and Reading, H.G., 1986. Sedimentation and tectonics. *In: Reading, H.G. (Ed.). Sedimentary environments and facies.* 2nd. ed., Blackwell, Oxford, 615pp.

Monty, C.L., 1967. Distribution and structure of recent stromatolitic algal mats, Eastern Andros Island, Bahamas. *Ann. Soc. geol. Belg.*, **90**, 55-100.

Monty, C.L., 1972. Recent algal stromatolitic deposits, Andros Island, Bahamas. *Geol. Rdsch.*, **61**, 742-783.

Moores, E.M., 1991. Southwest U.S. - East Antarctic (SWEAT) connection: A hypothesis. *Geology*, **19**, 425-428.

Mullins, H.T., 1983. Modern carbonate slopes and basins of the Bahamas. *In: Cook, H.E., Hine, A.C. and Mullins, H.T. (Eds.). Platform Margin and Deep-water Carbonates. Soc. econ. Paleont. Miner. Short Course No. 12.*

Mullins, H.T. and Neumann, A.C., 1979. Deep carbonate bank margin structure and sedimentation in the northern Bahamas. *In: Doyle, L.J. and Pilkey, O.H. (Eds). Geology of continental slopes. Spec. Publ. Soc. econ. Paleont. Miner.*, **27**.

Newell, N.D., E.G. Purdy and Imbrie, J., 1960. Bahamian oolite sand. *J. Geol.*, **68**, 481-497.

Newton, A.R. and Boyle T.P., 1989. New data from LANDSAT image interpretation in the Richtersveld. *S. Afr. J. Geol.*, **92(2)**, 125-133.

Nystuen, J.P., 1985. Facies and preservation of glaciogenic sequences from the Varanger ice age in Scandinavia and other parts of the North Atlantic region. *Palaeogeog., Palaeoclim., Palaeoecol.*, **51**, 209-229.

Onstott, T.C., Hargraves, R.B. and Reid, D.L., 1986. Constraints on the tectonic evolution of the Namaqua Province III: paleomagnetic and 40Ar/39Ar results from the Gannakouriep dyke swarm. *Trans. geol. Soc. S. Afr.*, **89**, 171-183.

Orl, G.G. and Roveri, M., 1987. Geometries of Gilbert-type deltas and large channels in the Meteora Conglomerate, Meso-Hellenic basin (Oligo-Miocene), central Greece. *Sedimentology*, **34**, 845-859.

Page, D.C. and Watson, M.D., 1976. The Pb-Zn Deposit of Rosh Pinah, South West Africa. *Econ. Geol.*, **71**, 306-327.

Papike, J.J., Ross, M. and Baldwin, K., 1974. Amphiboles and Pyroxenes: Characterization of other than quadrilateral components and estimates of ferric iron from microprobe data. *Geol. Soc. America (Abs. with programs)*, 6, 1053-1054.

Piper, J.D.A., 1987. *Palaeomagnetism and Continental Evolution*. Open University Press, Milton Keynes.

Playford, P.E., *et al.*, 1976. Devonian stromatolites from the Canning Basin, Western Australia; 543-563. *In: Walter, M.R. (Ed.) Stromatolites*, Elsevier, Amsterdam.

Plyusnina, L.P., 1982. Geothermometry and geobarometry of plagioclase-hornblende bearing assemblages. *Contr. Mineral. Petrol.*, **80**, 140-146.

Poldervaart, A. and Hess, H.H., 1951. Pyroxenes in the crystallization of basaltic magma. *Journ. Geol.*, **4**, p. 143.

Porada, H., 1979. The Damara-Ribeira orogen of the Pan-African/Brasiliano Cycle in Namibia and Brazil as interpreted in terms of continental collision. *Tectonophysics*, **57**, 237-265.

Porada, H., 1983. Geodynamic model for the geosynclinal development of the Damara Orogen, Namibia/South West Africa. 503-541. *In: Martin, H. and Eder, F.W. (Eds.). Intracontinental Fold Belts*. Springer, Berlin, 945pp.

Porada, H., 1985. Stratigraphy and facies in the Upper Proterozoic Damara Orogen, Namibia, based on a geodynamic model. *Precambrian Res.*, **29**, 235-264.

Porada, H., 1989. Pan-African rifting and orogenesis in Southern to Equatorial Africa and Eastern Brazil. *Precambrian Res.*, **44**, 103-136.

Powell, R. and Holland, T.J.B., 1988. An internally consistent dataset with uncertainties and correlations: 3. Applications to geobarometry, worked examples and a computer program. *J. Metam. Geol.*, **6**, 173-204.

Range, P., 1912. Geologie des seutschen Namalandes: Beitr. geol. Erforsch. dt. Schutzgeb., **2**, 1-104.

Rao, C.P., 1981a. Criteria for recognition of cold-water carbonate sedimentation: Berridale Limestone (Lower Permian), Tasmania. *J. Sed. Petrol.*, **51**, 491-506.

Rao, C.P., 1981b. Geochemical differences between tropical (Ordocvician) and subpolar (Permian) carbonates, Tasmania, Australia. *Geology*, **9**, 205-209.

Rao, C.P. and Green, D.C., 1982. Oxygen and carbon isotopes of Early Permian cold-water carbonates, Tasmania, Australia. *J. Sed. Petrol.*, **52**, 1111-1125.

Reading, H.G., 1986. *Sedimentary environments and facies.* Blackwell Scientific Publications, 557 pp.

Reid, D.L., 1977. Geochemistry of Precambrian igneous rocks in the Lower Orange River region. *Bull. Precambr. Res. Unit, Univ. Cape Town,* **22**, 397pp.

Reid, D.L., 1979. The Late Precambrian Gannakouriep mafic dyke swarm, lower Orange River region. *Trans. geol. Soc. S. Afr.*, **82**, 305-311.

Reineck, H.E. and Singh, I.B., 1975. *Depositional sedimentary environments.* Springer-Verlag, Heidelberg, 439 pp.

Ritter, U., 1978. The southwestern Richtersveld between Eksteenfontein and Klein Helskloof, its relationship to gariep metamorphism and tectonism and to the Namaqua Metamorphic Complex. *A. Rep. Precambr. Res. Unit, Univ. Cape Town,* **26**, 276pp.

Ritter, U., 1980. The Precambrian evolution of the Eastern Richtersveld. *Bull. Precambr. Res. Unit, Univ. Cape Town,* **26**, 276pp.

Rogers, A.W., 1916. The geology of part of Namaqualand. *Trans. Geol. Soc. S. Afr.*, **18**, 72-101.

Rogers, A.W., 1929. The Ventersdorp System. *In*: Steinmann, G., and Wilckens, O. (Eds.). *Handbuch der Regionalen Geologie*, **Bd. VII**, (7 Abt.), The Union of South Africa, Carl Winters Universitätsbuchhandlungen, Heidelberg.

Rusnak, G.A., 1960. Sediments of Laguna Madre. 153-196. *In: Shepard, F.P., Phleger, F.B. and van Andel, T.H. (Eds.). Recent Sediments, Northwest Gulf of Mexico. Am. Soc. Petrol. Geol., Tulsa.*

Ruxton, P.A. and Clemmey, H., 1986. Late Proterozoic stratabound red bed-copper deposits of the Witvlei Area, South West Africa/Namibia. *In: C.R. Anhaeusser and S. Maske (Eds.), Mineral Deposits of Southern Africa II. Geol. Soc. S. Afr., Johannesburg,* 1739-1754.

SACS (South African Committee For Stratigraphy), 1980. Gariep Complex, 415-423. *In*: Kent, L.E. (Comp.) Stratigraphy of Southern Africa. I. Lithostratigraphy of South

Africa, South West Africa/Namibia and the Republics of Bophuthatswana, Transkei and Venda. *Handbk. geol. Soc. S. Afr.*, **8**, 690pp.

Sarg, J.F., 1988. Carbonate sequence stratigraphy. *In: Wilgus, C.K. et al. (Eds.). Sea-level changes: an integrated approach. Soc. Econ. Mineral. Spec. Publ.*, **42**, 155-181.

Schreuder, C.P., 1975. *Carbonate-bearing eruptives between the Great Karas Mountains and the Bremen Igneous Compex, S.W.A.* M.Sc. thesis (unpubl.), Univ. Stellenbosch.

Schultz, A.W., 1984. Subaerial debris-flow deposition in the Upper Plaeozoic Cutler Formation, Western Colorado. *J. Sediment. Petrol.* **54**, 759-772.

Sclater, J.G. and Christie, P.A.F., 1980. Continental stretching: An explanation of the Post-Mid-Cretaceouss subsidence of the central North Sea basin. *J. geophys. Res.*, **85**, 3711-3739.

Siegfried, P.R., 1990. *Aspects of the Geology of the Mountain Ore Body, Rosh Pinah Mine, Namibia*. Unpubl. M.Sc. thesis, Univ. Cape Town. 145pp.

Siegfried, P.R., 1992/1993. Results of preliminary investigations into the geology of the Diaz Point Formation, Lüderitzbucht, Namibia. *Communs. geol. Surv. Namibia*, **8**, 119-126.

Siegfried, P.R. and Moore, J.M., 1990. The Rosh Pinah Zn-Pb-Cu-Ag massive sulphide deposit - a product of early rift-related volcanism? *Abstracts, Geocongress 1990, Cape Town*, 512-513.

Smith, H.S. and Hartnady, C.J.H., 1984. Geochemistry of Grootderm Formation lavas: indication of tectonic environment of extrusion. *Abstracts, Conference on Middle to Late Proterozoic Lithosphere Evolution*, 20-21.

Smith, N.D., 1971. Transverse bars and braiding in the lower Platte River, Nebraska. *Bull. Geol. Soc. Am.*, **82**, 3407-3420.

Söhnge, P.G. and de Villiers, J., 1946. Resume of the geology of the Richtersveld and the eastern Sperrgebiet. *Trans. geol. Soc. S. Afr.*, **49**, 263-276.

Spear, F.S. and Cheney, J.T., 1989. A petrogenetic grid for pelitic schists in the system SiO2-Al2O3-FeO-MgO-K2O-H2O. *Contr. Mineral. Petrol.*, **101**, 149-164.

Spencer, A.M., 1981. The Late Precambrian Port Askaig Tillite in Scotland. 732-636. *In: Hambrey, M.J. and Harland, W.B. (Eds.). Earth's pre-Pleistocene glacial record. Cambridge Univ. Press, Cambridge, 1004pp.*

Spencer, A.M., 1985. Mechanisms and environments of deposition of Late Precambrian geosynclinal tillites: Scotland and east Greenland. *Palaeogeog. Palaeoclim. Palaeoecol.*, **51**, 142-157.

Stanistreet, I.G., 1989. Trace fossil associations related to facies of an upper Ordovician low wave energy shoreface and shelf, Oslo-Asker district, Norway. *Lethaia*, **22**, 345-358.

Stanistreet, I.G. and McCarthy, T.S., 1991. Changing tectono-sedimentary scenarios relevant to the development of the late Archaean Witwatersrand Basin. *J. Afr. Earth Sci.*, **13**, 65-81.

Stanistreet, I.G., Kukla, P.A. and Henry, G., 1991. Sedimentary basinal responses to a Late Precambrian Wilson Cycle: the Damara Orogen and Nama Foreland, Namibia. *J. Afr. Earth. Sci.*, **13**, 141-156.

Steel, R. and Aasheim, S.M., 1978. Alluvial sand deposition in a rapidly subsiding basin (Devonian, Norway). *In: Miall, A.D. (Ed.). Fluvial Sedimentology; Mem. Can. Soc. petrol. Geol.*, **5**, 385-412.

Stow, D.A.V. and Bowen, A.J., 1980. A physical model for the transport and sorting of fine-grained sediment by turbidity currents. *Sedimentology*, **27**, 31-46.

Stowe, C.W., Hartnady, C.J.N, and Joubert, P., 1984. Proterozoic tectonic provinces of Soethern Africa. *(Abs.) Precambr. Res. Unit*, **25**, 229-231.

SWA/Namibia Geosurvey Map, 1982.

Taylor, G.C. and Stott, D.F., 1973. Tuchodi Lakes map-area, British Columbia. *Geol. Surv. Canada, Memoir*, **373**, 37pp.

Theart, H.F.J., 1980. The geology of the Precambrian terrane in parts of western Namaqualand. *Bull. Precambr. Res. Unit, Univ. Cape Town*, **30**, 103pp.

Thompson, R.I., Mercier, E. and Roots, C., 1987. Extension and its influence on Canadian Cordilleran passive-margin evolution. 409-417. *In: Coward, M.P., Dewey, J.F. and Hancock, P.L. (Eds.). Continental Extension Tectonics. Special Publication of the Geological Society of London*, **28**.

Trendall, A.F. and Morris, R,C., 1983. *Iron-formation: facts and Problems*. Elsevier, Amsterdam, 558pp.

Tucker, M.E., 1990. Carbonate depositional systems I: marine shallow-water and lacustrine carbonates. 101-227. *In: Tucker, M.E. and Wright, V.P. (Eds.). Carbonate Sedimentology*. Blackwell, Oxford, 482pp.

Turner, F.J. and Weiss, L.E., 1963. Structural analysis of metamorphic tectonites. *McGraw-Hill, New York, 545pp.*

Van Biljon, S., 1939. The Kuboos batholith in Namaqualand, South Africa. *Trans. geol. Soc. S. Africa.*, **42**, 123-219.

Van Vuuren, C.J.J., 1986. Regional setting and structure of the Rosh Pinah Zinc-Lead deposit, South West Africa/Namibia. *In: Anhaeusser, C.R., and Maske, S. (Eds.) Mineral Deposits of Southern Africa. Vol II. Geol. Soc. S. Afr., Johannesburg,* 1593-1607.

Viljoen, R.P., Minnitt, R.C.A. and Viljoen, M.J., 1986. Porphyry Copper-Molybdenum Mineralization at Lorelei, South West Africa/Namibia. *In: Anhaeusser, C.R., and Maske, S. (Eds.) Mineral Deposits of Southern Africa. Vol II. Geol. Soc. S. Afr., Johannesburg, 1559--1566.*

Von Veh, M.W., 1988. *The stratigraphy and structural evolution of the late Proterozoic Gariep Belt in the Sendelingsdrif - Annisfontein area, northwestern Cape Province.* PhD thesis (Unpubl.), Univ. Cape Town, 121 pp.

Vogt, P.R., Crane, K. and Sundvor, E., 1993. Glacigenic Mudflows on the Bear Island Submarine Fan. *EOS*, **74**, 449-453.

Vorren, T.O., Hald, M. and Lebesbye, E., 1988. Late Cenozoic environments in the Barents Sea. *Paleoceanography*, **3**, 601.

Vorren, T.O., Richardson, G., Knutsen, S.M. and Hensiken, 1991. Cenozoic erosion and sedimentation in the western Barents Sea. *Mar. Petrol. Geol.*, **8**, 317.

Walker, R.G., 1976. Facies models, 2. Turbidites and associated coarse clastic deposits. *Geosci. Can.*, **3**, 25-36.

Walker, R.G., 1978. Deep-water sandstone facies and ancient submarine fans; models for exploration for stratigraphic traps. *Bull. Amer. Assoc. Petrol. Geol.*, **62**, 932-966.

Walker, R.G. (Ed.), 1984. *Facies models* (2nd ed.). Geoscience Canada, Reprint Series 1, 317pp.

Walter, M.R. and Bauld, J., 1983. The association of sulphate evaporites, stromatolitic carbonates and glacial sediments: Examples from the Proterozoic of Australia and the Cainizoic of Antarctica. *Precambrian Res.*, **21**, 129-148.

Watson, M.D., 1980. *The geology, mineralogy and origin of the Zn-Pb-Cu deposit at Rosh Pinah, South West Africa.* PhD thesis (Unpubl.), Univ. Pretoria, 250pp.

Welke, H.J., Burger, A.J., Corner, B., Kröner, A. and Blignault, H.J., 1979. U-Pb and Rb-Sr age determination on middle Proterozoic rocks from the Lower Orange River area, South West Africa. *Trans. geol. Soc. S. Afr.*, **82**, 205-214.

Wells, N.A., 1984. Sheet debris flow and sheet flood conglomerate in Cretaceous cool-maritime alluvial fans, South Orkney Oslands, Antarctica. *In: E.H. Koster and R.J. Steel (Eds.), Sedimentology of Gravels and Conglomerates. Mem. Can Soc. Pet. Geol.*, **10**, 133-145.

Wescott and Etheridge, 1980. Fan-delta sedimentology and tectonic setting - Yallah fan-delta, southeast Jamaica. *Bull. Am. Ass. petrol. Geol.*, **64**, 374-399.

Wilson, J.L., 1975. *Carbonate facies in geologic history.* Springer, New York, 470pp.

Wyley, A.W., 1857. Report upon the mineral and geological structure of south Namaqualand and the adjoining mineral districts. *Cape of Good Hope Parl. Rep.*, G 36, Cape Town.

APPENDIX 1: *Microprobe analyses of pyroxenes from sample RP60.*

	1	2	3	4	5	6	1	2	3	4	5
SiO_2	48.20	47.71	44.34	43.52	46.25	45.19	45.37	45.59	46.01	47.36	47.65
TiO_2	1.79	1.96	3.28	3.69	1.98	2.32	2.35	2.67	2.47	2.15	2.29
Al_2O_3	5.39	5.71	8.13	8.81	7.17	7.36	8.31	7.04	7.08	6.05	5.80
Cr_2O_3	.10	.00	.00	.01	.05	.00	.00	.02	.00	.03	.13
Fe_2O_3	4.13	3.06	4.90	4.05	2.29	3.83	2.76	3.86	4.21	3.65	2.34
MgO	14.12	13.49	11.35	10.35	9.30	8.63	9.06	11.43	12.26	13.23	13.22
CaO	23.79	23.64	23.81	23.18	23.09	23.11	23.08	23.39	23.88	23.99	23.80
MnO	.08	.06	.09	.17	.18	.32	.22	.15	.08	.14	.09
FeO	1.79	2.60	3.16	4.58	8.36	8.35	8.07	4.24	3.27	2.70	3.31
Na_2O	.37	.39	.43	.52	.51	.53	.51	.46	.30	.31	.34
K_2O	.00	.01	.00	.01	.01	.01	.00	.02	.02	.00	.00
Sum	99.76	98.62	99.49	98.88	99.19	99.64	99.73	98.86	99.57	99.59	98.98
Cations:											
Si	1.787	1.790	1.672	1.658	1.767	1.731	1.726	1.729	1.726	1.766	1.785
Ti	.050	.055	.093	.106	.057	.067	.067	.076	.070	.060	.065
Al	.236	.252	.361	.395	.323	.332	.373	.314	.313	.266	.256
Fe^{3+}	.115	.086	.139	.116	.066	.110	.079	.110	.119	.102	.066
Cr	.003	.000	.000	.000	.002	.000	.000	.001	.000	.001	.004
Mg	.780	.754	.638	.588	.530	.493	.514	.646	.686	.735	.738
Ca	.945	.950	.962	.946	.945	.949	.941	.950	.960	.958	.955
Mn	.002	.002	.003	.005	.006	.010	.007	.005	.003	.004	.003
Fe^{2+}	.055	.082	.100	.146	.267	.267	.257	.134	.102	.084	.104
Na	.027	.028	.031	.039	.037	.039	.037	.034	.022	.022	.025
K	.000	.000	.000	.001	.001	.000	.000	.001	.001	.000	.000
Sum	4.000	4.000	4.000	4.000	4.000	4.000	4.000	4.000	4.000	4.000	4.000
Site occupation											
Si	1.787	1.790	1.672	1.658	1.767	1.731	1.726	1.729	1.726	1.766	1.785
Al	.213	.210	.328	.342	.233	.269	.274	.271	.274	.234	.215
Fe^{3+}	.000	.000	.000	.000	.000	.000	.000	.000	.000	.000	.000
Sum	2.000	2.000	2.000	2.000	2.000	2.000	2.000	2.000	2.000	2.000	2.000
Y											
Al	.022	.042	.034	.053	.090	.064	.098	.043	.039	.032	.041
Fe^{3+}	.115	.086	.139	.116	.066	.110	.079	.110	.119	.102	.066
Cr	.003	.000	.000	.000	.002	.000	.000	.001	.000	.001	.004
Ti	.050	.055	.093	.106	.057	.067	.067	.076	.070	.060	.065
Mg	.780	.754	.638	.588	.530	.493	.514	.646	.686	.735	.738
Fe^{2+}	.030	.062	.096	.137	.256	.266	.242	.124	.087	.069	.086
Mn	.000	.000	.000	.000	.000	.000	.000	.000	.000	.000	.000
Sum	1.000	1.000	1.000	1.000	1.000	1.000	1.000	1.000	1.000	1.000	1.000
X											
Mg	.000	.000	.000	.000	.000	.000	.000	.000	.000	.000	.000
Fe^{2+}	.026	.019	.004	.009	.011	.001	.015	.010	.015	.015	.017
Mn	.002	.002	.003	.005	.006	.010	.007	.005	.003	.004	.003
Ca	.945	.950	.962	.946	.945	.949	.941	.950	.960	.958	.955
Na	.027	.028	.031	.039	.037	.039	.037	.034	.022	.022	.025
K	.000	.000	.000	.001	.001	.000	.000	.001	.001	.000	.000
Sum	1.000	1.000	1.000	1.000	1.000	1.000	1.000	1.000	1.000	1.000	1.000

APPENDIX 2: *Microprobe analyses of amphiboles from sample AN.*

	1.00	2.00	3.00	4.00	5.00	6.00	7.00	8.00	1.00	2.00	3.00	4.00	5.00	7.00	8.00	9.00	10.00	1.00	2.00	3.00	4.00	5.00
SiO2	53.23	53.51	52.58	53.65	43.95	52.95	52.68	52.52	46.27	47.78	51.87	52.12	52.63	53.17	53.99	53.77	54.47	53.03	48.96	51.67	51.99	51.90
TiO2	0.05	0.08	0.04	0.01	0.26	0.00	0.05	0.01	0.26	0.18	0.14	0.09	0.07	0.05	0.03	0.07	0.01	0.01	0.17	0.05	0.52	0.08
Al2O3	1.92	2.16	2.40	1.92	9.54	2.31	2.69	2.66	7.90	7.00	2.99	2.80	2.41	1.91	0.95	1.58	1.34	2.20	5.55	2.31	2.44	4.5
Fe2O3	1.33	0.99	1.40	0.79	4.30	1.39	1.58	0.80	3.87	3.27	1.30	1.62	1.02	0.82	0.94	0.84	0.32	1.16	2.29	2.45	0.91	1.48
Cr2O3	0.03	0.00	0.05	0.00	0.00	0.00	0.00	0.00	0.00	0.00	0.03	0.00	0.01	0.00	0.00	0.00	0.03	0.03	0.00	0.03	0.03	0.00
MgO	13.76	14.05	13.54	13.77	8.53	13.85	13.58	13.17	9.62	10.38	13.17	13.67	13.43	13.25	14.44	14.35	14.79	14.06	11.49	13.94	13.78	13.29
CaO	12.17	12.01	12.12	12.13	11.22	11.93	12.00	11.85	11.49	11.07	11.84	11.75	11.89	12.11	12.20	11.89	12.07	12.25	11.51	12.15	12.26	11.94
MnO	0.43	0.48	0.36	0.38	0.47	0.46	0.46	0.46	0.42	0.44	0.38	0.41	0.50	0.29	0.35	0.48	0.38	0.39	0.52	0.40	0.43	0.39
FeO	14.74	13.94	14.49	15.06	16.52	14.37	14.35	15.24	16.43	16.06	14.44	13.92	14.35	15.71	14.54	14.32	14.23	13.88	15.13	12.99	14.11	14.37
Na2O	0.30	0.42	0.40	0.28	1.33	0.39	0.45	0.29	1.10	1.07	0.45	0.48	0.43	0.26	0.22	0.32	0.19	0.36	0.84	0.40	0.46	0.36
K2O	0.13	0.06	0.10	0.09	0.40	0.10	0.08	0.14	0.32	0.28	0.15	0.14	0.13	0.10	0.06	0.09	0.05	0.10	0.20	0.10	0.14	0.12
Sum	98.09	97.70	97.47	98.07	96.52	97.74	97.90	97.13	97.66	97.52	96.74	97.04	96.85	97.68	97.72	97.70	97.90	97.47	96.66	96.49	97.06	96.57
Cations																						
Si	7.745	7.770	7.696	7.792	6.717	7.716	7.672	7.719	6.944	7.125	7.650	7.649	7.738	7.782	7.856	7.815	7.871	7.732	7.309	7.631	7.641	7.669
Ti	0.005	0.009	0.004	0.001	0.029	0.000	0.005	0.001	0.029	0.020	0.015	0.010	0.007	0.005	0.003	0.007	0.001	0.001	0.019	0.006	0.057	0.009
Al	0.329	0.369	0.413	0.328	1.719	0.397	0.462	0.460	1.396	1.231	0.520	0.485	0.417	0.329	0.163	0.270	0.228	0.378	0.977	0.401	0.422	0.461
Fe3	0.145	0.108	0.154	0.086	0.495	0.152	0.173	0.088	0.437	0.367	0.144	0.179	0.113	0.091	0.103	0.092	0.035	0.127	0.257	0.272	0.101	0.165
Cr	0.004	0.000	0.005	0.000	0.000	0.000	0.000	0.000	0.000	0.000	0.000	0.003	0.000	0.001	0.000	0.000	0.003	0.003	0.000	0.004	0.003	0.000
Mg	2.984	3.041	2.955	2.981	1.943	3.009	2.948	2.885	2.151	2.307	2.896	2.991	2.943	2.892	3.132	3.108	3.187	3.055	2.556	3.068	3.019	2.928
Ca	1.898	1.868	1.901	1.887	1.838	1.863	1.872	1.868	1.848	1.769	1.871	1.848	1.872	1.899	1.902	1.851	1.870	1.914	1.841	1.922	1.930	1.890
Mn	0.053	0.059	0.044	0.047	0.061	0.057	0.056	0.058	0.053	0.055	0.048	0.051	0.063	0.036	0.043	0.059	0.047	0.048	0.066	0.050	0.053	0.049
Fe2	1.794	1.693	1.774	1.829	2.111	1.751	1.747	1.873	2.062	2.002	1.781	1.709	1.764	1.922	1.770	1.741	1.720	1.693	1.889	1.604	1.734	1.775
Na	0.085	0.119	0.113	0.078	0.394	0.110	0.126	0.083	0.320	0.310	0.128	0.138	0.121	0.075	0.061	0.090	0.053	0.102	0.243	0.115	0.130	0.103
K	0.024	0.012	0.018	0.017	0.077	0.018	0.015	0.026	0.061	0.053	0.029	0.026	0.024	0.018	0.012	0.017	0.010	0.019	0.038	0.019	0.025	0.022
Sum	15.065	15.048	15.079	15.047	15.383	15.073	15.077	15.060	15.300	15.238	15.082	15.089	15.063	15.049	15.045	15.050	15.093	15.074	15.196	15.092	15.117	15.071
Site occupation																						
T																						
Si	7.745	7.770	7.696	7.792	6.717	7.716	7.672	7.719	6.944	7.125	7.650	7.649	7.738	7.782	7.856	7.815	7.871	7.732	7.309	7.631	7.641	7.669
Al	0.255	0.230	0.304	0.208	1.283	0.284	0.328	0.281	1.056	0.875	0.350	0.351	0.262	0.218	0.144	0.185	0.129	0.268	0.691	0.369	0.359	0.331
Cr	0.000	0.000	0.000	0.000	0.000	0.000	0.000	0.000	0.000	0.000	0.000	0.000	0.000	0.000	0.000	0.000	0.000	0.000	0.000	0.000	0.000	0.000
Fe3	0.000	0.000	0.000	0.000	0.000	0.000	0.000	0.000	0.000	0.000	0.000	0.000	0.000	0.000	0.000	0.000	0.000	0.000	0.000	0.000	0.000	0.000
Sum	8.000	8.000	8.000	8.000	8.000	8.000	8.000	8.000	8.000	8.000	8.000	8.000	8.000	8.000	8.000	8.000	8.000	8.000	8.000	8.000	8.000	8.000
C																						
Al	0.074	0.139	0.110	0.120	0.435	0.113	0.134	0.179	0.330	0.355	0.169	0.134	0.155	0.111	0.019	0.085	0.100	0.110	0.285	0.032	0.063	0.130
Cr	0.004	0.000	0.005	0.000	0.000	0.000	0.000	0.000	0.000	0.000	0.000	0.003	0.000	0.001	0.000	0.000	0.003	0.003	0.000	0.004	0.003	0.000
Fe3	0.145	0.108	0.154	0.086	0.495	0.152	0.173	0.088	0.437	0.367	0.144	0.179	0.113	0.091	0.103	0.092	0.035	0.127	0.257	0.272	0.101	0.165
Ti	0.005	0.009	0.004	0.001	0.029	0.000	0.005	0.001	0.029	0.020	0.015	0.010	0.007	0.005	0.003	0.007	0.001	0.001	0.019	0.006	0.057	0.009
Mg	2.984	3.041	2.955	2.981	1.943	3.009	2.948	2.885	2.151	2.307	2.896	2.991	2.943	2.892	3.132	3.108	3.187	3.055	2.556	3.068	3.019	2.928
Fe2	1.788	1.693	1.771	1.811	2.098	1.726	1.740	1.847	2.042	1.951	1.776	1.682	1.764	1.901	1.743	1.708	1.674	1.693	1.882	1.604	1.734	1.768
Mn	0.000	0.010	0.000	0.000	0.000	0.000	0.000	0.000	0.000	0.000	0.000	0.000	0.017	0.000	0.000	0.000	0.000	0.010	0.000	0.015	0.022	0.000
Sum	5.000	5.000	5.000	5.000	5.000	5.000	5.000	5.000	5.000	5.000	5.000	5.000	5.000	5.000	5.000	5.000	5.000	5.000	5.000	5.000	5.000	5.000
B																						
Mg	0.000	0.000	0.000	0.000	0.000	0.000	0.000	0.000	0.000	0.000	0.000	0.000	0.000	0.000	0.000	0.000	0.000	0.000	0.000	0.000	0.000	0.000
Fe2	0.006	0.000	0.002	0.018	0.013	0.025	0.007	0.026	0.020	0.051	0.006	0.026	0.000	0.022	0.026	0.033	0.046	0.000	0.007	0.000	0.000	0.007
Mn	0.053	0.049	0.044	0.047	0.061	0.057	0.056	0.058	0.053	0.055	0.048	0.051	0.045	0.036	0.043	0.059	0.047	0.038	0.066	0.036	0.031	0.049
Ca	1.898	1.868	1.901	1.887	1.838	1.863	1.872	1.868	1.848	1.769	1.871	1.848	1.872	1.899	1.902	1.851	1.870	1.914	1.841	1.922	1.930	1.890
Na	0.043	0.083	0.053	0.048	0.088	0.054	0.065	0.048	0.080	0.125	0.075	0.074	0.083	0.044	0.028	0.057	0.037	0.048	0.086	0.042	0.039	0.053
Sum	2.000	2.000	2.000	2.000	2.000	2.000	2.000	2.000	2.000	2.000	2.000	2.000	2.000	2.000	2.000	2.000	2.000	2.000	2.000	2.000	2.000	2.000
A																						
Na	0.042	0.036	0.060	0.030	0.305	0.055	0.061	0.034	0.240	0.185	0.053	0.064	0.039	0.031	0.033	0.033	0.016	0.054	0.157	0.074	0.091	0.049
K	0.024	0.012	0.018	0.017	0.077	0.018	0.015	0.026	0.061	0.053	0.029	0.026	0.024	0.018	0.012	0.017	0.010	0.019	0.038	0.019	0.025	0.022
Sum	0.065	0.048	0.079	0.047	0.383	0.073	0.077	0.060	0.300	0.238	0.082	0.089	0.063	0.049	0.045	0.050	0.026	0.074	0.196	0.092	0.117	0.071
Na auf B	0.043	0.083	0.053	0.048	0.088	0.054	0.065	0.048	0.080	0.125	0.075	0.074	0.083	0.044	0.028	0.057	0.037	0.048	0.086	0.042	0.039	0.053
Mg/Mg+	0.625	0.642	0.625	0.620	0.479	0.632	0.628	0.606	0.511	0.535	0.619	0.636	0.625	0.601	0.639	0.641	0.649	0.643	0.575	0.657	0.635	0.623
Fe3/Fe3+	0.663	0.438	0.584	0.417	0.532	0.575	0.564	0.330	0.562	0.508	0.460	0.573	0.421	0.450	0.845	0.518	0.261	0.537	0.474	0.895	0.616	0.559
Si/Cell	7.745	7.770	7.696	7.792	6.717	7.716	7.672	7.719	6.944	7.125	7.650	7.649	7.738	7.782	7.856	7.815	7.871	7.732	7.309	7.631	7.641	7.669
ln(Ca/Na)	3.778	3.118	3.584	3.673	3.034	3.533	3.363	3.652	3.138	2.649	3.213	3.215	3.121	3.768	4.223	3.486	3.914	3.683	3.062	3.826	3.906	3.567
Na/Ca	4.28	5.97	5.62	3.96	17.65	5.56	6.32	4.25	14.75	14.93	6.42	6.93	6.08	3.80	3.10	4.63	2.77	5.08	11.68	5.66	6.31	5.16
Al/Si	4.08	4.53	5.10	4.04	20.37	4.89	5.67	5.63	16.74	14.73	6.36	5.96	5.12	4.06	2.03	3.35	2.82	4.66	11.79	4.99	5.24	5.67

APPENDIX 3: *Microprobe analyses of plagioclases from amphibolite samples A1, A5, AN, RP60 and garnet-chlorite schist samples P2 and 235.*

	A1 F1 9	A1 F1 11	A1 F1 12	A1 F1 13	A1 F1 14	A1 F1 15	A1 F1 16	A1 F3 1	A1 F3 2	A1 F3 3	A3 F3 4	A3 F3 5	A3 F3 6	A1 F4 7	A1 F4 8	A1 F5 1	A1 F5 2	A1 F5 3	A1 F5 4	A1 F6 1	A1 F6 2	A1 F6 3
SiO2	62.53	63.32	62.62	62.34	63.63	63.05	63.59	64.13	63.47	63.95	62.80	62.70	62.93	62.66	63.17	62.48	63.18	62.89	63.42	62.84	62.82	62.53
Al2O3	23.34	23.05	23.00	23.09	22.50	22.93	22.80	22.77	22.83	22.64	23.35	23.36	23.40	23.68	23.03	23.25	22.96	23.24	22.84	23.30	23.16	22.94
MgO	0.01	0.01	0.00	0.00	0.00	0.00	0.00	0.00	0.00	0.02	0.00	0.00	0.00	0.03	0.00	0.00	0.00	0.02	0.00	0.00	0.00	0.00
CaO	4.84	4.55	4.66	4.81	4.24	4.62	4.78	4.14	4.40	4.27	4.73	4.75	4.98	5.33	4.39	4.88	4.31	4.59	4.15	4.86	4.78	4.78
MnO	0.02	0.00	0.00	0.00	0.00	0.01	0.01	0.04	0.00	0.00	0.00	0.00	0.00	0.00	0.00	0.05	0.02	0.00	0.05	0.00	0.03	0.00
FeO	0.12	0.09	0.08	0.09	0.08	0.09	0.13	0.11	0.16	0.07	0.12	0.13	0.05	0.21	0.23	0.22	0.22	0.36	0.28	0.13	0.10	0.10
BaO	0.00	0.07	0.00	0.06	0.00	0.07	0.00	0.00	0.11	0.02	0.02	0.00	0.00	0.00	0.00	0.03	0.00	0.00	0.00	0.00	0.06	0.00
Na2O	8.97	9.13	8.92	8.90	9.27	8.88	8.77	9.45	9.11	9.13	8.99	8.96	8.80	8.38	9.00	8.78	8.99	8.81	9.31	8.77	8.77	8.84
K2O	0.02	0.04	0.05	0.05	0.06	0.05	0.02	0.04	0.09	0.04	0.06	0.06	0.03	0.07	0.08	0.08	0.08	0.09	0.07	0.07	0.06	0.07
Total	99.85	100.27	99.32	99.33	99.78	99.69	100.09	100.68	100.17	100.15	100.07	99.96	100.18	100.35	99.50	99.75	99.74	100.00	100.12	99.97	99.78	99.26
Cations																						
Si	2.774	2.794	2.789	2.780	2.817	2.797	2.807	2.815	2.804	2.819	2.779	2.777	2.779	2.765	2.796	2.776	2.800	2.784	2.803	2.782	2.786	2.788
Al	1.220	1.199	1.207	1.214	1.174	1.199	1.186	1.178	1.189	1.176	1.218	1.219	1.218	1.232	1.207	[illegible]	1.199	1.212	1.190	1.215	1.211	1.205
Mg	0.000	0.001	0.000	0.000	0.000	0.000	0.000	0.000	0.000	0.001	0.000	0.000	0.000	0.002	0.000	[illegible]	0.000	0.001	0.000	0.000	0.000	0.000
Ca	0.230	0.215	0.222	0.230	0.201	0.219	0.226	0.195	0.208	0.202	0.224	0.226	0.236	0.252	0.201	[illegible]	0.204	0.218	0.197	0.230	0.227	0.229
Mn	0.001	0.000	0.000	0.000	0.000	0.000	0.000	0.002	0.000	0.000	0.000	0.000	0.000	0.000	0.000	0.002	0.001	0.000	0.002	0.000	0.001	0.000
Fe	0.004	0.003	0.003	0.003	0.003	0.003	0.005	0.004	0.006	0.003	0.005	0.005	0.002	0.008	0.008	0.008	0.008	0.013	0.010	0.005	0.004	0.004
Ba	0.000	0.001	0.000	0.001	0.000	0.001	0.000	0.000	0.002	0.000	0.000	0.000	0.000	0.000	0.000	0.001	0.000	0.000	0.000	0.000	0.001	0.000
Na	0.772	0.781	0.770	0.770	0.796	0.764	0.751	0.805	0.781	0.781	0.771	0.770	0.754	0.717	0.773	0.756	0.772	0.756	0.798	0.753	0.754	0.764
K	0.001	0.002	0.003	0.003	0.003	0.003	0.001	0.002	0.005	0.002	0.003	0.003	0.002	0.004	0.005	0.004	0.005	0.005	0.004	0.004	0.004	0.004
Total	5.002	4.998	4.994	5.000	4.995	4.987	4.976	5.000	4.994	4.984	5.000	5.000	4.998	4.989	4.992	4.996	4.989	4.990	5.003	4.989	4.987	4.994
Si+Al	3.994	3.994	3.996	3.993	3.992	3.996	3.993	3.993	3.993	3.995	3.996	3.996	3.997	3.997	3.998	3.993	3.999	3	3.993	3.997	3.997	3.993
Na+Ca+	1.003	1.000	0.995	1.005	1.000	0.987	0.978	1.002	0.995	0.985	0.999	0.998	0.991	0.973	0.985	0.993	0.981	0.9	0.998	0.987	0.986	0.997
AN(Si/Al)	22.14	19.97	20.74	21.43	17.52	19.87	18.72	17.86	18.86	17.67	21.75	21.94	21.80	23.14	20.11	21.76	19.83	21	19.04	21.51	21.04	20.59
AB(Si/Al)	77.75	79.66	79.00	78.21	82.16	79.70	81.16	81.90	80.46	82.09	77.87	77.73	78.04	76.45	79.42	77.76	79.71	78.[illegible]	80.59	78.07	78.49	78.99
Diff.:	0.82%	1.55%	1.62%	1.49%	2.60%	2.35%	4.39%	1.59%	2.06%	2.82%	0.67%	0.66%	1.97%	2.75%	1.02%	1.61%	1.00%	1.03%	0.65%	1.61%	2.02%	2.34%
AN(Na/Ca	22.96	21.52	22.35	22.91	20.12	22.22	23.11	19.45	20.92	20.49	22.42	22.60	23.77	25.89	21.12	23.38	20.83	22.24	19.69	23.32	23.06	22.93
AB(Na/Ca	76.94	78.10	77.38	76.72	79.57	77.36	76.77	80.31	78.41	79.27	77.20	77.08	76.07	73.70	78.41	76.14	78.71	77.24	79.94	76.26	76.47	76.65
OR	0.11	0.25	0.26	0.27	0.32	0.30	0.12	0.24	0.49	0.21	0.35	0.33	0.16	0.41	0.47	0.43	0.46	0.51	0.37	0.42	0.37	0.42
CE	0.00	0.13	0.00	0.10	0.00	0.12	0.00	0.00	0.19	0.03	0.03	0.00	0.00	0	0.00	0.05	0.00	0.00	0.00	0.00	0.10	0.00

	A5 F2 6	A5 F2 7	A5 F2 8	A5 F2 5	A5 F2 10	A5 F3 7	A5 F3 10	A5 F4 1	A5 F4 2	A5 F4 3	A5 F4 4	A5 F4 5	A5 F5 6	A5 F5 7	A5 F5 8
SiO2	68.67	67.82	68.69	68.36	69.17	68.33	68.79	68.87	69.63	69.39	69.06	69.47	69.59	68.92	69.46
Al2O3	20.31	19.96	20.00	20.10	19.78	19.72	20.19	19.89	19.84	20.03	20.15	19.71	20.02	19.82	19.97
MgO	0.02	0.01	0.01	0.00	0.00	0.00	0.00	0.02	0.00	0.00	0.01	0.01	0.04	0.00	0.05
CaO	0.60	0.50	0.18	0.58	0.39	0.28	0.42	0.18	0.04	0.14	0.35	0.09	0.20	0.29	0.39
MnO	0.04	0.00	0.00	0.00	0.00	0.00	0.00	0.00	0.00	0.00	0.00	0.00	0.00	0.00	0.00
FeO	0.03	0.06	0.04	0.15	0.07	0.10	0.08	0.08	0.01	0.10	0.06	0.16	0.00	0.11	0.01
BaO	0.01	0.09	0.00	0.00	0.02	0.00	0.00	0.06	0.02	0.00	0.00	0.02	0.02	0.02	0.00
Na2O	11.37	11.24	11.49	11.39	11.49	11.52	11.44	11.30	11.73	11.59	11.77	11.61	11.36	11.51	11.53
K2O	0.00	0.05	0.04	0.01	0.02	0.03	0.00	0.04	0.03	0.04	0.04	0.04	0.02	0.03	0.05
Total	101.05	99.75	100.45	100.59	100.94	99.98	100.92	100.43	101.29	101.28	101.43	101.10	101.24	100.68	101.46
Cations															
Si	2.969	2.973	2.984	2.972	2.988	2.985	2.977	2.991	2.998	2.990	2.976	2.999	2.995	2.989	2.989
Al	1.035	1.031	1.024	1.029	1.008	1.016	1.030	1.018	1.007	1.017	1.023	1.003	1.016	1.013	1.013
Mg	0.001	0.001	0.001	0.000	0.000	0.000	0.000	0.001	0.000	0.000	0.001	0.001	0.002	0.000	0.003
Ca	0.028	0.023	0.008	0.027	0.018	0.013	0.020	0.008	0.002	0.006	0.016	0.004	0.009	0.013	0.018
Mn	0.001	0.000	0.000	0.000	0.000	0.000	0.000	0.000	0.000	0.000	0.000	0.000	0.000	0.000	0.000
Fe	0.001	0.003	0.002	0.005	0.002	0.004	0.003	0.003	0.000	0.003	0.002	0.006	0.000	0.004	0.000
Ba	0.000	0.001	0.000	0.000	0.000	0.000	0.000	0.001	0.000	0.000	0.000	0.000	0.000	0.000	0.000
Na	0.953	0.955	0.968	0.960	0.964	0.976	0.960	0.952	0.979	0.968	0.983	0.971	0.948	0.968	0.962
K	0.000	0.003	0.002	0.001	0.001	0.002	0.000	0.002	0.002	0.002	0.002	0.002	0.001	0.001	0.003
Total	4.990	4.991	4.989	4.994	4.986	4.995	4.989	4.977	4.989	4.987	5.005	4.986	4.972	4.989	4.987
Si+Al	4.005	4.004	4.008	4.001	4.000	4.001	4.006	4.009	4.005	4.007	4.000	4.002	4.011	4.002	4.001
Na+Ca+	0.981	0.983	0.978	0.988	0.983	0.991	0.979	0.963	0.983	0.977	1.002	0.978	0.959	0.983	0.982
AN(Si/Al)	3.50	3.08	2.38	2.94	0.84	1.57	2.95	1.79	0.68	1.70	2.33	0.27	1.54	1.31	1.26
AB(Si/Al)	96.48	96.47	97.41	96.99	99.04	98.25	97.05	97.88	99.11	98.08	97.45	99.48	98.3[illegible]	[illegible].51	98.46
Diff.:	0.65%	[illegible]%	1.51%	0.21%	1.01%	0.23%	0.95%	0.91%	0.5[illegible]%	1.04%	0.73%	0.16%	0.6[illegible]%	1.05%	0.58%
AN(Na/Ca	2.85		0.87	2.73	1.85	1.34	2.01	0.88	0.17	0.66	1.61	0.43	0.94	1.37	1.84
AB(Na/Ca	97.13	97.18	98.92	97.20	98.03	98.48	97.99	98.79	99.62	99.12	98.17	99.32	98.91	98.46	97.89
OR	0.00	0.31	0.21	0.07	0.09	0.18	0.00	0.23	0.17	0.23	0.22	0.23	0.11	0.15	0.27
CE	0.02	0.15	0.00	0.00	0.03	0.00	0.00	0.10	0.04	0.00	0.00	0.03	0.04	0.03	0.00

	235.0000 F1 1	235.0000 F1 2	235.0000 Fi 3	235.0000 F1 4	235.0000 F1 5
SiO2	66.68	65.93	65.95	65.11	67.08
Al2O3	18.76	18.68	18.56	18.30	18.89
MgO	0.00	0.12	0.03	0.30	0.02
CaO	0.00	0.00	0.01	0.01	0.00
MnO	0.00	0.05	0.02	0.00	0.02
FeO	0.06	0.47	0.03	0.49	0.08
BaO	0.04	0.04	0.07	0.07	0.10
Na2O	0.10	0.14	0.14	0.14	0.15
K2O	15.08	14.98	14.99	14.85	14.77
Total	100.74	100.41	99.80	99.27	101.10
Cations					
Si	3.025	3.010	3.023	3.010	3.027
Al	1.003	1.005	1.002	0.997	1.005
Mg	0.000	0.008	0.002	0.020	0.001
Ca	0.000	0.000	0.000	0.000	0.000
Mn	0.000	0.002	0.001	0.000	0.001
Fe	0.002	0.018	0.001	0.019	0.003
Ba	0.001	0.001	0.001	0.001	0.002
Na	0.009	0.013	0.012	0.012	0.013
K	0.873	0.873	0.877	0.876	0.850
Total	4.914	4.929	4.920	4.936	4.902
Si+Al	4.029	4.016	4.025	4.007	4.032
Na+Ca+	0.883	0.886	0.891	0.890	0.865
AN(Si/Al)	0.00	0.01	0.00	-0.00	0.00
AB(Si/Al)	1.04	1.40	1.41	1.42	1.53
Diff.:	0.01%	0.01%	0.05%	0.06%	0.01%
AN(Na/Ca	0.01	0.00	0.06	0.06	0.00
AB(Na/Ca	1.04	1.41	1.36	1.36	1.54
OR	98.87	98.51	98.44	98.44	98.26
CE	0.08	0.08	0.15	0.15	0.20

	AN F1 7	AN F1 10	AN F2 1	AN F2 2	AN F2 3	AN F2 4	AN F3 6	AN F3 7	AN F3 8	AN F3 9	AN F3 10	AN F4 1	AN F4 2	AN F4 3	AN F4 4	AN F4 5	AN F5 6	AN F5 7	AN F5 8	AN F5 9
SiO2	68.98	69.39	69.22	68.65	69.43	69.11	69.55	69.34	69.12	68.75	68.97	68.49	68.83	69.09	68.97	69.21	69.62	68.55	68.89	68.61
Al2O3	19.54	19.89	19.83	19.91	19.81	20.17	19.62	20.01	19.64	19.[illegible]	19.44	19.33	19.45	19.32	19.41	19.56	19.65	19.42	19.32	19.52
MgO	0.03	0.01	0.03	0.19	0.02	0.00	0.00	0.01	0.00	[illegible]	0.01	0.00	0.02	0.02	0.01	0.00	0.00	0.02	0.04	0.00
CaO	0.15	0.16	0.13	0.22	0.20	0.20	0.18	0.19	0.18	0.3[illegible]	0.26	0.31	0.21	0.25	0.17	0.2[illegible]	0.18	0.25	0.16	0.24
MnO	0.02	0.00	0.03	0.04	0.02	0.04	0.00	0.00	0.00	0.00	0.03	0.00	0.03	0.00	0.00	0.02	0.00	0.00	0.00	0.02
FeO	0.13	0.06	0.05	0.18	0.09	0.22	0.14	0.07	0.04	0.00	0.04	0.09	0.11	0.11	0.04	0.13	0.17	0.19	0.17	0.15
BaO	0.02	0.02	0.00	0.00	0.05	0.00	0.00	0.00	0.00	0.02	0.01	0.00	0.05	0.01	0.00	0.05	0.03	0.01	0.09	0.00
Na2O	8.85	11.21	11.46	11.29	11.52	11.64	11.55	11.55	11.57	11.22	11.50	11.43	11.27	11.56	11.78	11.40	11.49	11.32	11.53	11.32
K2O	4.23	0.09	0.06	0.08	0.10	0.10	0.05	0.06	0.06	0.08	0.08	0.41	0.17	0.12	0.09	0.09	0.08	0.10	0.06	0.09
Total	101.95	100.84	100.81	100.55	101.23	101.50	101.08	101.24	100.61	99.74	100.33	100.05	100.14	100.48	100.47	100.70	101.21	100.07	100.26	99.94
Cations																				
Si	2.997	2.999	2.995	2.982	2.995	2.978	3.003	2.989	2.998	3.006	3.001	2.996	3.001	3.004	2.999	3.001	3.002	2.995	3.002	2.997
Al	1.001	1.013	1.011	1.019	1.007	1.024	0.998	1.017	1.004	0.996	0.997	0.997	0.999	0.990	0.995	1.000	0.999	1.000	0.993	1.005
Mg	0.002	0.001	0.002	0.012	0.001	0.000	0.000	0.001	0.000	0.000	0.001	0.000	0.002	0.001	0.000	0.000	0.000	0.002	0.002	0.000
Ca	0.007	0.008	0.006	0.010	0.009	0.009	0.008	0.009	0.008	0.015	0.012	0.014	0.010	0.012	0.008	0.011	0.008	0.012	0.007	0.011
Mn	0.001	0.000	0.001	0.001	0.001	0.002	0.000	0.000	0.000	0.000	0.001	0.000	0.001	0.000	0.000	0.001	0.000	0.000	0.000	0.001
Fe	0.005	0.002	0.002	0.006	0.003	0.008	0.005	0.003	0.002	0.000	0.001	0.003	0.004	0.004	0.002	0.005	0.006	0.007	0.005	0.005
Ba	0.000	0.000	0.000	0.000	0.001	0.000	0.000	0.000	0.000	0.000	0.000	0.000	0.001	0.000	0.000	0.001	0.000	0.000	0.002	0.000
Na	0.745	0.939	0.961	0.951	0.964	0.972	0.966	0.966	0.973	0.951	0.971	0.969	0.953	0.974	0.993	0.958	0.960	0.976	0.974	0.958
K	0.235	0.005	0.003	0.004	0.006	0.005	0.003	0.003	0.004	0.004	0.004	0.023	0.009	0.007	0.005	0.005	0.004	0.005	0.004	0.005
Total	4.992	4.967	4.982	4.986	4.986	4.999	4.983	4.987	4.988	4.973	4.988	5.002	4.980	4.992	5.002	4.981	4.981	4.996	4.990	4.982
Si+Al	3.998	4.012	4.006	4.001	4.002	4.002	4.001	4.006	4.002	4.003	3.998	3.992	4.001	3.994	3.994	4.000	4.001	3.994	3.995	4.002
Na+Ca+	0.987	0.952	0.971	0.966	0.979	0.987	0.977	0.978	0.985	0.971	0.987	1.006	0.973	0.993	1.006	0.975	0.973	0.993	0.987	0.975
AN(Si/Al)	0.05	1.27	1.11	1.90	0.69	2.42	-0.19	1.65	[illegible]39	-0.36	-0.32	-0.34	-0.05	-1.02	-0.50	-0.04	-0.09	-0.01	-0.75	0.47
AB(Si/Al)	76.16	98.17	98.54	97.66	98.63	97.03	99.93	98.01	[illegible]25	99.87	99.88	98.05	99.02	100.33	100.00	99.42	99.60	99.47	100.22	98.99
Diff.:	0.67%	0.49%	0.49%	0.83%	0.24%	1.47%	1.04%	0.71%	[illegible]%	1.87%	1.57%	1.77%	1.07%	2.21%	1.28%	1.15%	0.94%	1.21%	1.50%	0.66%
AN(Na/Ca	0.72	0.79	0.62	1.07	0.93	0.95	0.85	0.92	0.84	1.51	1.24	1.42	1.82	1.19	0.78	1.11	0.85	1.20	0.75	1.13
AB(Na/Ca	75.49	98.66	99.03	98.49	98.40	98.58	98.89	98.74	98.81	97.99	98.31	96.28	97.95	98.12	98.73	98.18	98.66	98.25	98.72	98.33
OR	23.75	0.52	0.35	0.44	0.58	0.55	0.26	0.34	0.35	0.46	0.44	2.30	0.95	0.68	0.49	0.52	0.44	0.53	0.36	0.54
CE	0.04	0.04	0.00	0.00	0.09	0.00	0.00	0.00	0.00	0.04	0.01	0.00	0.05	0.02	0.00	0.09	0.05	0.02	0.16	0.00

	P2 F1 F2	P2 F1 F4	P2 F1 F5	P2 F1 F6	P2 F1 F7	P2 P1 F8	P2 F2 F10
SiO2	63.43	60.64	61.93	61.00	59.97	60.51	60.19
Al2O3	23.49	24.92	25.47	25.07	25.16	24.71	25.51
MgO	0.00	0.00	0.00	0.05	0.00	0.00	0.00
CaO	5.07	6.54	6.67	6.00	6.98	6.68	7.35
MnO	0.02	0.03	0.01	0.00	0.00	0.02	0.00
FeO	0.05	0.26	0.25	0.24	0.19	0.17	0.14
BaO	0.00	0.00	0.09	0.00	0.00	0.00	0.06
Na2O	8.64	7.79	6.30	7.43	7.41	7.79	7.58
K2O	0.06	0.05	0.02	0.24	0.04	0.05	0.05
Total	100.74	100.22	100.75	100.03	99.75	99.92	100.87
Cations							
Si	2.784	2.692	2.716	2.706	2.676	2.695	2.662
Al	1.215	1.304	1.317	1.310	1.323	1.297	1.330
Mg	0.000	0.000	0.000	0.003	0.000	0.000	0.000
Ca	0.238	0.311	0.313	0.285	0.334	0.319	0.348
Mn	0.001	0.001	0.000	0.000	0.000	0.001	0.000
Fe	0.002	0.010	0.009	0.009	0.007	0.006	0.005
Ba	0.000	0.000	0.002	0.000	0.000	0.000	0.001
Na	0.735	0.671	0.536	0.639	0.641	0.673	0.650
K	0.003	0.003	0.001	0.014	0.002	0.003	0.003
Total	4.978	4.892	4.894	4.966	4.984	4.994	4.999
Si+Al	3.999	3.997	4.033	4.016	4.000	3.993	3.992
Na+Ca+	0.976	0.985	0.852	0.938	0.977	0.995	1.002
AN(Si/Al)	21.46	30.45	30.56	30.09	32.25	29.85	33.12
AB(Si/Al)	78.22	69.28	69.12	68.44	67.50	69.85	66.50
Diff.:	2.95%	1.15%	6.22%	0.32%	1.91%	2.20%	1.65%
AN(Na/Ca	24.41	31.59	36.78	30.41	34.16	32.05	34.77
AB(Na/Ca	75.27	68.13	62.90	68.12	65.59	67.65	64.88
OR	0.32	0.28	0.13	1.47	0.25	0.30	0.28
CE	0.00	0.00	0.18	0.00	0.00	0.00	0.10

	RP60 F2 1	RP60 F2 2	RP60 F2 3	RP60 F2 4	RP60 F3 9	RP60 F4 13	RP60 F5 6	RP60 F5 8	RP60 F5 9	RP60 F7 5	RP60 F7 7	RP60 F7 8
SiO2	67.55	68.18	67.48	68.49	68.32	67.52	65.23	67.72	67.47	68.83	68.17	68.45
Al2O3	19.53	19.38	19.42	19.72	19.40	19.65	19.42	19.83	19.71	19.62	19.36	19.48
MgO	0.02	0.00	0.00	0.03	0.00	0.00	0.84	0.01	0.00	0.02	0.04	0.02
CaO	0.20	0.18	0.17	0.12	0.09	0.13	1.57	0.17	0.36	0.30	0.16	0.34
MnO	0.00	0.00	0.01	0.00	0.04	0.00	0.04	0.00	0.02	0.02	0.05	0.00
FeO	0.23	0.00	0.07	0.03	0.04	0.13	1.96	0.11	0.10	0.05	0.13	0.10
BaO	0.00	0.00	0.00	0.04	0.02	0.06	0.04	0.00	0.00	0.04	0.00	0.00
Na2O	11.18	11.04	11.58	11.39	11.22	11.40	10.40	11.16	11.20	11.38	11.29	10.95
K2O	0.05	0.04	0.03	0.07	0.04	0.03	0.08	0.06	0.03	0.02	0.07	0.06
Total	98.76	98.82	98.76	99.89	99.15	98.92	99.56	99.07	98.94	100.34	99.28	99.41
Cations												
Si	2.987	3.005	2.986	2.992	3.003	2.982	2.907	2.982	2.979	2.995	2.998	3.001
Al	1.017	1.006	1.013	1.015	1.005	1.023	1.020	1.029	1.025	1.006	1.003	1.006
Mg	0.001	0.000	0.000	0.002	0.000	0.000	0.055	0.001	0.000	0.001	0.003	0.001
Ca	0.009	0.008	0.008	0.006	0.004	0.006	0.075	0.008	0.017	0.014	0.007	0.016
Mn	0.000	0.000	0.000	0.000	0.001	0.000	0.001	0.000	0.001	0.001	0.002	0.000
Fe	0.008	0.000	0.003	0.001	0.001	0.005	0.073	0.004	0.004	0.002	0.005	0.004
Ba	0.000	0.000	0.000	0.001	0.000	0.001	0.001	0.000	0.000	0.001	0.000	0.000
Na	0.959	0.943	0.994	0.965	0.956	0.976	0.898	0.953	0.954	0.960	0.962	0.931
K	0.003	0.002	0.002	0.004	0.002	0.002	0.004	0.004	0.002	0.004	0.004	0.004
Total	4.985	4.965	5.005	4.985	4.974	4.995	5.035	4.981	4.991	4.984	4.984	4.963
AN(Na/Ca	0.97	0.89	0.79	0.58	0.44	0.62	7.68	0.85	1.73	1.45	0.76	1.67
AB(Na/Ca	98.72	98.88	99.02	98.94	99.33	99.11	91.81	98.79	98.11	98.05	98.84	97.95
OR	0.31	0.24	0.19	0.41	0.26	0.15	0.44	0.37	0.16	0.44	0.40	0.38
CE	0.00	0.68	0.00	0.07	0.03	0.11	0.07	0.00	0.00	0.07	0.00	0.00
CaFs	0.010	0.009	0.008	0.006	0.004	0.006	0.077	0.008	0.017	0.014	0.008	0.017

APPENDIX 4: *Microprobe analyses of the epidote samples A1, A2, RP60.*

Analysis	A1 F5	A1 F7	A1 F7	A1 F7
	8.00	1.00	2.00	3.00
SiO_2	37.18	37.00	37.28	37.18
TiO_2	0.04	0.05	0.05	0.05
Al_2O_3	23.71	23.49	23.67	24.09
Cr_2O_3	0.00	0.04	0.00	0.00
Fe_2O_3	12.78	13.81	13.08	12.56
MgO	0.00	0.00	0.00	0.00
CaO	22.84	22.51	22.60	22.61
MnO	0.26	0.13	0.08	0.18
BaO	0.00	0.00	0.04	0.09
Na_2O	0.00	0.01	0.00	0.00
K_2O	0.00	0.00	0.00	0.01
Sum	96.81	97.04	96.80	96.76
Cations				
Si	5.979	5.949	5.991	5.974
Ti	0.005	0.006	0.006	0.006
Al	4.494	4.452	4.484	4.561
Cr	0.000	0.005	0.000	0.000
Fe^{3+}	1.546	1.671	1.582	1.518
Mg	0.000	0.000	0.000	0.000
Ca	3.936	3.878	3.892	3.891
Mn	0.036	0.018	0.011	0.024
Ba	0.000	0.000	0.003	0.006
Na	0.001	0.002	0.000	0.000
K	0.000	0.000	0.001	0.002
Sum	15.997	15.982	15.970	15.982
Xps	0.256	0.273	0.261	0.250
Site occupation				
Si	5.979	5.949	5.991	5.974
Al(IV)	0.021	0.051	0.009	0.026
Sum	6.000	6.000	6.000	6.000
Al(VI)	4.473	4.401	4.476	4.535
Ti	0.005	0.006	0.006	0.006
Cr	0.000	0.005	0.000	0.000
Fe^{3+}	1.546	1.671	1.582	1.518
Sum	6.024	6.084	6.064	6.058
Mg	0.000	0.000	0.000	0.000
Ca	3.936	3.878	3.892	3.891
Mn	0.036	0.018	0.011	0.024
Ba	0.000	0.000	0.003	0.006
Na	0.001	0.002	0.000	0.000
K	0.000	0.000	0.001	0.002
Sum	3.973	3.898	3.906	3.924
Total:	15.997	15.982	15.970	15.982
XPs	0.257	0.275	0.261	0.251
ACF				
A:	43.40	43.40	43.40	43.40
C:	55.92	55.92	55.92	55.92
F:	0.68	0.68	0.68	0.68

Analysis	A2 F1	A2 F1	A2 F1
	1.00	2.00	3.00
SiO_2	36.79	37.04	37.40
TiO_2	0.13	0.07	0.13
Al_2O_3	23.23	23.20	23.25
Cr_2O_3	0.00	0.08	0.05
Fe_2O_3	13.05	12.97	12.95
MgO	0.00	0.00	0.00
CaO	23.09	23.11	22.97
MnO	0.38	0.33	0.24
BaO	0.00	0.00	0.00
Na_2O	0.04	0.04	0.01
K_2O	0.01	0.01	0.02
Sum	96.71	96.86	97.01
Cations			
Si	5.946	5.974	6.009
Ti	0.015	0.009	0.016
Al	4.426	4.410	4.402
Cr	0.000	0.010	0.006
Fe^{3+}	1.587	1.573	1.565
Mg	0.000	0.000	0.000
Ca	3.999	3.993	3.954
Mn	0.052	0.045	0.033
Ba	0.000	0.000	0.000
Na	0.012	0.014	0.004
K	0.002	0.002	0.003
Sum	16.040	16.029	15.993
Xps	0.264	0.263	0.262
Site occupation			
Si	5.946	5.974	6.009
Al(IV)	0.054	0.026	0.000
Sum	6.000	6.000	6.009
Al(VI)	4.372	4.383	4.402
Ti	0.015	0.009	0.016
Cr	0.000	0.010	0.006
Fe^{3+}	1.587	1.573	1.565
Sum	5.974	5.975	5.989
Mg	0.000	0.000	0.000
Ca	3.999	3.993	3.954
Mn	0.052	0.045	0.033
Ba	0.000	0.000	0.000
Na	0.012	0.014	0.004
K	0.002	0.002	0.003
Sum	4.056	4.054	3.995
Total:	16.040	16.029	15.993
XPs	0.266	0.264	0.262
ACF			
A:	43.40	43.40	43.40
C:	55.92	55.92	55.92
F:	0.68	0.68	0.68

Analysis	RP60 F8	RP60 F8
	1.00	4.00
SiO_2	37.58	39.35
TiO_2	0.12	0.06
Al_2O_3	25.69	24.96
Cr_2O_3	0.00	0.03
Fe_2O_3	10.24	8.91
MgO	0.00	0.00
CaO	23.33	21.75
MnO	0.06	0.03
BaO	0.06	0.00
Na_2O	0.01	1.35
K_2O	0.01	0.00
Sum	97.09	96.43
Cations		
Si	5.969	6.241
Ti	0.014	0.007
Al	4.808	4.665
Cr	0.000	0.003
Fe^{3+}	1.224	1.063
Mg	0.000	0.000
Ca	3.970	3.696
Mn	0.008	0.004
Ba	0.003	0.000
Na	0.002	0.416
K	0.001	0.000
Sum	16.002	16.094
Xps	0.203	0.186
Site occupation		
Si	5.969	6.241
Al(IV)	0.031	0.000
Sum	6.000	6.241
Al(VI)	4.778	4.665
Ti	0.014	0.007
Cr	0.000	0.003
Fe^{3+}	1.224	1.063
Sum	6.016	5.738
Mg	0.000	0.000
Ca	3.970	3.696
Mn	0.008	0.004
Ba	0.003	0.000
Na	0.002	0.416
K	0.001	0.000
Sum	3.986	4.115
Total:	16.002	16.094
XPs	0.204	0.186
ACF		
A:	43.40	43.40
C:	55.92	55.92
F:	0.68	0.68

APPENDIX 5: ***Microprobe analyses of white micas from samples 35, 235, RP185, P1.***

Sample	35 P1 4	35 P1 5	35 P1 6	35 P2 6	35 P2 7	35 P2 8	35 P2 9	35 P2 10	35 P2 11	35 P3 1	35 P3 2	35 P3 3	35 P3 4	35 P4 1	35 P4 3	35 P4 3	35 P4 4	35 P5 5	35 P6 1	35 P6 2	35 P6 3
SiO2	48.71	48.86	48.21	49.20	49.36	48.93	47.84	47.05	47.50	46.87	47.42	49.03	48.68	47.56	47.75	47.44	48.05	46.78	48.68	48.94	47.65
TiO2	1.27	1.15	1.22	1.37	1.20	1.20	1.20	1.12	1.06	1.13	1.02	1.12	1.12	1.13	1.12	1.11	1.04	1.00	1.13	1.13	1.06
Al2O3	28.59	28.86	29.85	28.17	28.06	27.78	29.57	30.13	30.31	29.67	29.42	27.16	28.64	28.57	29.15	29.51	29.15	29.51	29.10	28.42	29.21
Cr2O3	0.01	0.04	0.02	0.03	0.00	0.00	0.00	0.04	0.03	0.00	0.03	0.00	0.02	0.00	0.01	0.05	0.02	0.00	0.00	0.03	0.02
MgO	2.32	2.35	1.98	2.49	2.50	2.41	2.12	1.73	1.69	1.85	1.87	2.62	2.31	2.21	2.09	1.97	2.17	2.04	2.13	2.33	1.95
CaO	0.00	0.01	0.00	0.01	0.02	0.00	0.01	0.00	0.00	0.00	0.00	0.00	0.00	0.00	0.00	0.00	0.05	0.05	0.01	0.00	0.00
MnO	0.00	0.03	0.03	0.03	0.03	0.00	0.05	0.05	0.00	0.00	0.07	0.04	0.11	0.00	0.02	0.06	0.04	0.00	0.04	0.02	0.03
FeO	3.95	4.01	4.06	3.98	3.77	3.79	3.95	3.84	3.85	3.65	3.77	3.42	3.55	3.81	3.96	3.94	3.70	3.76	3.83	3.56	3.55
BaO	0.11	0.06	0.06	0.14	0.01	0.06	0.04	0.09	0.04	0.06	0.00	0.17	0.03	0.01	0.02	0.04	0.09	0.04	0.06	0.07	0.13
Na2O	0.26	0.26	0.20	0.22	0.20	0.33	0.20	0.24	0.27	0.27	0.29	0.18	0.22	0.26	0.30	0.27	0.28	0.34	0.26	0.27	0.25
K2O	9.87	9.62	9.49	9.85	9.55	10.61	9.94	10.46	10.62	10.15	10.34	10.57	10.59	10.55	10.65	10.64	10.35	10.52	9.45	10.77	10.73
H2O	4.45	4.47	4.46	4.47	4.45	4.43	4.44	4.41	4.44	4.37	4.40	4.40	4.45	4.38	4.42	4.42	4.43	4.38	4.45	4.46	4.41
Total	99.53	99.71	99.58	99.96	99.16	99.54	99.35	99.16	99.83	98.02	98.63	98.72	99.73	98.49	99.50	99.43	99.38	98.41	99.15	99.98	98.98
Si	6.566	6.561	6.479	6.603	6.648	6.618	6.464	6.395	6.410	6.426	6.468	6.677	6.563	6.507	6.474	6.438	6.503	6.411	6.561	6.586	6.487
Ti	0.129	0.116	0.123	0.139	0.122	0.122	0.121	0.114	0.108	0.117	0.105	0.115	0.114	0.116	0.114	0.113	0.106	0.103	0.115	0.115	0.108
Al	4.541	4.568	4.729	4.455	4.454	4.428	4.708	4.826	4.821	4.794	4.729	4.359	4.550	4.607	4.658	4.720	4.649	4.767	4.622	4.507	4.688
Cr	0.001	0.004	0.002	0.004	0.000	0.000	0.000	0.004	0.003	0.000	0.003	0.000	0.002	0.000	0.001	0.005	0.002	0.000	0.000	0.004	0.002
Mg	0.466	0.470	0.397	0.498	0.502	0.486	0.427	0.351	0.340	0.377	0.381	0.533	0.464	0.451	0.423	0.399	0.437	0.416	0.429	0.468	0.395
Ca	0.000	0.001	0.000	0.001	0.002	0.000	0.002	0.000	0.000	0.000	0.000	0.000	0.000	0.000	0.000	0.000	0.008	0.007	0.001	0.000	0.000
Mn	0.000	0.004	0.003	0.003	0.004	0.000	0.005	0.005	0.000	0.000	0.008	0.005	0.013	0.000	0.002	0.006	0.004	0.000	0.005	0.002	0.004
Fe	0.445	0.450	0.456	0.446	0.425	0.428	0.446	0.436	0.435	0.418	0.430	0.389	0.401	0.436	0.449	0.447	0.419	0.431	0.431	0.401	0.404
Ba	0.006	0.003	0.003	0.007	0.000	0.003	0.002	0.005	0.002	0.003	0.000	0.009	0.001	0.000	0.001	0.002	0.005	0.002	0.003	0.003	0.007
Na	0.067	0.068	0.051	0.058	0.053	0.086	0.052	0.063	0.071	0.072	0.076	0.048	0.059	0.070	0.078	0.072	0.073	0.091	0.068	0.069	0.065
K	1.697	1.648	1.627	1.687	1.640	1.831	1.714	1.814	1.828	1.775	1.800	1.836	1.822	1.842	1.842	1.841	1.788	1.838	1.625	1.849	1.864
Total	13.917	13.894	13.871	13.901	13.850	14.004	13.943	14.014	14.019	13.983	13.999	13.971	13.987	14.029	14.042	14.043	13.995	14.067	13.860	14.003	14.024
X(Fe)	0.49	0.49	0.53	0.47	0.46	0.47	0.51	0.55	0.56	0.53	0.53	0.42	0.46	0.49	0.52	0.53	0.49	0.51	0.50	0.46	0.51
Si	6.566	6.561	6.479	6.603	6.648	6.618	6.464	6.395	6.410	6.426	6.468	6.677	6.563	6.507	6.474	6.438	6.503	6.411	6.561	6.586	6.487
Al IV	1.434	1.439	1.521	1.397	1.352	1.382	1.536	1.605	1.590	1.574	1.532	1.323	1.437	1.493	1.526	1.562	1.497	1.589	1.439	1.414	1.513
tetr.	8.000	8.000	8.000	8.000	8.000	8.000	8.000	8.000	8.000	8.000	8.000	8.000	8.000	8.000	8.000	8.000	8.000	8.000	8.000	8.000	8.000
Al VI	3.823	3.823	3.823	3.822	3.823	3.823	3.823	3.823	3.823	3.823	3.823	3.823	3.823	3.823	3.823	3.823	3.823	3.823	3.823	3.823	3.823
Cr	0.001	0.004	0.002	0.004	0.000	0.000	0.000	0.004	0.003	0.000	0.003	0.000	0.002	0.000	0.001	0.005	0.002	0.000	0.000	0.004	0.002
Ti	0.129	0.116	0.123	0.139	0.122	0.122	0.121	0.114	0.108	0.117	0.105	0.115	0.114	0.116	0.114	0.113	0.106	0.103	0.115	0.115	0.108
Fe 2+=to	0.445	0.450	0.456	0.446	0.425	0.428	0.446	0.436	0.435	0.418	0.430	0.389	0.401	0.436	0.449	0.447	0.419	0.431	0.431	0.401	0.404
Mn	0.000	0.004	0.003	0.003	0.004	0.000	0.005	0.005	0.000	0.000	0.008	0.005	0.013	0.000	0.002	0.006	0.004	0.000	0.005	0.002	0.004
Mg	0.466	0.470	0.397	0.498	0.502	0.486	0.427	0.351	0.340	0.377	0.381	0.533	0.464	0.451	0.423	0.399	0.437	0.416	0.429	0.468	0.395
okta.	4.147	4.174	4.189	4.148	4.154	4.084	4.173	4.132	4.118	4.133	4.123	4.078	4.106	4.117	4.121	4.128	4.122	4.129	4.163	4.081	4.089
Ba	0.006	0.003	0.003	0.007	0.000	0.003	0.002	0.005	0.002	0.003	0.000	0.009	0.001	0.000	0.001	0.002	0.005	0.002	0.003	0.003	0.007
Ca	0.000	0.001	0.000	0.001	0.002	0.000	0.002	0.000	0.000	0.000	0.000	0.000	0.000	0.000	0.000	0.000	0.008	0.007	0.001	0.000	0.000
Na	0.067	0.068	0.051	0.058	0.053	0.086	0.052	0.063	0.071	0.072	0.076	0.048	0.059	0.070	0.078	0.072	0.073	0.091	0.068	0.069	0.065
K	1.697	1.648	1.627	1.687	1.640	1.831	1.714	1.814	1.828	1.775	1.800	1.836	1.822	1.842	1.842	1.841	1.788	1.838	1.625	1.849	1.864
interlayer	1.770	1.720	1.682	1.753	1.696	1.920	1.770	1.882	1.901	1.851	1.876	1.893	1.882	1.912	1.921	1.915	1.874	1.938	1.697	1.922	1.936
Sum	13.917	13.894	13.871	13.901	13.850	14.004	13.943	14.014	14.019	13.983	13.999	13.971	13.987	14.029	14.042	14.043	13.995	14.067	13.860	14.003	14.024

Sample	235.00 F2 1.00	235.00 F2 2.00	235.00 F2 3.00	235.00 F2 4.00	235.00 F3 1.00	235.00 F3 2.00	235.00 F4 2.00	235.00 F4 3.00	235.00 F5 2.00	235.00 F5 3.00	235.00 F5 4.00	235.00 F7 1.00	235.00 F7 4.00	235.00 F7 5.00	235.00 F7 6.00	235.00 F8 2.00	235.00 F9 1.00	235.00 F9 2.00	235.00 F9 3.00	239.00 F9 4.00	239.00 F9 5.00
SiO2	48.61	48.28	48.66	47.85	47.11	62.60	47.92	72.31	47.84	47.54	47.20	33.02	48.54	48.25	48.13	47.41	47.98	46.17	46.87	47.49	45.74
TiO2	0.22	0.17	0.25	0.50	0.40	0.01	0.39	0.02	0.34	0.34	0.44	0.11	1.24	0.91	0.78	0.38	0.29	0.48	0.42	0.39	0.43
Al2O3	33.60	33.84	33.36	33.64	33.72	18.30	32.68	15.48	33.93	33.60	33.61	17.63	32.92	32.92	32.30	33.03	33.33	33.48	34.59	34.90	34.39
Cr2O3	0.04	0.04	0.00	0.01	0.04	0.00	0.00	0.00	0.02	0.02	0.06	0.01	0.00	0.00	0.00	0.01	0.00	0.03	0.06	0.01	0.02
MgO	1.53	1.53	1.49	1.40	1.30	0.05	1.57	0.01	1.46	1.46	1.42	13.03	1.81	1.41	1.98	1.53	1.63	1.30	1.13	1.09	1.02
CaO	0.00	0.00	0.01	0.02	0.05	0.08	0.01	0.10	0.00	0.00	0.00	0.15	0.00	0.00	0.01	0.02	0.03	0.00	0.00	0.04	0.00
MnO	0.06	0.01	0.04	0.08	0.04	0.01	0.01	0.02	0.00	0.03	0.05	0.17	0.02	0.01	0.04	0.07	0.00	0.10	0.03	0.00	0.00
FeO	1.66	1.65	1.47	1.71	1.31	1.17	1.57	0.28	1.50	1.71	1.53	18.44	1.87	1.53	1.52	1.49	1.89	1.53	1.55	1.50	1.38
BaO	0.21	0.24	0.25	0.28	0.19	0.05	0.07	0.04	0.23	0.10	0.15	0.00	0.30	0.25	0.11	0.22	0.23	0.24	0.34	0.36	0.36
Na2O	0.62	0.56	0.47	0.62	0.56	0.27	0.54	0.32	0.56	0.46	0.50	0.09	0.34	0.34	0.27	0.42	0.61	0.53	0.68	0.55	0.60
K2O	9.99	9.98	10.10	9.50	9.66	14.41	9.84	12.26	10.11	10.10	10.18	3.53	10.13	9.95	9.80	10.03	9.70	10.08	9.80	10.15	10.12
H2O	4.57	4.56	4.56	4.53	4.48	4.58	4.49	4.92	4.54	4.51	4.50	3.68	4.59	4.53	4.51	4.48	4.53	4.43	4.52	4.56	4.44
Total	101.10	100.87	100.68	100.14	98.85	101.53	99.07	105.74	100.53	99.86	99.62	89.85	101.77	100.10	99.53	99.07	100.20	98.38	99.99	101.02	98.51
Si	6.375	6.346	6.403	6.330	6.305	8.188	6.402	8.813	6.313	6.317	6.293	5.386	6.344	6.386	6.401	6.350	6.350	6.246	6.225	6.243	6.181
Ti	0.021	0.017	0.026	0.050	0.040	0.001	0.039	0.002	0.034	0.034	0.044	0.013	0.122	0.090	0.078	0.038	0.028	0.049	0.042	0.038	0.044
Al	5.194	5.243	5.174	5.245	5.320	2.821	5.145	2.223	5.277	5.263	5.281	3.389	5.071	5.135	5.063	5.213	5.200	5.338	5.414	5.408	5.477
Cr	0.004	0.004	0.000	0.001	0.004	0.000	0.000	0.000	0.002	0.002	0.006	0.002	0.000	0.000	0.000	0.001	0.000	0.004	0.006	0.001	0.002
Mg	0.298	0.301	0.292	0.277	0.258	0.011	0.312	0.001	0.287	0.289	0.282	3.169	0.352	0.279	0.393	0.305	0.321	0.262	0.225	0.213	0.206
Ca	0.000	0.000	0.001	0.002	0.007	0.011	0.001	0.013	0.000	0.000	0.000	0.026	0.000	0.000	0.001	0.002	0.004	0.000	0.000	0.006	0.001
Mn	0.007	0.001	0.005	0.009	0.004	0.001	0.001	0.002	0.000	0.003	0.005	0.023	0.002	0.001	0.004	0.008	0.000	0.012	0.003	0.000	0.000
Fe	0.182	0.182	0.162	0.189	0.147	0.128	0.176	0.028	0.166	0.190	0.171	2.516	0.204	0.169	0.169	0.167	0.209	0.174	0.172	0.165	0.156
Ba	0.011	0.012	0.013	0.015	0.010	0.002	0.004	0.002	0.012	0.005	0.008	0.000	0.016	0.013	0.006	0.012	0.012	0.013	0.018	0.018	0.019
Na	0.158	0.143	0.120	0.158	0.146	0.067	0.139	0.074	0.142	0.117	0.129	0.029	0.086	0.088	0.068	0.109	0.156	0.138	0.176	0.139	0.158
K	1.671	1.674	1.696	1.603	1.649	2.404	1.677	1.905	1.702	1.712	1.731	0.734	1.689	1.679	1.679	1.713	1.637	1.740	1.660	1.702	1.744
Total	13.920	13.922	13.892	13.878	13.890	13.635	13.895	13.064	13.935	13.931	13.950	15.287	13.886	13.840	13.863	13.916	13.918	13.974	13.941	13.934	13.987
X(Fe)	0.38	0.38	0.36	0.41	0.36	0.92	0.36	0.97	0.37	0.40	0.38	0.44	0.37	0.38	0.30	0.35	0.39	0.40	0.43	0.44	0.43
Si	6.375	6.346	6.403	6.330	6.305	8.188	6.402	8.813	6.313	6.317	6.293	5.386	6.344	6.386	6.401	6.350	6.350	6.246	6.225	6.243	6.181
Al IV	1.625	1.654	1.597	1.670	1.695	-0.188	1.598	-0.813	1.687	1.683	1.707	2.614	1.656	1.614	1.599	1.650	1.650	1.754	1.775	1.757	1.819
etr.	8.000	8.000	8.000	8.000	8.000	8.000	8.000	8.000	8.000	8.000	8.000	8.000	8.000	8.000	8.000	8.000	8.000	8.000	8.000	8.000	8.000
Al VI	3.823	3.823	3.823	3.823	3.823	3.823	3.823	3.823	3.823	3.823	3.823	3.823	3.823	3.823	3.823	3.823	3.823	3.823	3.823	3.823	3.823
Cr	0.004	0.004	0.000	0.001	0.004	0.000	0.000	0.000	0.002	0.002	0.006	0.002	0.000	0.000	0.000	0.001	0.000	0.004	0.006	0.001	0.002
Ti	0.021	0.017	0.026	0.050	0.040	0.001	0.039	0.002	0.034	0.034	0.044	0.013	0.122	0.090	0.078	0.038	0.028	0.049	0.042	0.038	0.044
Fe 2+=to	0.182	0.182	0.162	0.189	0.147	0.128	0.176	0.028	0.166	0.190	0.171	2.516	0.204	0.169	0.169	0.167	0.209	0.174	0.172	0.165	0.156
Mn	0.007	0.001	0.005	0.009	0.004	0.001	0.001	0.002	0.000	0.003	0.005	0.023	0.002	0.001	0.004	0.008	0.000	0.012	0.003	0.000	0.000
Mg	0.298	0.301	0.292	0.277	0.258	0.011	0.312	0.001	0.287	0.289	0.282	3.169	0.352	0.279	0.393	0.305	0.321	0.262	0.225	0.213	0.206
ktn.	4.080	4.093	4.062	4.101	4.079	3.150	4.074	3.069	4.079	4.097	4.082	6.498	4.095	4.060	4.109	4.081	4.109	4.083	4.087	4.069	4.065
Ba	0.011	0.012	0.013	0.015	0.010	0.002	0.004	0.002	0.012	0.005	0.008	0.000	0.016	0.013	0.006	0.012	0.012	0.013	0.018	0.018	0.019
Ca	0.000	0.000	0.001	0.002	0.007	0.011	0.001	0.013	0.000	0.000	0.000	0.026	0.000	0.000	0.001	0.002	0.004	0.000	0.000	0.006	0.001
Na	0.158	0.143	0.120	0.158	0.146	0.067	0.139	0.074	0.142	0.117	0.129	0.029	0.086	0.088	0.068	0.109	0.156	0.138	0.176	0.139	0.158
K	1.671	1.674	1.696	1.603	1.649	2.404	1.677	1.905	1.702	1.712	1.731	0.734	1.689	1.679	1.679	1.713	1.637	1.740	1.660	1.702	1.744
nterlayer	1.839	1.829	1.830	1.777	1.811	2.485	1.821	1.995	1.856	1.834	1.868	0.789	1.791	1.780	1.754	1.835	1.809	1.890	1.854	1.865	1.922
Sum	13.920	13.922	13.892	13.878	13.890	13.635	13.895	13.064	13.935	13.931	13.950	15.287	13.886	13.840	13.863	13.916	13.918	13.974	13.941	13.934	13.987
Mn	0.00	0.00	0.05	0.12	0.37	0.44	0.07	0.66	0.00	0.00	0.00	3.30	0.00	0.00	0.04	0.12	0.24	0.00	0.00	0.34	0.03
Fe	8.63	7.87	6.63	8.96	8.11	-9.42	7.64	-40.63	7.71	6.41	6.94	3.69	4.84	4.97	3.91	5.95	8.67	7.33	9.59	7.52	8.32
Ce	18.73	17.29	20.16	16.48	15.26	109.42	20.08	140.63	15.67	15.86	14.66	0.00	17.20	19.29	20.05	17.48	17.52	12.28	11.26	12.17	9.04
Mg	72.63	74.84	73.16	74.43	76.26	-0.44	72.21	-0.66	76.62	77.73	78.41	93.01	77.96	75.74	76.00	76.65	73.57	80.38	79.15	79.97	82.61
Fy	8.55	9.15	9.20	11.97	10.26	-23.59	9.20	1.01	7.78	8.56	7.00	61.87	11.23	11.64	12.63	8.92	10.34	6.12	8.17	7.96	4.91
Mu	64.08	65.69	64.01	62.58	66.36	23.59	63.07	0.00	68.84	69.17	71.41	34.44	66.73	64.10	63.41	67.65	63.47	74.26	70.97	72.35	77.74
Fy + Ce + Mu = 100																					
Fy	9.36	9.93	9.85	13.15	11.17	-21.56	9.97	0.71	8.43	9.15	7.52	64.24	11.81	12.25	13.14	9.48	11.32	6.61	9.04	8.60	5.35
Ce	20.50	18.77	21.59	18.11	16.61	100.00	21.74	99.29	16.98	16.95	15.75	0.00	18.07	20.30	20.87	18.59	19.19	13.25	12.46	13.16	9.86
Mu	70.13	71.30	68.56	68.74	72.22	21.56	68.29	0.00	74.59	73.91	76.73	35.76	70.12	67.45	65.99	71.93	69.49	80.14	78.50	78.24	84.79
Sum	100.00	100.00	100.00	100.00	100.00	100.00	100.00	100.00	100.00	100.00	100.00	100.00	100.00	100.00	100.00	100.00	100.00	100.00	100.00	100.00	100.00
Fe tot	0.182	0.182	0.162	0.189	0.147	0.128	0.176	0.028	0.166	0.190	0.171	2.516	0.204	0.169	0.169	0.167	0.209	0.174	0.172	0.165	0.156
Fe 2+	0.098	0.062	0.137	0.103	0.087	2.179	0.129	2.814	0.060	0.062	0.055	-3.770	0.114	0.197	0.086	0.083	0.058	0.032	0.043	0.068	0.018
Fe 3+	0.084	0.119	0.025	0.086	0.060	-2.051	0.047	-2.785	0.106	0.128	0.116	6.286	0.090	-0.028	0.083	0.084	0.151	0.141	0.129	0.096	0.137
Diagrams																					
A'KF																					
A:	55.99	56.46	56.23	57.72	58.83	11.53	55.65	10.99	56.83	56.22	56.38	17.78	54.01	56.66	54.11	55.92	55.81	56.77	59.25	59.20	59.16
K:	27.81	27.59	28.39	26.54	27.51	79.30	28.03	86.15	28.18	28.02	28.53	4.96	27.69	28.25	27.40	28.25	26.83	28.54	27.50	28.25	28.85
F:	16.20	15.94	15.38	15.74	13.66	9.17	16.32	2.97	14.99	15.76	15.10	77.26	18.30	15.09	18.49	15.83	17.36	14.68	13.24	12.55	11.98
AFM(Ms)																					
A:	0.16	0.19	0.09	0.32	0.32	1.07	0.10	1.02	0.16	0.12	0.09	0.09	0.00	0.10	0.02	0.07	0.21	0.12	0.35	0.29	0.25
F:	0.38	0.38	0.36	0.41	0.36	0.92	0.36	0.97	0.37	0.40	0.38	0.44	0.37	0.38	0.30	0.35	0.39	0.40	0.43	0.44	0.43
M:	0.62	0.62	0.64	0.59	0.64	0.08	0.64	0.03	0.63	0.60	0.62	0.56	0.63	0.62	0.70	0.65	0.61	0.60	0.57	0.56	0.57
AFM(Kl)																					
A:	0.79	0.79	0.79	0.80	0.82	0.60	0.78	0.84	0.80	0.79	0.80	0.19	0.75	0.79	0.75	0.79	0.77	0.81	0.83	0.83	0.84
F:	0.38	0.38	0.36	0.41	0.36	0.92	0.36	0.97	0.37	0.40	0.38	0.44	0.37	0.38	0.30	0.35	0.39	0.40	0.43	0.44	0.43
M:	0.62	0.62	0.64	0.59	0.64	0.08	0.64	0.03	0.63	0.60	0.62	0.56	0.63	0.62	0.70	0.65	0.61	0.60	0.57	0.56	0.57

Sample	RP185 F1 1.00	RP185 F1 2.00	RP185 F1 3.00	RP185 F1 4.00	RP185 F1 5.00	RP185 F2 1.00	RP185 F2 2.00	RP185 F2 3.00	RP185 F2 4.00	RP185 F2 5.00	RP185 F2 6.00	RP185 F2 7.00	RP185 F2 8.00	RP185 F6 1.00	RP185 F6 2.00	RP185 F6 3.00	RP185 F6 4.00	RP185 F6 5.00	AN F1 6.00
SiO2	46.80	47.67	48.48	48.85	48.08	48.67	48.52	48.36	48.86	48.75	48.11	47.15	48.63	47.85	48.11	48.50	48.19	48.23	31.45
TiO2	1.21	0.86	0.97	0.97	0.91	0.82	1.22	1.31	1.04	0.83	0.83	1.18	1.11	1.09	1.17	1.04	0.84	0.99	0.34
Al2O3	31.31	30.89	30.90	31.25	30.87	31.63	31.87	31.62	30.67	31.76	31.55	31.68	31.47	31.82	31.92	31.62	30.44	30.34	15.43
Cr2O3	0.03	0.03	0.03	0.00	0.04	0.06	0.00	0.04	0.03	0.02	0.00	0.05	0.02	0.00	0.00	0.00	0.01	0.00	0.00
MgO	1.74	2.39	2.20	2.13	2.13	2.18	1.82	1.84	2.23	2.00	2.09	1.65	2.10	1.88	1.87	2.00	2.21	2.25	14.64
CaO	0.02	0.00	0.00	0.00	0.00	0.00	0.00	0.00	0.04	0.00	0.00	0.00	0.01	0.00	0.00	0.02	0.02	0.01	0.31
MnO	0.03	0.00	0.00	0.02	0.00	0.00	0.06	0.03	0.02	0.04	0.02	0.00	0.02	0.00	0.00	0.04	0.01	0.00	0.32
FeO	1.63	1.88	2.08	1.79	1.95	2.09	1.80	1.77	1.93	2.00	2.01	1.61	2.10	1.61	1.73	1.80	1.96	2.09	23.19
BaO	0.44	0.44	0.61	0.55	0.34	0.32	0.62	0.57	0.52	0.40	0.43	0.59	0.58	0.55	0.55	0.61	0.41	0.43	0.13
Na2O	0.32	0.27	0.27	0.31	0.36	0.23	0.26	0.33	0.28	0.20	0.31	0.31	0.45	0.31	0.31	0.26	0.32	0.29	0.06
K2O	10.10	10.22	10.39	10.50	9.99	9.50	9.83	10.18	10.27	9.40	9.66	10.10	10.49	9.55	9.39	9.52	9.66	10.47	2.25
H2O	4.41	4.45	4.50	4.53	4.47	4.53	4.53	4.52	4.51	4.52	4.49	4.44	4.55	4.48	4.50	4.51	4.45	4.47	3.65
Total	98.05	99.10	100.43	100.90	99.13	100.21	100.52	100.56	100.39	99.92	99.50	98.75	101.52	99.14	99.53	99.91	98.52	99.55	91.78
Si	6.366	6.420	6.456	6.462	6.457	6.449	6.421	6.412	6.493	6.462	6.427	6.367	6.412	6.405	6.409	6.445	6.501	6.477	5.161
Ti	0.123	0.087	0.097	0.097	0.092	0.082	0.121	0.130	0.104	0.082	0.083	0.120	0.110	0.110	0.117	0.104	0.085	0.100	0.042
Al	5.020	4.903	4.849	4.872	4.886	4.939	4.971	4.942	4.803	4.963	4.968	5.042	4.890	5.020	5.012	4.952	4.840	4.802	2.984
Cr	0.004	0.004	0.003	0.000	0.005	0.006	0.000	0.004	0.003	0.002	0.000	0.005	0.002	0.000	0.000	0.000	0.001	0.000	0.000
Mg	0.354	0.479	0.436	0.420	0.427	0.431	0.358	0.364	0.442	0.396	0.417	0.333	0.413	0.375	0.372	0.396	0.444	0.450	3.583
Ca	0.002	0.000	0.000	0.000	0.000	0.000	0.000	0.000	0.006	0.000	0.000	0.000	0.002	0.000	0.000	0.003	0.003	0.002	0.055
Mn	0.004	0.000	0.000	0.002	0.000	0.000	0.006	0.003	0.002	0.005	0.002	0.000	0.002	0.000	0.000	0.004	0.001	0.000	0.044
Fe	0.185	0.211	0.231	0.198	0.219	0.231	0.199	0.196	0.215	0.221	0.224	0.181	0.231	0.180	0.192	0.200	0.221	0.234	3.183
Ba	0.023	0.023	0.032	0.029	0.018	0.027	0.032	0.029	0.027	0.021	0.023	0.031	0.030	0.029	0.028	0.032	0.022	0.023	0.008
Na	0.085	0.070	0.070	0.078	0.092	0.059	0.067	0.085	0.071	0.050	0.081	0.082	0.114	0.081	0.080	0.068	0.085	0.076	0.019
K	1.752	1.755	1.766	1.771	1.711	1.605	1.659	1.722	1.741	1.590	1.647	1.741	1.764	1.630	1.595	1.613	1.663	1.793	0.471
Total	13.918	13.953	13.939	13.930	13.907	13.828	13.836	13.889	13.907	13.793	13.870	13.901	13.971	13.831	13.806	13.816	13.867	13.957	15.550
X(Fe)	0.34	0.31	0.35	0.32	0.34	0.35	0.36	0.35	0.33	0.36	0.35	0.35	0.36	0.32	0.34	0.34	0.33	0.34	0.47
Si	6.366	6.420	6.456	6.462	6.457	6.449	6.421	6.412	6.493	6.462	6.427	6.367	6.412	6.405	6.409	6.445	6.501	6.477	5.161
Al IV	1.634	1.580	1.544	1.538	1.543	1.551	1.579	1.588	1.507	1.538	1.573	1.633	1.588	1.595	1.591	1.555	1.499	1.523	2.839
tetr.	8.000	8.000	8.000	8.000	8.000	8.000	8.000	8.000	8.000	8.000	8.000	8.000	8.000	8.000	8.000	8.000	8.000	8.000	8.000
Al VI	3.823	3.823	3.823	3.823	3.823	3.823	3.823	3.823	3.823	3.823	3.823	3.823	3.823	3.823	3.823	3.823	3.823	3.823	3.823
Cr	0.004	0.004	0.003	0.000	0.005	0.006	0.000	0.004	0.003	0.002	0.000	0.005	0.002	0.000	0.000	0.000	0.001	0.000	0.000
Ti	0.123	0.087	0.097	0.097	0.092	0.082	0.121	0.130	0.104	0.082	0.083	0.120	0.110	0.110	0.117	0.104	0.085	0.100	0.042
Fe 2+=to	0.185	0.211	0.231	0.198	0.219	0.231	0.199	0.196	0.215	0.221	0.224	0.181	0.231	0.180	0.192	0.200	0.221	0.234	3.183
Mn	0.004	0.000	0.000	0.002	0.000	0.000	0.006	0.003	0.002	0.005	0.002	0.000	0.002	0.000	0.000	0.004	0.001	0.000	0.044
Mg	0.354	0.479	0.436	0.420	0.427	0.431	0.358	0.364	0.442	0.396	0.417	0.333	0.413	0.375	0.372	0.396	0.444	0.450	3.583
Mg okta.	4.055	4.104	4.072	4.051	4.086	4.138	4.077	4.051	4.061	4.132	4.120	4.048	4.061	4.090	4.102	4.100	4.094	4.063	6.997
Ba	0.023	0.023	0.032	0.029	0.018	0.027	0.032	0.029	0.027	0.021	0.023	0.031	0.030	0.029	0.028	0.032	0.022	0.023	0.008
Ca	0.002	0.000	0.000	0.000	0.000	0.000	0.000	0.000	0.006	0.000	0.000	0.000	0.002	0.000	0.000	0.003	0.003	0.002	0.055
Na	0.085	0.070	0.070	0.078	0.092	0.059	0.067	0.085	0.071	0.050	0.081	0.082	0.114	0.081	0.080	0.068	0.085	0.076	0.019
K	1.752	1.755	1.766	1.771	1.711	1.605	1.659	1.722	1.741	1.590	1.647	1.741	1.764	1.630	1.595	1.613	1.663	1.793	0.471
interlayer	1.864	1.849	1.867	1.878	1.821	1.691	1.759	1.837	1.845	1.661	1.750	1.853	1.910	1.741	1.704	1.716	1.773	1.894	0.553
Sum	13.918	13.953	13.939	13.930	13.907	13.828	13.836	13.889	13.907	13.793	13.870	13.901	13.971	13.831	13.806	13.816	13.867	13.957	15.550
Ma	0.13	0.00	0.00	0.00	0.00	0.00	0.00	0.00	0.34	0.00	0.00	0.00	0.09	0.00	0.00	0.17	0.17	0.08	10.04
Pa	4.64	3.86	3.81	4.23	5.13	3.52	3.89	4.72	3.91	3.06	4.66	4.48	6.07	4.75	4.76	4.04	4.84	4.08	3.51
Ce	18.29	20.98	22.78	23.11	22.86	22.44	21.04	20.62	24.64	23.11	21.33	18.35	20.60	20.24	20.47	22.24	25.06	23.85	0.00
Mu	76.93	75.16	73.41	72.66	72.02	74.04	75.07	74.66	71.10	73.84	74.01	77.17	73.25	75.01	74.77	73.56	69.93	71.99	86.45
Py	8.11	8.72	8.23	7.52	9.84	16.82	13.66	9.61	9.40	17.99	13.64	8.89	6.09	14.42	16.24	15.94	12.60	6.51	75.51
Mu	68.96	66.44	65.19	65.14	62.17	57.22	61.41	65.05	62.05	55.85	60.36	68.28	67.25	60.59	58.53	57.79	57.51	65.56	20.98
Py + Ce + Mu = 100																			
Py	8.51	9.07	8.55	7.85	10.37	17.44	14.22	10.09	9.78	18.56	14.31	9.20	6.49	15.14	17.05	16.61	13.24	6.79	78.26
Ce	19.18	21.82	23.68	24.13	24.09	23.25	21.89	21.64	25.65	23.84	22.37	19.21	21.93	21.25	21.49	23.17	26.33	24.87	0.00
Mu	72.31	69.11	67.77	68.02	65.53	59.31	63.89	68.27	64.58	57.61	63.31	71.58	71.59	63.61	61.46	60.22	60.43	68.34	21.74
Sum	100.00	100.00	100.00	100.00	100.00	100.00	100.00	100.00	100.00	100.00	100.00	100.00	100.00	100.00	100.00	100.00	100.00	100.00	100.00
Fe tot	0.185	0.211	0.231	0.198	0.219	0.231	0.199	0.196	0.215	0.221	0.224	0.181	0.231	0.180	0.192	0.200	0.221	0.234	3.183
Fe 2+	0.135	0.023	0.116	0.139	0.122	0.100	0.184	0.179	0.155	0.149	0.093	0.154	0.109	0.139	0.155	0.153	0.143	0.126	-4.380
Fe 3+	0.050	0.188	0.115	0.059	0.097	0.131	0.015	0.017	0.060	0.073	0.131	0.028	0.122	0.041	0.038	0.047	0.078	0.108	7.563
Diagrams																			
A'KF																			
A:	52.86	49.53	49.28	50.10	50.66	52.80	53.80	52.38	49.44	53.97	52.49	53.76	49.64	54.69	55.06	53.77	50.79	48.11	15.04
K:	29.11	28.25	28.68	29.36	28.11	25.87	27.52	28.79	28.78	25.83	26.67	29.06	29.07	26.95	26.33	26.52	27.32	29.43	2.84
F:	18.02	22.22	21.84	20.54	21.23	21.33	18.68	18.83	21.78	20.20	20.84	17.18	21.29	18.36	18.61	19.71	21.88	22.47	82.12
AFM(Ms)																			
A:	-0.28	-0.36	-0.50	-0.56	-0.23	0.09	-0.01	-0.25	-0.47	0.14	0.02	-0.21	-0.45	0.10	0.17	0.09	-0.13	-0.73	0.10
F:	0.34	0.31	0.35	0.32	0.34	0.35	0.36	0.35	0.33	0.36	0.35	0.35	0.36	0.32	0.34	0.34	0.33	0.34	0.47
M:	0.66	0.69	0.65	0.68	0.66	0.65	0.64	0.65	0.67	0.64	0.65	0.65	0.64	0.68	0.66	0.66	0.67	0.66	0.53
AFM(Kl)																			
A:	0.75	0.70	0.70	0.72	0.71	0.72	0.75	0.74	0.70	0.73	0.72	0.76	0.71	0.75	0.75	0.74	0.70	0.69	0.16
F:	0.34	0.31	0.35	0.32	0.34	0.35	0.36	0.35	0.33	0.36	0.35	0.35	0.36	0.32	0.34	0.34	0.33	0.34	0.47
M:	0.66	0.69	0.65	0.68	0.66	0.65	0.64	0.65	0.67	0.64	0.65	0.65	0.64	0.68	0.66	0.66	0.67	0.66	0.53

Sample	P1 F1 1.00	P1 F1 2.00	P1 F1 3.00	P1 F1 4.00	P1 F1 7.00	P1 F1 8.00	P1 F2 1.00	P1 F2 2.00	P1 F2 3.00	P1 F2 4.00	P1 F2 5.00	P1 F2 6.00	P1 F2 7.00	P1 F2 8.00	P1 F3 77.00	P1 F3 78.00	P1 F3 79.00	P1 F3 80.00	P1 F3 81.00	P1 F3 82.00	P1 F3 83.00
SiO2	47.48	47.98	48.09	47.03	47.61	47.08	47.69	47.25	47.33	47.39	47.24	46.18	47.44	47.55	48.36	47.75	48.50	48.14	50.15	50.88	47.99
TiO2	0.25	0.32	0.39	0.19	0.32	0.28	0.27	0.23	0.28	0.21	0.16	0.22	0.27	0.28	0.31	0.31	0.34	0.34	0.21	0.24	0.32
Al2O3	36.09	35.34	35.37	36.44	36.19	35.57	35.30	36.38	36.21	35.01	36.14	35.98	35.59	34.97	36.29	35.56	35.25	35.47	33.77	32.35	36.66
Cr2O3	0.04	0.07	0.01	0.00	0.02	0.00	0.03	0.00	0.02	0.00	0.02	0.01	0.05	0.03	0.03	0.0	0.00	0.03	0.06	0.02	0.05
MgO	0.63	0.88	1.00	0.67	0.68	0.76	0.91	0.58	0.57	0.89	0.68	0.48	0.80	0.82	0.64	0.93	0.91	0.92	0.94	0.76	0.64
CaO	0.00	0.01	0.00	0.00	0.05	0.06	0.01	0.04	0.02	0.00	0.00	0.03	0.00	0.02	0.05	0.02	0.12	0.34	0.08	0.02	0.02
MnO	0.00	0.01	0.00	0.00	0.00	0.03	0.02	0.02	0.03	0.03	0.06	0.06	0.02	0.02	0.02	0.01	0.10	0.10	0.05	0.00	0.03
FeO	0.99	1.08	1.16	1.10	1.03	1.02	1.20	0.88	0.97	0.94	1.07	0.93	1.14	1.07	0.81	1.25	1.20	1.01	2.03	1.17	1.00
BaO	0.19	0.13	0.1.	0.21	0.18	0.14	0.10	0.13	0.11	0.12	0.17	0.32	0.10	0.18	0.21	0.11	0.24	0.13	0.18	0.11	0.14
Na2O	1.44	1.14	1.19	1.35	1.17	1.11	1.20	1.52	1.34	1.18	1.28	1.46	1.24	1.18	1.55	1.22	1.13	1.08	1.24	1.27	1.43
K2O	8.67	8.93	8.88	9.07	8.30	8.21	8.90	8.78	8.92	8.74	8.94	8.70	8.75	8.81	8.90	8.69	8.69	8.31	7.82	8.17	8.52
H2O	4.58	4.58	4.60	4.58	4.58	4.52	4.57	4.58	4.58	4.52	4.57	4.50	4.56	4.54	4.64	4.58	4.61	4.60	4.63	4.58	4.64
Total	100.37	100.45	100.82	100.62	100.13	98.76	100.19	100.39	100.37	99.02	100.32	98.80	99.95	99.46	101.81	100.42	101.09	100.46	101.17	99.56	101.43
Si	6.219	6.281	6.274	6.164	6.230	6.244	6.265	6.190	6.204	6.285	6.201	6.160	6.240	6.289	6.246	6.250	6.309	6.282	6.494	6.665	6.209
Ti	0.024	0.032	0.033	0.019	0.031	0.027	0.026	0.023	0.028	0.021	0.015	0.022	0.027	0.028	0.030	0.031	0.033	0.034	0.020	0.024	0.032
Al	5.571	5.451	5.438	5.629	5.582	5.559	5.464	5.617	5.593	5.472	5.591	5.656	5.518	5.450	5.24	5.487	5.404	5.455	5.155	4.994	5.589
Cr	0.005	0.007	0.001	0.000	0.002	0.000	0.003	0.000	0.002	0.000	0.002	0.001	0.005	0.003	0.003	0.000	0.000	0.004	0.006	0.002	0.005
Mg	0.123	0.171	0.194	0.131	0.132	0.150	0.179	0.113	0.111	0.176	0.133	0.096	0.157	0.162	0.122	0.131	0.176	0.178	0.182	0.148	0.124
Ca	0.000	0.001	0.000	0.000	0.006	0.008	0.001	0.005	0.002	0.000	0.000	0.00	0.00	0.002	0.007	0.003	0.017	0.047	0.011	0.002	0.003
Mn	0.000	0.001	0.000	0.000	0.000	0.003	0.002	0.003	0.004	0.003	0.006	0.000	0.002	0.002	0.002	0.001	0.011	0.011	0.005	0.000	0.003
Fe	0.109	0.119	0.127	0.120	0.113	0.113	0.132	0.096	0.106	0.104	0.118	0.104	0.125	0.118	0.087	0.137	0.131	0.110	0.220	0.128	0.108
Ba	0.010	0.007	0.007	0.011	0.009	0.007	0.005	0.007	0.005	0.006	0.009	0.017	0.005	0.009	0.011	0.005	0.012	0.006	0.009	0.006	0.007
Na	0.366	0.288	0.300	0.344	0.298	0.285	0.306	0.385	0.341	0.304	0.326	0.378	0.315	0.302	0.389	0.310	0.284	0.272	0.310	0.323	0.358
K	1.449	1.491	1.479	1.516	1.385	1.398	1.491	1.467	1.491	1.479	1.496	1.480	1.469	1.486	1.467	1.451	1.442	1.384	1.293	1.366	1.406
Total	13.876	13.848	13.858	13.933	13.788	13.785	13.874	13.906	13.887	13.849	13.898	13.918	13.863	13.851	13.888	13.856	13.819	13.783	13.706	13.658	13.844
X(Fe)	0.47	0.41	0.39	0.48	0.46	0.43	0.42	0.46	0.49	0 37	0.47	0.52	0.44	0.42	0.42	0.43	0.43	0.38	0.55	0.46	0.47
Si	6.219	6.281	6.274	6.164	6.230	6.244	6.265	6.190	6.204	6.285	6.201	6.160	6.240	6.289	6.246	6.250	6.309	6.282	6.494	6.665	6.209
Al IV	1.781	1.719	1.726	1.836	1.770	1.756	1.735	1.810	1.796	1.715	1.799	1.840	1.760	1.711	1.754	1.750	1.691	1.718	1.506	1.335	1.791
tetr.	8.000	8.000	8.000	8.000	8.000	8.000	8.000	8.000	8.000	8.000	8.000	8.000	8.000	8.000	8.000	8.000	8.000	8.000	8.000	8.000	8.000
Al VI	3.823	3.823	3.823	3.823	3.823	3.823	3.823	3.823	3.823	3.823	3.823	3.823	3.823	3.823	3.823	3.823	3.823	3.823	3.823	3.823	3.823
Cr	0.005	0.007	0.001	0.000	0.002	0.000	0.003	0.000	0.002	0.000	0.002	0.001	0.005	0.003	0.003	0.000	0.000	0.004	0.006	0.002	0.005
Ti	0.024	0.032	0.038	0.019	0.031	0.027	0.026	0.022	0.028	0.021	0.015	0.022	0.027	0.028	0.030	0.031	0.033	0.034	0.020	0.024	0.032
Fe 2+ =to	0.109	0.119	0.127	0.120	0.113	0.113	0.132	0.096	0.106	0.104	0.118	0.104	0.125	0.118	0.087	0.137	0.131	0.110	0.220	0.128	0.108
Mn	0.000	0.001	0.000	0.000	0.000	0.003	0.002	0.003	0.004	0.003	0.006	0.000	0.002	0.002	0.002	0.001	0.011	0.011	0.005	0.000	0.003
Mg	0.123	0.171	0.194	0.131	0.132	0.150	0.179	0.113	0.111	0.176	0.133	0.095	0.157	0.162	0.122	0.181	0.176	0.178	0.182	0.148	0.124
okta.	4.051	4.061	4.072	4.063	4.090	4.097	4.071	4.041	4.047	4.061	4.067	4.039	4.074	4.051	4.015	4.086	4.064	4.073	4.083	3.961	4.070
Ba	0.010	0.007	0.007	0.011	0.009	0.007	0.005	0.007	0.005	0.006	0.009	0.017	0.005	0.009	0.011	0.005	0.012	0.006	0.009	0.006	0.007
Ca	0.000	0.001	0.000	0.000	0.006	0.008	0.001	0.005	0.002	0.000	0.000	0.004	0.000	0.002	0.007	0.003	0.017	0.047	0.011	0.002	0.003
Na	0.366	0.288	0.300	0.344	0.298	0.285	0.306	0.385	0.341	0.304	0.326	0.378	0.315	0.302	0.389	0.310	0.284	0.272	0.310	0.323	0.358
K	1.449	1.491	1.479	1.516	1.385	1.398	1.491	1.467	1.491	1.479	1.496	1.480	1.469	1.486	1.467	1.451	1.442	1.384	1.293	1.366	1.406
interlayer	1.826	1.787	1.786	1.870	1.698	1.688	1.804	1.864	1.840	1.789	1.831	1.878	1.799	1.800	1.874	1.769	1.756	1.710	1.623	1.697	1.774
Sum	13.876	13.848	13.858	13.933	13.788	13.785	13.874	13.906	13.887	13.849	13.898	13.918	13.863	13.851	13.888	13.856	13.819	13.783	13.706	13.658	13.844
Ma	0.02	0.06	0.01	0.00	0.38	0.48	0.05	0.26	0.12	0.00	0.00	0.21	0.00	0.13	0.40	0.16	0.99	2.78	0.70	0.13	0.16
Pa	20.18	16.19	16.88	18.48	17.63	16.93	17.03	20.74	18.60	17.04	17.90	20.31	17.67	16.88	20.86	17.56	16.32	15.97	19.21	19.12	20.28
Ce	10.96	14.04	13.72	8.19	11.50	12.20	13.23	9.49	10.19	14.23	10.06	8.00	12.00	14.43	12.31	12.52	15.43	14.09	24.72	33.26	10.47
Mu	68.84	69.72	69.39	73.33	70.49	70.39	69.69	69.50	71.09	68.73	72.04	71.48	70.33	68.56	66.43	69.77	67.26	67.16	55.36	47.49	69.09
Py	9.22	11.06	11.06	7.03	15.56	16.36	10.12	7.37	8.36	10.87	8.87	7.10	10.79	10.59	7.23	11.94	13.69	17.21	19.86	12.56	11.81
Mu	59.64	58.71	58.34	66.30	55.01	54.51	59.62	62.40	62.83	57.86	63.17	64.59	59.54	58.10	59.60	57.98	54.56	52.73	36.21	32.07	57.45
Py + Ce + Mu = 100																					
Py	11.55	13.19	13.30	8.63	19.25	19.69	12.19	9.30	10.29	13.10	10.81	8.91	13.11	12.74	9.13	14.49	16.36	20.59	19.24	14.81	
Ce	13.74	16.76	16.51	10.04	13.96	14.69	15.94	11.97	12.52	17.16	12.25	10.04	14.58	17.36	15.56	15.18	18.44	16.78	30.60	41.12	13.1
Mu	74.72	70.05	70.19	81.33	66.79	65.62	71.87	78.73	77.19	69.74	76.94	81.04	72.31	69.90	75.31	70.33	65.20	62.75	44.81	39.65	72.06
Sum	100.00	100.00	100.00	100.00	100.00	100.00	100.00	100.00	100.00	100.00	100.00	100.00	100.00	100.00	100.00	100.00	100.00	100.00	100.00	100.00	100.00
Fe tot	0.109	0.119	0.127	0.120	0.113	0.113	0.132	0.096	0.106	0.104	0.118	0.104	0.125	0.118	0.087	0.137	0.131	0.110	0.220	0.128	0.108
Fe 2+	0.121	0.141	0.158	0.052	0.129	0.122	0.112	0.099	0.120	0.130	0.083	0.087	0.110	0.154	0.154	0.101	0.166	0.137	0.338	0.541	0.117
Fe 3+	-0.012	-0.02	0.009	0.068	-0.017	-0.008	0.020	-0.003	-0.015	-0.026	0.035	0.017	0.015	-0.036	-0.066	0.036	-0.035	-0.027	-0.113	-0.413	-0.009
Diagrams																					
A'KF																					
A:	66.26	63.94	63.31	65.13	67 53	66.93	63.40	66.55	66.05	64.36	65.21	65.90	64.71	64.10	63.99	64.09	63.91	65.71	62.76	63.27	67.11
K:	25.57	25.95	25.58	26.19	23.99	23.91	25.79	25.94	26.19	25.79	25.89	26.07	25.46	26.01	26.39	24.97	25.05	23.93	22.84	26.14	24.66
F:	8.18	10.11	11.11	8.68	8.48	9.17	10.82	7.51	7.75	9.87	8.90	7.03	9.83	9.89	7.62	10.95	11.05	10.35	14.40	10.58	8.24
AFM(Ms)																					
A:	0.73	0.63	0.61	0.68	0.74	0.73	0.61	0.74	0.72	0.65	0.69	0.75	0.66	0.64	0.73	0.64	0.64	0.69	0.61	0.7	0.75
F:	0.47	0.41	0.39	0.48	0.46	0.43	0.42	0.46	0.49	0.37	0.47	0.52	0.44	0.42	0.42	0.43	0.43	0.38	0.55	0.41	0.47
M:	0.53	0.59	0.61	0.52	0.54	0.57	0.58	0.54	0.51	0.63	0.53	0.48	0.56	0.58	0.58	0.57	0.57	0.62	0.45	0.54	0.53
AFM(Kl)																					
A:	0.90	0.87	0.86	0.89	0.90	0.89	0.86	0.91	0.90	0.88	0.89	0.91	0.88	0.88	0.91	0.86	0.87	0.88	0.83	0.87	0.90
F:	0.47	0.41	0.39	0.48	0.46	0.43	0.42	0.46	0.49	0.37	0.47	0.52	0.44	0.42	0.42	0.43	0.43	0.38	0.55	0.46	0.47
M:	0.53	0.59	0.61	0.52	0.54	0.57	0.58	0.54	0.51	0.63	0.53	0.48	0.56	0.58	0.58	0.57	0.57	0.62	0.45	0.54	0.53

Sample	P1 F3 84.00	P1 F3 85.00	P1 F3 86.00	P1 F4 1.00	P1 F4 2.00	P1 F4 3.00	P1 F4 4.00	P1 F4 5.00	P1 F5 1.00	P1 F5 2.00	P1 F5 2.00	P1 F5 5.00	P1 F5 6.00
SiO2	47.60	47.64	46.93	47.29	46.94	48.00	48.09	49.37	47.27	46.67	46.67	48.60	48.69
TiO2	0.28	0.34	0.23	0.33	0.26	0.20	0.22	0.24	0.28	0.27	0.27	0.33	0.34
Al2O3	35.46	35.48	35.08	34.84	36.37	35.59	35.85	34.49	35.70	35.73	35.73	35.5	34.49
Cr2O3	0.00	0.05	0.08	0.00	0.00	0.03	0.00	0.06	0.00	0.02	0.02	0.03	0.00
MgO	0.78	0.83	0.68	0.87	0.66	0.74	0.91	0.55	0.72	0.62	0.62	0.78	0.83
CaO	0.00	0.02	0.51	0.54	0.40	0.09	0.02	0.03	0.01	0.00	0.00	0.03	0.05
MnO	0.00	0.00	0.08	0.03	0.00	0.03	0.03	0.00	0.01	0.00	0.00	0.00	0.01
FeO	1.09	0.93	1.14	1.10	1.02	1.07	1.14	0.80	1.00	1.05	1.05	1.32	1.26
BaO	0.18	0.22	0.11	0.18	0.23	0.16	0.22	0.24	0.17	0.14	0.14	0.12	0.20
Na2O	1.32	1.27	1.73	1.10	1.38	1.28	1.14	1.40	1.21	1.31	1.31	0.98	0.95
K2O	8.89	8.78	7.38	8.75	8.70	8.57	8.88	8.21	8.99	8.71	8.71	8.49	8.16
H2O	4.56	4.57	4.51	4.52	4.58	4.58	4.61	4.59	4.55	4.51	4.51	4.61	4.56
Total	100.18	100.12	98.45	99.05	100.55	100.31	101.10	99.97	99.96	99.02	99.02	100.82	99.55
Si	6.254	6.256	6.245	6.272	6.154	6.282	6.256	6.451	6.228	6.199	6.199	6.318	6.398
Ti	0.028	0.034	0.023	0.033	0.026	0.020	0.021	0.024	0.027	0.027	0.027	0.032	0.033
Al	5.495	5.492	5.501	5.445	5.619	5.489	5.498	5.312	5.544	5.594	5.594	5.442	5.341
Cr	0.000	0.005	0.009	0.000	0.000	0.000	0.000	0.006	0.000	0.002	0.002	0.003	0.000
Mg	0.152	0.162	0.134	0.173	0.129	0.144	0.177	0.108	0.141	0.123	0.123	0.152	0.163
Ca	0.000	0.003	0.072	0.076	0.056	0.012	0.002	0.004	0.001	0.000	0.000	0.004	0.007
Mn	0.000	0.000	0.009	0.003	0.000	0.003	0.003	0.000	0.002	0.000	0.000	0.000	0.001
Fe	0.120	0.102	0.127	0.122	0.112	0.117	0.124	0.088	0.110	0.116	0.116	0.143	0.138
Ba	0.009	0.011	0.006	0.010	0.012	0.008	0.011	0.012	0.009	0.007	0.007	0.006	0.010
Na	0.336	0.324	0.447	0.284	0.351	0.326	0.288	0.354	0.309	0.337	0.337	0.247	0.244
K	1.490	1.470	1.253	1.395	1.455	1.431	1.474	1.369	1.510	1.476	1.476	1.408	1.368
Total	13.884	13.859	13.827	13.813	13.914	13.832	13.855	13.727	13.882	13.882	13.882	13.755	13.705
X(Fe)	0.44	0.39	0.49	0.41	0.46	0.45	0.41	0.45	0.44	0.49	0.49	0.49	0.46
Si	6.254	6.256	6.245	6.272	6.154	6.282	6.256	6.451	6.228	6.199	6.199	6.318	6.398
Al IV	1.746	1.744	1.755	1.728	1.846	1.718	1.744	1.549	1.772	1.801	1.801	1.682	1.602
tetr.	8.000	8.000	8.000	8.000	8.000	8.000	8.000	8.000	8.000	8.000	8.000	8.000	8.000
Al VI	3.823	3.823	3.823	3.823	3.823	3.823	3.823	3.823	3.823	3.823	3.823	3.823	3.823
Cr	0.000	0.005	0.009	0.000	0.000	0.000	0.000	0.006	0.000	0.002	0.002	0.003	0.000
Ti	0.028	0.034	0.023	0.033	0.026	0.020	0.021	0.024	0.027	0.027	0.027	0.032	0.033
Fe 2+=to	0.120	0.102	0.127	0.122	0.112	0.117	0.124	0.088	0.110	0.116	0.116	0.143	0.138
Mn	0.000	0.000	0.009	0.003	0.000	0.003	0.003	0.000	0.002	0.000	0.000	0.000	0.001
Mg	0.152	0.162	0.134	0.173	0.129	0.144	0.177	0.108	0.141	0.123	0.123	0.152	0.163
okta.	4.049	4.050	4.049	4.047	4.041	4.055	4.079	3.989	4.053	4.062	4.062	4.090	4.075
Ba	0.009	0.011	0.006	0.010	0.012	0.008	0.011	0.012	0.009	0.007	0.007	0.006	0.010
Ca	0.000	0.003	0.072	0.076	0.056	0.012	0.002	0.004	0.001	0.000	0.000	0.004	0.007
Na	0.336	0.324	0.447	0.284	0.351	0.326	0.288	0.354	0.309	0.337	0.337	0.247	0.244
K	1.490	1.470	1.253	1.396	1.455	1.431	1.474	1.369	1.510	1.476	1.476	1.408	1.368
interlayer	1.835	1.809	1.778	1.766	1.873	1.777	1.776	1.739	1.829	1.820	1.820	1.665	1.630
Sum	13.884	13.859	13.827	13.813	13.914	13.832	13.855	13.727	13.882	13.882	13.882	13.755	13.705
Ma	0.00	0.15	4.08	4.34	3.00	0.69	0.13	0.21	0.07	0.00	0.00	0.24	0.44
Pa	18.39	18.04	25.24	16.15	18.85	18.41	16.31	20.49	16.95	18.61	18.61	14.89	15.08
Ce	12.69	12.81	12.25	13.59	7.68	14.09	12.81	22.56	11.41	9.97	9.97	15.89	19.90
Mu	68.92	69.00	58.43	65.92	70.47	66.81	70.74	56.75	71.57	71.43	71.43	68.99	64.57
Py	8.71	10.27	14.99	16.00	9.71	12.15	11.89	13.86	9.05	9.33	9.33	17.24	19.37
Mu	60.21	58.88	47.51	54.26	63.76	55.34	58.99	43.09	62.59	62.10	62.10	51.99	45.64
Py + Ce + Mu = 100													
Py	10.68	12.54	20.05	19.08	11.97	14.89	14.20	17.43	10.89	11.46	11.46	20.25	22.81
Ce	15.55	15.63	16.39	16.20	9.46	17.27	15.31	28.37	13.74	12.25	12.25	18.66	23.44
Mu	73.78	71.83	63.56	64.71	78.57	67.83	70.49	54.20	75.36	76.29	76.29	61.08	53.75
Sum	100.00	100.00	100.00	100.00	100.00	100.00	100.00	100.00	100.00	100.00	100.00	100.00	100.00
Fe tot	0.120	0.102	0.127	0.122	0.112	0.117	0.124	0.088	0.110	0.116	0.116	0.143	0.138
Fe 2+	0.130	0.128	0.135	0.132	0.050	0.158	0.101	0.367	0.115	0.103	0.103	0.198	0.268
Fe 3+	-0.010	-0.027	-0.007	-0.010	0.062	-0.041	0.023	-0.280	-0.005	0.013	0.013	-0.054	-0.130
Diagram:													
A'KF													
A:	64.33	64.93	67.95	65.41	66.29	65.59	64.22	67.10	64.89	65.92	65.92	65.45	65.38
F:	26.13	25.82	22.39	24.26	25.29	25.15	25.35	25.59	26.31	25.73	25.73	24.34	24.00
K:	9.55	9.25	9.66	10.34	8.42	9.26	10.43	7.30	8.80	8.35	8.35	10.20	10.62
AFM(Ma)													
A:	0.65	0.67	0.77	0.68	0.72	0.70	0.64	0.76	0.67	0.71	0.71	0.67	0.67
F:	0.44	0.39	0.49	0.41	0.46	0.45	0.41	0.45	0.44	0.49	0.49	0.49	0.46
M:	0.56	0.61	0.51	0.59	0.54	0.55	0.59	0.55	0.56	0.51	0.51	0.51	0.54
AFM(K)													
A:	0.88	0.88	0.89	0.87	0.90	0.89	0.87	0.91	0.89	0.90	0.90	0.87	0.87
F:	0.44	0.39	0.49	0.41	0.46	0.45	0.41	0.45	0.44	0.49	0.49	0.49	0.46
M:	0.56	0.61	0.51	0.59	0.54	0.55	0.59	0.55	0.56	0.51	0.51	0.51	0.54

APPENDIX 6: *Microprobe analyses of chlorites from sample P2.*

Analysis	P2 F1 C1	P2 F1 C2	P2 F1 C4	P2 F1 C5	P2 F1 C6	P2 F1 C7	P2 F1 C8	P2 F1 C9	P2 F1 C11	P2 F1 C12	P2 F1 C13	P2 F1 C14	P2 F1 C15	P2 F1 C16	P2 F1 C17	P2 F1 C18	P2 F1 C19	P2 F1 C20	P2 F1 C21	P2 F1 C23	P2 F1 C24	P2 F1 C25	P2 F1 C26	P2 F1 C27	P2 F2 C3	P2 F2 C4	P2 F2 C5	P2 F3 C2	P2 F3 C3	P2 F3 C4	P2 F3 C5
SiO_2	24.61	24.56	24.37	24.39	24.52	24.73	23.96	24.16	24.15	23.82	24.56	24.64	24.48	23.87	24.40	24.29	27.91	24.24	24.13	24.94	24.19	24.91	24.12	24.70	24.00	24.24	24.59	23.72	23.98	24.05	23.81
TiO_2	0.03	0.03	0.07	0.04	0.07	0.08	0.03	0.06	0.03	0.05	0.06	0.05	0.09	0.00	0.06	0.10	0.06	0.02	0.04	0.00	0.03	0.06	0.06	0.02	0.10	0.13	0.03	0.01	0.07	0.05	0.06
Al_2O_3	23.39	23.55	23.81	23.37	22.70	23.96	22.59	22.93	23.49	22.95	23.74	23.55	22.88	23.07	23.25	23.36	22.52	23.33	23.32	23.31	23.16	23.79	22.97	22.97	23.28	23.30	23.12	23.43	23.14	22.95	23.27
MgO	14.83	13.34	14.85	14.93	15.16	14.60	14.87	14.37	14.66	14.12	14.56	15.47	15.39	13.79	16.17	15.74	14.78	15.19	14.95	15.19	14.01	15.40	15.55	14.69	15.15	14.85	14.15	14.56	14.87	14.33	13.93
CaO	0.07	0.15	0.08	0.03	0.05	0.14	0.02	0.09	0.06	0.06	0.17	0.05	0.02	0.06	0.07	0.04	0.08	0.03	0.05	0.05	0.08	0.10	0.06	0.07	0.04	0.05	0.07	0.03	0.06	0.09	0.04
MnO	0.80	0.71	0.70	0.80	0.73	0.74	0.69	0.64	0.67	0.84	0.77	0.68	0.73	0.77	0.61	0.64	0.72	0.69	0.75	0.62	0.87	0.67	0.66	0.76	0.70	0.82	0.69	0.71	0.78	0.79	0.81
FeO	23.50	22.47	22.24	22.88	22.64	23.24	23.36	22.69	23.05	23.78	22.75	22.78	22.57	23.28	23.21	22.68	22.84	23.15	22.92	22.42	23.41	22.52	22.43	22.81	22.88	22.49	23.34	22.98	22.87	22.85	23.46
Na_2O	0.02	0.26	0.10	0.07	0.10	0.18	0.04	0.16	0.06	0.05	0.04	0.04	0.05	0.09	0.04	0.00	0.00	0.00	0.00	0.03	0.05	0.32	0.03	0.01	0.00	0.00	0.02	0.05	0.05	0.03	0.04
K_2O	0.03	0.21	0.02	0.00	0.05	0.00	0.00	0.00	0.00	0.01	0.00	0.01	0.03	0.03	0.03	0.02	0.00	0.00	0.02	0.02	0.02	0.01	0.02	0.06	0.00	0.02	0.00	0.00	0.02	0.02	0.02
Total:	**87.28**	**85.26**	**86.34**	**86.50**	**86.02**	**87.67**	**85.46**	**85.10**	**86.17**	**85.66**	**86.65**	**87.26**	**86.25**	**84.96**	**86.83**	**86.87**	**88.90**	**86.64**	**86.17**	**86.5**	**85.82**	**87.68**	**85.88**	**86.10**	**86.**	**85.89**	**86.01**	**85.49**	**85.84**	**85.16**	**85.45**
Cations																															
Si	5.175	5.265	5.150	5.161	5.218	5.163	5.153	5.198	5.135	5.128	5.180	5.158	5.190	5.166	5.124	5.111	5.682	5.127	5.130	5.247	5.182	5.179	5.135	5.247	5.104	5.159	5.240	5.089	5.124	5.179	5.127
Ti	0.005	0.005	0.012	0.006	0.011	0.012	0.005	0.009	0.004	0.008	0.005	0.008	0.014	0.000	0.009	0.016	0.009	0.003	0.006	0.000	0.005	0.009	0.009	0.004	0.015	0.021	0.005	0.002	0.011	0.008	0.009
Al	5.796	5.950	5.932	5.828	5.691	5.897	5.728	5.815	5.887	5.823	5.899	5.809	5.717	5.885	5.756	5.794	5.402	5.817	5.843	5.780	5.846	5.830	5.767	5.753	5.835	5.843	5.806	5.927	5.828	5.825	5.907
Mg	4.647	4.263	4.681	4.710	4.808	4.546	4.769	4.610	4.646	4.533	4.577	4.827	4.865	4.449	5.064	4.938	4.485	4.739	4.739	4.764	4.474	4.775	4.935	4.654	4.804	4.712	4.496	4.657	4.735	4.601	4.472
Ca	0.016	0.034	0.019	0.007	0.012	0.032	0.006	0.022	0.014	0.013	0.038	0.011	0.004	0.015	0.015	0.009	0.018	0.007	0.010	0.010	0.017	0.023	0.013	0.015	0.009	0.011	0.016	0.008	0.014	0.020	0.010
Mn	0.142	0.128	0.125	0.143	0.132	0.131	0.126	0.116	0.120	0.152	0.137	0.121	0.131	0.141	0.109	0.114	0.124	0.123	0.135	0.110	0.157	0.119	0.120	0.137	0.126	0.148	0.124	0.129	0.141	0.145	0.147
Fe^{2+}	4.132	4.028	3.932	4.049	4.028	4.058	4.184	4.082	4.099	4.282	4.013	3.988	4.002	4.213	3.900	3.992	3.888	4.096	4.076	3.944	4.194	3.916	3.994	4.053	4.070	4.002	4.160	4.123	4.086	4.115	4.226
Na	0.009	0.107	0.039	0.027	0.039	0.073	0.015	0.065	0.024	0.022	0.016	0.018	0.021	0.038	0.017	0.000	0.000	0.000	0.000	0.011	0.022	0.090	0.012	0.002	0.000	0.000	0.008	0.020	0.019	0.012	0.018
K	0.007	0.057	0.006	0.000	0.015	0.000	0.000	0.000	0.000	0.002	0.000	0.002	0.008	0.008	0.008	0.004	0.000	0.000	0.006	0.005	0.004	0.003	0.004	0.017	0.000	0.004	0.000	0.000	0.005	0.004	0.005
Sum	**19.930**	**19.836**	**19.894**	**19.932**	**19.953**	**19.912**	**19.986**	**19.918**	**19.929**	**19.964**	**19.870**	**19.940**	**19.952**	**19.915**	**20.001**	**19.978**	**19.608**	**19.962**	**19.945**	**19.871**	**19.903**	**19.943**	**19.983**	**19.883**	**19.963**	**19.901**	**19.856**	**19.955**	**19.963**	**19.909**	**19.922**
Site occupation																															
Si	5.175	5.265	5.150	5.161	5.218	5.163	5.153	5.198	5.135	5.128	5.180	5.158	5.190	5.166	5.124	5.111	5.682	5.127	5.130	5.247	5.182	5.179	5.135	5.247	5.104	5.159	5.240	5.089	5.124	5.179	5.127
Al(IV)	2.825	2.735	2.850	2.839	2.782	2.837	2.847	2.802	2.865	2.872	2.820	2.842	2.810	2.834	2.876	2.889	2.318	2.873	2.870	2.753	2.818	2.821	2.865	2.753	2.896	2.841	2.760	2.911	2.876	2.821	2.873
Sum	**8.000**	**8.000**	**8.000**	**8.000**	**8.000**	**8.000**	**8.000**	**8.000**	**8.000**	**8.000**	**8.000**	**8.000**	**8.000**	**8.000**	**8.000**	**8.000**	**8.000**	**8.000**	**8.000**	**8.000**	**8.000**	**8.000**	**8.000**	**8.000**	**8.000**	**8.000**	**8.000**	**8.000**	**8.000**	**8.000**	**8.000**
Al(VI)	2.971	3.215	3.082	2.989	2.908	3.061	2.881	3.013	3.022	2.952	3.079	2.966	2.907	3.051	2.880	2.905	3.084	2.944	2.973	3.027	3.029	3.009	2.897	3.000	2.940	3.002	3.046	3.016	2.952	3.004	3.034
Ti	0.005	0.005	0.012	0.006	0.011	0.012	0.005	0.009	0.004	0.008	0.009	0.008	0.014	0.000	0.009	0.016	0.009	0.003	0.006	0.000	0.005	0.009	0.009	0.004	0.015	0.021	0.005	0.002	0.011	0.008	0.009
Mg	4.647	4.263	4.681	4.710	4.808	4.546	4.769	4.610	4.646	4.533	4.577	4.827	4.865	4.449	5.064	4.938	4.485	4.739	4.739	4.764	4.474	4.775	4.935	4.654	4.804	4.712	4.496	4.657	4.735	4.601	4.472
Ca	0.016	0.034	0.019	0.007	0.012	0.032	0.006	0.022	0.014	0.013	0.038	0.011	0.004	0.015	0.015	0.009	0.018	0.007	0.010	0.010	0.017	0.023	0.013	0.015	0.009	0.011	0.016	0.008	0.014	0.020	0.010
Mn	0.142	0.128	0.125	0.143	0.132	0.131	0.126	0.116	0.120	0.152	0.137	0.121	0.131	0.141	0.109	0.114	0.124	0.123	0.135	0.110	0.157	0.119	0.120	0.137	0.126	0.148	0.124	0.129	0.141	0.145	0.147
Fe^{2+}	4.132	4.028	3.932	4.049	4.028	4.058	4.184	4.082	4.099	4.282	4.013	3.988	4.002	4.213	3.900	3.992	3.888	4.096	4.076	3.944	4.194	3.916	3.994	4.053	4.070	4.002	4.160	4.123	4.086	4.115	4.226
Na	0.009	0.107	0.039	0.027	0.039	0.073	0.015	0.065	0.024	0.022	0.016	0.018	0.021	0.038	0.017	0.000	0.000	0.000	0.000	0.011	0.022	0.090	0.012	0.002	0.000	0.000	0.008	0.020	0.019	0.012	0.018
K	0.007	0.057	0.006	0.000	0.015	0.000	0.000	0.000	0.000	0.002	0.000	0.002	0.008	0.008	0.008	0.004	0.000	0.000	0.006	0.005	0.004	0.003	0.004	0.017	0.000	0.004	0.000	0.000	0.005	0.004	0.005
Sum	**11.930**	**11.836**	**11.894**	**11.932**	**11.953**	**11.912**	**11.986**	**11.918**	**11.929**	**11.964**	**11.870**	**11.940**	**11.952**	**11.915**	**12.001**	**11.978**	**11.608**	**11.962**	**11.945**	**11.871**	**11.903**	**11.943**	**11.983**	**11.883**	**11.963**	**11.901**	**11.856**	**11.955**	**11.963**	**11.909**	**11.922**
Total:	**19.930**	**19.836**	**19.894**	**19.932**	**19.953**	**19.912**	**19.986**	**19.918**	**19.929**	**19.964**	**19.870**	**19.940**	**19.952**	**19.915**	**20.001**	**19.978**	**19.608**	**19.962**	**19.945**	**19.871**	**19.903**	**19.943**	**19.983**	**19.883**	**19.963**	**19.901**	**19.856**	**19.955**	**19.963**	**19.909**	**19.922**
A:	24.49	26.03	25.30	24.65	24.06	25.17	23.97	24.77	24.90	24.48	25.18	24.51	24.10	25.02	24.05	24.24	24.08	24.39	24.59	24.66	24.84	24.81	24.13	24.51	24.46	24.77	24.81	24.94	24.51	24.70	25.01
C:	0.14	0.29	0.16	0.06	0.10	0.27	0.05	0.18	0.12	0.11	0.32	0.09	0.04	0.12	0.13	0.08	0.16	0.06	0.09	0.09	0.15	0.19	0.11	0.13	0.07	0.09	0.13	0.07	0.12	0.17	0.09
F:	75.38	73.67	74.54	75.29	75.84	74.56	75.99	75.04	74.98	75.41	74.50	75.40	75.86	74.86	75.82	75.68	75.76	75.55	75.32	75.25	75.01	75.00	75.77	75.36	75.46	75.14	75.05	74.99	75.38	75.14	74.90
A(Ms):	0.24	0.26	0.25	0.25	0.24	0.25	0.24	0.25	0.25	0.24	0.25	0.25	0.24	0.25	0.24	0.24	0.24	0.24	0.25	0.25	0.25	0.25	0.24	0.24	0.24	0.25	0.25	0.25	0.24	0.25	0.25
A(Kf):	0.25	0.26	0.26	0.25	0.24	0.26	0.24	0.25	0.25	0.25	0.26	0.25	0.24	0.25	0.24	0.24	0.24	0.25	0.25	0.25	0.25	0.25	0.24	0.25	0.25	0.25	0.25	0.25	0.25	0.25	0.25
F:	0.47	0.49	0.46	0.46	0.46	0.47	0.47	0.47	0.47	0.49	0.47	0.45	0.45	0.49	0.44	0.45	0.46	0.46	0.46	0.45	0.48	0.45	0.48	0.47	0.46	0.46	0.48	0.47	0.46	0.47	0.49
M:	0.53	0.51	0.54	0.54	0.54	0.53	0.53	0.53	0.53	0.51	0.53	0.55	0.55	0.51	0.56	0.55	0.54	0.54	0.54	0.55	0.52	0.55	0.52	0.53	0.54	0.54	0.52	0.53	0.54	0.53	0.51
Diagrams																															
TRÖGER (1982)																															
mol% al4	70.63	68.38	71.24	70.97	69.56	70.91	71.17	70.04	71.62	71.79	70.50	71.06	70.24	70.85	71.91	72.23	57.96	71.82	71.74	68.82	70.44	70.52	71.62	68.82	72.39	71.04	68.99	72.77	71.90	70.53	71.82
mol% fe6	47.07	48.59	45.65	46.23	45.59	47.16	46.74	46.96	46.87	48.58	46.71	45.24	45.13	48.64	43.51	44.70	46.43	46.10	46.24	45.29	48.39	45.05	44.72	46.55	45.86	45.92	48.06	46.96	46.32	47.21	48.58
HEY (1957)																															
XFe	0.47	0.49	0.46	0.46	0.46	0.47	0.47	0.47	0.47	0.49	0.47	0.45	0.45	0.49	0.44	0.45	0.46	0.46	0.46	0.45	0.48	0.45	0.48	0.47	0.46	0.46	0.48	0.47	0.46	0.47	0.49
Si	5.17	5.26	5.15	5.16	5.22	5.16	5.15	5.20	5.14	5.13	5.18	5.16	5.19	5.17	5.12	5.11	5.68	5.13	5.13	5.25	5.18	5.18	5.14	5.25	5.10	5.16	5.24	5.09	5.12	5.18	5.13

APPENDIX 7: *Microprobe analyses of illmenites from samples P2, A2, RP60, AN.*

Sample	P2 F2 I1	P2 F2 I2	P2 F2 I3	P2 F2 I6	P2 F2 I7	P2 F2 I9	P2 F2 I10	P2 F2 I1X	P2 F2 I2X	P2 F2 I3X	P2 F2 I6X	P2 F2 I9X	P2 F2 I10X
SiO2	0.03	0.00	0.05	0.00	0.23	0.02	0.04	0.11	0.04	0.01	0.00	0.02	0.10
TiO2	52.36	53.06	54.17	53.10	54.96	53.10	52.50	53.30	53.02	54.28	53.75	53.21	53.41
Al2O3	0.00	0.00	0.00	0.00	0.00	0.00	0.00	0.00	0.00	0.00	0.00	0.00	0.00
Cr2O3	0.00	0.00	0.00	0.00	0.05	0.01	0.00	0.00	0.05	0.03	0.00	0.05	0.00
Fe2O3	0.04	0.00	0.00	0.00	0.00	0.00	0.00	0.00	0.00	0.00	0.00	0.00	0.00
MgO	0.01	0.02	0.03	0.00	0.02	0.03	0.00	0.00	0.00	0.00	0.00	0.00	0.00
MnO	22.45	21.76	16.94	21.76	6.60	23.35	23.38	22.30	21.87	17.64	19.97	23.49	23.19
FeO	24.42	23.92	27.69	24.73	33.17	23.24	22.94	23.76	24.41	27.29	25.80	21.87	22.16
Total:	99.31	98.76	98.88	99.57	95.03	99.76	98.86	99.47	99.38	99.25	99.52	98.64	98.85
Cations													
Si	0.002	0.000	0.003	0.000	0.012	0.001	0.002	0.005	0.002	0.000	0.000	0.001	0.005
Ti	1.997	2.024	2.052	2.014	2.128	2.010	2.007	2.019	2.014	2.051	2.033	2.029	2.031
Al	0.000	0.000	0.000	0.000	0.000	0.000	0.000	0.000	0.000	0.000	0.000	0.000	0.000
Cr	0.000	0.000	0.000	0.000	0.002	0.001	0.000	0.000	0.002	0.001	0.000	0.002	0.000
Fe3+	0.002	0.000	0.000	0.000	0.000	0.000	0.000	0.000	0.000	0.000	0.000	0.000	0.000
Mg	0.001	0.001	0.002	0.000	0.002	0.002	0.000	0.000	0.000	0.000	0.000	0.000	0.000
Mn	0.964	0.935	0.723	0.929	0.288	0.995	1.006	0.951	0.935	0.750	0.850	1.009	0.993
Fe2+	1.035	1.015	1.166	1.043	1.428	0.978	0.975	1.000	1.031	1.146	1.085	0.927	0.936
XMg:	0.001	0.001	0.002	0.000	0.001	0.002	0.000	0.000	0.000	0.000	0.000	0.000	0.000
Site occupation													
A-Position:													
Si	0.002	0.000	0.003	0.000	0.012	0.001	0.002	0.005	0.002	0.000	0.000	0.001	0.005
Ti	1.997	2.024	2.052	2.014	2.128	2.010	2.007	2.019	2.014	2.051	2.033	2.029	2.031
Al	0.000	0.000	0.000	0.000	0.000	0.000	0.000	0.000	0.000	0.000	0.000	0.000	0.000
Cr	0.000	0.000	0.000	0.000	0.002	0.001	0.000	0.000	0.002	0.001	0.000	0.002	0.000
Fe3+	0.002	0.000	0.000	0.000	0.000	0.000	0.000	0.000	0.000	0.000	0.000	0.000	0.000
Total:	2.000	2.025	2.055	2.014	2.142	2.012	2.009	2.024	2.018	2.052	2.033	2.033	2.035
B-Position:													
Mg	0.001	0.001	0.002	0.000	0.002	0.002	0.000	0.000	0.000	0.000	0.000	0.000	0.000
Mn	0.964	0.935	0.723	0.929	0.288	0.995	1.006	0.951	0.935	0.750	0.850	1.009	0.993
Fe2+	1.035	1.015	1.166	1.043	1.428	0.978	0.975	1.000	1.031	1.146	1.085	0.927	0.936
Total:	2.000	1.951	1.891	1.972	1.718	1.976	1.981	1.951	1.966	1.897	1.935	1.936	1.929
A + B:	4.000	3.975	3.945	3.986	3.859	3.988	3.991	3.976	3.983	3.949	3.967	3.968	3.965
Endmembers													
Ilmenit:	51.77	52.04	61.68	52.88	84.75	49.52	49.20	51.27	52.49	60.43	56.06	47.90	48.54
Pyrophanit:	48.20	47.92	38.22	47.12	16.75	50.38	50.80	48.73	47.57	39.57	43.94	52.10	51.46
Geikielith:	0.03	0.07	0.10	0.00	0.10	0.10	0.00	0.00	0.00	0.00	0.00	0.00	0.00
A:	0.04	0.00	0.00	0.00	0.00	0.00	0.00	0.00	0.00	0.00	0.00	0.00	0.00
C:	0.00	0.00	0.00	0.00	0.00	0.00	0.00	0.00	0.00	0.00	0.00	0.00	0.00
F:	99.96	100.00	100.00	100.00	100.00	100.00	100.00	100.00	100.00	100.00	100.00	100.00	100.00
A':	0.31	0.31	0.31	0.31	0.31	0.31	0.31	0.31	0.31	0.31	0.31	0.31	0.31
K:	0.00	0.00	0.00	0.00	0.00	0.00	0.00	0.00	0.00	0.00	0.00	0.00	0.00
F:	100.00	100.00	100.00	100.00	100.00	100.00	100.00	100.00	100.00	100.00	100.00	100.00	100.00
A:	-0.443	-0.443	-0.443	-0.443	-0.443	-0.443	-0.443	-0.443	-0.443	-0.443	-0.443	-0.443	-0.443
F:	0.999	0.999	0.998	1.000	0.999	0.998	1.000	1.000	1.000	1.000	1.000	1.000	1.000
M:	0.001	0.001	0.002	0.000	0.001	0.002	0.000	0.000	0.000	0.000	0.000	0.000	0.000

Sample	A2 F1 5	A2 F1 6	A2 F1 7	RP60 F2 5	R60 F2 6	AN F4 6
SiO2	0.00	0.03	0.01	14.28	14.65	1.71
TiO2	50.10	49.35	49.44	0.02	0.00	2.87
Al2O3	0.00	0.00	0.00	0.86	0.99	0.08
Cr2O3	0.05	0.00	0.00	0.04	0.05	0.00
Fe2O3	3.29	3.54	2.82	57.70	57.41	95.68
MgO	0.25	0.26	0.26	0.09	0.13	0.09
MnO	1.35	1.28	1.24	0.03	0.03	0.03
FeO	45.62	45.15	45.33	0.00	0.00	2.21
Total:	100.66	99.70	99.10	73.02	73.26	102.58
Cations						
Si	0.000	0.002	0.001	0.898	0.915	0.087
Ti	1.903	1.893	1.908	0.001	0.000	0.110
Al	0.000	0.000	0.000	0.064	0.073	0.005
Cr	0.002	0.000	0.000	0.002	0.003	0.000
Fe3+	0.125	0.136	0.109	2.729	2.696	3.669
Mg	0.019	0.027	0.020	0.009	0.012	0.000
Mn	0.058	0.055	0.054	0.002	0.001	0.001
Fe2+	1.927	1.925	1.945	0.000	0.000	0.094
XMg:	0.010	0.014	0.010	1.000	1.000	0.000
Site occupation						
A-Position:						
Si	0.000	0.002	0.001	0.898	0.915	0.087
Ti	1.903	1.893	1.908	0.001	0.000	0.110
Al	0.000	0.000	0.000	0.064	0.073	0.005
Cr	0.002	0.000	0.000	0.002	0.003	0.000
Fe3+	0.125	0.136	0.109	2.729	2.696	3.669
Total:	2.030	2.039	2.018	3.694	3.686	3.871
B-Position:						
Mg	0.019	0.027	0.020	0.009	0.012	0.000
Mn	0.058	0.055	0.054	0.002	0.001	0.001
Fe2+	1.927	1.925	1.945	0.000	0.000	0.094
Total:	2.003	2.008	2.019	0.010	0.013	0.095
A + B:	4.033	4.038	4.037	3.704	3.699	3.966
Endmembers						
Ilmenit:	96.18	95.90	96.22	0.00	0.00	98.64
Pyrophanit:	2.89	2.74	2.67	17.35	10.57	1.36
Geikielith:	0.94	1.36	1.00	82.65	89.43	0.00
A:	3.03	3.28	2.62	99.26	99.07	95.06
C:	0.00	0.00	0.00	0.00	0.00	0.00
F:	96.97	96.72	97.38	0.74	0.93	4.94
A':	0.31	0.31	0.31	0.31	0.31	0.31
K:	0.00	0.00	0.00	0.00	0.00	0.00
F:	100.00	100.00	100.00	100.00	100.00	100.00
A:	-0.443	-0.443	-0.443	-0.443	-0.443	-0.443
F:	0.990	0.986	0.990	0.000	0.000	1.000
M:	0.010	0.014	0.010	1.000	1.000	0.000

APPENDIX 8: *Microprobe analyses of garnet from sample P2.*

Sample	P2 F2 1	P2 F2 2	P2 F2 3	P2 F2 4	P2 F2 5	P2 F2 6	P2 F2 7	P2 F2 8	P2 F2 9	P2 F2 10	P2 F2 11	P2 F2 12	P2 F2 13	P2 F2 14	P2 F2 15	P2 F2 16	P2 F2 17	P2 F3 G1 1	P2 F3 G2 1	P2 F3 G3 1	P2 F3 G4 1
SiO_2	36.73	36.14	36.10	36.35	36.12	36.23	36.69	36.40	36.27	36.54	36.60	36.53	36.84	36.61	36.73	36.54	36.64	36.78	36.81	36.81	36.89
TiO_2	0.10	0.12	0.14	0.17	0.21	0.17	0.11	0.16	0.15	0.14	0.12	0.13	0.12	0.17	0.24	0.08	0.17	0.14	0.10	0.14	0.08
Al_2O_3	20.75	20.27	20.30	20.33	20.59	20.40	20.56	20.50	20.27	20.55	20.66	20.47	20.72	20.77	20.51	20.63	20.63	20.72	20.49	20.38	20.63
Cr_2O_3	0.00	0.00	0.00	0.00	0.06	0.00	0.01	0.00	0.00	0.02	0.06	0.00	0.02	0.00	0.00	0.01	0.01	0.00	0.00	0.04	0.05
Fe_2O_3	0.44	0.68	1.06	0.98	0.83	0.71	0.48	0.22	0.69	1.05	0.69	0.82	0.43	0.39	0.60	0.95	0.94	0.45	0.73	0.40	0.41
MgO	0.91	0.94	0.97	0.98	1.02	0.96	0.97	0.97	0.99	1.01	1.01	0.98	1.09	1.00	0.96	0.99	1.03	1.01	1.09	1.04	1.01
CaO	4.33	4.24	4.29	4.72	4.54	4.50	4.89	4.50	4.57	4.58	4.76	5.27	4.71	5.30	5.16	5.39	5.17	5.24	4.80	5.16	5.11
MnO	18.31	18.29	18.12	17.39	17.56	17.58	17.26	17.45	17.35	17.93	17.61	17.56	17.77	17.42	17.34	17.48	17.38	17.56	17.68	17.50	17.42
FeO	18.50	17.88	18.20	18.54	18.51	18.48	18.56	18.48	18.44	18.47	18.45	17.78	18.28	17.94	18.27	17.89	18.31	17.94	18.13	17.61	18.15
Sum	100.08	98.57	99.19	99.45	99.45	99.04	99.52	98.68	98.73	100.28	99.95	99.54	99.98	99.58	99.80	99.97	100.28	99.82	99.73	99.07	99.75
Cations																					
Si	5.965	5.962	5.930	5.945	5.909	5.948	5.979	5.983	5.968	5.930	5.947	5.955	5.973	5.955	5.969	5.934	5.934	5.968	5.985	6.010	5.990
Ti	0.012	0.015	0.018	0.021	0.026	0.021	0.014	0.020	0.019	0.017	0.015	0.016	0.015	0.021	0.029	0.009	0.021	0.016	0.012	0.017	0.010
Al	3.972	3.941	3.930	3.919	3.969	3.948	3.949	3.970	3.930	3.932	3.956	3.934	3.960	3.981	3.928	3.949	3.937	3.963	3.925	3.923	3.947
Cr	0.000	0.000	0.000	0.000	0.008	0.000	0.001	0.000	0.000	0.002	0.007	0.000	0.003	0.000	0.000	0.001	0.002	0.000	0.000	0.005	0.006
Fe^{3+}	0.054	0.085	0.132	0.120	0.103	0.088	0.058	0.027	0.085	0.129	0.084	0.100	0.053	0.048	0.073	0.116	0.115	0.054	0.077	0.049	0.050
Mg	0.221	0.232	0.237	0.238	0.248	0.235	0.235	0.238	0.244	0.244	0.244	0.237	0.264	0.242	0.233	0.240	0.249	0.245	0.265	0.253	0.245
Ca	0.754	0.750	0.755	0.827	0.796	0.791	0.854	0.793	0.805	0.796	0.828	0.921	0.818	0.924	0.898	0.938	0.897	0.911	0.837	0.903	0.889
Mn	2.518	2.556	2.520	2.409	2.434	2.445	2.382	2.428	2.418	2.465	2.424	2.425	2.440	2.400	2.387	2.405	2.385	2.414	2.434	2.420	2.396
Fe^{2+}	2.513	2.467	2.501	2.535	2.533	2.537	2.530	2.540	2.537	2.507	2.508	2.424	2.478	2.440	2.483	2.430	2.480	2.434	2.465	2.405	2.465
X_{Fe}	0.92	0.91	0.91	0.91	0.91	0.92	0.91	0.91	0.91	0.91	0.91	0.91	0.90	0.91	0.91	0.91	0.91	0.91	0.90	0.90	0.91
X_{Mn}	0.48	0.49	0.48	0.46	0.47	0.47	0.46	0.47	0.47	0.47	0.47	0.48	0.47	0.47	0.47	0.47	0.47	0.47	0.47	0.48	0.47
Site occupation																					
Si	5.965	5.962	5.930	5.945	5.909	5.948	5.979	5.983	5.968	5.930	5.947	5.955	5.973	5.955	5.969	5.934	5.934	5.968	5.985	6.010	5.990
Fe^{3+}	0.035	0.038	0.070	0.055	0.091	0.052	0.021	0.017	0.032	0.070	0.053	0.045	0.027	0.045	0.031	0.066	0.066	0.032	0.015	0.000	0.010
Al	0.000	0.000	0.000	0.000	0.000	0.000	0.000	0.000	0.000	0.000	0.000	0.000	0.000	0.000	0.000	0.000	0.000	0.000	0.000	0.000	0.000
Tetr. Z:	6.000	6.000	6.000	6.000	6.000	6.000	6.000	6.000	6.000	6.000	6.000	6.000	6.000	6.000	6.000	6.000	6.000	6.000	6.000	6.010	6.000
Ti	0.012	0.015	0.018	0.021	0.026	0.021	0.014	0.020	0.019	0.017	0.015	0.016	0.015	0.021	0.029	0.009	0.021	0.016	0.012	0.017	0.010
Al	3.972	3.941	3.930	3.919	3.969	3.948	3.949	3.970	3.930	3.932	3.956	3.934	3.960	3.981	3.928	3.949	3.937	3.963	3.925	3.923	3.947
Cr	0.000	0.000	0.000	0.000	0.008	0.000	0.001	0.000	0.000	0.002	0.007	0.000	0.003	0.000	0.000	0.001	0.002	0.000	0.000	0.005	0.006
Fe^{3+}	0.019	0.047	0.061	0.066	0.011	0.037	0.038	0.010	0.053	0.059	0.032	0.056	0.026	0.002	0.043	0.051	0.049	0.023	0.062	0.049	0.040
Oct. Y:	4.004	4.004	4.009	4.006	4.015	4.005	4.002	4.000	4.002	4.010	4.010	4.005	4.003	4.004	4.000	4.010	4.008	4.002	4.000	3.993	4.003
Mg	0.221	0.232	0.237	0.238	0.248	0.235	0.235	0.238	0.244	0.244	0.244	0.237	0.264	0.242	0.233	0.240	0.249	0.245	0.265	0.253	0.245
Ca	0.754	0.750	0.755	0.827	0.796	0.791	0.854	0.793	0.805	0.796	0.828	0.921	0.818	0.924	0.898	0.938	0.897	0.911	0.837	0.903	0.889
Mn	2.518	2.556	2.520	2.409	2.434	2.445	2.382	2.428	2.418	2.465	2.424	2.425	2.440	2.400	2.387	2.405	2.385	2.414	2.434	2.420	2.396
Fe^{2+}	2.513	2.467	2.501	2.535	2.533	2.537	2.530	2.540	2.537	2.507	2.508	2.424	2.478	2.440	2.483	2.430	2.480	2.434	2.465	2.405	2.465
X-Pos :	6.005	6.005	6.013	6.008	6.010	6.008	6.001	6.000	6.003	6.013	6.004	6.007	6.001	6.006	6.000	6.013	6.010	6.004	6.001	5.982	5.995
Total:	16.009	16.009	16.022	16.014	16.025	16.013	16.003	15.999	16.006	16.021	16.014	16.012	16.004	16.010	16.000	16.023	16.019	16.006	16.001	15.985	15.999
Endmembers																					
Ur:	0.00	0.01	0.00	0.00	0.20	0.00	0.03	0.00	0.00	0.05	0.18	0.01	0.07	0.00	0.00	0.04	0.04	0.00	0.00	0.12	0.16
Ad:	0.79	1.56	1.97	2.15	0.93	1.43	1.29	0.74	1.79	1.90	1.15	1.78	1.02	0.57	1.81	1.50	1.73	0.98	1.87	1.64	1.24
Gr:	11.76	10.93	10.59	11.61	12.29	11.73	17.94	12.48	11.62	11.34	12.02	13.56	12.60	14.81	13.10	14.10	13.18	14.19	12.07	13.45	13.56
Al:	41.84	41.08	41.58	42.19	42.06	42.23	42.15	42.34	42.26	41.68	41.69	40.34	41.27	40.63	41.38	40.39	41.24	40.53	41.08	40.15	41.05
Sp:	41.93	42.56	41.91	40.09	40.41	40.70	39.68	40.48	40.27	40.98	40.30	40.36	40.64	39.96	39.78	39.98	39.66	40.20	40.56	40.41	39.90
Py:	3.68	3.87	3.95	3.96	4.11	3.91	3.92	3.97	4.06	4.06	4.06	3.95	4.40	4.03	3.88	3.99	4.14	4.08	4.42	4.23	4.08
An:	25.10	25.11	25.24	25.16	25.30	25.14	25.03	24.99	25.06	25.25	25.18	25.14	25.06	25.11	25.01	25.26	25.21	25.07	25.01	24.92	25.00
Cs:	9.40	9.35	9.39	10.30	9.89	9.85	10.66	9.92	10.05	9.90	10.32	11.48	10.22	11.52	11.22	11.66	11.16	11.37	10.45	11.34	11.12
Fs:	65.50	65.54	65.37	64.54	64.80	65.00	64.30	65.09	64.89	64.85	64.50	63.38	64.73	63.36	63.77	63.07	63.63	63.56	64.54	63.74	63.87
An':	25.12	25.12	25.28	25.18	25.35	25.17	25.04	24.99	25.07	25.28	25.21	25.16	25.06	25.14	25.01	25.31	25.25	25.08	25.01	24.91	25.00
Ks:	0.00	0.00	0.00	0.00	0.00	0.00	0.00	0.00	0.00	0.00	0.00	0.00	0.00	0.00	0.00	0.00	0.00	0.00	0.00	0.00	0.00
Fs:	74.88	74.88	74.72	74.82	74.65	74.83	74.96	75.01	74.93	74.72	74.79	74.84	74.94	74.86	74.99	74.69	74.75	74.92	74.99	75.09	75.00
An:	0.25	0.24	0.24	0.24	0.25	0.24	0.24	0.25	0.24	0.24	0.25	0.24	0.25	0.25	0.24	0.24	0.24	0.25	0.24	0.24	0.24
Fs:	0.92	0.91	0.91	0.91	0.91	0.92	0.91	0.91	0.91	0.91	0.91	0.91	0.90	0.91	0.91	0.91	0.91	0.91	0.90	0.90	0.91
Mt:	0.08	0.09	0.09	0.09	0.09	0.08	0.09	0.09	0.09	0.09	0.09	0.09	0.10	0.09	0.09	0.09	0.09	0.09	0.10	0.10	0.09

Sample	-24.00	-25.00	-26.00	-27.00	-28.00	-29.00	-30.00	-31.00	-32.00	-33.00	P2GTPR2	-2.00 1	-3.00 1	-4.00 1	-5.00 1	-6.00 1	-7.00 1	-8.00 1	-9.00 1	-10.00 1	-11.00 1	-12.00 1
SiO_2	36.46	36.71	36.49	36.40	36.58	36.62	36.55	36.39	36.63	36.29	36.32	36.48	36.52	36.58	36.64	36.53	36.63	36.33	36.49	36.51	36.60	36.42
TiO_2	0.08	0.17	0.09	0.12	0.13	0.15	0.15	0.12	0.10	0.12	0.17	0.16	0.13	0.10	0.16	0.11	0.15	0.10	0.10	0.12	0.11	0.15
Al_2O_3	20.37	20.62	20.66	20.51	20.26	20.50	20.44	20.29	20.32	20.52	20.10	20.35	20.46	20.00	20.45	20.44	20.49	20.38	20.43	20.48	20.38	20.66
Cr_2O_3	0.01	0.00	0.06	0.00	0.00	0.00	0.00	0.00	0.00	0.01	0.00	0.02	0.00	0.01	0.00	0.03	0.03	0.04	0.00	0.00	0.01	0.00
Fe_2O_3	0.60	0.49	0.48	0.65	1.18	0.74	0.70	1.02	0.76	0.49	1.04	0.58	1.03	0.94	0.98	1.38	0.69	0.91	0.58	0.69	0.75	0.71
MgO	0.92	1.01	1.02	1.03	1.07	1.04	1.00	1.03	1.00	1.08	1.02	0.96	1.02	1.07	0.99	1.06	0.99	1.02	1.05	1.05	1.06	1.12
CaO	4.85	4.84	4.74	4.82	4.87	5.39	4.80	5.11	4.95	4.85	4.88	4.76	5.19	4.87	5.12	4.89	4.84	4.83	4.89	4.95	4.81	4.86
MnO	17.89	17.69	17.71	17.77	17.86	17.28	17.64	17.59	17.58	17.21	17.56	17.41	17.77	17.49	17.54	17.86	17.78	17.71	17.58	17.66	17.90	17.42
FeO	17.77	18.21	18.13	17.90	17.88	17.85	18.17	17.72	17.99	18.18	17.88	18.33	17.71	17.82	18.14	18.12	18.08	17.93	17.95	17.88	17.79	18.25
Sum	98.93	99.74	99.37	99.22	99.83	99.57	99.44	99.28	99.33	98.74	98.96	99.05	99.82	98.87	100.02	100.41	99.72	98.25	99.02	99.32	99.41	99.58
Cations																						
Si	5.978	5.969	5.958	5.955	5.956	5.961	5.966	5.953	5.983	5.958	5.964	5.977	5.943	6.003	5.951	5.921	5.964	5.947	5.976	5.963	5.974	5.935
Ti	0.010	0.021	0.010	0.015	0.016	0.018	0.018	0.015	0.012	0.014	0.021	0.020	0.015	0.012	0.019	0.014	0.018	0.012	0.012	0.014	0.014	0.018
Al	3.939	3.952	3.975	3.955	3.887	3.933	3.932	3.912	3.912	3.970	3.890	3.931	3.923	3.868	3.915	3.905	3.931	3.933	3.942	3.942	3.921	3.968
Cr	0.001	0.000	0.008	0.001	0.000	0.000	0.000	0.000	0.000	0.002	0.000	0.003	0.000	0.001	0.000	0.004	0.010	0.005	0.000	0.000	0.001	0.000
Fe^{3+}	0.074	0.060	0.059	0.080	0.145	0.091	0.086	0.126	0.093	0.061	0.128	0.071	0.126	0.115	0.120	0.169	0.085	0.112	0.072	0.084	0.093	0.087
Mg	0.226	0.245	0.249	0.252	0.260	0.253	0.244	0.251	0.244	0.264	0.249	0.235	0.248	0.262	0.240	0.256	0.239	0.248	0.256	0.254	0.258	0.271
Ca	0.852	0.844	0.830	0.844	0.849	0.939	0.839	0.896	0.867	0.853	0.858	0.835	0.904	0.856	0.891	0.850	0.845	0.848	0.858	0.866	0.841	0.849
Mn	2.486	2.437	2.448	2.463	2.463	2.383	2.439	2.436	2.432	2.393	2.442	2.417	2.449	2.430	2.413	2.452	2.451	2.456	2.431	2.443	2.474	2.404
Fe^{2+}	2.438	2.476	2.475	2.449	2.434	2.430	2.481	2.424	2.458	2.496	2.455	2.512	2.409	2.445	2.463	2.456	2.462	2.455	2.458	2.443	2.429	2.487
X_{Fe}	0.92	0.91	0.91	0.91	0.90	0.91	0.91	0.91	0.91	0.90	0.91	0.91	0.91	0.90	0.91	0.91	0.91	0.91	0.91	0.91	0.90	0.90
X_{Mn}	0.48	0.47	0.47	0.48	0.48	0.47	0.47	0.48	0.47	0.46	0.47	0.47	0.48	0.47	0.47	0.47	0.48	0.48	0.47	0.48	0.48	0.47
Site occupation																						
Si	5.978	5.969	5.958	5.955	5.956	5.961	5.966	5.953	5.983	5.958	5.964	5.977	5.943	6.003	5.951	5.921	5.964	5.947	5.976	5.963	5.974	5.935
Fe^{3+}	0.022	0.031	0.042	0.045	0.044	0.039	0.034	0.047	0.017	0.042	0.036	0.023	0.057	0.000	0.049	0.079	0.036	0.053	0.024	0.037	0.026	0.065
Al	0.000	0.000	0.000	0.000	0.000	0.012	0.000	0.000	0.000	0.000	0.000	0.000	0.000	0.000	0.000	0.000	0.000	0.000	0.000	0.000	0.000	0.000
Tetr. Z:	6.000	6.000	6.000	6.000	6.000	6.000	6.000	6.000	6.000	6.000	6.000	6.000	6.000	6.003	6.000	6.000	6.000	6.000	6.000	6.000	6.000	6.000
Ti	0.010	0.021	0.010	0.015	0.016	0.018	0.018	0.015	0.012	0.014	0.021	0.020	0.015	0.012	0.019	0.014	0.018	0.012	0.012	0.014	0.014	0.018
Al	3.939	3.952	3.975	3.955	3.887	3.933	3.932	3.912	3.912	3.970	3.890	3.931	3.923	3.868	3.915	3.905	3.931	3.933	3.942	3.942	3.921	3.968
Cr	0.001	0.000	0.008	0.001	0.000	0.000	0.000	0.000	0.000	0.002	0.000	0.003	0.000	0.001	0.000	0.004	0.010	0.005	0.000	0.000	0.001	0.000
Fe^{3+}	0.052	0.029	0.017	0.035	0.101	0.052	0.052	0.078	0.077	0.019	0.092	0.048	0.069	0.115	0.071	0.04	0.049	0.059	0.048	0.047	0.067	0.022
Oct. Y:	4.003	4.002	4.009	4.005	4.005	4.003	4.003	4.006	4.001	4.005	4.003	4.002	4.007	3.996	4.005	4.013	4.008	4.009	4.002	4.004	4.003	4.008
Mg	0.226	0.245	0.249	0.252	0.260	0.253	0.244	0.251	0.244	0.264	0.249	0.235	0.248	0.262	0.240	0.256	0.239	0.248	0.256	0.254	0.258	0.271
Ca	0.852	0.844	0.830	0.844	0.849	0.939	0.839	0.896	0.867	0.853	0.858	0.835	0.904	0.856	0.891	0.850	0.845	0.848	0.858	0.866	0.841	0.849
Mn	2.486	2.437	2.448	2.463	2.463	2.383	2.439	2.436	2.432	2.393	2.442	2.417	2.449	2.430	2.413	2.452	2.451	2.456	2.431	2.443	2.474	2.404
Fe^{2+}	2.438	2.476	2.475	2.449	2.434	2.430	2.481	2.424	2.458	2.496	2.455	2.512	2.409	2.445	2.463	2.456	2.462	2.455	2.458	2.443	2.429	2.487
X-Pos :	6.002	6.002	6.002	6.007	6.007	6.005	6.004	6.000	6.001	6.006	6.004	5.998	6.010	5.993	6.008	6.013	5.997	6.007	6.003	6.006	6.002	6.012
Total:	16.004	16.004	16.011	16.012	16.011	16.009	16.006	16.013	16.002	16.011	16.007	16.000	16.017	15.993	16.013	16.025	16.005	16.016	16.005	16.009	16.005	16.020
Endmembers																						
Uv:	0.04	0.00	0.19	0.01	0.00	0.00	0.00	0.01	0.00	0.05	0.00	0.07	0.00	0.03	0.09	0.09	0.24	0.12	0.01	0.00	0.02	0.00
Ad:	1.56	1.24	0.67	1.25	2.93	1.76	1.75	2.33	2.22	0.84	2.82	1.71	2.10	3.19	2.26	2.58	1.67	1.79	1.69	1.54	2.01	1.00
Gr:	12.64	13.13	13.13	12.80	11.20	13.89	12.22	13.58	12.22	13.36	11.47	12.30	12.95	11.09	12.57	11.53	12.38	12.31	12.80	12.87	11.99	13.13
Al:	40.60	41.15	41.16	40.76	40.53	40.46	41.32	40.84	40.96	41.54	40.89	41.84	40.09	40.79	41.00	40.81	40.95	40.82	40.94	40.68	40.46	41.37
Sp:	41.41	40.60	40.71	40.99	41.00	39.68	40.63	40.55	40.53	39.83	40.68	40.26	40.74	40.54	40.17	40.73	40.77	40.84	40.50	40.67	41.21	39.99
Py:	3.76	4.09	4.13	4.19	4.34	4.22	4.08	4.18	4.07	4.39	4.15	3.92	4.13	4.36	4.00	4.26	3.98	4.12	4.27	4.24	4.30	4.51
A:	25.05	25.05	25.15	25.14	25.13	25.10	25.07	25.15	25.02	25.13	25.07	25.01	25.20	24.94	25.14	25.30	25.08	25.19	25.06	25.11	25.06	25.22
C:	10.64	10.54	10.35	10.52	10.58	11.72	10.47	11.16	10.83	10.63	10.70	10.44	11.25	10.72	11.10	10.55	10.55	10.56	10.71	10.79	10.50	10.56
F:	64.30	64.42	64.50	64.34	64.29	63.19	64.45	63.68	64.15	64.24	64.22	64.55	63.55	64.34	63.76	64.14	64.37	64.25	64.23	64.10	64.44	64.22
A':	25.06	25.05	25.17	25.16	25.15	25.11	25.08	25.18	25.02	25.15	25.08	25.01	25.23	24.93	25.16	25.35	25.10	25.22	25.07	25.12	25.07	25.25
K:	0.00	0.00	0.00	0.00	0.00	0.00	0.00	0.00	0.00	0.00	0.00	0.00	0.00	0.00	0.00	0.00	0.00	0.00	0.00	0.00	0.00	0.00
F:	74.94	74.95	74.83	74.84	74.85	74.89	74.92	74.82	74.98	74.85	74.92	74.99	74.77	75.07	74.84	74.65	74.90	74.78	74.93	74.88	74.93	74.75
A:	0.24	0.24	0.25	0.24	0.24	0.24	0.24	0.24	0.24	0.25	0.24	0.24	0.24	0.24	0.24	0.24	0.24	0.24	0.24	0.24	0.24	0.25
F:	0.92	0.91	0.91	0.91	0.90	0.91	0.91	0.91	0.91	0.90	0.91	0.91	0.91	0.90	0.91	0.91	0.91	0.91	0.91	0.91	0.90	0.90
M:	0.08	0.09	0.09	0.09	0.10	0.09	0.09	0.09	0.09	0.10	0.09	0.09	0.09	0.10	0.09	0.09	0.09	0.09	0.09	0.09	0.10	0.10

Sample	-13.00 1	-14.00 1	-15.00 1	-16.00 1	-17.00 1	-18.00 1	-19.00 1	-20.00 1	-21.00 1	-22.00 1	-23.00 1	-24.00 1	-25.00 1	-26.00 1	-27.00 1	-28.00 1	-29.00 1	-32.00 1	-33.00 1	-34.00 1	-35.00 1
SiO_2	36.49	36.49	36.76	36.27	36.45	36.36	36.45	36.53	36.77	36.47	36.45	36.78	36.36	36.72	36.71	36.48	36.30	36.10	37.06	36.68	37.02	36.65
TiO_2	0.13	0.09	0.13	0.13	0.12	0.18	0.13	0.21	0.14	0.11	0.12	0.09	0.11	0.07	0.13	0.03	0.12	0.18	0.04	0.12	0.12	0.13
Al_2O_3	20.59	20.64	20.66	20.46	20.46	20.64	20.44	20.62	20.86	20.46	20.55	20.65	20.72	20.69	20.59	20.63	20.74	20.66	20.92	20.61	20.89	20.69
Cr_2O_3	0.04	0.04	0.00	0.02	0.00	0.04	0.01	0.02	0.02	0.00	0.02	0.00	0.00	0.02	0.01	0.09	0.00	0.04	0.03	0.00	0.00	0.00
Fe_2O_3	0.70	0.24	0.36	0.79	0.53	0.74	0.50	0.31	0.19	0.89	0.57	0.07	0.77	0.86	0.58	0.96	0.42	0.32	0.18	0.43	0.17	0.59
MgO	1.07	1.01	1.02	1.06	1.16	1.09	1.06	0.98	1.04	1.03	1.07	1.01	1.04	0.99	1.13	1.05	1.08	1.05	1.01	1.07	1.03	1.04
CaO	4.73	4.95	5.02	4.68	4.82	4.94	4.69	4.94	5.06	5.14	4.76	4.83	4.87	4.90	4.78	5.04	4.98	5.00	4.93	4.90	4.74	4.89
MnO	17.86	17.29	17.65	17.80	17.23	17.38	17.41	17.43	17.44	17.34	17.52	17.48	17.82	17.98	17.63	17.39	17.24	17.40	17.65	17.40	17.55	17.38
FeO	18.01	18.15	17.97	17.95	18.12	18.20	18.26	18.21	18.29	18.06	18.17	18.18	18.01	18.13	18.14	18.04	18.25	18.22	18.39	18.25	18.71	18.17
Sum	99.60	98.90	99.60	99.15	98.89	99.55	98.94	99.25	99.81	99.50	99.23	99.10	99.71	100.37	99.70	99.91	99.13	99.64	100.21	99.45	100.26	99.78
Cations																						
Si	5.947	5.975	5.979	5.942	5.972	5.928	5.974	5.967	5.966	5.949	5.959	6.006	5.923	5.945	5.970	5.931	5.937	5.979	5.988	5.977	5.987	5.955
Ti	0.016	0.011	0.016	0.015	0.014	0.022	0.016	0.026	0.017	0.013	0.014	0.011	0.014	0.009	0.015	0.004	0.015	0.022	0.005	0.014	0.015	0.015
Al	3.955	3.984	3.961	3.951	3.950	3.966	3.949	3.969	3.989	3.934	3.960	3.974	3.979	3.948	3.946	3.953	3.999	3.958	3.985	3.958	3.978	3.962
Cr	0.005	0.005	0.000	0.003	0.000	0.005	0.001	0.003	0.003	0.000	0.003	0.000	0.000	0.003	0.001	0.011	0.000	0.005	0.004	0.000	0.000	0.000
Fe^{3+}	0.086	0.029	0.044	0.098	0.065	0.090	0.062	0.038	0.023	0.110	0.070	0.009	0.095	0.105	0.071	0.118	0.051	0.039	0.021	0.052	0.020	0.072
Mg	0.259	0.247	0.248	0.258	0.283	0.264	0.258	0.237	0.252	0.251	0.261	0.246	0.253	0.239	0.275	0.255	0.264	0.254	0.243	0.259	0.248	0.251
Ca	0.826	0.868	0.876	0.821	0.846	0.863	0.824	0.864	0.879	0.899	0.834	0.846	0.850	0.849	0.833	0.877	0.873	0.870	0.854	0.855	0.821	0.911
Mn	2.466	2.398	2.433	2.470	2.391	2.400	2.417	2.411	2.397	2.396	2.426	2.417	2.459	2.466	2.428	2.422	2.389	2.395	2.416	2.401	2.402	2.378
Fe^{2+}	2.454	2.486	2.444	2.459	2.483	2.482	2.503	2.488	2.483	2.464	2.483	2.483	2.454	2.455	2.467	2.453	2.496	2.476	2.486	2.487	2.528	2.468
X_{Fe}	0.90	0.91	0.91	0.91	0.90	0.90	0.91	0.91	0.91	0.91	0.90	0.91	0.91	0.91	0.90	0.91	0.90	0.91	0.91	0.91	0.91	0.91
X_{Mn}	0.48	0.47	0.47	0.48	0.46	0.47	0.47	0.47	0.47	0.47	0.47	0.47	0.48	0.48	0.47	0.47	0.46	0.47	0.47	0.47	0.46	0.47
Site occupation																						
Si	5.947	5.975	5.979	5.942	5.972	5.928	5.974	5.967	5.966	5.949	5.959	6.006	5.923	5.945	5.970	5.931	5.937	5.979	5.988	5.977	5.987	5.955
Fe^{3+}	0.053	0.025	0.021	0.058	0.028	0.072	0.026	0.033	0.023	0.051	0.041	0.000	0.077	0.055	0.030	0.069	0.051	0.021	0.012	0.023	0.013	0.045
Al	0.000	0.000	0.000	0.000	0.000	0.000	0.000	0.000	0.011	0.000	0.000	0.000	0.000	0.000	0.000	0.000	0.012	0.000	0.000	0.000	0.000	0.000
Tetr. Z:	6.000	6.000	6.000	6.000	6.000	6.000	6.000	6.000	6.000	6.000	6.000	6.006	6.000	6.000	6.000	6.000	6.000	6.000	6.000	6.000	6.000	6.000
Ti	0.016	0.011	0.016	0.015	0.014	0.022	0.016	0.026	0.017	0.013	0.014	0.011	0.014	0.009	0.015	0.004	0.015	0.022	0.005	0.014	0.015	0.015
Al	3.955	3.984	3.961	3.951	3.950	3.966	3.949	3.969	3.978	3.934	3.960	3.974	3.979	3.948	3.946	3.953	3.987	3.958	3.98	3.958	3.978	3.962
Cr	0.005	0.005	0.0	0.003	0.000	0.005	0.001	0.003	0.0	0.000	0.003	0.000	0.000	0.003	0.001	0.011	0.000	0.005	0.00	0.000	0.000	0.000
Fe^{3+}	0.033	0.005	0.02	0.040	0.038	0.018	0.036	0.005	0.000	0.059	0.029	0.009	0.018	0.050	0.040	0.049	0.000	0.018	0.010	0.030	0.007	0.027
Oct. Y:	4.009	4.005	4.001	4.009	4.002	4.011	4.002	4.003	3.9	4.006	4.006	3.994	4.011	4.009	4.003	4.016	4.002	4.002	4.003	4.001	4.000	4.009
Mg	0.259	0.247	0.248	0.258	0.283	0.264	0.258	0.237	0.252	0.251	0.261	0.246	0.253	0.239	0.275	0.255	0.264	0.254	0.243	0.259	0.248	0.251
Ca	0.826	0.868	0.876	0.821	0.846	0.863	0.824	0.864	0.879	0.899	0.834	0.846	0.850	0.849	0.833	0.877	0.873	0.870	0.854	0.855	0.821	0.911
Mn	2.466	2.398	2.433	2.470	2.391	2.400	2.417	2.411	2.397	2.396	2.426	2.417	2.459	2.466	2.428	2.422	2.389	2.395	2.416	2.401	2.402	2.378
Fe^{2+}	2.454	2.486	2.444	2.459	2.483	2.482	2.503	2.488	2.483	2.464	2.483	2.483	2.454	2.455	2.467	2.453	2.496	2.476	2.486	2.487	2.528	2.468
X-Pos :	6.005	6.000	6.001	6.009	6.003	6.009	6.001	6.000	6.010	6.010	6.005	5.991	6.016	6.009	6.003	6.008	6.021	5.996	5.999	6.002	6.009	6.007
Total:	16.014	16.005	16.002	16.017	16.006	16.010	16.004	16.002	16.009	16.016	16.010	15.991	16.026	16.018	16.006	16.025	16.023	15.998	16.002	16.004	15.999	16.012
Endmembers																						
Uv:	0.13	0.13	0.01	0.07	0.00	0.11	0.04	0.06	0.07	0.00	0.07	0.00	0.00	0.07	0.02	0.27	0.00	0.12	0.11	0.00	0.00	0.00
Ad:	1.22	0.38	0.99	1.37	1.30	1.01	1.30	0.77	0.43	1.79	1.08	0.49	0.79	1.46	1.39	1.31	0.38	1.00	0.36	1.09	0.55	1.06
Gr:	12.51	14.07	13.60	12.27	12.80	13.34	12.42	13.62	14.19	13.16	12.81	13.62	13.34	12.66	12.49	13.26	14.12	13.50	13.85	13.15	13.14	14.10
Al:	40.82	41.38	40.72	40.90	41.37	41.26	41.69	41.44	41.28	41.01	41.33	41.44	40.80	40.82	41.09	40.72	41.45	41.25	41.40	41.43	42.14	41.09
Sp:	41.02	39.92	40.54	41.08	39.83	39.89	40.26	40.16	39.85	39.87	40.37	40.35	40.87	41.00	40.43	40.20	39.67	39.90	40.23	40.00	40.03	39.56
Py:	4.31	4.11	4.14	4.29	4.71	4.38	4.29	3.95	4.18	4.17	4.34	4.10	4.20	3.98	4.57	4.24	4.38	4.23	4.05	4.32	4.14	4.18
A:	25.17	25.07	25.02	25.20	25.06	25.23	25.05	25.04	25.03	25.18	25.13	24.95	25.29	25.22	25.07	25.31	25.17	25.00	25.03	25.04	24.99	25.14
C:	10.29	10.85	10.94	10.22	10.56	10.74	10.29	10.79	10.97	11.19	10.40	10.59	10.55	10.57	10.40	10.91	10.84	10.89	10.67	10.68	10.27	11.35
F:	64.54	64.09	64.04	64.58	64.37	64.03	64.67	64.17	64.00	63.63	64.47	64.46	64.15	64.21	64.53	63.79	63.99	64.12	64.30	64.28	64.74	63.51
A':	25.20	25.08	25.02	25.23	25.07	25.27	25.06	25.04	25.03	25.21	25.15	24.94	25.34	25.25	25.08	25.36	25.20	25.00	25.04	25.05	24.99	25.16
K:	0.00	0.00	0.00	0.00	0.00	0.00	0.00	0.00	0.00	0.00	0.00	0.00	0.00	0.00	0.00	0.00	0.00	0.00	0.00	0.00	0.00	0.00
F:	74.80	74.92	74.98	74.77	74.93	74.73	74.94	74.96	74.97	74.79	74.85	75.06	74.66	74.75	74.92	74.64	74.80	75.00	74.96	74.95	75.01	74.84
A:	0.24	0.25	0.25	0.24	0.24	0.25	0.24	0.25	0.25	0.24	0.25	0.25	0.25	0.24	0.24	0.24	0.25	0.25	0.25	0.25	0.25	0.25
F:	0.90	0.91	0.91	0.91	0.90	0.90	0.91	0.91	0.91	0.91	0.90	0.91	0.91	0.91	0.90	0.91	0.90	0.91	0.91	0.91	0.91	0.91
M:	0.10	0.09	0.09	0.09	0.10	0.10	0.09	0.09	0.09	0.09	0.10	0.09	0.09	0.09	0.10	0.09	0.10	0.09	0.09	0.09	0.09	0.09

Sample	P2 F2 G5 P2 F1 GR 1	-1	-2.00	-3.00	-5.00	-6.00	-7.00	-8.00	-9.00	-10.00	-11.00	-12.00	-13.00	-14.00	-16.00	-17.00	-18.00	-19.00	-20.00	-21.00	-22.00	-23.00
SiO_2	36.62	36.48	36.64	36.37	36.27	36.55	36.36	36.65	36.29	36.67	36.58	36.33	36.44	36.48	36.76	36.41	36.23	36.48	36.58	36.90	36.41	36.76
TiO_2	0.10	0.13	0.12	0.14	0.15	0.16	0.14	0.06	0.19	0.11	0.10	0.17	0.12	0.12	0.07	0.10	0.15	0.15	0.13	0.20	0.16	0.10
Al_2O_3	20.54	20.36	20.39	20.35	20.14	20.31	20.47	20.48	20.53	20.49	20.62	20.54	20.43	20.48	20.47	20.64	20.32	20.02	20.42	20.41	20.50	20.51
Cr_2O_3	0.08	0.00	0.00	0.05	0.00	0.02	0.00	0.00	0.01	0.00	0.04	0.00	0.01	0.01	0.02	0.00	0.00	0.01	0.00	0.00	0.05	0.00
Fe_2O_3	0.89	0.69	0.78	0.92	0.78	1.20	0.84	0.77	0.77	0.66	0.65	0.69	0.75	0.37	0.54	0.79	1.16	0.76	0.79	0.61	0.59	0.34
MgO	1.08	1.03	1.05	1.05	1.08	1.00	1.04	1.01	1.08	1.00	1.08	1.06	1.02	1.04	1.00	0.99	0.98	1.06	1.10	1.00	0.98	1.04
CaO	4.92	4.56	4.70	5.09	4.98	5.12	4.90	4.85	5.25	4.93	4.88	4.86	4.94	4.96	4.85	4.97	5.51	4.97	4.71	5.61	5.09	5.04
MnO	17.70	17.66	17.81	17.53	17.29	17.54	17.55	17.51	17.26	17.66	17.68	17.50	17.82	17.52	17.76	17.65	17.38	17.41	17.66	17.34	17.55	17.61
FeO	18.04	18.29	18.10	17.74	17.75	18.06	18.07	18.34	17.82	18.08	18.02	18.10	17.71	17.81	18.03	18.10	17.53	17.67	18.14	17.63	17.81	17.80
Sum	99.96	99.21	99.58	99.24	98.43	99.94	99.37	99.67	99.19	99.58	99.66	99.13	99.24	98.79	99.50	99.67	99.26	98.52	99.52	99.70	99.12	99.21
Cations																						
Si	5.948	5.972	5.974	5.949	5.976	5.946	5.943	5.970	5.933	5.974	5.955	5.942	5.959	5.981	5.992	5.934	5.928	6.002	5.966	5.992	5.957	5.999
Ti	0.013	0.016	0.014	0.017	0.019	0.019	0.018	0.007	0.024	0.014	0.013	0.020	0.015	0.015	0.009	0.013	0.018	0.018	0.016	0.025	0.019	0.012
Al	3.932	3.929	3.918	3.923	3.910	3.893	3.942	3.932	3.956	3.934	3.956	3.959	3.938	3.957	3.932	3.965	3.920	3.882	3.924	3.907	3.953	3.945
Cr	0.010	0.000	0.000	0.006	0.000	0.002	0.000	0.001	0.001	0.000	0.006	0.000	0.001	0.001	0.003	0.000	0.000	0.001	0.000	0.000	0.006	0.000
Fe^{3+}	0.109	0.085	0.096	0.114	0.096	0.147	0.104	0.094	0.095	0.080	0.079	0.085	0.092	0.046	0.066	0.097	0.143	0.094	0.096	0.074	0.072	0.042
Mg	0.261	0.251	0.256	0.256	0.265	0.242	0.253	0.244	0.264	0.242	0.263	0.259	0.248	0.253	0.242	0.241	0.240	0.260	0.267	0.241	0.240	0.253
Ca	0.856	0.799	0.821	0.892	0.879	0.892	0.857	0.847	0.919	0.860	0.850	0.851	0.866	0.871	0.847	0.868	0.966	0.875	0.823	0.976	0.893	0.880
Mn	2.435	2.449	2.459	2.429	2.413	2.417	2.429	2.415	2.390	2.437	2.438	2.424	2.469	2.434	2.451	2.436	2.408	2.427	2.439	2.384	2.432	2.434
Fe^{2+}	2.450	2.504	2.468	2.427	2.445	2.457	2.471	2.499	2.437	2.464	2.453	2.475	2.423	2.443	2.458	2.467	2.399	2.431	2.475	2.394	2.437	2.429
X_{Fe}	0.90	0.91	0.91	0.90	0.90	0.91	0.91	0.91	0.90	0.91	0.90	0.91	0.91	0.91	0.91	0.91	0.91	0.90	0.90	0.91	0.91	0.91
X_{Mn}	0.47	0.47	0.47	0.48	0.47	0.47	0.47	0.47	0.47	0.47	0.47	0.47	0.48	0.47	0.48	0.47	0.48	0.47	0.47	0.47	0.48	0.48
Site occupation																						
Si	5.948	5.972	5.974	5.949	5.976	5.946	5.943	5.970	5.933	5.974	5.955	5.942	5.959	5.981	5.992	5.934	5.928	6.002	5.966	5.992	5.957	5.999
Fe^{3+}	0.052	0.028	0.026	0.051	0.024	0.054	0.057	0.030	0.067	0.026	0.045	0.058	0.041	0.019	0.008	0.066	0.072	0.000	0.034	0.008	0.043	0.001
Al	0.000	0.000	0.000	0.000	0.000	0.000	0.000	0.000	0.000	0.000	0.000	0.000	0.000	0.000	0.000	0.000	0.000	0.000	0.000	0.000	0.000	0.000
Tetr. Z:	6.000	6.000	6.000	6.000	6.000	6.000	6.000	6.000	6.000	6.000	6.000	6.000	6.000	6.000	6.000	6.000	6.000	6.002	6.000	6.000	6.000	6.000
Ti	0.013	0.016	0.014	0.017	0.019	0.019	0.018	0.007	0.024	0.014	0.013	0.020	0.015	0.015	0.009	0.013	0.018	0.018	0.016	0.025	0.019	0.012
Al	3.932	3.929	3.918	3.923	3.910	3.893	3.942	3.932	3.956	3.934	3.956	3.959	3.938	3.957	3.932	3.965	3.920	3.882	3.924	3.907	3.953	3.945
Cr	0.010	0.000	0.000	0.006	0.000	0.002	0.000	0.001	0.001	0.000	0.006	0.000	0.001	0.001	0.003	0.000	0.000	0.001	0.000	0.000	0.006	0.000
Fe^{3+}	0.057	0.057	0.070	0.063	0.072	0.092	0.046	0.064	0.027	0.054	0.034	0.027	0.051	0.027	0.058	0.031	0.071	0.094	0.062	0.066	0.029	0.041
Oct. Y:	4.012	4.002	4.002	4.009	4.001	4.007	4.007	4.004	4.008	4.002	4.008	4.006	4.005	4.001	4.001	4.009	4.009	3.996	4.003	3.997	4.007	3.998
Mg	0.261	0.251	0.256	0.256	0.265	0.242	0.253	0.244	0.264	0.242	0.263	0.259	0.248	0.253	0.242	0.241	0.240	0.260	0.267	0.241	0.240	0.253
Ca	0.856	0.799	0.821	0.892	0.879	0.892	0.857	0.847	0.919	0.860	0.850	0.851	0.866	0.871	0.847	0.868	0.966	0.875	0.823	0.976	0.893	0.880
Mn	2.435	2.449	2.459	2.429	2.413	2.417	2.429	2.415	2.390	2.437	2.438	2.424	2.469	2.434	2.451	2.436	2.408	2.427	2.439	2.384	2.432	2.434
Fe^{2+}	2.450	2.504	2.468	2.427	2.445	2.457	2.471	2.499	2.437	2.464	2.453	2.475	2.423	2.443	2.458	2.467	2.399	2.431	2.475	2.394	2.437	2.429
X-Pos :	6.002	6.003	6.003	6.004	6.001	6.007	6.010	6.005	6.010	6.003	6.004	6.010	6.006	6.000	5.998	6.013	6.013	5.993	6.005	5.996	6.001	5.997
Total:	16.014	16.005	16.005	16.013	16.002	16.014	16.816	16.009	16.018	16.005	16.012	16.016	16.011	16.001	15.999	16.022	16.022	15.991	16.008	15.993	16.008	15.995
Endmembers																						
Ur:	0.25	0.00	0.01	0.15	0.00	0.05	0.00	0.01	0.04	0.00	0.14	0.00	0.03	0.04	0.07	0.00	0.00	0.03	0.00	0.00	0.15	0.00
Ad:	1.74	1.83	2.10	1.99	2.27	2.79	1.60	1.78	1.27	1.71	1.17	1.18	1.64	1.07	1.66	1.10	2.23	2.82	1.96	2.27	1.21	1.34
Gr:	12.49	11.48	11.57	12.86	12.38	12.05	12.66	12.32	14.02	12.63	12.97	12.98	12.78	13.44	12.45	13.34	13.84	11.78	11.75	14.01	13 65	13.34
Al:	40.72	41.72	41.10	40.36	40.74	40.88	41.11	41.61	40 53	41.04	40.80	41.19	40.33	40.70	40.95	41.03	39.89	40.55	41.21	39.93	40.54	40.50
Sp:	40.47	40.80	40.96	40.40	40.20	40.21	40.42	40.21	39.75	40.60	40.55	40.33	41.09	40.55	40.84	40.51	40.03	40.49	40.62	39.76	40.46	40.59
Py:	4.33	4.17	4.26	4.25	4.42	4.03	4.20	4.06	4.39	4.03	4.37	4.32	4.13	4.22	4.04	4.01	3 99	4.33	4.45	4.03	3.99	4.22
A:	25.18	25.06	25.06	25.16	25.03	25.16	25.18	25.10	25.20	25.06	25.15	25.18	25.12	25.01	25.00	25.25	25.25	24.91	25.08	24.92	25.11	24.95
C:	10.67	9.97	10.24	11.12	10.98	11.11	10.67	10.56	11.44	10.74	10.60	10.59	10.80	10.88	10.59	10.80	12.01	10.97	10.27	12.22	11.14	11.02
F:	64.14	64.97	64.70	63.72	63.99	63.73	64.14	64.33	63.35	64.20	64.25	64.23	64.08	64.11	64.41	63.96	62.74	64.12	64.64	62.85	63.75	64.03
A':	25.22	25.07	25.07	25.19	25.03	25.19	25.22	25.12	25.24	25.07	25.18	25.20	25.14	25.02	25.00	25.29	25.30	24.90	25.10	24.91	25.13	24.94
K:	0.00	0.00	0.00	0.00	0.00	0.00	0.00	0.00	0.00	0.00	0.00	0.00	0.00	0.00	0.00	0.00	0.00	0.00	0.00	0.00	0.00	0.00
F:	74.78	74.93	74.93	74.81	74.97	74.81	74.78	74.88	74.76	74.93	74.82	74.80	74.86	74.98	75.00	74.71	74.70	75.10	74.90	75.09	74.87	75.06
A:	0.24	0.24	0.24	0.24	0.24	0.24	0.24	0.24	0.24	0.24	0.25	0.25	0.24	0.25	0.24	0.25	0.24	0.24	0.24	0.24	0.24	0.24
F:	0.90	0.91	0.91	0.90	0.90	0.91	0.91	0.91	0.90	0.91	0.90	0.91	0.91	0.91	0.91	0.91	0.91	0.90	0.90	0.91	0.91	0.91
M:	0.10	0.09	0.09	0.10	0.10	0.09	0.09	0.09	0.10	0.09	0.10	0.09	0.09	0.09	0.09	0.09	0.09	0.10	0.10	0.09	0.09	0.09

APPENDIX D: *Garnet-muscovite geithermometers of Dickenson and Hewitt (1986), Ghent et al. (1987) and Hynes and Forest (1988).*

Granat: Chlorit:

P2 F1 P2
Profil1 F1
-1.00 C8
P (kbar): *5.00* T (°C):
DICKINSON & HEWITT (1986): *411*
GHENT et al. (1987): *413*

Granat: Chlorit:

P2 F1 P2
Profil1 F1
-2.00 C9
P (kbar): *5.00* T (°C):
DICKINSON & HEWITT (1986): *422*
GHENT et al. (1987): *423*

Granat: Chlorit:

P2 F1 P2
Profil1 F1
-3.00 C11
P (kbar): *5.00* T (°C):
DICKINSON & HEWITT (1986): *425*
GHENT et al. (1987): *426*

Granat: Chlorit:

P2 F1 P2
Profil1 F1
-5.00 C12
P (kbar): *5.00* T (°C):
DICKINSON & HEWITT (1986): *451*
GHENT et al. (1987): *449*

Granat: Chlorit:

P2 F1 P2
Profil1 F1
-6.00 C12
P (kbar): *5.00* T (°C):
DICKINSON & HEWITT (1986): *426*
GHENT et al. (1987): *426*

Granat: Chlorit:

P2 F1 P2
Profil1 F1
-7.00 C14
P (kbar): *5.00* T (°C):
DICKINSON & HEWITT (1986): *402*
GHENT et al. (1987): *405*

Granat: Chlorit:

P2 F1 P2
Profil1 F1
-8.00 C23
P (kbar): 5.00 T (°C):
DICKINSON & HEWITT (1986): 391
GHENT et al. (1987): 395

Granat: Chlorit:

P2 F1 P2
Profil1 F1
-9.00 C24
P (kbar): 5.00 T (°C):
DICKINSON & HEWITT (1986): 449
GHENT et al. (1987): 447

Granat: Chlorit:

P2 F1 P2
Profil1 F1
-10.00 C25
P (kbar): 5.00 T (°C):
DICKINSON & HEWITT (1986): 390
GHENT et al. (1987): 394

Granat: Chlorit:

P2 F1 P2
Profil1 F1
-10.00 C26
P (kbar): 5.00 T (°C):
DICKINSON & HEWITT (1986): 387
GHENT et al. (1987): 392

Granat: Chlorit:

P2 F1 P2
Profil1 F1
-11.00 C27
P (kbar): 5.00 T (°C):
DICKINSON & HEWITT (1986): 426
GHENT et al. (1987): 427

Granat: Chlorit:

P2 F1 P2
Profil2 F1
-1.00 C15
P (kbar): 5.00 T (°C):
DICKINSON & HEWITT (1986): 399

Granat: Chlorit:

P2 F1 P2
Profil2 F1
-2.00 C16
P (kbar): 5.00 T (°C):
DICKINSON & HEWITT (1986): 413
GHENT et al. (1987): 415

Granat: Chlorit:

P2 F1 P2
Profil2 F1
-3.00 C17
P (kbar): 5.00 T (°C):
DICKINSON & HEWITT (1986): 387
GHENT et al. (1987): 392

Granat: Chlorit:

P2 F1 P2
Profil2 F1
-4.00 C18
P (kbar): 5.00 T (°C):
DICKINSON & HEWITT (1986): 407
GHENT et al. (1987): 410

Granat: Chlorit:

P2 F1 P2
Profil2 F1
-5.00 C19
P (kbar): 5.00 T (°C):
DICKINSON & HEWITT (1986): 402
GHENT et al. (1987): 405

Granat: Chlorit:

P2 F1 P2
Profil2 F1
-6.00 C20
P (kbar): 5.00 T (°C):
DICKINSON & HEWITT (1986): 415
GHENT et al. (1987): 417

Granat: Chlorit:

P2 F1 P2
Profil2 F1
-7.00 C21
P (kbar): 5.00 T (°C):
DICKINSON & HEWITT (1986): 399

GHENT et al. (1987): 403

Granat:	Chlorit:
P2 F1	P2
Profil2	F1
-8.00	C1

P (kbar): 5.00 T (°C):
DICKINSON & HEWITT (1986): 417
GHENT et al. (1987): 418

Granat:	Chlorit:
P2 F1	P2
Profil2	F1
-9.00	C2

P (kbar): 5.00 T (°C):
DICKINSON & HEWITT (1986): 440
GHENT et al. (1987): 439

Granat:	Chlorit:
P2 F1	P2
Profil2	F1
-10.00	C4

P (kbar): 5.00 T (°C):
DICKINSON & HEWITT (1986): 410
GHENT et al. (1987): 412

Granat:	Chlorit:
P2 F1	P2
Profil2	F1
-11.00	C5

P (kbar): 5.00 T (°C):
DICKINSON & HEWITT (1986): 421
GHENT et al. (1987): 422

Granat:	Chlorit:
P2 F1	P2
Profil2	F1
-12.00	C6

P (kbar): 5.00 T (°C):
DICKINSON & HEWITT (1986): 421
GHENT et al. (1987): 422

Granat-Phengit-Thermometrie nach HYNES & FOREST (1988):

S1:

Granat: P1 F3	Phengit: P1 F3	Granat: P1 F3	Phengit: P1 F3	Granat: P1 F3	Phengit: P1 F2
1	85	2	84	3	4
P(kbar): 5		P(kbar): 5		P(kbar): 5	
T(°C): 458		T(°C): 484		T(°C): 456	
mg(Ph): 61		mg(Ph): 56		mg(Ph): 63	

Granat: P1 F3	Phengit: P1 F3	Granat: P1 F3	Phengit: P1 F3	Granat: P1 F3	Phengit: P1 F2
27	83	29	83	26	2
P(kbar): 5		P(kbar): 5		P(kbar): 5	
T(°C): 497		T(°C): 489		T(°C): 492	
mg(Ph): 53		mg(Ph): 53		mg(Ph): 54	

S2:

Granat: P1 F3	Phengit: P1 F3	Granat: P1 F3	Phengit: P1 F4	Granat: P1 F3	Phengit: P1 F4
30	77	31	1	32	3
P(kbar): 5		P(kbar): 5		P(kbar): 5	
T(°C): 477		T(°C): 472		T(°C): 489	
mg(Ph): 58		mg(Ph): 59		mg(Ph): 55	

Granat: P1 F3	Phengit: P1 F3	Granat: P1 F3	Phengit: P1 F3	Granat: P1 F3	Phengit: P1 F3
59	77	58	79	56	79
P(kbar): 5		P(kbar): 5		P(kbar): 5	
T(°C): 468		T(°C): 485		T(°C): 480	
mg(Ph): 58		mg(Ph): 57		mg(Ph): 57	

Granat:	Phengit:
P1 F3	P1 F1
4	3
P(kbar):	5
T(°C):	468
mg(Ph):	61

Granat:	Phengit:
P1 F3	P1 F3
25	85
P(kbar):	5
T(°C):	459
mg(Ph):	61

Granat:	Phengit:
P1 F3	P1 F4
33	4
P(kbar):	5
T(°C):	477
mg(Ph):	59

Granat:	Phengit:
P1 F3	P1 F3
54	80
P(kbar):	5
T(°C):	464
mg(Ph):	62





Author: Jasper Marold Jens Uwe.

Name of thesis: Sedimentology and structural geology of the Gariep Belt in Southern Namibia.

PUBLISHER:

University of the Witwatersrand, Johannesburg
©2015

LEGALNOTICES:

Copyright Notice: All materials on the University of the Witwatersrand, Johannesburg Library website are protected by South African copyright law and may not be distributed, transmitted, displayed or otherwise published in any format, without the prior written permission of the copyright owner.

Disclaimer and Terms of Use: Provided that you maintain all copyright and other notices contained therein, you may download material (one machine readable copy and one print copy per page)for your personal and/or educational non-commercial use only.

The University of the Witwatersrand, Johannesburg, is not responsible for any errors or omissions and excludes any and all liability for any errors in or omissions from the information on the Library website.